Jayeeta Chattopadhyay · Rahul Singh
Om Prakash   *Editors*

Innovation in Materials Science and Engineering

Proceedings of ICEMIT 2017, Volume 2

Springer

Innovation in Materials Science and Engineering

Jayeeta Chattopadhyay · Rahul Singh
Om Prakash

Editors

Innovation in Materials Science and Engineering

Proceedings of ICEMIT 2017, Volume 2

Springer

Editors
Jayeeta Chattopadhyay
Department of Chemistry
Amity University
Ranchi, Jharkhand, India

Om Prakash
Department of Mechanical Engineering
National Institute of Technology, Patna
Patna, Bihar, India

Rahul Singh
Department of Mechanical Engineering
Amity University
Ranchi, Jharkhand, India

Preface

The book entitled "Innovation in Materials Science and Engineering" will aim at all the scientists, academicians, research scholars, and students, who are interested to understand the current research persuading in the field of materials science. This book will assemble the scientific work on materials science going to be presented in International Conference on Energy, Materials and Information Technology, 2017, at Amity University Jharkhand, India. The materials science domain is immense and diverse by itself. This extravagance is both a product of advances in materials and a challenge in its future growth. This book emphasizes in all aspects of materials, from synthesis to its extraordinary and effective applications, from its physical characterizations to its cost-effectiveness. At one point, it provides an intrinsic knowledge on the nano-structured materials with their challenging and innovative applications; at some other point, it will be a source of knowledge towards the biotechnologists and pharmacologists for the recent knowledge of biomaterials research. It has also covered the essential and state-of-the-art research work of various engineering materials with important physical characteristics of materials which can be used to protect civilization from landslide hazards. Overall, a multidisciplinary scientific education on materials science and technology can be spread to the top quality experts who have a generic background in the different subdisciplines such as electronics, physics, chemistry, material science, and biotechnology.

Ranchi, India
Jayeeta Chattopadhyay
Rahul Singh

Acknowledgement

It is our pleasure to present this volume consisting of selected papers based on the oral presentation in International Conference on Energy, Materials and Information Technology at Amity University Jharkhand, Ranchi, India, on 23–24 December 2017. We would like to take this opportunity to thank all of the participants in the conference—invited speakers, presenters, and audience alike. Our special thanks go to all the keynote speakers present in the conference. We would like to thank SERB-DST for financial sponsorship for this conference. We express our heartfelt thanks to our Founder President, Dr. Ashok K Chauhan, and Chancellor, Dr. Atul Chauhan, for showing us the right path. We would like to thank Prof. (Dr.) R.K. Jha, Vice Chancellor, Amity University Jharkhand, for his enormous support. We thank Prof. (Dr.) Ajit Kr. Pandey, Director, Amity University Jharkhand, for his valuable guidance. Here, we would like to give special thanks to Dr. Nitya Garg and Mr. Pravin Singh, without whom this proceedings would not have taken proper shape. We would like to thank all the faculty, staff, and students of Amity University Jharkhand for their continuous support for making this conference successful.

Contents

Contents

About the Editors

Jayeeta Chattopadhyay received her Bachelor of Science with Honours in Chemistry from Bethune College, Calcutta University. She got her Master of Science in Chemistry from Devi Ahilya Vishwavidyalaya, Indore (2003), and Master of Technology in Fuels and Combustion from Birla Institute of Technology, Mesra, Ranchi (2005). She obtained her Ph.D. in New Energy Engineering with best doctoral thesis award from Seoul National University of Science and Technology, S. Korea (2010). She has obtained the prestigious Fast Track Young Scientist Award (2010) and early Career Research Award (2017) from Department of Science and Technology, Govt. of India. She has published more than 20 research and review articles in high-impact peer-reviewed international journals, and she is owner of one international patent. She is the reviewer of more than ten high-impact international journals and has been included in editorial board of two international journals. Her research interest includes nano-structured materials for energy applications and thero-degradation of solid waste materials. She also works on oscillatory chemical reactions and pattern formation in reaction diffusion system. Earlier she was working as Research Scientist in Birla Institute of Technology, Mesra, Deoghar Off-campus, Jharkhand. She is presently working as Senior Assistant Professor, Amity University, Jharkhand, Ranchi, India.

Mr. Rahul Singh graduated in Mechanical engineering in 2009 form BIT, post graduated in Machine Design with distinction from BIT MESRA, Ranchi in2014, and pursuing Ph.D. from National Institute of Technology, Patna since 2014. He is now an assistant professor in the department of mechanical and automation engineering at AMITY University Jharkhand, Ranchi. He had served in various organization like SSIPMT Raipur, Jain University Belgaum, and Sikkim Manipal University Gangtok. His specialized field of research are: Design of machine components, Heat and mass transfer analysis, Renewable energy, assessment of wind power and Micro wind turbine. He has done more than 10 publications in journal of national and international repute alongside conference proceedings. He had attended and organized seminar, workshop, and conference of national and international repute. Apart from research publication, he published four books on titles like fluid mechanics, fluid machinery and dynamics of machines. His subject of interest is: Fluid mechanics, Heat and Mass transfer, Strength of materials, Kinematics of machines and machine design.

Prof. (Dr.) Om Prakash: Om Prakash, graduated in Mechanical engineering in 1994, post graduated in Design and Production of Thermal Power Equipment from NIT Tiruchirappalli in 1997, and Ph.D. from Indian Institute of Technology Delhi in 2005. He is now a professor in the department of mechanical engineering and dean of faculty welfare at National institute of technology, Patna. He had served in various organization like Indian Airforce, Directorate of Training and Technical Education, Delhi college of Engineering, and Rajaram Sinde College of Engineering. His specialized field of research are: Heat and mass transfer analysis, Energy audit and energy efficiency, biogas fueled diesel engine, and Micro wind turbine. He has done more than 30 publications in journal of national and international repute. Apart from publication, he guided more than 15 students for M.Tech and 10 students (completed and ongoing) for Ph.D. He had attended and organized seminar, workshop, and conference of national and

international repute. He is the life member of professional bodies like SAEINDIA, Indian Society of Heating, Refrigerating and Air Conditioning Engineers (ISHRAE), Indian Society for Technical Education (ISTE), the Institution of Engineers (India), and Society of Energy Engineers and Managers (SEEM).

Effect of Polymer Modification on Structural and Mechanical Properties of Concrete Using Epoxy Emulsion as the Modifier

Shilpa Pal, Sachin Tiwari, Khushboo Katyal and Aditi Singh

1 Introduction

Concrete is a building material with high compressive strength, temperature resistance, and high durability and also has some limitations that include low tensile strength and low chemical resistance which have been cited by Park and Lee [1], Gorninski et al. [2], and Muthukumar and Mohan [3]. In order to reduce these disadvantages, many attempts of using polymers such as urea-formaldehyde resin, unsaturated polyester resin, methyl methacrylate, epoxy resin furan resins, and polyurethane resins have been used by researchers Ohama [4], Pratap [5] to make polymer-modified mortar(PMM)/polymer-modified concrete (PMC) as shown in Fig. 1. McKeown and Morgan [6] used epoxy polymer in concrete matrix to enhance the durability and mechanical strength of concrete. El-Hawary and Jaleel [7] studied the replacement of cement by epoxy with the percentage of 0–100 which has achieved acceptable corrosion resistance in hot marine environments at 20% of epoxy resin. Laredo Dos Reis [8] used epoxy resin which increased the compressive strength after adding glass/carbon fibers. Studies on polymer concrete with different dosage of epoxy under temperature of 22–120 °C was done which showed that there were no negative changes in the properties of concrete at 14% of epoxy dosage up to 60 °C in the study carried out by Vipulanandan and Dharmarajan [9]. Laredo Dos Reis [10] prepared prismatic and cylindrical specimens with epoxy and polyester resins and tested specimens at 23–90 °C which resulted in the decrease of flexural and compressive strengths after 60 °C. The present study focuses on the mechanical strength of polymer-modified concrete and effect of the temperature on polymer-modified concrete specimen at the age of 7, 28, and 56 days.

S. Pal · S. Tiwari · K. Katyal · A. Singh (✉)
Department of Civil Engineering, Gautam Buddha University,
Greater Noida, Uttar Pradesh, India
e-mail: aditi.peace@gmail.com
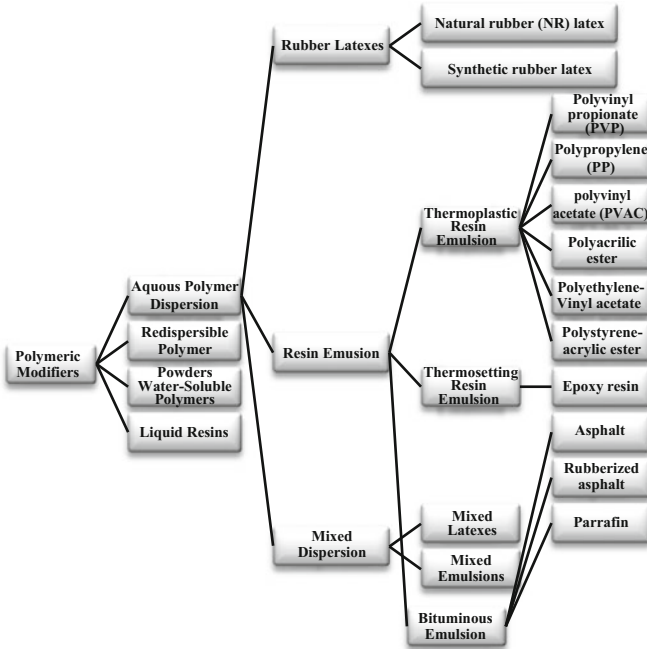
Fig. 1 Classification of polymeric modifiers for PMC and PMM

2 Methodology

Epoxy emulsion was prepared by emulsifying diglycidyl ether of bisphenol-A-based epoxy resin and amino-amide-based hardener in water by using a non-ionic surfactant. Antifoaming agent was used as an additive. The prepared epoxy emulsion had density of 1.03 g/cm^3 and total solids of 40.5 $\pm$ 2%. The quantities of polymer contents are 47, 56.4, and 70.5 kg/m^3 at 10, 12, and 15% polymer-to-cement (p/c) ratio, respectively. Coarse aggregate of 10 mm nominal size was used in the design mix. To carry out the research work, the standard tests were performed in the laboratory as per the codal provision [11]. To study the mechanical properties, four concrete mixes named C1 (control mix), C2, C3, and C4 with p/c ratio of 0, 10, 12, and 15%, respectively, and a design mix of M-40 were prepared. Slump of 70–75 mm was maintained in all the specimens. For determining the compressive strength, cube specimen of 70.6 × 70.6 × 70.6 mm (three cubes for each mix) was cast and then tested by compression testing machine (CTM) test technique [12]. Beams specimen of 100 × 100 × 500 mm (three beams for each mix) was cast for determining the flexural strength of the hardened concrete. Also, the effect of temperature on the compressive strength of the hardened concrete was carried out for which three cubes of each mix of 70.6 × 70.6 × 70.6 mm were cast. The test was carried out at of 7, 28, and 56 days. To prepare samples for SEM testing, 100 g of hardened concrete

Table 1 Concrete mix design for all the concrete mixes

Ingredients	Cement	Water (w/c = 0.4)	FA	CA	PC
C1 (control mix)	470	188	913.614	838.245	–
C2 (10% p/c)	423	188	913.614	838.245	47
C3 (12% p/c)	413.6	188	913.614	838.245	56.4
C4 (15% p/c)	399.5	188	913.614	838.245	70.5

FA Fine aggregate
CA Coarse aggregate
PC Polymer content

sample of each mix was crushed and then passed through 75-micron sieve. And 10 g of passing content of each mix was then collected and tested.

3 Mix Design

A concrete mix (control mix) of grade M-40 as per IS 10262-2009 and IS 456-2000 procedure has been designed as follows in Table 1.

4 Tests and Results of Concrete

4.1 Slump Test

Slump test was carried out on all the mixes as per IS: 1199-1959 [11] to check the workability of the fresh concrete. From Table 2, it can be seen that the slump value of all the specimens is between 70 and 75 mm.

Table 2 Slump test results

Mix design	C1	C2	C3	C4
Slump (mm)	75	73	73	74

Table 3 Compressive strength test results of M-40 grade

Days	C1 (N/mm^2) [control mix]	C2 (N/mm^2) [10% p/c]	C3 (N/mm^2) [12% p/c]	C4 (N/mm) [15% p/c]
7	31.88	22.17	28.86	33.24
28	42.74	31.12	40.33	45.71
56	45.99	35.86	44.89	50.98

4.2 Compressive Strength Test

To find out the compressive strength of control mix and polymer-modified concrete, cubes of 70.6 × 70.6 × 70.6 mm of each mix were cast. The test was performed on the cube specimens at the ages of 7, 28, and 56 day results of which are shown as in Table 3.

The results show that the compressive strength of polymer-modified concrete increases with the addition of the polymers in the design mix. The compressive strength of PMC is less than that of control mix when p/c ratio is less than 12% while it increases when the p/c ratio is 15%. After 28 days of curing, the percentage decrease in compressive strength is 27.18 and 5.63% for mix C2 and C3, respectively, while the percentage increase in strength is 6.76% for mix C4. The reason for the decrease in compressive strength can be attributed to epoxy emulsion enclosing the unhydrated cement particles, preventing such particles from hydrating with water, delaying the reaction of cement hydration. The strength of polymer-modified concrete is increased because of formation of polymer film on the surface that coarse aggregates and cement particles develop a strong bond between cement and aggregates that help in retaining internal pressure and also bridge the micro-cracks and prevent crack propagation. Decrease in porosity due to the filling effect of polymer also contributes to increase of strength. Maximum strength was gained in mix C4 which is PMC with 15% p/c ratio showing that epoxy emulsion-modified concrete shows better strength than conventional concrete as illustrated in Fig. 2. It is also observed that there is an increment in the strength of PMC as compared to conventional concrete after 28 and 56 days of curing, by 6.94 and 10.85%, respectively. This is because in PMC the process of polymerization continues for long period of time while in case of conventional concrete cement hydration is almost completed at the age of 28 days.

4.3 Effect of Temperature on Compressive Strength

To find the effect of temperature on compressive strength, cubes of 70.6 × 70.6 × 70.6 mm of each mix were cast and kept at 200 °C for 3 h prior to the testing. From the results of the testing as shown in Table 4, it is observed that the strength of conventional concrete increased with temperature while it decreased in case of PMC. The percentage increase in unmodified concrete after 56 days of curing is

Fig. 2 Comparison between compressive strength of control mix and PMC at different age of curing
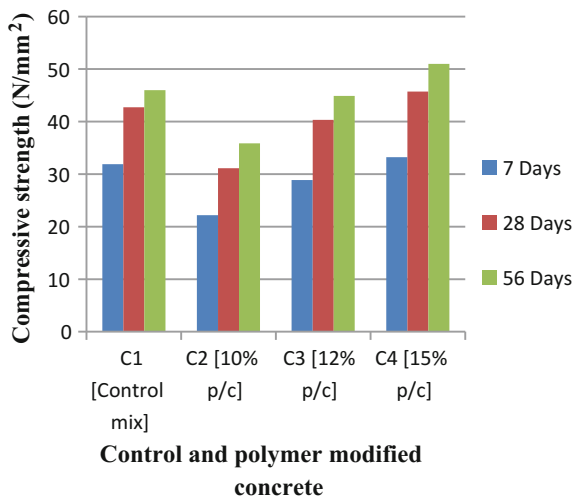
Table 4 Test results of effect of heating on compressive strength of concrete

Days	C1 (N/mm^2) [control mix]	C2 (N/mm^2) [10% p/c]	C3 (N/mm^2) [12% p/c]	C4 (N/mm^2) [15% p/c]
7	34.73	20.93	26.56	30.06
28	43.96	29.11	37.2	42.36
56	47.54	32.17	41.89	47.95

3.3% and the decrease in strength is 10.29, 6.68, and 5.94% for mix C2, C3, and C4, respectively. The decrease in strength was the highest in case of mix C2 with 10% p/c ratio as shown in Fig. 3.

The reason for loss in compressive strength due to increase in temperature in case of PMC can be attributed to the dehydration of cement paste and also due to debonding between the cement paste, the polymer, and the aggregate that leads to breakdown of interfacial bond. The strength of unmodified concrete is increased to a great extent because of increased rate of heat of hydration.

4.4 Flexural Test

For flexural testing, three beams of $100 \times 100 \times 500$ mm of each mix were cast and cured for 7, 28, and 56 days. The test was performed as per IS: 516-1959 [12]. The control mix C1 beams were cured in water, whereas the other three PMC specimens were air-cured. Table 5 shows the test results which lead to the conclusion that flexural strength of concrete increases with increase in p/c ratio and flexural strength of PMC with 15% p/c ratio is more than that of control mix as shown in Fig. 4.

Fig. 3 Comparison between effect of temperature on compressive strength of control mix and PMC
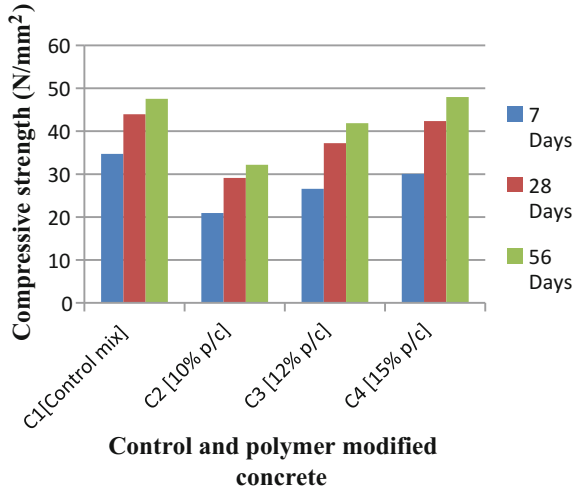
Table 5 Flexural strength test results

Days	C1 (N/mm^2) (control mix)	C2 (N/mm^2) [10% p/c]	C3 (N/mm^2) [12% p/c]	C4 (N/mm^2) [15% p/c]
7	5.37	3.53	4.7	5.67
28	6.1	4.6	5.67	6.5
56	6.56	5.28	6.17	7.13

Fig. 4 Comparison between flexural strength of control mix and PMC at different age of curing
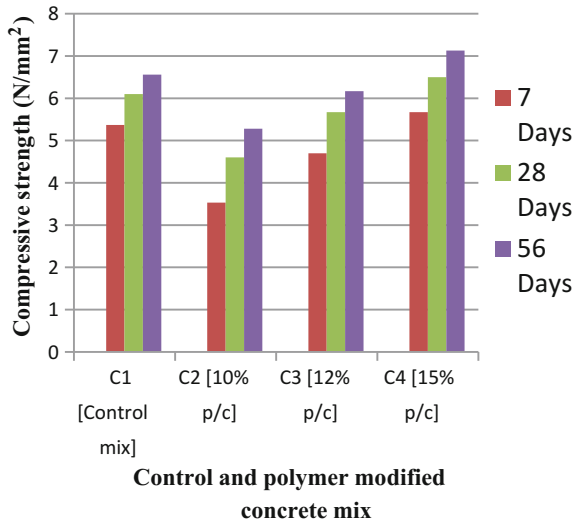
The strength of PMC is less than that of control mix when p/c ratio is less than 12% while it increases when the p/c ratio is 15%. After 28 days of curing, the percentage

decrease in flexural strength is 24.59 and 7.05% for mix C2 and C3, respectively, while the percentage increase in strength is 6.55% for mix C4. It is also observed that there is a great increment in strength of PMC as compared to conventional concrete after 56 days of curing, with percentage increment of strength of mix C4 being 8.68% while percentage increase in strength when compared to the strength gained after 28 days is 7.54% for unmodified concrete and 9.69% for C4 mix.

4.5   Scanning Electron Microscope (SEM)

SEM is a type of microscope that provides information about the structure and composition of the given sample by producing various signals from electrons and atoms of the sample's interaction [13].

To prepare samples for SEM testing, hardened concrete of each mix was crushed in the mortar and pestle (manually) and then passed through 75-micron sieve. And 10 g of passing content of each mix was then collected and tested. SEM images of the four mixes as shown in Figs. 5, 6, 7, and 8 illustrate the difference between the ratio (C2 mix).

By seeing the images, it is observed that in epoxy emulsion-modified concrete, polymer particles surround the aggregates, showing that polymer acts as a binder. The micro-cracks form a three-dimensional structure through polymer film and hence eliminate the micro-cracks to a great extent. Modification by epoxy emulsion decreased the amount of porosity, and the bridge phases appeared between the matrix and the aggregate. Due to this property of polymer, it can bridge the cracks
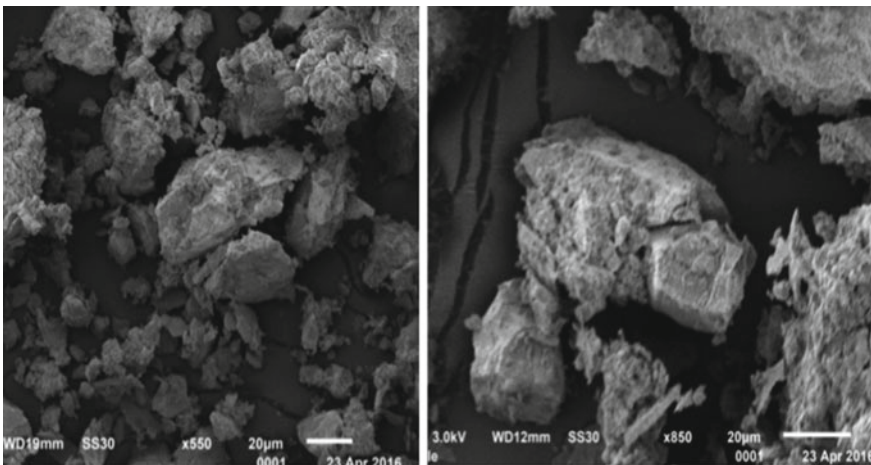
Fig. 5 SEM images of unmodified concrete (C1mix)
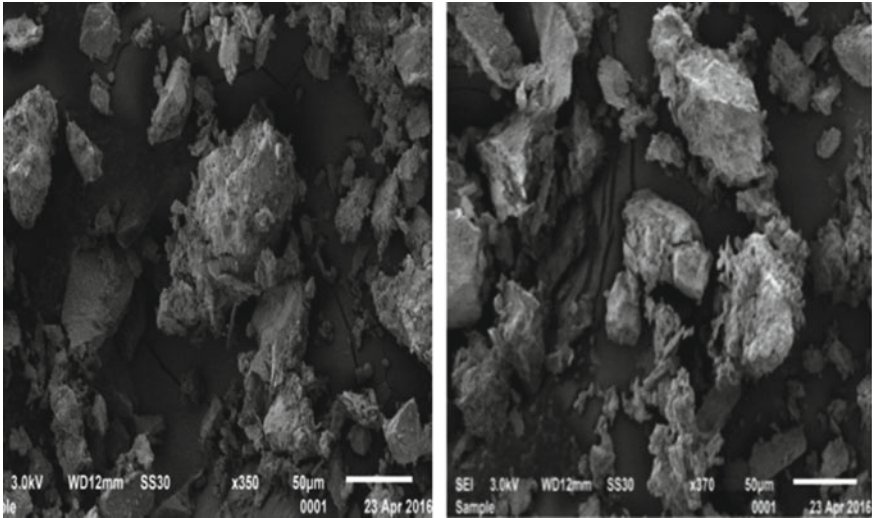
Fig. 6 SEM images of PMC with 10% p/c ratio (C2 mix)
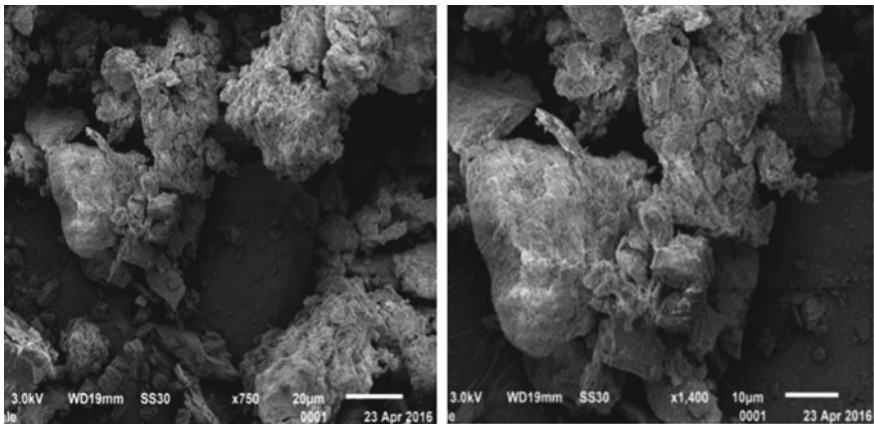
Fig. 7 SEM images of PMC with 12% p/c ratio (C3 mix)

formed when the PMC is under the stress, preventing further expansion of crack, which results in the better strength and durability to PMC.

5   Conclusions

- The compressive and flexural strength results showed that the strength increases with increase in epoxy polymer content. Both compressive and flexural strengths
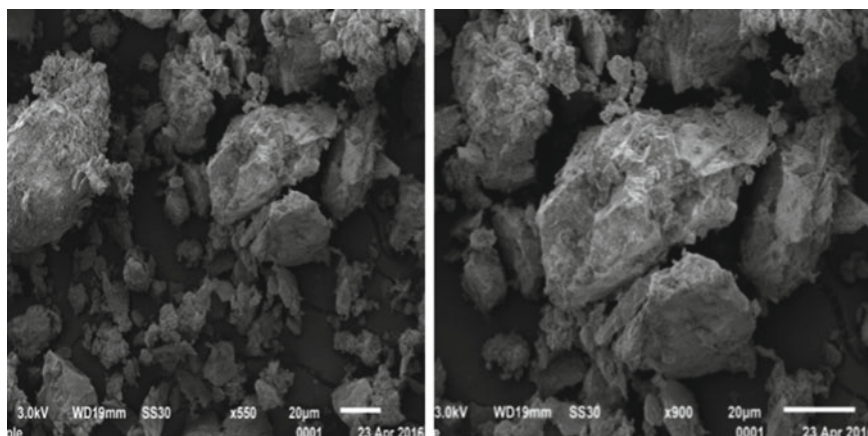
Fig. 8 SEM images of PMC with 15% p/c ratio (C4 mix)

of the PMC are greater than that of control mix when the polymer-to-cement ratio is 15%.

- The compressive and flexural strengths of PMC after 56 days of curing increased to a great extent in comparison to the strength gained after 28 days of curing.
- The compressive strength of conventional concrete increases with increase in temperature while it decreases in case of PMC.
- SEM results showed that polymer particles surround the aggregates showing that it acts as a binder. The micro-cracks formed a three-dimensional structure through polymer film which results in elimination of the micro-cracks to a great extent.

References

1. Park SB, Lee BI. Mechanical properties of carbon-fiber-reinforced polymer-impregnated cement composites. Cement Concrete Composites 1993; 15(3):153–163.
2. Gorninski Dal JP, Molin DC, Kazmierczak CS. Strength degradation of polymer concrete in acidic environments. Cement Concrete Composite 2007; 29(8):637–645.
3. Muthukumar M, Mohan D. Studies on furan polymer Concrete. Journal Polymer Research 2005; 12:231–241.
4. Ohama Y. Recent progress in concrete-polymer composites. Advance Cement Material 1997; 5(2):31–40.
5. Pratap A. Vinyl ester and acrylic based polymer concrete for electrical applications. Progress in Crystal Growth and Characterization of Materials 2002; 45:117–125.
6. McKeown PA, Morgan GH. Epoxy granite: a structural material for precision machines. Precision Engineer 1979; 1:4227–4229.
7. El-Hawary MM, Jaleel AA. Durability assessment of epoxy modified concrete. Construction Building Materials 2010; 24:1523–1528.
8. Laredo Dos Reis JM. Mechanical characterization of fiber reinforced polymer concrete. Material Research 2005; 8:357–360.

9. Vipulanandan C, Dharmarajan N. Effect of temperature on the fracture properties of epoxy polymer concrete. Cement Concrete Research 1988; 18(2):265–276.
10. Laredo Dos Reis JM. Effect of temperature on the mechanical properties of polymer mortars. Material Research 2012; 15(4):645–649.
11. IS 1199 (Reaffirmed 2004). Methods of sampling and analysis of concrete. Bureau Indian Standard 1959:8–10.
12. IS 516 (Reaffirmed 2004). Method of test for strength of concrete. Bureau Indian Standard 1959:9–18.
13. https://www.nts.com/services/advancedanalytical-services/sem-eds-analysis.

Moisture Absorption Behavior and Mechanical Properties of Banana Fiber-Reinforced Fly Ash/Epoxy Composites

Badremanir Kauser, Vikas Upadhyay, Vineet Chak and Faisal Hasan

1 Introduction

The natural fiber-reinforced polymer composites are now increasingly investigated by the scientific community because of increasing environmental awareness and sustainability issue. A variety of natural fibers are abundantly available across the world, availability of which depends on geographical and climatic conditions. They offer a wide range of properties such as high specific strength and modulus, lightweight, low cost, recyclability making them suitable for a large number of engineering applications [1]. Natural fibers such as jute, banana, hemp, sisal, flax, and nettle are easily available in abundance and can meet the demand of renewability, biodegradability, and recyclability of composites. Apart from the mentioned advantages, natural fiber composites also have certain shortcomings such as poor interface bonding and wettability, low modulus of elasticity, high moisture absorption, less durability, and variable properties.

Natural fiber composite (NFC) can be fully biodegradable or partially degradable depending upon whether the fiber and matrix both are biodegradable or only fiber is biodegradable. This work focuses on partially biodegradable banana fiber composite. Banana fiber is an agricultural waste which can be suitably used as reinforcement in NFC. Pothan et al. [2] reported that volume fraction of banana fiber in reinforced polyester composite affects the mechanical property and maximum strength was

B. Kauser (✉) · V. Upadhyay
Mechanical Engineering Department, National Institute of Technology
Patna, Patna 800005, India
e-mail: badremani@gmail.com

V. Chak
Forge Technology Department, NIFFT Ranchi, Ranchi 834003, India

F. Hasan
Zakir Hussain College of Engineering and Technology,
Aligarh Muslim University, Aligarh, India

observed at 40% fiber loading. Pujari et al. [3] reported that alkali treatment of banana fibers reduces the fiber impurity, decreases moisture absorption, and improves matrix reinforcement interaction. Bakria et al. [4] also reported that alkaline-treated fiber composites have superior properties than untreated fiber composites. Mukta and Keerthi [5] reported that fire resistance and moisture absorption capability of banana fiber-reinforced polyester composite increase with an increase in composite thickness.

Fly ash is a by-product of coal-fired power plant, and its composition mainly depends on the coal properties and combustion temperature. It is now increasingly used in concrete and bricks in large volumes and thus provides environmental solution to the disposal of fly ash. Some attempts have also been made in manufacturing sector such as: Fly ash was used as filler in polymer composites by Dadkar et al. [6], Shanmugam et al. [7], Goh et al. [8], just to name a few. Fly ash was also used with natural fiber composites. Acharya et al. [9] investigated the effect of ash on mechanical properties of jute polymer composite by mixing epoxy matrix with 30% fly ash to fabricate woven jute fiber composite. They reported that cracking of fiber structure was avoided due to the adherence of fly ash particles. Raghavendra et al. [10] studied the effect of fly ash on mechanical properties of the natural fiber hybrid epoxy composite. They fabricated composite with jute fiber, glass fiber, fly ash, and epoxy matrix by hand lay-up technique and reported that the addition of fly ash in jute epoxy composite increased tensile strength by 10% and flexural strength by 20%.

This work focuses on studying the effect of addition of fly ash in banana fiber epoxy composite and compares the performance of epoxy composite and fly ash/epoxy composite in terms of moisture absorption and mechanical properties.

2 Experimental Details

2.1 Fabrication Procedure

Banana fibers were purchased from the commercial market and were dried in sunlight to remove the moisture. After that, fibers were arranged in the proper orientation and cut into 20 cm length. Fly ash used in this work was acquired from Obra Thermal Power Station, Obra, Uttar Pradesh. Epoxy resin and hardener (diethylene triamine) were purchased from ASES Chemical Works, Jodhpur. Both composites were then fabricated by hand lay-up technique using plastic sheet, roller, releasing agent, etc. During the fabrication of composites, epoxy resin with or without fly ash was mixed with hardener and applied on fibers by a brush. A releasing agent was used to easily remove the fabricated composite from the mold. A roller was used to remove air or voids from the uncured composite. After removing the air, a constant load was applied on the uncured composite for 24 h. After curing, the composites were taken out from the mold and are shown in Fig. 1. Epoxy composite contains epoxy and
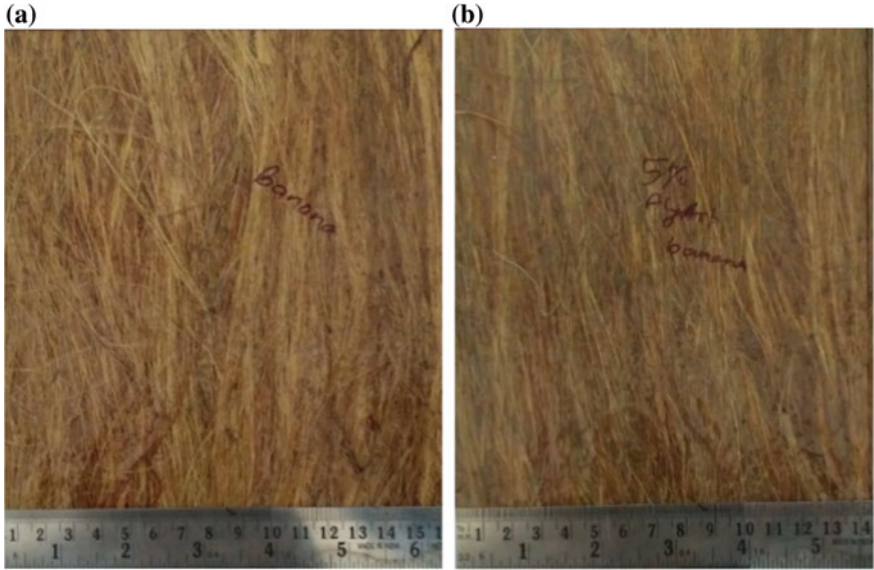
Fig. 1 Banana epoxy composite and banana fly ash epoxy composite

hardener mixed in the ratio of 10:1 with 10% fiber content whereas epoxy fly ash composite contains 5% fly ash mixed with epoxy in former composition.

2.2 *Moisture Absorption*

Moisture absorption test was carried out to know the amount of moisture absorbed by the composite because absorption of moisture adversely affects the properties of the composite. For the measurement of moisture absorption, specimens were cut from each composite as per ASTM D 570 and dipped into distilled water. The test specimens were taken out from distilled water at every 12 h interval, and the excess water was removed from the surface. These samples were then weighed, and the moisture absorption was calculated by the formula given below for each 12 h time interval [9].

$$\text{Moisture absorption } (\%) = [(W_t - W_o)/W_o] \times 100$$

where

W_t final weight of specimen
W_o initial weight of specimen
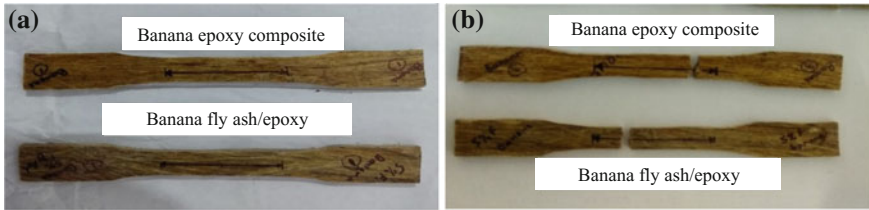
Fig. 2 Representative samples of banana epoxy composites and banana fly ash/epoxy composites **a** before tensile test and **b** after tensile test

2.3 Tensile Test

For tensile testing, three specimens from each composite were cut as per ASTM D 638 as shown in Fig. 2a. Gauge length of specimens was taken as 50 mm. A universal testing machine at 5 mm/min speed was used to test the tensile strength of specimens. After tensile test (Fig. 2 b), the tensile properties of each composite were calculated by determining the average of three replications.

3 Results and Discussion

The moisture absorption values of banana composite with and without fly ash up to saturation point are presented in Table 1. It is evident from the table that banana composite had a very high moisture absorption rate in first 24 h which accounts for almost 50% of the total moisture absorbed by the composite up to saturation point. After 24 h, the rate of moisture absorption in banana composite was decreased and it becomes saturated by absorbing 14.74% water. Banana composites with fly ash absorbed less moisture (12.43%) as compared to banana composites without fly ash reducing it by 15.67%. However, the trend of moisture absorption was found similar to epoxy composite; i.e., almost 50% of total moisture was absorbed in first 24 h. Composites with fly ash absorbed less moisture because fly ash may have restricted the path (capillary/gaps) through which moisture reaches to fibers.

It is evident from Table 2 that banana composites with fly ash had higher value of tensile strength, Young's modulus, and toughness as compared to banana composites without fly ash. The addition of fly ash increased tensile strength by 15.7% and Young's modulus by 12.38% as the fly ash particle increased interfacial bonding due to adherence of fly ash [9]. Increase in toughness was also significant accounting for 18.39%. However, the addition of fly ash adversely affects the stiffness and reduces it by 3.43%.

Table 1 Moisture gained in banana composite with and without fly ash up to saturation point

Time (h)	Weight gain (%)	
	Banana composite without fly ash	Banana composite with 5% fly ash
0	0	0
12	5.73	4.52
24	7.82	6.28
36	8.28	6.64
48	9.19	7.41
60	9.92	7.91
72	10.37	8.40
84	10.83	8.76
96	11.37	9.18
108	11.46	9.32
120	12.10	9.96
132	12.46	10.38
144	12.65	10.52
156	12.92	10.80
168	13.19	11.08
180	13.47	11.23
192	13.74	11.44
204	13.92	11.58
216	14.10	11.72
228	14.10	11.79
240	14.47	12.07
252	14.65	12.22
264	14.74	12.36
276	14.74	12.43
288	14.74	12.43
300	14.74	12.43
312	14.74	12.43

Table 2 Tensile properties of fabricated composite materials

S. No	Name of composites	Ultimate tensile strength (MPa)	Young's modulus (MPa)	Stiffness (KN/m)	Toughness (KJ/m^3)
1	Banana epoxy	20.4	680.57	835.8	600.16
2	Banana fly ash/epoxy	23.6	764.8	807.1	710.52

4   Conclusions

The experimental study revealed that banana fiber-reinforced fly ash/epoxy composite absorbed less moisture (15.67%) as compared to banana fiber-reinforced composite. Moreover, fly ash/epoxy composite also provided improved mechanical properties such as: Tensile strength was 15.7%, Young's modulus was 12.38%, and toughness was 18.39% higher than epoxy composites. However, the addition of fly ash in epoxy composite resulted in the reduction of stiffness accounting for 3.43%. The results obtained were encouraging, but a detailed study is essential to fully explore the effects of fly ash addition in banana-reinforced epoxy composites.

References

1. T P Sathishkumar, P Navaneetha krishnan, S Shankar, R Rajasekar and N Rajini, "Characterization of natural fiber and composites – A review", Journal of Reinforced Plastics and Composites, 32(19) 1457–1476.
2. Pothan L.A., Oommen Z., Thomas S., "Dynamic mechanical analysis of banana fiber reinforced polyester composites", Composites Science and Technology; 2003; 63: 283–293.
3. Pujari Satish, Ramakrishna A., Suresh Kumar M, "Comparision of Jute and Banana Fiber Composite: A Review", International Journal of Current Engineering and Technology 2014:121–126.
4. Muhammad Khusairy Bin Bakria, Elammaran Jayamania, Sinin Hamdanb, "Processing and Characterization of Banana Fiber/Epoxy Composites: Effect of Alkaline Treatment", Materials Today: Proceedings 4 (2017) 2871–2878.
5. K.Muktha & B.S.Keerthi Gowda, "Investigation of Water Absorption and Fire Resistance of Untreated Banana Fibre Reinforced Polyester Composites", Materials Today: Proceedings 4 (2017) Volume 4, Issue 8 8307–8312.
6. Nandan Dadkar, Bharat S. Tomar, Bhabani K. Satapathy, Evaluation of flyash-filled and aramid fibre reinforced hybrid polymer matrix composites (PMC) for friction braking applications Materials and Design 30 (2009) 4369–4376.
7. Nagendiran Shanmugam, Ibnelwaleed A. Hussein, Adel Badghaish, Abdelrahman Nasr Shuaib, Sarfaraz Ahmed Furquan, Mohammed H. Al-Mehthel, Evaluation of oil fly ash as a light stabilizer for epoxy composites: Accelerated weathering study, Polymer Degradation and Stability 112 (2015) 94–103.
8. C.K.Goh, S.E.Valavan, T.K.Low, L.H.Tang, Effects of different surface modification and contents on municipal solid waste incineration fly ash/epoxy composites, Waste Management, 58, 2016, 309–315.
9. Acharya S.K., Mishra P, Mishra S C, "Effect on Environment on Mechanical properties of Fly Ash Jute Polymer Composite", Indian Journal of Engineering and material science. Vol.15, December 2008, PP 483–488.
10. Raghvendra G, Acharyar S.K., Pal S.K., Ojha S., "Mechanical Properties of fly ash filler in Natural Fiber-Hybrid Epoxy Composites", 7th symposium on feed stock recycling of polymeric materials, 23–26 October 2013.

Effect of Chemical Modification on Physical Properties of Natural Fiber-Reinforced Hybrid Polymer Composites

Debasmita Pani and Punyapriya Mishra

1 Introduction

Development of new materials is essential for growth of civilization. Composites prepared with natural fibers as reinforcements in polymer matrices are an emerging field in polymer science. Vegetal fibers have a complex structure, composed of vast variety of organic compounds such as (1) cellulose and hemicellulose which make up more than 50% of the fiber and provide the required tensile strength, (2) lignin having high molecular weight which provides rigidity as well as acts as binder for cellulosic fibers and energy storage system waxes, (3) carbon content for providing stiffness, and (4) varied fatty acids and pectins. The percentage composition of all these constituents in a fiber depends on the maturity, origin, and the conditions in which the fibers are obtained from its sources [1]. The hydrophilic natural fibers suffer from certain drawbacks such as incapability of stronger interaction with the hydrophobic polymer matrix, proneness to assemble as clusters during processing, and its high moisture absorption tendency remarkably influence its suitability as reinforcement with polymer matrix [2]. Surface modification of fibers through various physical and chemical treatments is generally recommended to combat the incompatibility of fibers despite the fact that these treatments have unfavorable influence on economics. Chemical treatments can positively alter the interfacial interaction and bonding between the hydrophilic fiber and hydrophobic matrix and reduce the moisture absorption rate of fibers thus altering the characteristic features of natural fibers [3].

D. Pani (✉) · P. Mishra
Department of Mechanical Engineering, Veer Surendra Sai University of Technology, Burla, Odisha 768018, India
e-mail: pani.debasmita317@gmail.com

Table 1 Chemical composition and crystallinity index of fibers [5]

Fiber type	Density (g/cm^3)	Cellulose (wt%)	Hemicellulose (wt%)	Lignin (wt%)	Ashes (wt%)	Crystallinity index (%)
Luffa cylindrica	0.82	62	20	11.2	0.40	59.1
Bagasse	1.25	69.4	21	4.4	0.6	45.2
Coir	1.2	43–53	14.7	38–40	–	44

2 Materials Required

2.1 Luffa Fiber

Luffa is a plant grown as tropical and subtropical vines belonging to the cucumber or Cucurbitaceae family. They are of the following three species: Luffa acutangula, Luffa cylindrica (also known as Luffa aegyptiaca), and Luffa operculata. In the present study, Luffa sponge from Luffa cylindrica plant was bought from local market of Burla, Odisha, India. The hoop wall in longitudinal section (woven mat form) is taken as reinforcement in the present study.

2.2 Bagasse Fiber

Bagasse is the fibrous matter that remains after extraction of juice from sugarcane in sugar and alcohol industry. Outer layer of bagasse is called rind (lignocellulosic layer), and inner layer is called pith (containing most of sucrose). In the present study, outer rind portion of bagasse fibers are taken as short fiber reinforcements of embedded length greater than 9.18 mm such that the fiber does not pullout or rupture during fiber pull out test [4]. Bagasse fiber was collected locally for the present study.

2.3 Coir Dust

Coir is a lignocellulosic fiber obtained from the husk of ripened coconuts grown extensively in tropical countries. In the present study, coconut coir was collected locally and was used in fine coir dust form as particulate reinforcement in the fabricated composite.

The percentage composition of the fibers and the density of the three chosen fibers are given in Table 1.

2.4 NaOH

Sodium hydroxide with molarity 40.00 g/mol was used in the present study.

2.5 Epoxy and Hardener

Epoxy (LY556) also known as DGEBA (diglycidyl ether of bisphenol-A) resin was used. Hardener (HY951) also known as triethylenetetraamine (TETA) (IUPAC name NN0-bis (2-aminoethylethane-1, 2-diamin)) was used.

3 Experimentation

3.1 Chemical Treatment

The collected fibers were first washed thoroughly with normal tap water to separate out the dirt and other particles adhered to the fiber surface. Then the fibers were mercerized with 5% NaOH solution for 4 h at room temperature by maintaining solution to fiber ratio of 15:1. The treated fibers were then washed several times with distilled water to clear away any NaOH clinging to the surface of the fiber till neutral pH of 7 was attained. This treatment of fibers was followed by first drying them at room temperature for 48 h and then in oven at 100 °C for 6 h. The mercerization of natural fiber occurs according to Eq. (1) [6].

$$Fiber - OH + NaOH \rightarrow Fiber - O^- - Na^+ + H_2O \qquad (1)$$
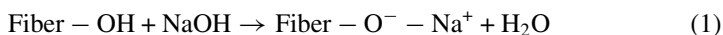
3.2 Characterization of Fibers

3.2.1 Fourier-Transform Infrared Spectroscopy (FTIR)

The alteration occurred on the surface of the fiber due to the chemical treatment was studied using FTIR. FTIR Nicolet 6700/Thermofisher Scientific in the region 500–4000 cm^{-1} and at a resolution of 0.5 cm^{-1} was used for FTIR analysis in the present study.

3.2.2 SEM Analysis

The morphology of the fibers prior to treatment and after treatment with NaOH was examined with 'Zeiss' manufactured Scanning Electron Microscope.

3.3 Preparation of Composite

3.3.1 Mold Preparation

Wooden molds with dimensions $(14 \times 12 \times 4)$ mm^3 were prepared and fixed over a cardboard. The mold was properly covered with silicon paper.

3.3.2 Composite Fabrication

Hand lay-up technique was employed for composite production. The matrix was prepared by properly mixing Epoxy LY556 and hardener HY951 in a ratio of 10:1 by weight. Then the chemically treated fibers according to fixed composition (Table 2) were added and well mixed with it. The mixture was then poured onto the mold and covered by silicon paper followed by glass plate. A weight of 5 kg was put over the glass plate for removal of trapped air inside the mixture. Curing of epoxy matrix compose occurs at room temperature over a period of 24–48 h. After 48 h, the mold was broken and the fabricated composites were ejected out. The images of fabricated composites are shown in Fig. 1.

Table 2 List of fabricated composites

Sl. No.	Composite composition	Represented as
1	Luffa single mat-reinforced composite	L
2	Bagasse 20 wt% reinforced composite	B
3	Coir dust 10 wt% reinforced composite	C
4	Coir dust 5 wt% and bagasse 5 wt% reinforced hybrid composite	CB
5	Bagasse 10 wt% sandwiched between two luffa fiber mat-reinforced hybrid composites	LBL
6	Coir 10 wt% sandwiched between two luffa fiber mat-reinforced hybrid composites	LCL
7	Coir 5 wt% and Bagasse 5 wt% sandwiched between two luffa fiber mat-reinforced hybrid composites	L(CB)L
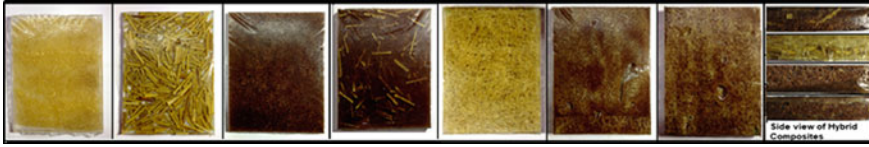
Fig. 1 Images of fabricated composites slabs

3.4 Study of Physical Properties

3.4.1 Density Measurement and Determination of Volume Fraction of Void

(i) Theoretical density was computed utilizing Eq. (2).

$$\text{Density} = \frac{\text{Mass of Composite (in grams)}}{\text{Volume of Composite (in cc)}} \tag{2}$$

(ii) Actual density was experimentally determined according to ASTM D-792 standard procedure.

(iii) Volume fraction of voids (V_v) in composites was computed according to Eq. (3).

$$V_v = \frac{\text{Theoretical Density} - \text{Actual Density}}{\text{Theoretical Density}} \tag{3}$$

4 Results and Discussion

4.1 Fourier-Transform Infrared Spectroscopy (FTIR)

The plot between %transmittance and wavenumber graph for the raw luffa fiber and chemically modified luffa fibers are plotted in the graphs shown in Figs. 2 (a and b).

The peak at 2850.7 cm^{-1} in both unmodified and modified fibers represents the aldehyde C–H. There are no changes in the main functional groups of Luffa cylindrica fiber after chemical treatment. Peak at 1047 cm^{-1} corresponds to aromatic C–H in plane deformation, and C–O deformation [7] for primary alcohol in lignin shows greater intensity in chemically modified luffa. There is a slight shift of peak around 862 cm^{-1} in treated fiber which represents an antisym out of phase ring. The wideness of –OH band reduced for alkali-treated fiber as compared to untreated fiber. Peak at 1738 cm^{-1} also reduced due to removal of hemicellulose. Removal of OH band decreased of the intensity at 1608 cm^{-1} by absorbing water molecules by alkalization [8].

(a)

(b)

(c)

(d)
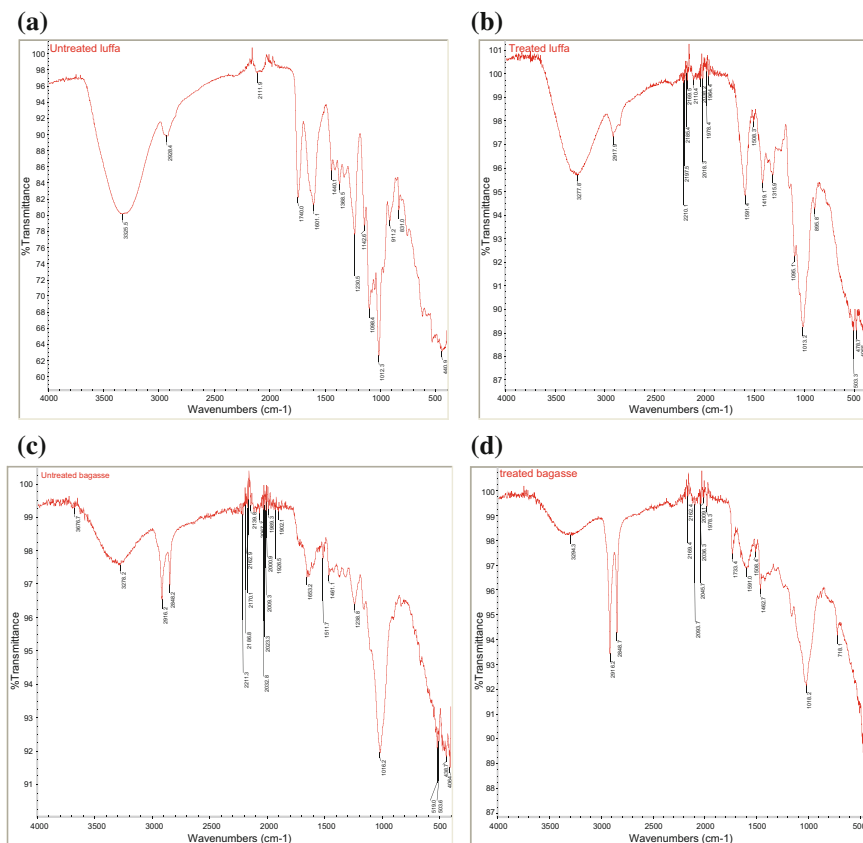
Fig. 2 **a** FTIR spectra of luffa fiber before treatment. **b** FTIR spectra of luffa fiber after treatment. **c** FTIR spectra of bagasse before alkali treatment. **d** FTIR spectra of bagasse after alkali treatment

Figures 2 (c and d) show FTIR spectra of raw and chemically altered bagasse. Mercerization caused the peak at 3409.76 cm^{-1} in bagasse to shift to 3418.88 cm^{-1}. Medium-intensity band could be seen in raw fiber at 828.32 cm^{-1} due to β-glycosidic linkage. The spectra reflect steady transformation of raw bagasse [9].

4.2 SEM Analysis

The SEM images of unmodified and modified luffa fiber, bagasse, and coir are depicted in Figs. 3, 4, and 5 (a) and (b), respectively. Untreated fiber shows the existence of an amorphous waxy protective layer on its surface which contributes to poor
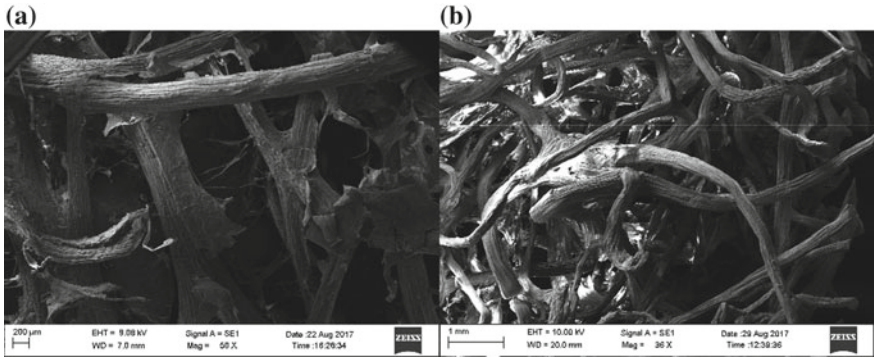
Fig. 3 Micrograph of luffa fiber. **a** Untreated luffa. **b** Chemically treated luffa
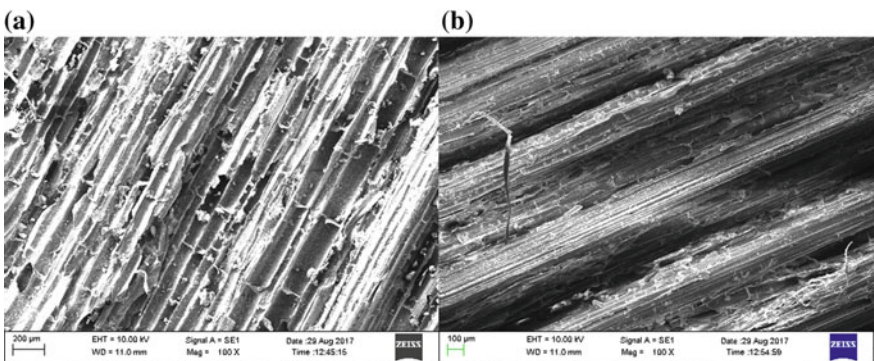
Fig. 4 Micrograph of bagasse fiber. **a** Untreated bagasse. **b** Treated bagasse

fiber–matrix adhesion [10]. The micrograph of treated fiber appears to be clean and smooth because of elimination of certain amount of lignin and hemicellulose which are gummy and waxy in nature. It can be observed that the alkali treatment caused disintegration of the micro fibrillar structure (fibrillation) and decrease in diameter of fiber due to removal of bonding components like lignin and hemicellulose [11, 12].

The fibrillation of fiber increases its available surface area to interact with the matrix [13] and thus improves the interfacial bonding between the fiber and the matrix. Ghali et al. [14] also studied the morphology of NaOH modified and unmodified luffa fibers using SEM analysis. The SEM results revealed elimination of lignin, pectin, and hemicellulose substances, and the alterations in the features of its surface structure.
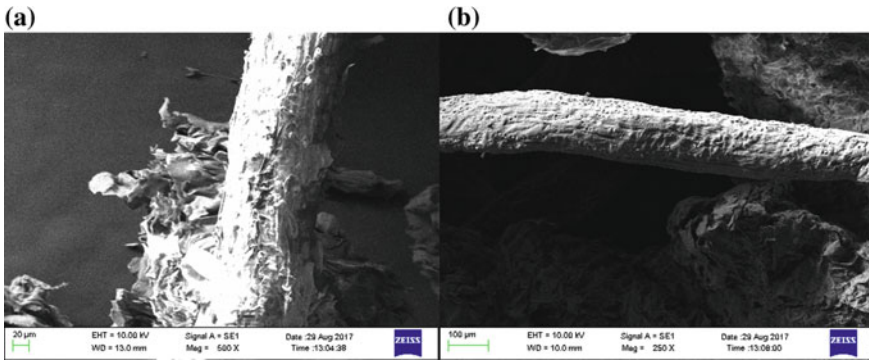
Fig. 5 Micrograph of coir fiber. **a** Untreated coir. **b** Treated coir

Fig. 6 Density of fabricated composites
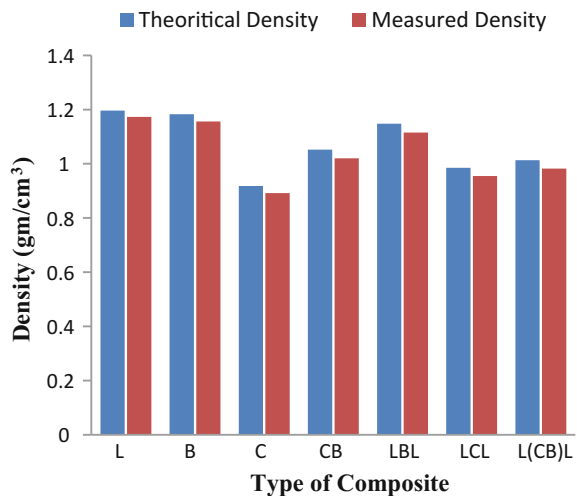
4.3 Density and Void Content

Bhagat et al. [15] studied luffa–coir fiber-reinforced epoxy hybrid composites and found that density and volume fraction of void content of composite increase with increasing fiber content. Density of different composites (theoretical obtained from Eq. 2; actual determined experimentally) is plotted in Fig. 6, and percentage of volume fraction of voids obtained for different composites according to Eq. (3) is graphically represented in Fig. 7. Density of composites depicted a reduction with the increase in fiber length of coir fibers in hybrid composites.

Luffa- and bagasse-reinforced composite depict a more compact structure than coir composites. This is because epoxy matrix enters the porous structure of luffa mat forming a very dense structure while in bagasse composite, the short fibers get dispersed in the matrix leaving very less amount of space for entrapping of air

Fig. 7 Volume fraction of voids of fabricated composites
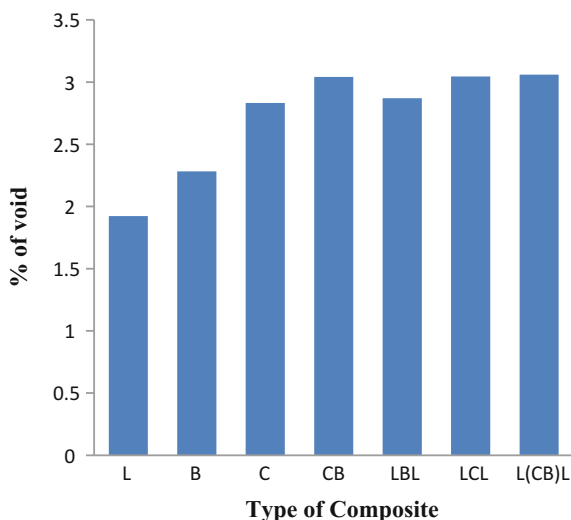
between them. Composite with coir dust reinforcements show lower density due to large amount of entrapped air particles. Percentage of void content should be less than 3% for the fabricated composites [16]. The values obtained are found to be within acceptable limits.

5 Conclusions

Composites with mercerized luffa, bagasse, and coir reinforcements in epoxy matrix were prepared by hand lay-up technique, and their physical properties like density and volume fraction of void were determined. The effect of mercerization was analyzed by FTIR and SEM analysis of the treated and untreated fibers.

References

1. P. H. F. Pereira Et Al., "Vegetal Fibers In Polymeric Composites: A Review," Polímeros, Vol. 25, No. 1, Pp. 9–22, Feb. 2015.
2. D. N. Saheb, J. P. Jog, D. Nabi Saheb, And J. P. Jog, "Natural Fiber Polymer Composites : A Review," Adv. Polym. Technol., Vol. 18, No. 4, Pp. 351–363, 1999.
3. X. Li, L. G. Tabil, And S. Panigrahi, "Chemical Treatments Of Natural Fiber For Use In Natural Fiber-Reinforced Composites: A Review," J. Polym. Environ., Vol. 15, No. 1, Pp. 25–33, 2007.
4. P. Mishra, "Development And Characterization Of Low Cost Composite From Sugarcane Bagasse Waste A Thesis Submitted In Partial Fulfilment Of Cost Composite From Sugarcane," Vol. 8, 2011.

 5. P. H. F. Pereira Et Al., "Vegetal Fibers In Polymeric Composites: A Review," Polímeros, Vol. 25, No. 1, Pp. 9–22, Feb. 2015.
 6. S. Kalia, B. S. Kaith, And I. Kaur, "Pretreatments Of Natural Fibers And Their Application As Reinforcing Material In Polymer Composites—A Review".
 7. E. Sinha And S. K. Rout, "Influence Of Fibre-Surface Treatment On Structural, Thermal And Mechanical Properties Of Jute Fibre And Its Composite," Bull. Mater. Sci., Vol. 32, No. 1, Pp. 65–76, 2009.
 8. S. O. Han And Y. M. Jung, "Characterization Of Henequen Natural Fiber By Using Two-Dimensional Correlation Spectroscopy," J. Mol. Struct., Vol. 883–884, No. 1–3, Pp. 142–148, 2008.
 9. G. H. Higgins, V. Goldsmith, And A. N. Mukherjee, "Journal Of Polymer Science," Vol. 32, P. 57, 1958.
10. S. Mishra Et Al., Studies On Mechanical Performance Of Biofibre/Glass Reinforced Polyester Hybrid Composites, Vol. 63. 2003.
11. C. H. Chen, C. Y. Chen, Y. W. Lo, C. F. Mao, And W. T. Liao, "Characterization Of Alkali-Treated Jute Fibers For Physical And Mechanical Properties," J. Appl. Polym. Sci., Vol. 80, No. 7, Pp. 1013–1020, 2001.
12. S. H. Aziz And M. P. Ansell, "The Effect Of Alkalization And Fibre Alignment On The Mechanical And Thermal Properties Of Kenaf And Hemp Bast Fibre Composites: Part 1 - Polyester Resin Matrix," Compos. Sci. Technol., Vol. 64, No. 9, Pp. 1219–1230, 2004.
13. E. Bodros, I. Pillin, N. Montrelay, And C. Baley, "Could Biopolymers Reinforced By Randomly Scattered Flax Fibre Be Used In Structural Applications?," Compos. Sci. Technol., Vol. 67, No. 3–4, Pp. 462–470, 2007.
14. L. Ghali, S. Msahli, M. Zidi, And F. Sakli, "Effect Of Pre-Treatment Of Luffa Fibres On The Structural Properties," Mater. Lett., Vol. 63, No. 1, Pp. 61–63, 2009.
15. V. Kumar Bhagat, A. Kumar Prasad, A. Kumar Lal Srivastava Professor, And A. Kumar Lal Srivastava, "Physical And Mechanical Performance Of Luffa-Coir Fiber Reinforced Epoxy Resin Based Hybrid Composites," Int. J. Civ. Eng. Technol., Vol. 8, No. 86, pp. 722–731, 2017.
16. S. P. Priya And S. K. Rai, "Impact, Compression, Density, Void Content, And Weight Reduction Studies On Waste Silk Fabric/Epoxy Composites," J. Reinf. Plast. Compos., Vol. 24, No. 15, Pp. 1605–1610, Oct. 2005.

Future Research Potentials of Hot Rolling Process: A Review

F. B. Kumar, A. Sharma and M. Oraon

1 Introduction

The manufacturing sectors tend to be competitive in the market, when the manufacturer develops supreme quality product at lowest processing time and monetary. The rolling process is a common technique utilized in manufacturing industry where the metals are shaped through heavy rolls. At least once in their production period metallic equipment is exposed for rolling and hence almost 80% of metallic equipment is exposed to rolling. In the rolling process, the grain size is refined especially in hot rolling. The metal stock is passed through one or more pairs of rolls to reduce the thickness which results the metal stock becomes harder in every pass. The rolling process is classified according to the temperature of the rolling process (cold rolling and hot rolling) and the numbers of rolls used in the forming process. Hot rolling (Fig. 1) is basic manufacturing process in which the cast or semi-finished product is passed through the arrangement of rollers. The rollers may be flat or have an impression. The incoming metal can be cold or preheated condition as per specific material.

F. B. Kumar · A. Sharma (✉)
Student of Production Engineering, Birla Institute of Technology, Mesra, off Campus-Patna, Bihar 800014, India
e-mail: ayush61811@gmail.com

M. Oraon (✉)
Faculty of Production Engineering, Birla Institute of Technology, Mesra, off Campus-Patna, Bihar 800014, India
e-mail: moraon@bitmesra.ac.in

Fig. 1 Schematic diagram
of rolling process
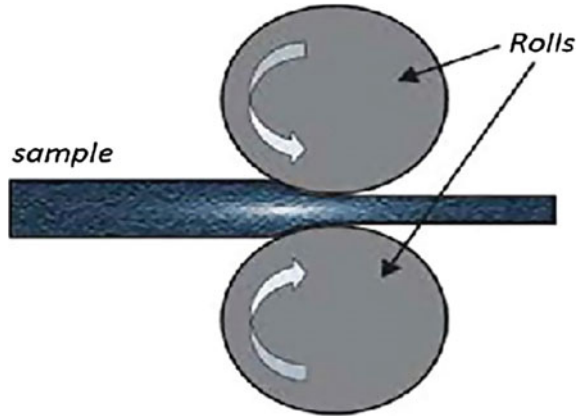
2 Literature Review

Hot rolling process specially used in the case of reduction of cross section of high carbon steels. The casted steel is compressed between rotating rolls. The arrangement of rolls in the rolling process as; two high mill roller, three high mill roller, four high mill roller, and cluster mill roller. Due to high productivity and low-cost production, rolling is one of the most widely used manufacturing process among all other metal-working processes [1]. In the rolling process, the incoming raw metals can be converted into various cross sections such as plate, I, T, L, and channel section throughout its length [2]. Biswas et al. investigated the control of temperature by using multiple planar waterjet during the hot rolling of steel. They concluded that the optimal temperature can improve the mechanical and metallurgical properties of the end product [3]. Yang et al. have investigated the hot slab rolling process with the consideration of process parameters such as roller diameter, workpiece height, friction coefficient, tensile force, and reduction rate by using the finite element method (FEM). The 2D models of the roll and the slab are developed by using thermomechanical coupling and isoparametric technology. It is found that the rolling force increases with rotational angular speed (ω) and shows a linear relation between them. They found that the rolling force reduces with the increasing temperature, moreover, when the temperature attains approximately 1200 °C, the rolling force remains invariable even with the continuous increase of temperature (Fig. 2) [4]. Kushwaha and Moharana investigated the effect of temperature (100, 150, 200, 250 °C) against the residual stresses. The finite element analysis (FEA) is carried out on ANSYS. They concluded that the residual stress is inversely proportional to the temperature (Fig. 3) [5]. Kumar and Kodli have investigated the effect of friction
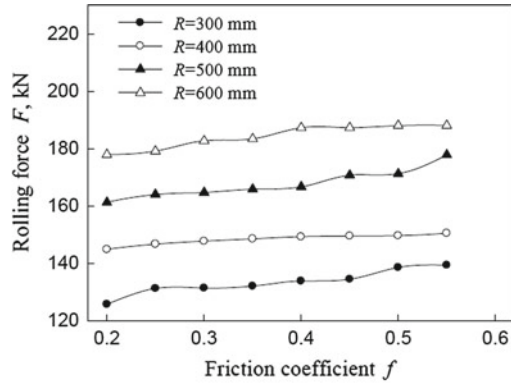
(a) Effect of Co-efficient of Friction on Rolling Force
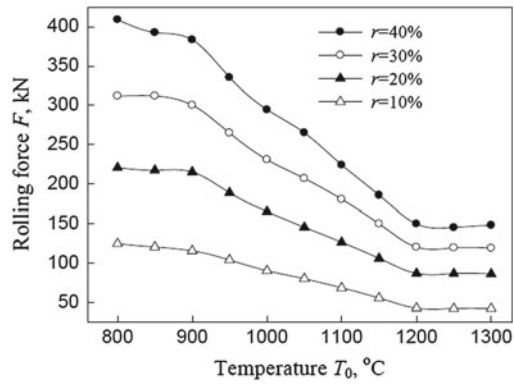
(b) Effect of Temperature on Rolling Force
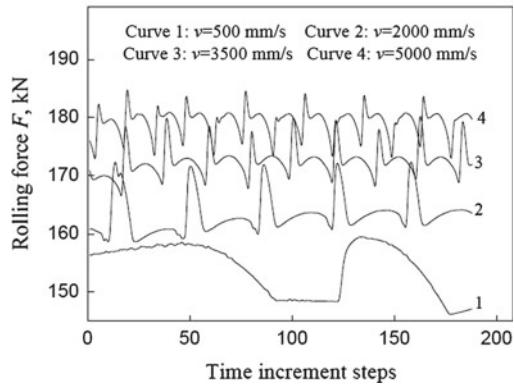
(c) Curve Plot Between Rolling Speed on Rolling Force

on effective stress. The experiments have been conducted at different mill speed for
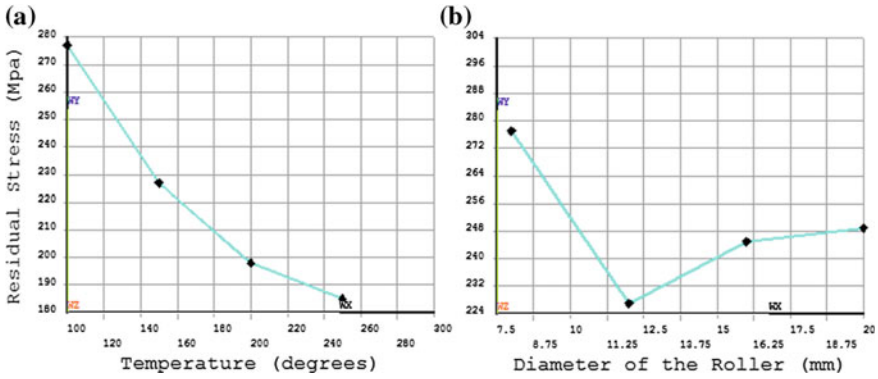
Fig. 3 a Variation of residual stress with temperature **b** with roller diameter

rolling of steel bar at coefficient of frictions, i.e., 0.20, 0.25, and 0.30 (Fig. 4). The simulation results indicate that the value of friction coefficient affects the effective stress. It has been found that the effective stress suddenly decreases as RPM of roller increases from 90 to 95, but the further increment of speed with a gap of 5 RPM leads to a constant effective stress [6]. Murthy et al. have investigated the effect of rolling speed and roll diameter on various rolling parameters such as residual stress, rolling force, heat transfer, friction coefficient, strain rate, Von-mises stress, plastic strain, and contact pressure [7]. The various rolling input parameters have been investigated by the researchers. The output and conclusion are presented in Table 1. Further, Murthy et al. have investigated the effect of roll diameter on the different stresses and found that the increase in roll diameter decreases in pressure, von-mises stress, shear stress, effective stress and effective strain [8].

3   Conclusion

The rolling process is one of the most essential processes for manufacturing sector such as steel industries where the parts are formed in a versatile condition. The various rolling parameters are to be controlled for the quality production.
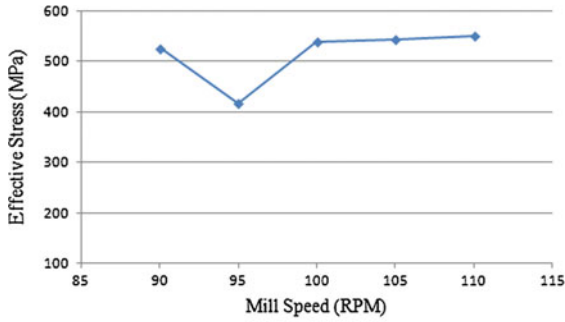
(a) Variation of Effective stress with Co-efficient of friction (0.20)
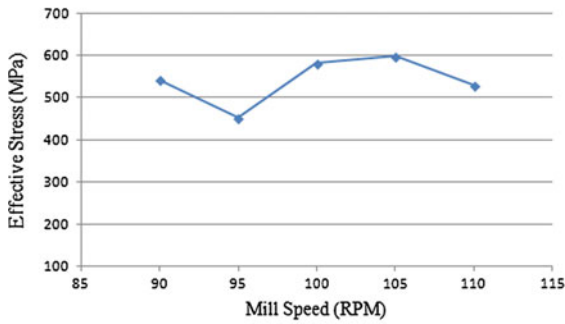
(b) Variation of Effective stress with Co-efficient of friction (0.25)
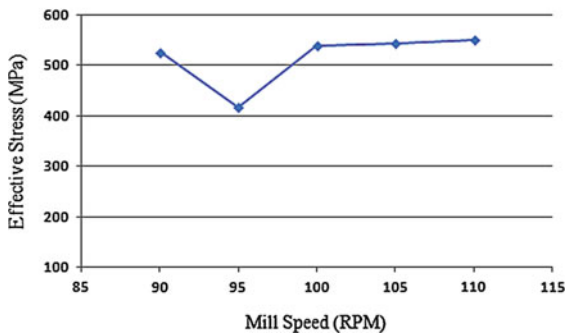
(c) Variation of Effective stress with Co-efficient of friction (0.30)

Fig. 4 Variation of effective stress at variable mill speed and coefficient of friction

The present study focused on the effect of roller diameter and roller pressure on the various stresses, coefficient of friction, RPM, etc. On the other hand, it is very

Table 1 Effect of various input rolling parameters on outputs

Input parameter	Targeted output	Discussion	Conclusion
Rolling speed	Rolling force	Increase in force with increased speed. Force has effect on strain rate	Lubrication can be used to minimize force. Strain rate results in hardness of material
Rolling speed	Friction coefficient	Decrease in friction coefficient with increase in speed	Further friction coefficient can be minimized by using lubrication
Roll size	Plastic strain, von-mises stress, and contact pressure	Higher roll diameter leads to decrease in plastic strain, von-mises stress and contact pressure	Plastic strain is always a source of weakness that can be reduced using higher sized rollers. Lower von-mises stress helps in roller capacity to take more rolling loads. Contact pressure will reduce rigidity required for the product
Temperature	Residual stress	As the temperature goes on increasing correspondingly the residual stresses decrease	Residual stress is inversely proportional to temperature

difficult to control the hot rolling process. The designers may solve the complexity of the rolling process by the application of FEA-based analysis.

References

1. Kalpakjian S, Schmid SR. A Case Study of the Effectiveness of Rolling Process to Manufacture the Strip of Leaf Spring. Manufacturing engineering and technology 2011, 1(1): 71–75.
2. Rao PN, Manufacturing technology. Tata McGraw Hill, 2008.
3. Biswas SK, Chen SJ, Satyanarayana A. Optimal temperature tracking for accelerated cooling processes in hot rolling of steel. Journal of Dynamical and Control Systems, 1997; 7: 327–340.
4. Yang L, Jinchen J, Hu j, Romagos A. Effect of process parameters on mechanical behavior in hot-slab rolling. MECHANIKA 201; 17(5): 474–479.
5. Kushwaha BR, Moharana B. Analysis for stress prediction in hot rolling with different process parameters by finite element method. International Research Journal of Engineering and Technology 2017; 4(3): 399–406.
6. Kumar S and Kodli BS. A study on thermomechanical analysis of hot rolling and estimation of residual stresses by using fem. IOSR Journal of Mechanical and Civil Engineering. 2013; 9(3): 26–34.

7. Murthy PLS, Patil H, Sarada BN. Analysis of roller speed and roller diameter- a review. 2016; 2(2): 1–5.
8. Murthy PLS, Patil H, Sarada BN. Studies on influence of roller diameter and roller speed on process parameters in hot rolling process using manufacturing simulation. Technical research organization India. 2016; 3(5): 24–27.

Analysis of Wire-EDM Input Parameters on Kerf Width and Surface Integrity for Al 6061 Alloy

K. Mandal, S. Sarkar, S. Mitra and D. Bose

1 Introduction

Wire-Electro Discharge Machining (Wire-EDM) is a spark deterioration process used to produce complex and intricate three-dimensional contour surface through electrically conductive materials using wire electrode. Spark generation takes place due to the potential difference between the workpiece and the tool electrode. The degree of accuracy and fine surface finishes of the workpiece is valuable for the applications of different tangled parts. Without Wire-EDM, the fabrication of precision shape and size requires many hours by a conventional process.

The input parameter setting has been selected based on trial runs, knowledge of workers and variable parameter tables delivered by machine tool manufacturer. The most momentous response measures in Wire-EDM are surface roughness (R_a) and kerf width (K_f). Pulse on time (T_{on}), pulse off time (T_{off}), servo voltage (SV) and wire tension (WT) are the variable input parameters which take on the response measures. The kerf width (K_f) is calculated by [(blank length–punch length)/2] as shown in Fig. 1. And corresponding dimensions are measured by optical measuring microscope. Another important performance is surface roughness (R_a) which determines

K. Mandal (✉) · S. Sarkar · S. Mitra
Production Engineering Department, Jadavpur University, Kolkata 700032, India
e-mail: mandal.kingshuk1@gmail.com

S. Sarkar
e-mail: s.sarkar.ju@gmail.com

S. Mitra
e-mail: mail.mitra.souren@gmail.com

D. Bose
Mechanical Engineering Department, National Institute of Technical Teachers
Training& Research, Kolkata 700106, India
e-mail: dipan88@yahoo.co.in
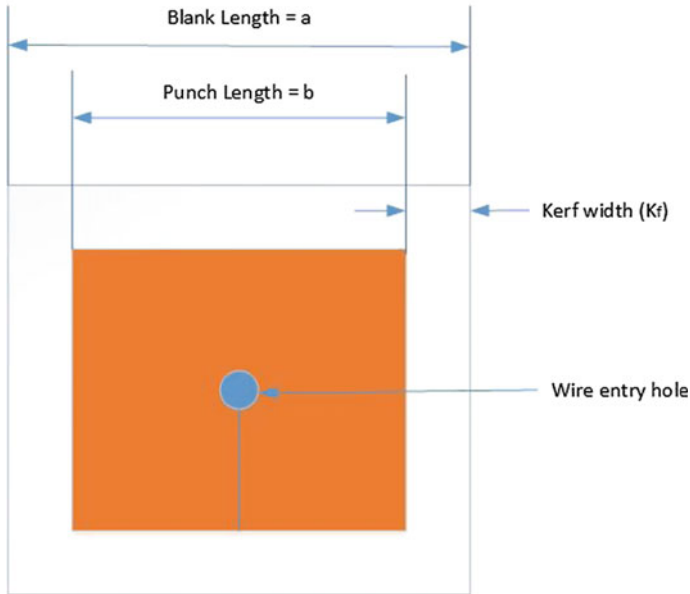
Fig. 1 Schematic diagram of the kerf width

the surface texture of the workpiece, and it is measured using precision roughness tester. The main goal in this research work is to minimize both the responses: kerf width and surface roughness.

Chain et al. [1] presented an effective approach for the optimization of Wire-EDM process formulation and solution of a multi-objective optimization problem for the selection of the optimal parameter settings. The machining input parameters have been optimized with deliberation of multiple performance features. Tosun et al. [2] analysed the importance of the machining parameters on the kerf width, MRR and determined by using analysis of variance (ANOVA). The variation of the output responses with machining parameters was mathematically modelled by using a regression analysis method. Rajurkar and Wang [3] analysed the wire rupture phenomena with a thermal model. The neural network structure is employed to find out the set of input parameters for the evaluation of machining speed and roughness of the workpiece. Spedding and Wang [4]gave an endeavour optimization of the input parameters combined with ANN and explained the surface texture and waviness of the workpiece contour and the machining speed. Liao et al. [5] gave an observation to fix up the input process parameters on the material removal rate, kerf gap and surface roughness. Lok and Lee [6] likened the output response in expressions of material removal rate and profile roughness of two different progressive ceramics. Huang et al. [7] observed the influence of variable input parameters on the kerf gap, surface roughness and white layer thickness on the workpiece couture. Rozenek et al. [8] used MMC as a workpiece and investigated the effects of process vari-

Table 1 Machining parameters, symbols and their ranges

Machining input parameters	Levels		
	1	2	3
T_{on} (μs)	0.1	0.2	0.3
T_{off} (μs)	15	25	35
SV (volt)	40	50	60
WT (kg)	0.8	1.1	1.4

ables on cutting velocity and surface integrity. Tosun and Cogun [9] experimentally examined the influence of input variables on tool wear rate based on the mass loss of electrode in Wire-EDM. Tosun et al. [10] presented a new statistical method to obtain the optimum variable input parameters to minimize the electrode crater size in Wire-EDM.

From the past literature review, research works on Wire EDM are conceptualize for optimization and determine the true surface topography, kerf width, machining speed, wire craters and wire rupture phenomenon of machining area with regards to the different cutting conditions. In the present work, the outcome of the input variables and their importance on kerf gap and the surface roughness are statistically estimated with the help of ANOVA. The variation of kerf width and surface roughness with respect to machining parameters for minimization of the response was experimentally investigated.

2 Experimental Planning and Procedure

The experimental work has been carried out on EXCETEK EX-40 Wire-EDM machine tool. Different settings of T_{on}, T_{off}, SV and WT have been used in the experiments shown in Table 1. Power mode (10), flushing pressure (4 kg/cm^2), wire feed rate (3 m/min) and servo sensitivity (15) have been kept constant throughout the experiments. Coated brass wire with 0.25-mm diameter and Al 6061 alloy as a workpiece have been chosen for the experiments.

The K_f and R_a have been measured using the Olympus STM 6 optical measuring microscope and Mitutoyo SJ 400 roughness tester. The average value of K_f along the cutting length has been considered in this study. Kerf width is calculate by using the following expression (shown in Fig. 1):

$$\text{Kerf width}(K_f) = \frac{(\text{blank length} - \text{punch length})}{2} = \frac{(a - b)}{2} \tag{1}$$

A well-defined design concept is essential to evaluate the effects of input process variables on output response and to recognize the outcome features under the

Table 2 Design of experiment for L9 array

Sl. No.	T_{on} (µs)	T_{off} (µs)	SV (V)	WT (kg)	K_f (mm)	R_a (µm)
1	0.1	15	40	0.8	0.332	2.227
2	0.1	25	50	1.1	0.330	2.178
3	0.1	35	60	1.4	0.329	2.432
4	0.2	15	50	1.4	0.368	2.399
5	0.2	25	60	0.8	0.321	2.729
6	0.2	35	40	1.1	0.330	2.604
7	0.3	15	60	1.1	0.367	2.585
8	0.3	25	40	1.4	0.373	3.280
9	0.3	35	50	0.8	0.398	3.461

optimum machining condition [11, 12]. In the present work, Taguchi quality design method has been used to identify the optimal machining parameters for minimizing the kerf gap and surface roughness. Four input parameters have been considered as controllable components, and each element is designed to corresponding three different levels (shown in Table 1). Taguchi L9 orthogonal design concept with nine rows (conforming to the number of trials) has been considered for the final experimentations (shown in Table 2).

3   Results and Discussions

The ANOVA has been applied to consecrate statistically cabalistic the input process variables and the % contribution of these factors on the kerf width and the surface roughness. In the statistical tool, a number of S/N ratios have to be used to figure out the existing features; lower is better, nominal is best, and higher is better. In this work, the lower is better type has been considered for the better performance of kerf width and surface roughness.

From the type of the performance measure of the process parameters, the greater value S/N ratio has been given the superior results. So that, the optimum level of the machining parameters is the level with the highest S/N ratio value. Based on the study of S/N ratio, the optimal input parameters for the kerf width have been obtained at 0.1 µs pulse on time (Level 1), 25 µs pulse off time (Level 2), 60 V servo voltage (Level 3) and 1.1 kg wire tension (Level 2) settings. Figure 2 has been also showing the outcome of input variables on the kerf width. It has been observed that from the means plot (Fig. 2) the two main dominating factors affecting kerf width are pulse on time and servo voltage. With the increase of T_{on} and SV, the kerf width also increases. Pulses off time and wire tension are the less significant parameters on kerf width. The optimal machining performance for the roughness value has been obtained at 0.1 µs pulse on time (Level 1), 15 µs pulse off time (Level 1), 60 V
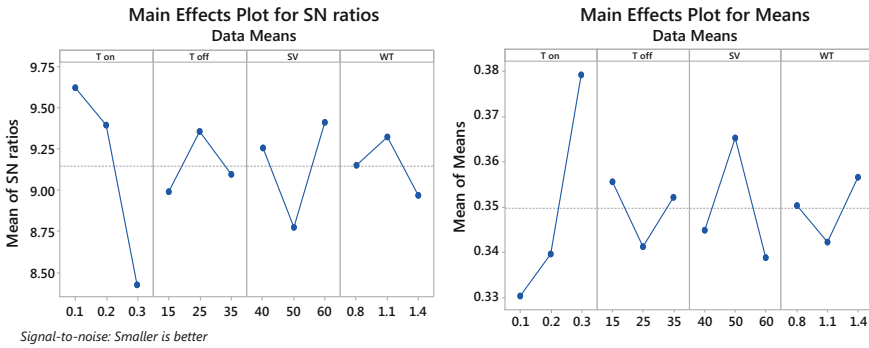
Fig. 2 S/N ratio and mean plot of kerf width
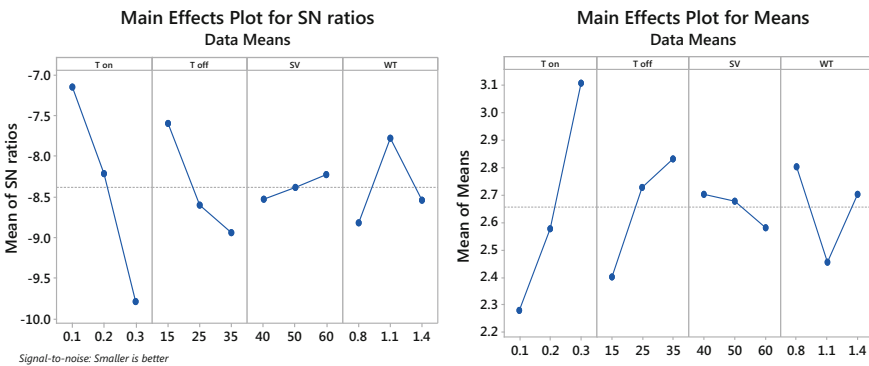
Fig. 3 S/N ratio and mean plot of surface roughness

servo voltage (Level 3) and 1.1 kg wire tension (Level 2) settings. Figure 3 shows the effect of input process parameters on the surface roughness.

The outcome of ANOVA for the response has been shown in Tables 3 and 4. The fit value is use to take measure the confidence level of the response. Larger fit value points out the mutation of input variables, and it plays a significant role in the outcome appearances. According to the exploration, furthermost operative input factors on K_f are T_{on} and SV, whereas the offshoots of T_{off} and WT on K_f were insignificant. Percentage contribution implies that the relative importance of the individual parameter. For a factor with a high-percentage contribution, a small variation will have a great significance on the performance observed. According to Table 3, pulse on time has found the major factor affecting the kerf width (69.41%), whereas SV becomes a second influencing factor (19.51%). From the F-test resolution, the quite significant parameters on the surface roughness are T_{on}, T_{off} and WT. The percentage contributions of the input parameters on R_a are shown in Table 4. From Table 4, it has been observed that the main distressing parameter on R_a is T_{on} (67.10%). The

Table 3 Results of the ANOVA for K_f

Source	DOF	Sum of square	Mean of square	F-value	% contribution
T_{on}	2	0.004062	0.002031	13.1032	69.41
T_{off}	2	0.000338	0.000169	1.0903	5.78
SV	2	0.001143	0.000571	3.6839	19.51
WT	2	0.000310	0.000155	1	5.30
Error	0				
Total	8	0.005852			

Table 4 Results of the ANOVA for R_a

Source	DOF	Sum of square	Mean of square	F-value	% contribution
T_{on}	2	1.05966	0.52983	42.6251	67.10
T_{off}	2	0.30027	0.15014	12.0788	19.01
SV	2	0.02487	0.01243	1	1.58
WT	2	0.19441	0.09720	7.8198	12.31
Error	0				
Total	8	1.57922			

percentage contributions of other parameters are T_{on} (19.01%), SV (1.58%) and WT (12.31%), respectively.

4   Conclusions

In the onward reporting, an endeavour has been made to analyse the parametric influence on two selected output parameters, kerf width and surface roughness. Taguchi optimization technique has been exploiting to assess the optimum input combination to achieve the desired result of kerf width and surface roughness with selected experimental reign. Factors like T_{on}, T_{off}, SV and WT have been established to play a momentous role in cutting operations for the minimization of kerf width and surface roughness.

- T_{on} and SV have found most significant parameters for kerf width for 95% confidence level, with percentage contributions of 69.41 and 19.51%, respectively. However, other parameters T_{off} (5.30%) and WT (5.78%) contribution in the variation of kerf width have been relatively less.
- T_{on}, T_{off} and WT have also found out the important parameters in surface roughness, with percentage contribution of 67.10, 19.01 and 12.31%, respectively.

References

1. Ko-Ta Chaing, Fu-Ping Chang. Optimization of the WEDM process of particle-reinforced material with multiple performance characteristics using grey relational analysis. Journal of Material Processing Technology 2006; 180:96-101.
2. Nihat Tosun, Can Cogun, Gul Tosun. A study on kerf and material removal rate in wire electrical discharge machining based on Taguchi method. Journal of Materials Processing Technology 2004; 152:316–322.
3. K.P. Rajurkar, W.M. Wang. Thermal modelling and on-line monitoring of wire-EDM. Journal of Material Processing Technology 1993; 38 (1–2):417–430.
4. T.A. Spedding, Z.Q. Wang. Parametric optimization and surface characterization of wire electrical discharge machining process. Precision Engineering 1997; 20 (1):5–15.
5. Y.S. Liao, J.T. Huang, H.C. Su. A study on the machining-parameters optimization of wire electrical discharge machining. Journal of Material Processing Technology 1997; 71:487–493.
6. Y.K. Lok, T.C. Lee. Processing of advanced ceramics using the wire-cut EDM process. Journal of Material Processing Technology 1997; 63 (1–3): 839–843.
7. J.T. Huang, Y.S. Liao. W.J. Hsue, Determination of finish cutting operation number and machining parameters setting in wire electrical discharge machining. Journal of Material Processing Technology 1999; 87:69– 81.
8. M. Rozenek, J. Kozak, L. DabroVwki, K. LubkoVwki. Electrical discharge machining characteristics of metal matrix composites. Journal of Material Processing Technology 2001; 109:367–370.
9. N. Tosun, C. Cogun, An investigation on wire wears in WEDM. Journal of Material Processing Technology 2003; 134 (3):273–278.
10. N. Tosun, C. Cogun, H. Pihtili, The effect of cutting parameters on wire crater sizes in wire EDM. International Journal of Advance Manufacturing Technology 2003; 21:857–865.
11. M.S. Chua, M. Rahman, Y.S. Wong, H.T. Loh, Determination of optimal cutting conditions using design of experiments and optimization techniques, International Journal of Machine Tools and Manufacturing 1993; 33 (2):297– 305.
12. S.H. Lee, S.H. Lee, Optimization of cutting parameters for burr minimization in face-milling operations. International Journal for Production Research 2003; 41 (3):497–511.

A Brief Study on Characteristics, Properties, and Applications of CdSe

Nitya Garg

1 Introduction

Cadmium selenide (CdSe) is a solid binary inorganic compound of cadmium (Cd) and selenium (Se) which falls into a category of II–VI group (due to the position of Cd and Se in the periodic table) and is a highly photosensitive semiconductor material of *n*-type crystallized in three different phases: hexagonal (wurtzite), cubic (zinc blende), and cubic rock salt. It consists of positively cadmium and negatively selenium charged ions that interact via a Coulomb potential, supplemented by short-range repulsion terms and van der Waals attractive terms. Cadmium selenide is often thought of as a covalent material. Each anion is surrounded by four cations at the corners of a tetrahedron, and vice versa. This tetrahedral coordination is typical of sp^3 covalent bonding, but this material also has a substantial ionic character. The usual crystal structure of bulk CdSe is hexagonal having a wide direct band gap nature and no inversion symmetry. This material is transparent to infrared (IR) light so that it can be used as window in fabrication of solar cells and in thin-film transistor. It is the most stable phase of CdSe at ambient conditions and occurs in the form of mineral cadmoselite [1]. Zinc-blende-type CdSe is metastable at ambient conditions and converts to the wurtzite form upon moderate heating. Under increasing pressure, the wurtzite structure transforms to the rocksalt structure [2]. Bulk CdSe has a broad and generally featureless absorption spectrum starting at ~716 nm (1.74 eV), with bulk exciton Bohr diameter 10.6 nm [3]. Current research on CdSe is mainly focused on nanomaterials, i.e., at least one dimension between 1 and 100 nm. The interest in these nanosized systems can be understood by their special properties, significantly different from the properties of the parent bulk compound that open the possibility of novel technological applications in the field of biological imaging and photonic

N. Garg (✉)
Amity School of Engineering & Technology, Amity University, Ranchi 834001,
Jharkhand, India
e-mail: nitu5958@gmail.com

devices [4]. In this paper, various properties and applications of CdSe are summarized so that its utilization in future applications can be done in a better way.

2   An Overview of Characteristics of CdSe

This section presents an overview of some of the concepts associated with CdSe characteristics such as band gap, quantum confinement, band structure, phonon dispersion curve, excitons, absorption, and fluorescence mechanism in order to understand its optical and electronic properties.

2.1   Direct Band Gap

The high luminescence efficiency of CdSe is due to direct band gap nature since the optical transition is dipole-allowed. For indirect band gap semiconductors, minimum and maximum values of conduction band and valence band lie at different points in the Brillouin zones. Conservation of momentum in indirect band gap material requires emission of phonon in addition to photon emission. This makes it a second-order process due to which probability of transition is relatively low.

2.2   Quantum Confinement Effect

Bound system of two charge carriers (an electron in the conduction band and hole in the valence band) in a semiconductor material is called exciton, and the physical distance between them is called exciton Bohr radius. The value of exciton Bohr radius for bulk CdSe is 5.6 nm. Electrostatic Coulomb interaction makes exciton energy to lie below the band gap energy of the semiconductor crystal. In bulk materials, exciton is free to move, whereas in nanomaterials, they are physically confined. This effect occurs when the size of the semiconductor crystals is less comparable to the bulk exciton Bohr radius which results in changing electronic band structure of the material from continuous energy levels to become discrete energy levels with band gap increases as size of crystal decreases. A blueshift is expected to occur in absorption spectra as well as in photoluminescence spectra with changes in electronic transition selection rules and fluorescence lifetime.
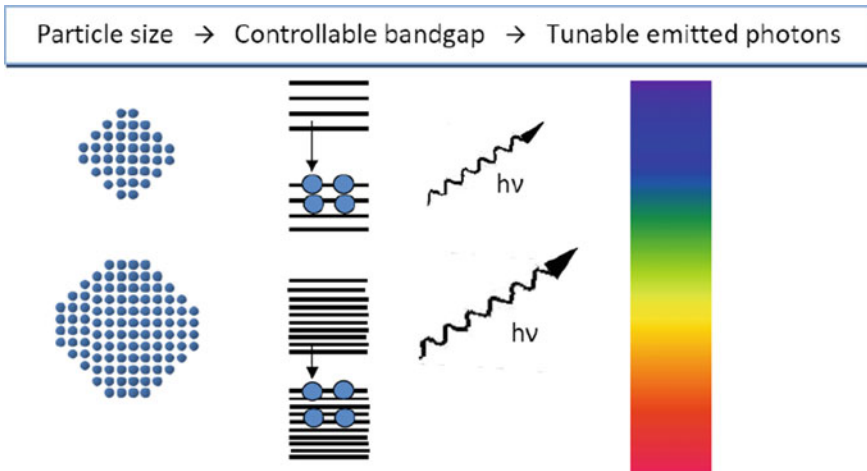
Fig. 1 Quantum dot particle size dictates emitted wavelength

2.3 Absorption Mechanism

Absorption of light by semiconductor material is related to its crystal size. Decrease in particle size leads to the quantization of energy levels in the absorption spectra which increases the band gap of material and hence changes the absorption wavelength toward lower value from the infrared to the visible region of the electromagnetic spectrum. Energy difference between different electronic states and the lifetimes of excited states can be studied using optical spectroscopic methods or time-resolved techniques. This spectrum helps to calculate the concentrations, absorption cross section, extinction coefficient, and particle size from the peak position of the first excitonic transition [5]. The shape of absorption peak depends on crystal shape as well as defect concentration present in material [6]. Coating the surface of material with inorganic or organic shells also changes the absorption spectra.

2.4 Strong Fluorescence

CdSe material shows strong fluorescence in the electromagnetic spectrum. Fluorescence means the emission of a photon from the material when an electron comes from an excited state to a ground state. The wavelength of emitted photon depends on the energy difference between states which is in turn dependent on the particle size as shown in Fig. 1. Thus, by controlling the size of material, one can control the wavelength emission of the material so that fluorescence can occur from entire visible spectrum as depicted in Table 1.

Table 1 Wavelengths of the visible spectrum

Color	Wavelength (nm)
Blue	450
Green	500
Yellow	550
Orange	600
Red	650

Weakly redshifted fluorescence can be observed in this material due to the presence of surface defect states or charge carriers recombination process between different trap states [7, 8]. Surface defects usually contain two different types of traps: deep traps and shallow traps [9]. Deep traps which lie at the middle of the energy gap usually confine at the lattice site defects, whereas shallow traps lie within a few millivolts below and above the conduction and valence band edges. When the material is in nanocrystalline form, splitting of energy levels takes place which is more significant for the shallow traps rather than for deep trap and the difference between shallow traps and the electronic states of the material fades away as shown in Fig. 2.
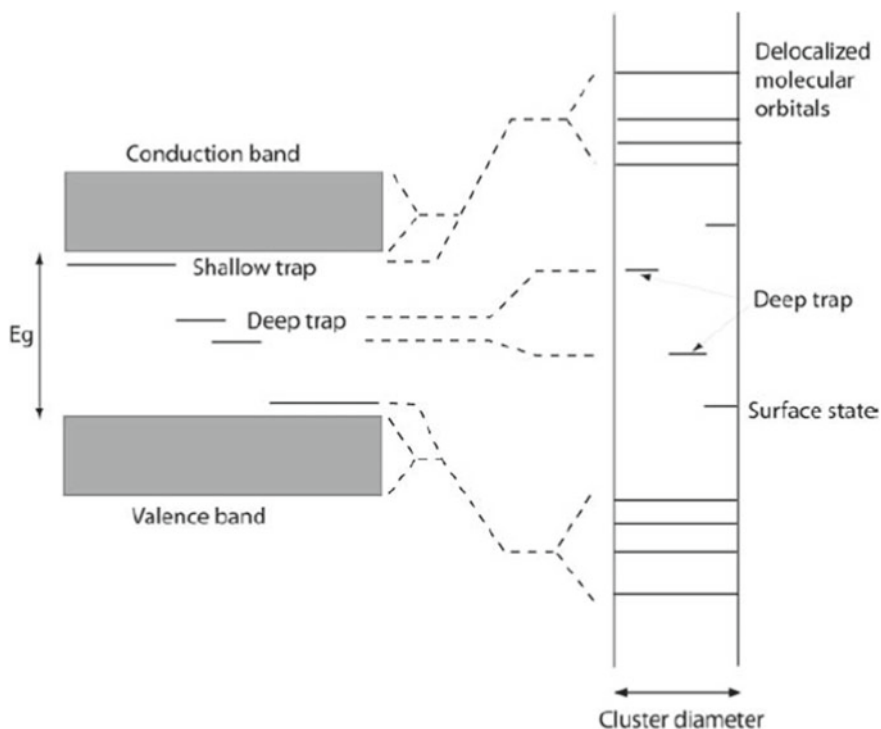
Fig. 2 Schematic diagram of the shallow and deep traps in the bulk (left) as well as in a semiconductor nanocrystal (right) [9]

Table 2 Variation of band gap values with different temperatures for cubic CdSe [14–16]

Temperature (K)	Band gap E_g (eV)
Low temperature	
5	1.78
9	1.765
10	1.75
80	1.74
Room temperature	
297	1.74
300	1.692

2.5 Band Structure

It is important to know the band structure of semiconductors for photoluminescence since the photoluminescence energy is directly related to the band gap of the semiconductor. Figure 3 shows the electronic band structures for cubic and wurtzite CdSe along the high symmetry directions [10, 11] which indicate that the highest of the valence band and the lowest of the conduction band occurring at the center of the Brillouin zone (Γ-point) where the momentum k is zero. This implies that CdSe is a direct gap material along the Γ-direction. As the temperature is increased, the semiconductor energy band gap is decreased. Table 2 shows variation in band gap values with temperature for cubic CdSe. The differences in both energy-band structure diagrams are observed close to the Γ-point. Theoretical work indicates that both structures have different sizing curve due to which wurtzite shows decrease in energy band gap with increasing particle size in a more gentle way [12]. A zinc-blende CdSe contains fourfold degenerate valence band levels at the Γ-point, whereas in wurtzite, the valence band is broken into two twofold degenerate levels by the crystal field [13]. Energy band gap increases linearly with pressure due to the decrease in interatomic distance and decreases with increasing temperature.
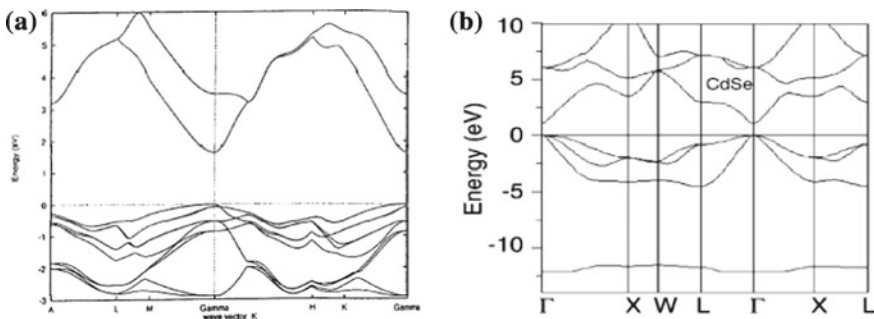
Fig. 3 Band structure (**a**) hexagonal structure [10] (**b**) zinc-blende [11]
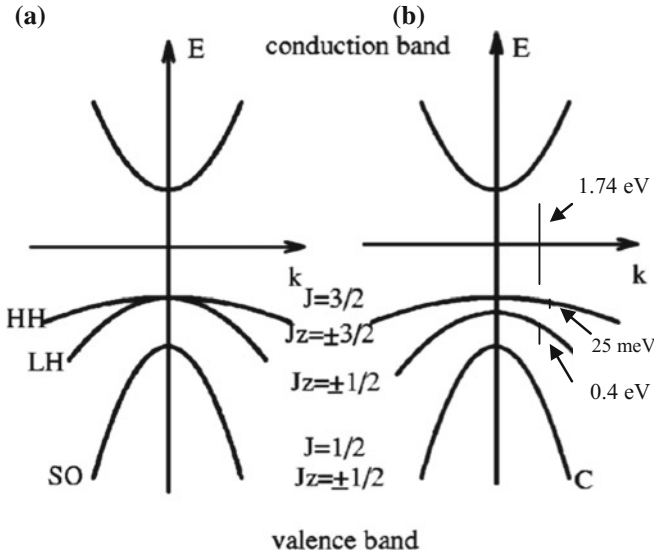
Fig. 4 Top of the valence band and the bottom of the conduction band of bulk CdSe with **a** zinc-blende- and **b** wurtzite-type structures [17]

Figure 4 shows the conduction band and valence band for bulk CdSe in the zinc-blende- and wurtzite-type structures. The valence band contains highest filled p-shells of the anions or sp^3 hybrid shells for covalent bonding, and the conduction band contains empty s-shells of the cations or sp^3 hybrid shells for antibonding. The valence band has an inherent sixfold degeneracy (including spin) at $k = 0$. Spin-orbital interaction leads to the splitting of valence band into a fourfold degenerate bands: heavy-hole (HH), light-hole (LH), and a twofold degenerate split-off (SO) bands. The spin–orbit coupling (ΔSO) increases with the atomic number. Heavy-hole and light-hole bands are degenerate at $k = 0$ in zinc-blende-type structure, whereas in wurtzite structure, this degeneracy is removed by the crystal field, and the corresponding energy difference between them is called the crystal field splitting ($\Delta cf = 25$ meV for CdSe). The conduction band has quantum number $J_z = 1/2$. The valence band has quantum number $J_z = 3/2$ for HH (this is the highest energy band), and other two sub-bands (LH and SO) have quantum number $J_z = 1/2$. The J and J_z are called total angular momentum quantum number and its z components due to spin-orbital coupling. The heavy hole and light hole have two different curvatures resulting in different effective masses. The effective mass of the conduction band is ~0.1, while the highest energy valence band has an effective mass of nearly 1 (thus, it is said that CdSe has a heavy "hole"). The band structure is found to be nondegenerate at any general k point of the Brillouin zone [17, 18].

Table 3 High- and low-frequency dielectric constant in wurtzite CdSe [21]

Modes of atom vibration	$\varepsilon_{O\parallel}$	$\varepsilon_{O\perp}$	$\varepsilon_{\infty\parallel}$	$\varepsilon_{\infty\perp}$
Dielectric constant	9.6	9.3	6.1	6.1

2.6 Phonon Dispersion Curve

Phonons which mean quantized mode of crystal lattice vibration are considered to be important for studying many physical properties of crystalline solids. The thermal, electrical conductivity as well as optical property of material is dependent on interaction of phonons with the excited charge carriers. CdSe phonon dispersion curve was obtained using density functional theory (DFT) or first principle calculation or abinitio calculation which shows separation between the optical and acoustic regions. The modes corresponding to atom vibrations perpendicular to the propagation vector were labeled as transverse optical (TO), and those parallel to atom vibration were labeled as longitudinal optical (LO). The phonon dispersion of bulk CdSe is partly available from inelastic neutron scattering experiments with sufficient accuracy [19]. Optical and acoustic phonon modes in nanomaterials are found with frequencies higher than the phonon modes in the bulk. Phonon confinement is responsible for the shape of the phonon dispersion curve near to the Γ-point. The stronger the confinement is, the more phonons far from the Γ-point contribute to the Raman scattering.

2.7 Dielectric Properties

The dielectric constant is one among important properties which determines electric charge storing ability of the material. The dielectric constant is different from material to material. Most of the bulk electronic properties as well as the surface properties of a material like the Coulomb interaction between excitons, Bohr radius of excitons, reflection coefficient, and refractive index are related to the medium dielectric constant. CdSe is having low dielectric constant and low dielectric loss in the high-frequency regions [20] as shown in Fig. 5. Very low dielectric loss figure is very important for the fabrication of materials for ferroelectric, photonic, and electro-optic devices as it indicates that material possesses good optical quality and contains less number of defects. High value of dielectric constant in the low-frequency regions is due to the presence of different types of polarization mechanisms like electronic, ionic, orientation, and space-charge polarization. The value of Fermi energy and polarizability can be calculated using the value of dielectric constant at higher frequencies. Reported value of static (low-frequency) and high-frequency dielectric for wurtzite CdSe is shown in Table 3.
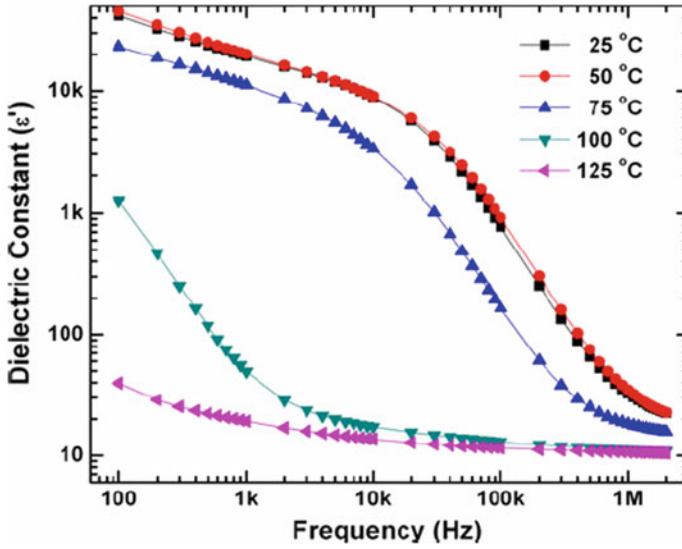
Fig. 5 Contrast of dielectric constant with frequency for different temperatures [20]

2.8 *Excitons in CdSe*

Exciton is a quasiparticle representing the lowest electronic excitation in a semiconductor. There are two types of exciton models, Frenkel excitons and Wannier excitons. In Frenkel excitons, electron–hole pairs are considered tightly bound to single atom or molecule, and in Wannier excitons, the electron–hole pairs are treated as weakly bound. In II–VI semiconductors, excitons are of the Wannier type, in which electron and hole are separated over many lattice constants, the exciton wavefunction is strongly delocalized, and the Coulomb interaction is reduced through the large dielectric constant. Such a free exciton transfers the excitation energy, not the electric charge because as a whole it is electrically neutral. The annihilation of an exciton is accompanied by a characteristic luminescence due to radiative recombination of the electron with the hole. The exciton is stable only if the attractive potential is strong enough to prevent it from breaking up owing to collisions with phonons. The exciton binding energy E_X must thus be higher than $\sim k_B T$ which indicates that excitons in semiconductors can occur only at low temperatures. Table 4 summarizes the basic exciton parameters in CdSe semiconductor.

2.9 *Multipole Moments (Dipole or Quadrupole Moment)*

Multipole moments depend on total charge densities, i.e., electronic and nuclear. A zinc-blende CdSe structure has zero dipole moments in *x, y,* and *z* directions, whereas

wurtzite CdSe has a large dipole moment due to the absence of inversion symmetry in hexagonal crystals [23] or from charge localized on the surface. Dipole moment is a structural property, depends on the exact structure of the crystal, and may vary significantly upon small structural changes [24].

2.10 Electronic Polarizability

Electronic polarizability is an important universal property required to explain the properties of molecular system which are related to electronic structure such as hardness/softness, acidity/basicity, or ionization potential. [25]. On increasing the particle size in a material, the electronic polarizability per atom increases slightly proceeded by the decrease in the energy gap. Increase in nanocrystal volume leads to the increase in total electronic polarizability of material. Direction of the induced dipole is in the direction of the applied external field. Nanowires have remarkable induced dipole moments due to their highly anisotropic shapes.

2.11 Elastic Property

The elastic constants of solid material provide important information of the nature of forces that occur and are responsible for material stability and stiffness. Room-temperature elastic stiffness (C_{ij}) and compliance (S_{ij}) for c-CdSe and w-CdSe [26] are listed in Table 5. Pressure dependence of bulk modulus and elastic stiffness for cubic CdSe is shown in Fig. 6, which shows monotonic increase in elastic moduli with pressure.

Table 4 Parameters of Wannier free excitons in CdSe [22]

Ground state radius	5.4 nm
Exciton binding energy	
Ground state binding energy	15.0 meV
Ist excited binding energy	13.2 meV
Exciton transition energy at 1.8 K	
$E_{g,ex}$ ($n = 1$)	1.82 eV
$E_{g,ex}$ ($n = 2$)	1.85 eV
$E_{g,ex}$ ($n = 3$)	2.25 eV

Table 5 Elastic stiffness (C_{ij}) and compliance (S_{ij}) for c-CdSe and w-CdSe

Stiffness (C_{ij}) (10^{11} dyne/cm^2)

Structure	C_{11}	C_{12}	C_{13}	C_{33}	C_{44}	C_{66}
Wurtzite	7.41	4.52	3.89	8.43	1.34	1.45
Cubic	6.67	4.63			2.23	

Compliance (S_{ij}) (10^{-12} cm^2/dyne)

Structure	S_{11}	S_{12}	S_{13}	S_{33}	S_{44}	S_{66}
Wurtzite	2.32	−1.12	−0.55	1.69	7.47	6.88
Cubic	3.48	−1.42			4.48	

Fig. 6 Pressure-dependence of elastic constants for cubic CdSe [11]
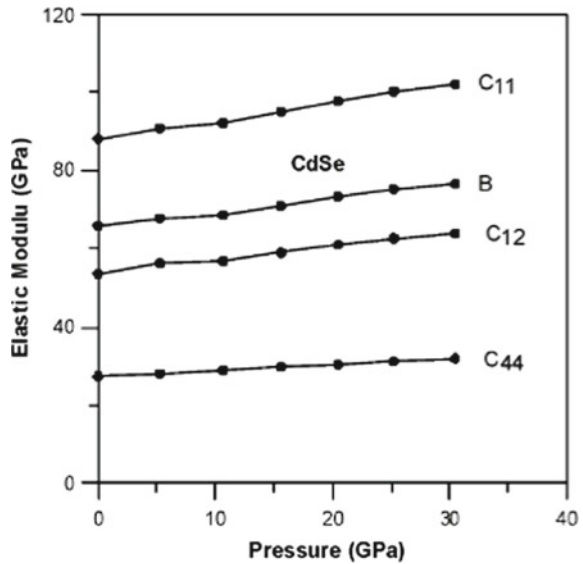
3 Properties of CdSe

Table 6 lists some basic physical properties of cubic and wurtzite CdSe structure. General properties of CdSe are mentioned below:

1. Highly luminescent material with large absorption coefficient.
2. CdSe is wide-band gap compound semiconductor having higher melting point.
3. CdSe shows strong absorption, fluorescence, and electroluminescence in entire visible spectrum which can be changed as per material particle size.
4. It possesses direct intrinsic band gap of 1.74 eV corresponding to a band-to-band emission wavelength of about 709 nm which makes it an interesting material for various optoelectronic devices [27].

Table 6 Basic physical properties of CdSe [26, 39, 40]

Material property	CdSe	
	Zinc Blende or cubic	Wurtzite or Hexagonal
Structural properties		
Appearance	Dark red color	
Ionicity (%)	70	
Molecular weight (a.m.u)	191.37	
Weight %		
Cadmium (Cd)	58.74	
Selenium (Se)	41.26	
Atomic charge on Cd & Se	1.18, −1.18	
Space group	F$\bar{4}$3m	P6$_3$mc
Point group	(T_d^2) 216	(C_{6v}^4) 186
Lattice parameter at 300 K (nm)	$a = 0.6077$	$a = b = 0.4299$ $c = 0.7010$
Bond length (Å)	2.62	2.63
Nearest neighbor distance at 300 K (Å)	2.631 (cation–anion), 4.297 (cation–cation)	
Unit cube volume (10^{-22} cm^3)	2.244	
Molecular density (10^{22} cm^{-3})	1.782	1.7816
Crystal density at 300 K (gm/cm^3)	5.664	5.6615
Cleavage plane	(110)	(11$\bar{2}$0)
		(10$\bar{1}$0)
Formulae/unit cell	4	2
Phase stable at 300 K	Wurtzite	
Structural phase transition temp (°C) from c-CdSe to w-CdSe	95 ± 5 °C	
Phase transition pressure (GPa) from w-CdSe to rock salt	3.0	
Bohr exciton radius (nm)	5.6	
Thermal properties		
Debye temperature (K)	281	230–135 ($T = 55$–300 K)
Melting point (K)	1512	

Table 6 (continued)

Material property	CdSe	
	Zinc Blende or cubic	Wurtzite or Hexagonal
Entropy of fusion (cal/mol K)	16.07	
Molar specific heat at constant volume and pressure (J/g K)		0.124–0.248 ($T = 55$–300 K)
Heat capacity (J/g K)		0.272
Linear expansion coefficient (10^{-6} K^{-1})	3.0	$\alpha_a = 4.13$, $\alpha_c = 2.76$ ($T = 300$ K)
Thermal conductivity (W/cm K)		0.09 ($T = 300$ K)
Heat of crystallization ΔH_{LS} (kJ/mol)	45	
Mechanical properties		
Young's modulus (10^{11} dyne/cm^2)	4.18	5
Poisson ratio	0.345	0.37
Bulk modulus (GPa)	45.6	53
Shear modulus (GPa)		15.3
Knoop hardness (kg/mm^2)		65
Flexure strength (MPa)		21
Microhardness (GPa)		0.90
Optical properties		
UV transparency (μm)		0.75
IR transparency (μm)		20
Energy gap E_g at 300 K (eV)	1.74, direct	
dE_g/dT (meV/K)	0.696	0.424 ± 0.02
Linear pressure coefficient (meV/GPa)		43.1
Refractive index	2.448 (ordinary ray) 2.467 (extraordinary ray)	
Absorption coefficient ($\lambda = 10.6 \,\mu$m) (cm^{-1})	≤ 0.0015	
Other properties		
Average phonon energy (meV)	18.9	25.4
Electronic polarizability (Å^3)		7.93
Deformation potential of the band gap (eV)	-2.7	-2.3

Table 6 (continued)

Material property	CdSe	
	Zinc Blende or cubic	Wurtzite or Hexagonal
Electron affinity χ (eV)		4.95
Spin–orbit split-off energy (eV)	0.41	
Equilibrium pressure at congruent melting point (atm)	1.0	
Minimum pressure at melting point (atm)	0.4–0.5	
Dielectric constant	10.2	
Dielectric constant at low and high $\frac{\varepsilon_0}{\varepsilon_\infty}$ frequency regions	9.5/6.2	
Electron effective mass $\left(\frac{m^*}{m_0}\right)$	0.13	
Hole effective mass $\left(\frac{m^*}{m_0}\right)$	0.45	
Exciton binding energy (meV)	15	
Core exciton binding energy (meV)	10	
Optical electronegativity	0.455	
Phonon mode location (cm^{-1}) Longitudinal optical (ω_{LO}) Transverse optical (ω_{TO}) Surface optical (ω_{SO})	210 169 184	
Ionization energy of phosphorus acceptor (meV)	83 ± 6	

5. CdSe offers large band gap and wavelength tunability. Band gap and wavelength of CdSe can be varied in a wide range from the bulk value by changing the size of the crystallite.
6. It often possesses *n*-type conductivity in bulk as well as in thin film [28].
7. Resistivity decreases with increasing temperature.
8. Bulk CdSe is diamagnetic in nature with the magnitude $= -43 \times 10^{-6}$ emu/mole, and magnetic behavior changes with decreasing size [29].
9. This material is characterized with high dark electrical resistance.
10. It exhibits quantum confinement effect when particle size is near or below the bulk Bohr exciton radius of material.
11. Cadmium selenide compound exists in two structures: cubic and hexagonal structures. The two crystal structures are very close to each other with respect to their crystallographic properties and energy. Both phases are known to coexist at room temperature especially in thin-film form depending on the deposition conditions.

12. CdSe quantum dots show broad absorption and narrow emission spectra [30].
13. CdSe is a low-phonon-energy material and translucent in infrared region of the spectra possessing unique optical properties like high linear and nonlinear indices of refraction, photoinduced changes of index of refraction, and high photosensitivity [31].
14. It forms complexes only with many readily soluble metal salts, e.g., Pb^{2+} but also with sparingly soluble substances like Bi^{3+} [32].
15. This material shows increase in oscillator strength with decrease in particle size.
16. CdSe nanoparticles have high luminescence decay time and show size-dependent extinction coefficient [33].
17. CdSe nanoparticles have high brightness, superior photostability, resistance against photobleaching and photocorrosion [34].
18. CdSe quantum dots can form more than one bound electron–hole pair by impact ionization.
19. CdSe nanoparticles have a very well-defined spherical shape.
20. Size effect can be observed for a crystallite as large as 106 Å [3].
21. CdSe quantum dots have excellent nonlinear optical properties and broad range of optical transmission [35].
22. The average grain size of CdSe nanoparticles increases with increase in pH and temperature of solution.
23. In CdSe nanoparticles, electron–phonon coupling is found and its strength increases with decreasing quantum dot size.
24. CdSe nanoparticles possess larger intrinsic dipole moments leading to fast charge separation [36].
25. Continuous electronic states of bulk CdSe become discrete on decreasing crystallite size.
26. Structure of CdSe changes to the NaCl and CsCl structure from the lower-pressure wurtzite structured phase at pressures near 3 and 94 GPa. Conductivity of CdSe indicates that it remains a semiconductor at up to a pressure of 50 GPa and is predicted to metallize near 180 GPa [37].
27. CdSe rocksalt phase has indirect band gap.
28. In this material, overheating phenomenon occurs when heated at melting point due to their high vapor pressure.
29. Thermal conductivity of CdSe decreases with increasing particle size due to the decrease in the population of phonons [38].

4 Applications of CdSe

CdSe in nanocrystalline form offers a broad range of applications from optoelectronic devices to biomedical technology. This material is found to be useful in the field of energy generation as well as in communication technology, etc. [41]. CdSe nanomaterials are mostly used as alternatives to conventional phosphors in solid-state lighting (SSL). CdSe nanoparticles have nearly continuous absorption spectra

from their band gap wavelength (near infrared) into ultraviolet, allowing multicolor emission by simultaneous excitation of different sized quantum dots. Their narrow emission spectra almost guarantee pure color emission. These specific advantages are reasons for implementing them as active agents in SSL. Their unique optical properties like no photobleaching are also useful for bioimaging purposes and could help make breakthroughs in the medical field. Useful applications of CdSe in photonic devices are the following:

1. CdSe nanomaterials found applications for practical use in LED and solar cell [42, 43] due to its high light-harvesting ability in the visible regions of sunlight. These semiconductor particles have been shown to be useful as chromophores in light-emitting diodes and have been employed in fabricating three different types of solar cells [44]: (i) metal junction solar cells, (ii) polymer hybrid solar cells, and (iii) quantum dot-sensitized solar cells. Current solar cells carry at best, a 31% efficiency, meaning only 31% of the sun's energy (rays) is converted into electricity as the remaining energy is wasted as heat, by the quantization effects in quantum dots, potentially realizing an increase in solar energy conversion to 66% via multiple exciton generation which results in 10% reduction in energy loss. It is an ideal material for use as the window layer of heterojunction solar cells.

2. CdSe nanoparticles have been investigated as a potential candidate in applications like lasers with low threshold current, photoresistors, many kinds of infrared photodetectors, and high-efficiency thin-film transistors [45, 46]. Theoretically, quantum dot lasers offer the potential of better performance than bulk semiconductor lasers. This potential arises from tighter confinement of carriers. In small, strongly confined dots, the separation between energy states is greater than the thermal carrier energies, inhibiting thermal depopulation of the lowest, "emitting" transition and resulting in a low, temperature-insensitive optical-gain threshold, a narrow emission line, and high-temperature stability.

3. CdSe nanoparticles having nonlinear optical property are used in the fabrication of filters to high-speed optical switches and optical window [47, 48].

4. Their outstanding optical properties found applications in electrophotography, gas sensors for the detection of oxygen, acousto-optical devices [49], photographic photoreceptors [50], optical recording materials and superionic materials, large-screen liquid crystal display [51], image intensifier tubes, very stable photoanode in wet photovoltaic cells, PEC cells [52], photoconductors [53], and gamma ray detectors [54].

5. CdSe forms an important class of low-phonon-energy materials transparent in infrared region of spectra with many interesting applications in optics, electronics, and optoelectronics (optical elements and memories, optical circuits, gratings, waveguides, fiber-, planar-, and nonlinear optical devices, photoresists, holographic elements, and generators), in chemistry, biology, medicine, and ecology (ionic sensing, laser ablation, tissue removal, surgical knives, emission spectral analyzers, remote sensors, evanescence wave- and in vivo sensors,

    etc.), in materials engineering and science (optical, electrical, and multilevel memories, micromachining, etc.).

6. Promising material for thermoelectric transducers at medium high temperature and for the design of modulators [55].
7. The unique magnetic properties of CdSe nanoparticles allow themselves to be used in designing nonvolatile memory devices and magneto-optical and magnetoelectronic devices. For example, Mn-doped CdSe nanoparticles are useful for spintronic applications such as spin injectors and magnetic memory elements [56].
8. CdSe quantum dots are used to build single-photon sources in the field of quantum information processing [57].
9. Cadmium selenide having high photosensitivity in the visible region of the spectrum can be utilized in a number of photoconductive, photovoltaic, and electroluminescent devices. For example, due to electroluminescence, it is used as multicolor displays in applications like small handheld television sets or large-area displays in shopping malls or airports.
10. CdSe quantum dots are used to build optical, chemical, thermal, and biosensors with adjustable properties [58–60].
11. CdSe has been considered useful in applications like carbon nanotube electronic device, optical transformers, nanoelectronic circuitry, chemical libraries [61], as new phosphors for displays, heterogeneous photocatalysts, and antireflecting coatings, etc. [62].
12. CdSe is a great material for use in optical amplifier media for telecommunication networks due to narrowband stimulated emission at room temperature [63].
13. CdSe nanoparticles have found application in high-bandwidth optical communication systems because of high optical index of refraction that is needed to guide light.
14. Semiconductor CdSe quantum dots can be used in photodynamic therapy (PDT). Drug made up of this photosensitive material is exposed to light, producing singlet oxygen to destroy cancer cells [64].
15. It is used for making multicolor fluorescent markers useful for biological applications such as bioimaging, biosensing, and biolabeling [65], e.g., diagnostic label in medicine, ultrasensitive detection of nucleic acids, protein interaction studies, and cell imaging.

5 Conclusion

This paper describes structural, thermal, elastic, lattice dynamic, electronic energy-band structure, and optical properties of one semiconductor material cadmium Selenide belonging to II–VI group of the periodic table. Wide, direct band gap, and photosensitive nature of this material is found to be useful for applications of photonic and biomedical application. Applications of this material in bulk and nanocrystalline form in different areas are also summarized in this paper.

References

1. U. Hotje, C. Rose, M. Binnewies. Solid State Sciences, **5** (2003) 1259–1262.
2. H. Stokes, J. Gunter, D.M. Hatch, J. Dong, H. Wang, J.P. Lewis. Physical Review B, **76** (2007) 12102 (1–4).
3. S.B. Zhang, S.H. Wei, A. Zunger. Journal of Applied Physics, **83** (1998) 3192–3196.
4. C. Ma, Y. Ding, D. Moore, X. Wang, Z.L. Wang. Journal of the American Chemical Society, **126** (2004) 708–709.
5. A. Striolo, J. Ward, J. M. Prausnitz, W. J. Parak, D. Zanchet, D. Gerion, D. J. Milliron. Journal of Physical Chemistry B, **106** (2002) 5500–5505.
6. L.S. Li, J. Hu, W. Yang, A.P. Alivisatos. Nanoletters, **1** (2001) 349–351.
7. F. Seker, K. Meeker, T.F. Kuech, A.B. Ellis. Chemical Reviews, **100** (2000) 2505–2536.
8. T.D. Krauss, L.E. Brus. Physical Review Letters, **83** (1999) 4840–4843.
9. L.E. Brus. Journal of Physical Chemistry, **90** (1986) 2555–2560.
10. R.K. Capek, I. Moreels, K. Lambert, D.D. Muynck, Q. Zhao, A.V. Tomme, F. Vanhaecke, Z. Hens. Journal of Physical Chemistry C, **114** (2010) 6371–6376.
11. E. Deligoz, K. Colakoglu, Y. Ciftci. Physica B, **373** (2006) 124–130.
12. A.D. Yoffe. Advances in Physics, **50** (2001) 1– 208.
13. A.L. Efros, M. Rosen, M. Kuno, M. Nirmal, D.J. Norris, M.G. Bawendi. Physical Review B, **54** (1996) 4843–4856.
14. C. Janowitz, O. Günther, G. Jungk, R.L. Johnson, P.V. Santos, M. Cardona, W. Faschinger, H. Sitter. Physical Review B, **50** (1994) 2181–2187.
15. N. Samarth, H. Luo, J.K. Kurdyna, S.B. Qadri, Y.R. Lee, A.K. Ramdas, N. Otsuka. Applied Physics Letters, **54** (1989) 2680–2682.
16. I. Hernández. Calderón. Optical properties and electronic structure of wide band gap II-VI semiconductors, In: M.C. Tamargo (ed.), II-VI Semiconductor Materials and their Applications, Taylor and Francis, New York, (2002) 113 –170.
17. L. Li. Anisotropy in CdSe Quantum Rods, University of California, Berkeley, 2003.
18. M. Jarosz. The physics and chemistry of transport in CdSe quantum dots solids, Massachusetts Institute of Technology, 2004.
19. F. Widulle, S. Kramp, N.M. Pyka, A. Gobel, T. Ruf, A. Debernardi, R. Lauck, M. Cardona. Physica B, **448** (1999) 263–264.
20. S. Suresh, C. Arunseshan. Applied Nanoscience, (2013) https://doi.org/10.1007/s13204-012-0186-5.
21. H.W. Verleur, A.S. Barker Jr. Physical Review, **155** (1967) 750–763.
22. K. Takemoto. Exciton Dephasing Mechanism of CdSe and CuBr Quantum Dots Embedded in Matrix, University of Tsukuba, 2003.
23. N.Q. Huong, J.L. Birman. Journal of Chemical Physics, **108** (1998) 1769–1970.
24. L.E. Brus. Journal of Chemical Physics, **110** (1999) 5355–5369.
25. P. Karamanis, G. Maroulis. Journal of Chemical Physics, **124** (2006) 071101–071102.
26. S. Sachi. Handbook on physical properties of semiconductors, Vol. 3, Kluwer Academic Publishers, USA, 2004.
27. J.E.B. Katari, V.L. Colvin, A.P. Alivisatos. Journal of Physical Chemistry, **98** (1994) 4109–4117.
28. M.G. Bawendi, M.L. Steigerwald, L.E. Brus. Annual Review of Physical Chemistry, **41** (1990) 477–496.
29. D.J. Chadi, R.M. White, W.A. Harrison. Physical Review Letters, **35** (1975) 1372–1375.
30. Y.Q. Zhang, X.A. Cao. Nanotechnology, **23** (2012) 275702 (1–6).
31. M. Frumar, B. Frumarova, P. Nemec, T. Wagner, J. Jedelsky, M. Hrdlicka. Journal of Non-Crystalline Solids, **352** (2006) 544–561.
32. A. Mondal, T.K. Chaudhuri, P. Pramanik. Solar Energy Materials, **7** (1983) 431–438.
33. S.O. Oluwafemi, N.Revaprasadu. Physica B, **404** (2009) 1204–1208.
34. M. Shingyoji, D. Gerion, D. Pinkel, J.W. Gray, F.Q. Chen. Talanta **67** (2005) 472–478.

35. P. Hu, D. Jia, Y. Cao, Y. Huang, L. Liu, J. Luo. Nanoscale Research Letters, **4** (2009) 437–443.
36. D.F. Underwood, T. Kippeny, S.J. Rosenthal. The European Physical Journal D, **16(1)** (2001) 241–244.
37. P. Cervantes, Q. Williams, M. Côté, O. Zakharov, M.L. Cohen. Physical Review B, **54** (1996) 17585–17590.
38. N. Al-Hosiny, A. Badawi, M.A.A. Moussa, R. El-Agmy, S. Abdallah. International Journal of Nanoparticles, **5** (2012) 258–266.
39. W.J. Tropf, M.E. Thomas, T.J. Harris. Properties of crystals and glasses in optical and physical properties of materials, In: M. Bass (ed.), Handbook of optics, Devices measurement and properties II, McGraw-Hill Inc., USA, 1978. 33.2–33.100.
40. C.K.S. Kasap, P. Capper. Wide-Bandgap II–VI Semiconductors: Growth and Properties in Part B Growth and Characterization, In: Handbook of electronic and photonic materials, Springer, Ed. Ist, (2006) 325–339.
41. M. Ohring. The Materials Science of Thin Films, Academic Press, New York, 1992.
42. S.K.J. Al-Ani, H.H. Mohammed, E.M.N. Al-Fwade. Renewable Energy, **25** (2002) 585–590.
43. S. Kang, C.K. Kumar, Z. Lee, K. Kim, C. Huh, E. Kim. Applied Physics Letters, **93** (2008) 191116 (1–3).
44. A.J. Nozik. Physica E, **14** (2002) 115–120.
45. K. Rajeshwar, N.R. de Tacconi, C.R. Chenthamarakshan. Chemistry of Materials, **13** (2001) 2765–2782.
46. F.C. Luo. Journal of Vacuum Science and Technology, **16** (1979) 1045–1048.
47. D.K. Ghosh, P.J. Samanta. Infrared Physics, **26** (1986) 335–336.
48. J.C. Udeajah, Deposition and Characterization of Chalcognide and Halide Thin Solid Films for Industrial Applications, University of Nigeria: Nsukka, 1996.
49. C. Trallero-Giner, A. Debernardi, M. Cardona, E. Menendez-Proupin, A.I. Ekimov. Physical Review B, **57** (1998) 4664–4669.
50. A.V. Gomonnai, Y.M. Azhniuk, V.O. Yukhymchuk, M. Kranjčec, V.V. Lopushansky. Physica Status Solidi B, **239** (2003) 490–499.
51. P.A.K. Moorthy, G.K. Shivakumar. Thin Solid Films, **121** (1984) 151–158.
52. S.J. Lade, M.D. Uplane, C.D. Lokhande. Material Chemistry and Physics, **68** (2001) 36–41.
53. V.M. Garcıa, M.T.S. Nair, P.K. Nair, R.A. Zingaro. Semiconductor Science and Technology, **11** (1996) 427–432.
54. M. Roth. Nuclear Instruments and Methods in Physics Research Section A, **283** (1989) 291–298.
55. S.P. Yordanov. Bulgarian Journal of Physics, **17** (1990) 507.
56. X. Tang, T.C.M. Graham, B. Urbaszek, C. Bradford, K.A. Prior, R.J. Warburton, B.C. Cavenett. Journal of Superconductivity: Incorporating Novel Magnetism, **16** (2003) 19–22.
57. K. Sebald, P. Michler, T. Passow, D. Hommel, G. Bacher, A. Forchel. Applied Physics Letters, **81** (2002) 2920-.
58. W.C.W. Chan, S. Nie. Science, **281** (1998) 2016–2018.
59. N.G. Patel, C.J. Panchal, K.K. Makhijia. Crystal Research and Technology, **29** (1994) 1013–1020.
60. V.L. Colvin, M.C. Schlamp, A.P. Alivisatos. Nature, **370** (1994) 354–357.
61. N. Gaponik, I.L. Radtchenko, G.B. Sukhorukov, H. Weller, A.L. Rogach. Advanced Materials, **14** (2002) 879–882.
62. J.H. Park, J.Y. Kim, B.D. Chin, Y.C. Kim, J.K. Kim, O.O. Park. Nanotechnology, **15** (2004) 1217–1220.
63. M. Harrison, S. Kershaw, M. Burt. Pure and Applied Chemistry, **72** (2000) 295–307.
64. X.H. Gao, S.M. Nie. Trends in Biotechnology, **21** (2003) 371–373.
65. X.H. Gao, Y.Y. Cui, R.M. Levenson, L.W.K. Chung, S.M. Nie. Nature Biotechnology, **22** (2004) 969–976.

Investigation of Mechanical Properties and Microstructure of Pure Al-SiC-Nanocomposite Casted by Stir-Squeeze Casting Process

Pooja Verma, Prabha Kumari, Joyjeet Ghose and Vijay Pandey

1 Introduction

Nano-metal matrix composites (NMMC) have high stiffness with high strength to weight ratio and wear resistance in general, and particularly aluminium metal matrix composite (Al-MMC) finds wide application in aerospace, biomedical, and automotive industries. Nanoparticles reinforced aluminium metal matrix composite (Al-NMMC) has superior properties in compression to the conventional microparticle-reinforced composites.

The use of nanoparticles in composites improves the strength of the metallic matrix with maintaining good ductility, high hardness, and fatigue strength as compared to microlevel composites, because hardness increases with decrease in the particle size [5].

However by reducing reinforcement particle size from micrometer to nano meter chances of agglomeration of particles increase and uniform distribution of particles in the matrix decrease cause of cohesive force between the particles more compare to adhesive force between matrix and particles that was reduced by adding 1 wt% Mg [4]. The reactive elements such as Mg, Ca, Ti or Zr are added to induce wettability [2]. Thus, it improves mechanical properties such as ultimate tensile strength, flexural modulus, and temperature resistance, high flexural modulus to carry demanding loads, high impact strength, durability, corrosion resistance, design flexibility, chemical Resistance.

One of the best-known properties of aluminium is that it is light in weight with density 2700 kg/m^3 one-third that of steel [1]; it is having good malleability, more corrosion resistance, good thermal conductivity (237 W/mK), and it is also having very low electrical resistivity (2.65×10^{-8} Ωm). Its Young's modulus is 70 GPa,

P. Verma (✉) · P. Kumari · J. Ghose · V. Pandey
Department of Production Engineering, Birla Institute of Technology, Mesra,
Ranchi 835215, Jharkhand, India
e-mail: poojakatheria@gmail.com

and its Brinell hardness is 15 HB. Al has melting point of 660.32 °C, and at high temperature, the strength of aluminium decreases. We can improve the mechanical properties of Al, such as ultimate tensile strength, flexural modulus, and temperature resistance, high flexural modulus to carry demanding loads, high impact strength, durability, corrosion resistance, design flexibility, chemical resistance by adding some reinforcement, called composites material. For fabrication nano-metal matrix composites take pure Al as a matrix and add SiC (nano-level) as reinforcement particles.

In this study, pure aluminium work as matrix and silicon carbide work as a reinforcement material. Silicon carbide, also known as carborundum, is a compound of silicon and carbon with chemical formula SiC; its melting point is 2730 °C and density is 3.21 g/cm^3. The SiC (grit size is <90 nm) with purity 99.9% nanoparticle can enhance the properties of pure aluminium in terms of tensile strength, hardness, microhardness, and mechanical strength.

In this paper, a new method stir-squeeze bottom pouring was used for preparation of SiC nanoparticle mix with aluminium matrix composites; step one was melting the Al in furnace and after that stirring the molten metal before mixing the reinforcement and then reheating the matrix and mixing the preheated reinforcement particles and again stirring for uniform distribution of the reinforcement into matrix and then, squeeze casting was done for sound casting of the ANMMC (Aluminum nano-metal matrix composites).

2 Description of Material and Procedure of Experiment

2.1 Raw Materials

Al metal (purity 99.9%) and silicon carbide (grit size is <90 nm with purity 99.9%) particulate forms were used. Pure aluminium was selected as the matrix. Because it is easily castable and low cost. The chemical composition of Al was given in Table 1. The ingots of aluminium were properly cleaned by using the abrasive paper to eliminate the surface impurity and then ingots were cut into small pieces, with the help of power hex saw which were easily melt in the furnace. The nano-silicon carbide particles were used as reinforcement in the aluminium matrix for improving the properties of the Al. The density of SiC is 3.21 g/cm^3 and melting point is 2730 °C.

Composition of element in pure aluminium

Aluminium: 99.0–99.95%,
Copper: 0.05–0.20%,
Iron: 0.95% max,
Manganese: 0.05% max,
Silicon: 0.95% max,
Zinc: 0.1% max,
Residuals: 0.15% max.

Table 1 Density and porosity

Samples	Dry weight	Shocked weight	Wei weight	Density(g/cm^3)	Porosity
1.	5.0993	5.102	3.2133	2.70	0.00148
2.	5.0974	5.1004	3.2086	2.78	0.00158
3.	4.4114	4.4125	2.7724	2.77	0.00067
4.	5.242	5.2463	3.2947	2.77	0.00169
5.	5.3122	5.3148	3.3463	2.78	0.00132

2.2 Manufacturing of Al-SiC Nanocomposites

Stir-squeeze casting process was used for fabrication of NAl-SiC composites. This process employs in sequence mechanical stirring of the melt followed by stirring the molten metal and followed by squeeze casting to definite shape, to take advantage of respective process.

The process was carried in a bottom pouring resistance heating furnace stirrer and squeeze casting attachment as shown in Fig. 1. The process starts by melting the aluminium alloy in the furnace and heating up to about 800 °C. Simultaneously nano-reinforcement particles were also heated in the preheated powder furnace as shown in Fig. 1. After melting the Al and when sufficient temperature is reached, the preheated particles were injected in the melt and mechanically stirred for about 10 min. The stirrer was then removed, and the furnace is closed again and reached 800 °C. The squeeze casting attachment was previously attached to the bottom of the furnace using a delivery pipe with path furnace. Squeeze casting is very useful for mass production, better metallurgical quality of matrix alloy due to solidification under pressure, and improvement in the *wettability* of the reinforcements by the liquid metal. There were two furnaces used for stir-squeeze casting method, mould furnace and pathway furnace. Mould furnace was used for melting the Al matrix, and pathway furnace was used for maintaining the temperature till the pouring metal. Once the entire mould fills by the molten metal, the mould of the plunger of the squeeze casting attachment is pressed on the mould with suitable load. The metal was solidifying in the mould under pressure and it was cooled at room temperature.

3 Mechanical Tests

The tensile strength was investigated by using UTM (88o1K1403). Tensile test was carried on specimens ASTM E8 standard with length of gauge 32 mm and a diameter of 6 mm. The specific dimensions of tensile test specimens are shown in Figs. 2 and 3. The microstructure was investigated with the help of optical microscopy, and distribution of reinforcement particles investigated by scanning electron microscope (SEM), and crystals' structure was found out by X-ray diffraction (XRD). Hardness
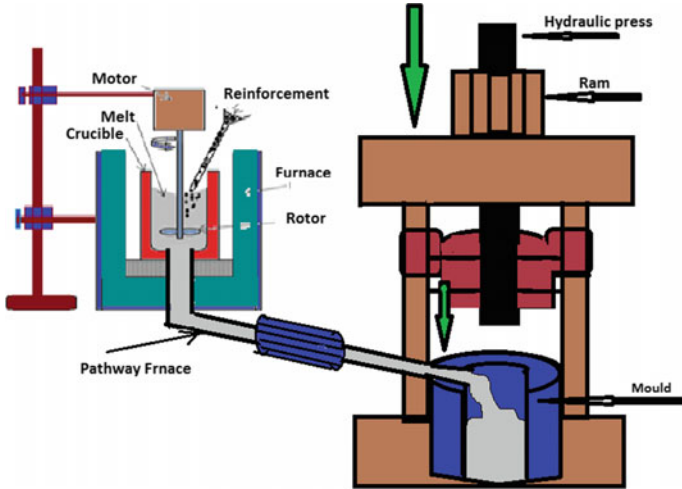
Fig. 1 Stir and squeeze casting machine

Fig. 2 Tensile test specimen with dimension

Fig. 3 Specimen after tensile test
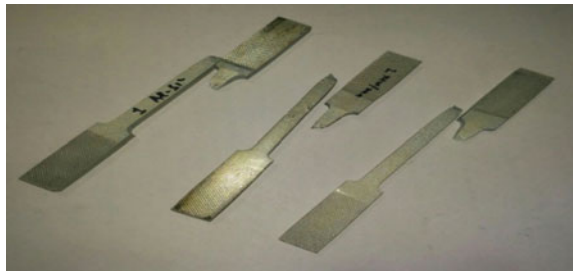
of the Al-SiC nanocomposites was studied using Brinell hardness tester; the applied load and dwell time were 500 kg and 15, respectively.

3.1 Microstructural Characterisation

The distribution of reinforcement SiC nanoparticles in aluminium matrix was found out by scanning electron microscope (SEM-JSM-6390LV). The SEM analysis was done after polishing of all the samples in polishing machine. The specimens for microstructure and SEM were mirror polished. Optical microstructures of the resulting composites were examined under a metallographic microscopy after being mirror polished after that etched by Keller's reagent (2 ml HF + 3 ml HCL + 5 ml HNO_3).

3.2 Tensile Test

Tensile tests were tested on universal testing machine (Instron, UK, 8801) at room temperature with two tensile rates 1 mm/min and 2 mm/min. Three specimens for tensile tests were cut with the help of EDM wire machine from composites ingot; one sample tests with 1 mm/min tensile rate, and two samples test with 2 mm/min tensile rate.

3.3 Hardness

Hardness test was tested on Brinell hardness tester. The applied load and dwell time were 500 kg and 15 s, respectively. An average of three reading was taken from each hardness value. The diameter of the steel ball was 10 mm.

3.4 Density and Porosity

Densities of samples were found out with the help of Archimedes' principle. There were three weight measures for finding density and porosity of samples; dry weight, shock weight, and suspended weight. Five samples for density and porosity tests were cut from composites ingot with the help of EDM wire machine, and the porosity and density reported in this paper were found with the help of the following formula:

$$\text{Relative density} = \text{Dry weight}/(\text{Shock Weight - Suspended weight})$$
$$\text{Approximate porosity} = (\text{Shock Weight - Dry weight})/(\text{Shock Weight} - \text{Suspended weight})$$

4 Results and Discussions

4.1 SEM and XRD Analysis Nano-Al-SiC Composites

Figures 4, 5, and 6 show the SEM and EDS images of Al-SiC nanocomposites. The microscopic examination of Al-SiC nanocomposites was studied with the help of SEM, and the interaction between matrix and reinforcement was examined by scanning electron microscope (SEM) with energy-dispersive spectrometry (EDS). Micrographs show that stir-squeeze casting process gives uniform distribution of and low agglomeration of particles in the matrix. The images show that stir-squeeze casting process causes the improvement of microstructural densification, lowering of porosity, grain refining, and the grains orientation in the extruded direction, finally gives the sound casting product.

In this study, the effective stirring system and 1 wt% Mg were used for uniform distribution of nanoparticles in the matrix. The stirring during the liquid state and adding Mg can help to break the surface tension on the surface of the composite powder, thus improving the wettability. Also, during solidification pressure approximately 30 mp was applied which reduces the porosity and gives defect free casting.

Fig. 4 SEM image of Al-SiC nanocomposite
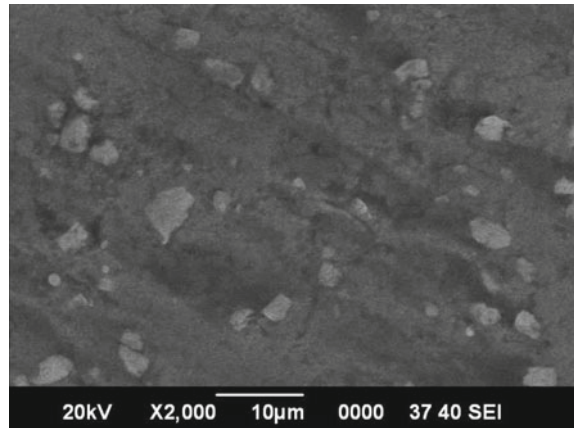
Fig. 5 EDS image of Al-SiC nanocomposite
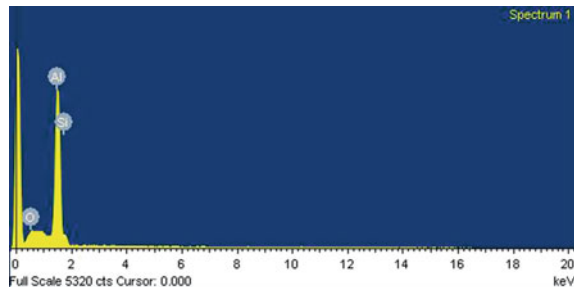
Fig. 6 SEM microstructure of composites reinforced with 1 wt% SiC nano-powder into Al matrix
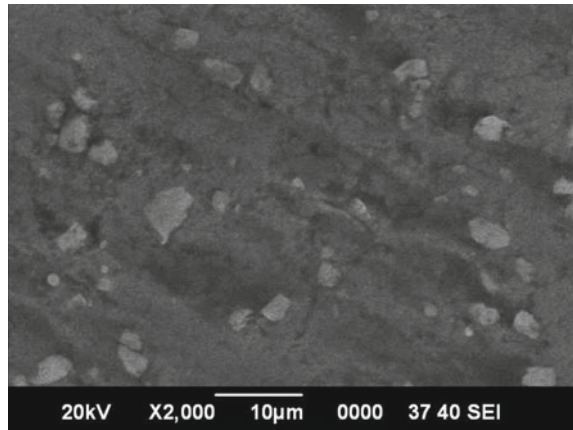
Fig. 7 X-ray diffraction of Al-1 wt% SiC nanocomposites
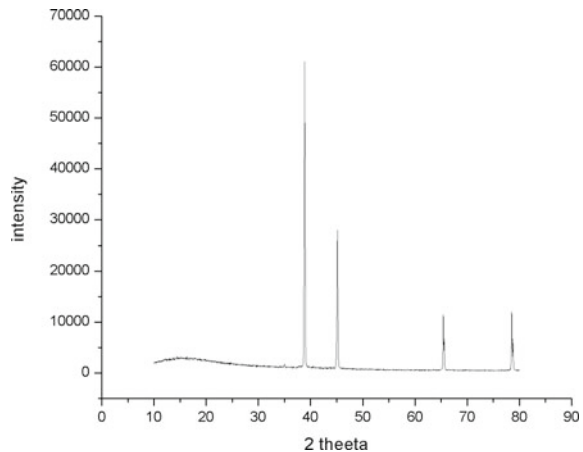
The interaction between Al and SiC nanoparticles was determined with the help of XRD (X-ray diffraction) analysis (Fig. 7).

Figures 7 and 8 shows the XRD analysis, was used to determine the possible interaction between nano powder and Al matrix. XRD pattern of pure aluminium showed cubic structure. The diffraction pattern very well matches with the composites graph, it shows that no change in the crystal structure of the composites when adding nano reinforcement.

4.2 Porosity and Density

According to the measured densities of composite samples and theoretical densities, it was found that the amount of porosity in samples decreases due to higher

Fig. 8 X-ray diffraction of
Al-1 wt% SiC
nanocomposites
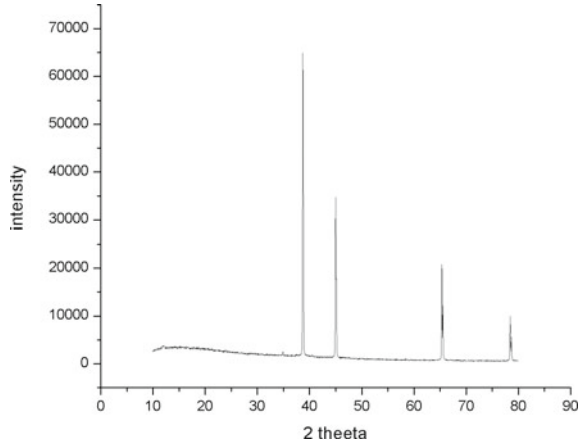
Table 2 Hardness in the samples

Sample Al-SiC nano	Indent diameter(mm) Load = 500 kgf, ball diameter = 10 mm		Average indent diameter(mm)	Average BHN value (in BHN)
1.	5.9	5.8	5.85	16.1
2.	5.91	6.1	6	16.01
3.	5.9	6.101	6.00	15.94
4.	5.84	6	5.9	15.92

pressure (approx. 31 mpa) applied during solidification in squeeze casting process. The porosity is generally increased because of some principles regions such as: (1) increase in contact area of surface with air caused by increasing the weight % and decreasing the particle size, (2) air entrapment during stirring, (3) hydrogen evolution, (4) the pouring distance from the furnace to the mould, and (5) shrinkage during solidification. Also, it is revealed that stirring speed of 450 rpm shows the best result in uniform distribution of SiC nanoparticle in Al matrix with stir-squeeze casting process. The density is almost constant in everywhere like top-middle and bottom portions of samples. Table 1 shows the density and porosity.

4.3 Hardness

Hardness test was done on Brinell hardness tester. Specimen for hardness was cut from top, middle, and bottom portions from the casted material. It was clear that the hardness of nanocomposites is higher than that of the matrix. Hardness of samples increases with decreasing the particles' size in matrix [3]. Table 2 shows the hardness in the samples.

Fig. 9 Stress–strain diagram with strain rate 1
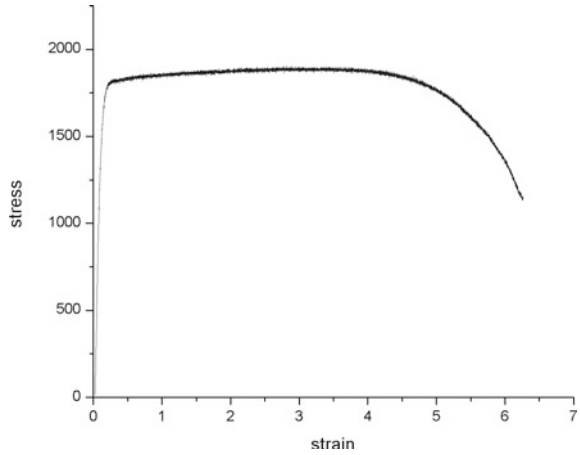
Fig. 10 Stress–strain diagram with strain rate 2
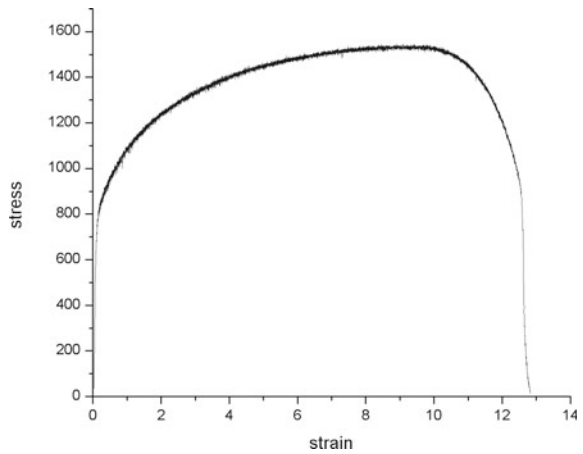
4.4 Tensile Strength

Tensile test was done on specimen prepared with gauge length of 32 mm and thickness of 6 mm (ASTM E8 standard) on EDM wire machine (Figs. 2 and 3). Tensile strength of the composites increases when nano-size particles added in the matrix, because nanoparticles maintain the ductility of the composites. Tensile tests were in universal testing machine (Instron, UK, 8801) at room temperature with tensile rate of 1 mm/min and 2 mm/min (Figs. 9 and 10).

4.5 Conclusion

Pure Al-1 wt% SiC nanocomposites were fabricated by stir-squeeze casting where nano-powder in particle form mix into the melt matrix. For investigation of effect of stir with 450 rmp and hot extrusion process, the microstructure and mechanical properties of the NAl-SiC samples were investigated. The following results were obtained:

1. SiC nanoparticles have a fine grain microstructure with low porosity due to using squeeze process.
2. The porosity volume per cent increased with increasing stir speed and decrease with extrusion process.
3. Using stir-squeeze casting process, nano-SiC particles were uniformly dispersed throughout the matrix with low agglomeration.
4. Due to extruded process, the higher strength and ductility maintain with lower porosity content, more uniform distribution of SiC in the matrix and grain refinement due to stirring and adding 1 wt% of Mg.

References

1. Seshan S, Guruprasad A, Prabha M, Sudhakar A (1996) Fibre-reinforced metal matrix composite-a review. Department of mechanical engineering, Indian Institute of science, Bangalore 76, 1–4.
2. Hashim J, Looney L, Hashmi M.S.J (1999) Metal matrix composites: production by stir casting. Material processing technology 92–93, 1–7.
3. Sajjadi S.A, Ezatpour H.R, Beygi H (2011) microstructure and mechanical properties of Al-Al_2O_3 micro and nano composites fabricated by stir casting. Material science and engineering A 528, 8765–8771.
4. Tahamtan S, Halvaee A, Emamy M, Zabihi M.S (2013) fabrication of Al/A206- Al_2O_3 nano/micro composite by combining ball milling and stir casting technology. Material and design 49, 347–359.
5. Valibeygloo N, Azari Khosroshahi R, Taherzadeh Mausavian R (2013) Microstructure and mechanical properties of Al-4.5wt% Cu reinforced with alumina nano particles by stir casting method. Minerals metallurgy and materials 20, 978–985.
6. Tony Thomas A, Parameshwaran R, Muthukrishanan A, Arvind Kumaran M (2014) Development of feeding and stirring mechanism for stir casting of aluminium matrix composites. Procedia material science 5, 1182–1191.

Study of the Oxidation of Sulphanilic Acid by Cr(VI)-Based Oxidants

A. Prameela

1 Introduction

Degradation process is used as a method of preparing different complexes of defined structures and properties [1–3] by using a number of oxidants in aqueous medium. To carry out such oxidative degradation and result in complexation, some of the workers have used oxidants like pyridine chromium peroxide, di-tertiary butyl chromate and di-isopropyl chromate. Among the various Cr(VI)-based oxidants, CrO_3 appears to be the most suitable one, as others suffer from a number of disadvantages, viz. thermal stability, hygroscopic nature, large excess requirements, poor selectivity and non-effectiveness for acid-sensitive substrates. Alam et al. [4] have prepared complexes of chromium with various organic substrates and tertiary butyl chromate in different solvents. Some mixed ligand complexes of chromium had been prepared by the interaction of CrO_3 with lactic acid and hydrazine hydrate by Mishra et al. [5].

Sulphanilic acid forms salts with bases but does not combine with acids. Oxidation of sulphanilic acid by the various oxidants has been carried out. When sulphanilic acid is treated with nitric acid, the sulphonic acid group is replaced by a nitro group to form para nitro aniline.

Oxidation of sulphanilic acid by peroxomonophosphoric acid to corresponding azoxy derivative was reported by Panigrahi et al. [6]. Also oxidation reaction of catechol with periodate in the presence of sulphanilic acid was also investigated spectrochemically.

In this research work, oxidation of sulphanilic acid is carried out by tertiary butyl chromate under various concentration conditions and a hope was there to get different degradation products complexed with Cr.

A. Prameela (✉)
Department of Chemistry, Ranchi University, Ranchi 834001, Jharkhand, India
e-mail: arya.pramila@gmail.com

1.1 Objective

In the present work, action of CrO_3 on sulphanilic acid has been studied by employing different reaction condition, as mentioned in the abstract with following objectives:

(a) Whether the process of oxidation is selective, will arresting the reaction up to different stages (by taking different molar ratios) result into same product or not?
(b) Whether any change in medium affects the reaction?

1.2 Experimental Section

Materials Used: The materials used for carrying out research were procured by Ranchi University from the following vendors:

1. Chromium trioxide
   Purity: 99.5%
   Vendor's Name: Intelligent Materials Pvt. Ltd. Mubarakpur, Dera Barsi.
2. Tertiary butyl alcohol
   Purity: 99.0%
   Vendor's Name: MP Biomedicals India Pvt. Ltd. Navi Mumbai.
3. Sulphanilic acid
   Purity: 99.5%
   Vendor's Name: Sisco Research Laboratory Pvt. Ltd.
4. 1,4-dioxan
   Purity: 99.5%
   Vendor's Name: Mehk Chemicals Pvt. Ltd.
5. Ammonia solution
   Purity: Ranging from 10 to 20%
   Vendor's Name: Trikaldarshi Chemical Industries, Mumbai.

1.3 Experimental Methodology

1. In each case, CrO_3 (oxidant) was dissolved in t-butyl alcohol.
2. Substrate (sulphanilic acid) was dissolved in 1,4 dioxan and ammonia solution.
3. These two solutions were mixed together, stirred and refluxed and in each case, solid products got separated out.
4. Solid products isolated were washed with acetone for four, respectively, to remove the impurities.
5. Pure solid products obtained were then subjected to Elemental and IR Analysis.
6. Empirical formulae of the products were determined.

7. Thermal analysis was carried out and TG, DTA peaks were recorded.
8. Finally, possible molecular formulations of the complexes were proposed.

1.4 Results and Discussion

Colours of the sample AP-5 and AP-6 obtained were brown, and on the basis of quantitative and spectroscopic analysis, the products were found to be the complexes of chromium involving oxidized fragments of the substrate as ligands along with water molecules (in some cases) that might have been formed during the oxidation process. With variation in concentration of CrO_3, the complexes have varying composition with reference to oxygen attached to the metal. Thermal analysis had further supported the results. The degree of oxidation, however, varies with variation of the relative amount of the substrate and the reagent. The results have been supported by thermal analysis. Characterization of these complexes throw light on oxidation products. The product occurs as ligand in complexes of Cr which come out as precipitate in course of reaction. The products of degradation find use in ascertaining the point of attacks of the oxidant on the substrate molecules.

1.5 Experimental Results and Discussion for the Sample AP-5

 (i) Colour of the sample AP-5: Brown
(ii) Composition of the sample:

Element	(%)
C	26.79
H	3.77
O	26.69
Cr	19.32
N	8.51
S	11.92

(iii) Empirical formula of the sample AP-5: $C_6 H_{10} O_5 NCrS$
(iv) IR peaks in the spectrum were studied, and group assignment was done accordingly.

Wave no. (cm^{-1})	Group assignment
3360.2	NH$_2$ stretch
3016.5	Aromatic C–H stretch
1219.7	S=O stretch
1002.6	HOH rocking due to coordinated water
827.2	p-di-substituted aromatic compound
558.9	Cr–O bonding

1.6   Discussion

The peak at 3360.2 cm^{-1} shows the NH$_2$ stretch and 3016.5 cm^{-1} shows the aromatic C–H stretch, respectively. Evidence for S–O stretching at 1219.7 cm^{-1} is hidden within number of peaks in the fingerprint zone. The peak at 1002.6 cm^{-1} is due to HOH rocking due to coordinated water. The peak at 827.2 cm^{-1} shows p-di-substituted compound. The absorption peak at 558.9 cm^{-1} region denotes metal–ligand bonding.

1.7   Thermal Analysis of the Sample AP-5

On heating AP-5, it loses 36.4 units of molecular mass due to loss of two molecules of water. On further heating at high temperature, it loses 192.4 units giving CrO as a constant mass residue. The steps involved in the process are all endothermic in character.

1.8   Results of Thermogravimetric Analysis

Sample/Emp. form. mass	% left	No. of gm per formula left	Wt. loss	Diff in wt. loss	Formula left after the loss of fragments
AP-5	(a) 86	224	36	–	2H$_2$O lost
260	(b) 26.15	68	156	120	CrO left

1.9 Experimental Results and Discussion for the Sample AP-6

i. Colour of the sample AP-6: Brown
ii. Composition of the sample:

Element	(%)
C	40.86
H	3.75
O	13.64
Cr	14.7
N	8.73
S	18.32

iii. Empirical formula of the sample AP-6: $C_{12}H_{13}O_3N_2S_2Cr$
iv. IR peaks in the spectrum AP-6 were studied, and group assignment was done accordingly.
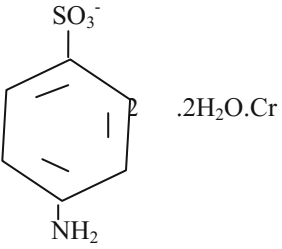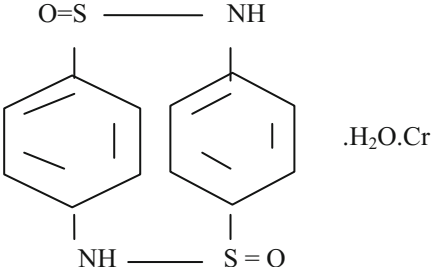
Wave no.	Group assignment
3323.3	NH_2 stretch
3021.5	Aromatic C–H stretch
1218.2	S=O stretch
1005.9	HOH rocking due to coordinated water
829.2	p-di-substituted benzene
562.8	Metal–ligand bonding

1.10 Discussion

The peak at 3323.3 cm^{-1} shows the O–H stretching and at 3021.5 cm^{-1} shows the aromatic C–H stretching, respectively. The peak at 1218.2 cm^{-1} is a S=O stretch. The peak at 1005.9 cm^{-1} is HOH rocking due to coordinated water . The absorption

peak at 829.2 cm^{-1} is p-di-substituted aromatic compound. The absorption peak at 562.8 cm^{-1} region denotes Cr–O bonding.

1.11 Findings for Samples AP-5 and AP-6 Are Given Below

Sample Substrate: CrO_3	Composition of the product	Structural formula
AP-5 1: 1.5	$C_6H_{10}O_5NCrS$	
AP-6 1: 1	$C_{12}H_{13}O_3N_2S_2Cr$	

2 Conclusion

The oxidation state of Cr in the complexes appears to be influenced by the molar substrate and oxidant ratio. In general, excess of oxidant appears to give complexes in which chromium has higher oxidation state. The complexes of chromium with sulphanilic acid and their degradation products are stable to heating but volatile since finally only chromium oxide complex is left out (Figs. 1, 2 and 3).
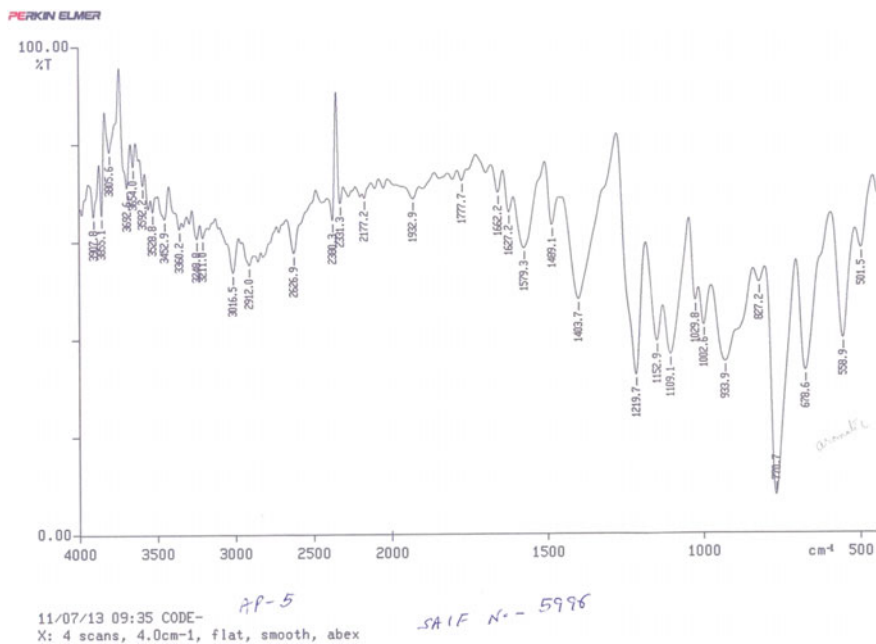
Fig. 1 IR spectra of sample AP-5

Fig. 2 IR spectra of sample AP-6

PERKIN ELMER

11/07/13 09:50 CODE- AP-6
X: 4 scans, 4.0cm-1, flat, smooth, abex   SAIF No -5996

Fig. 3 TG/DTA curves of sample AP-5

References

1. J. Fugita, K. Nakamoto and M. Kobyashy, J. AM. Chem. Soc. 98. 3963 (1956).
2. A. K. Laha & A. B. Kulkarni, J. Sc. Ind. Res. 506 (1985).
3. G. Mishra, M. Alam, Renuka Thakur & N. Mishra, J. Inst. Chem. (Ind.) 63,!66 (1991).
4. G. Mishra, M. Alam, N. Dwivedi & N. N. Mishra, J. Inst. Chem. (Ind.) 63, 169 (1991).
5. R. K. Dubey, U. K. Dubey, C. M. Mishra "Synthesis and physiochemical characterization of some Schiff base complexes of Cr(III) complexes". Indian J. Chem. 45A: 1638–1642 (2006).
6. G. P. Panigrahi et al. Vol. 21 Nov. 3 (1982) Pages 283–287.

Oxidation of Phthalic Acid by CrO_3 (VI)

A. Prameela

1 Introduction

A number of oxidants in non-aqueous medium have been used in recent years and in turn have given us the potential to use the process of degradation as a method of preparing complexes of defined structures and properties [1–3]. Some of the workers have used oxidants like pyridine chromium peroxide, di-tertiary butyl chromate, di-isopropyl chromate to carry out such oxidative degradation and result in complexation. Among the various Cr (VI)-based oxidants, CrO_3 appears to be the most suitable one, as others suffer from a number of disadvantages, viz. thermal stability, hygroscopic nature, large excess requirements, poor selectivity, non-effectiveness for acid-sensitive substrates. Alam et al. [4] have prepared complexes of chromium with various organic substrates and TBC in different solvents. Some mixed ligand complexes of chromium had been prepared by the interaction of CrO_3 with lactic acid and hydrazine hydrate by Mishra et al. [5].

Degradation of phthalic acid and benzoic acid from terephthalic acid is reported in J. Environ Sci Health [6]. My study of the oxidation of phthalic acid by CrO_3 in tertiary butyl chromate is carried out, and again, the reduced state of Cr is trapped by powerful chelating agent than the products of its oxidation. As a consequence, I get phthalate ion as the common ligand in all the products obtained by its oxidation with Cr (VI)-based oxidants in different solvents.

A. Prameela (✉)
Department of Chemistry, Ranchi University, Ranchi 834001, Jharkhand, India
e-mail: arya.pramila@gmail.com

2 Objective

In the present work, action of CrO_3 on phthalic acid has been studied by employing different reaction conditions, with an objective to see whether the process of oxidation is selective and will arresting the reaction up to different stages (by taking different molar ratios) result into same product or not? And if any change in medium affects the reaction?

3 Experimental Section

Material Used: The materials used for carrying out research were procured by Ranchi University from the following vendors:

1. Chromium trioxide
   Purity: 99.5%
   Vendor's name: Intelligent Materials Pvt. Ltd, Mubarakpur, Dera Barsi.
2. Tertiary butyl alcohol
   Purity: 99.0%
   Vendor's name: MP Biomedicals India Pvt. Ltd, Navi Mumbai.
3. Phthalic acid
   Purity: 99. %
   Vendor's name: Kamdhenu Chemicals, Ankleshwar, Gujarat.
4. 1,4-dioxan
   Purity: 99.5%
   Vendor's name: Mehk Chemicals Pvt. Ltd.

4 Experimental Methodology

- In each case, CrO_3 (oxidant) was dissolved in a suitable medium of t-butyl alcohol.
- Substrate (phthalic acid) was dissolved in 1,4-dioxan.
- The two solutions were mixed together, stirred, refluxed for about one hour, and in each case, solid products separated out.
- Solid products isolated were washed with acetone for four to five times repeatedly.
- Pure solid products obtained were then subjected to elemental and IR analysis.
- Empirical formulae of the products were determined.
- Thermal analysis was carried out, and TG, DTA peaks were recorded.
- Finally, possible molecular formulations of the complexes were proposed.

5   Results and Discussion

On the basis of quantitative and spectroscopic analysis, the products were found to be the complexes of chromium involving oxidized fragments of the substrate as ligands along with water molecules (in some cases) that might have been formed during the oxidation process. With variation of the relative amount of the substrate and the reagent, the degree of oxidation, however, varies. Thermal analysis had further supported the results. The characterization of these complexes throws light on the oxidation products of organic substrates. The degradation products that are identified help in ascertaining the point of attacks of the oxidant on the substrate molecules and provide information for subsequent works that can lead to mechanism of reactions.

6   Experimental Results and Discussion of Sample AP-8

   i.   Color of the sample AP-8: brown
  ii.   Composition of the sample:

Element	%
C	24.04
H	3.66
O	46.82
Cr	25.48

 iii.   Empirical formula of the sample AP-8: $C_8H_{14}O_{12}Cr_2$
  iv.   IR peaks in the sample and group assignment:

Wave no. (cm^{-1})	Group assignment
3370.6	O–H stretch
3022.5	Aromatic C–H stretch
2375	HOH rocking due to coordinated water
1524.0	C=O stretching, asymmetric in COO–
1405.7	C=O stretching, symmetric in COO–
1217.7	C–O stretch strong
1143.5	HOH rocking due to coordinated water
769.9	o-disubstituted benzene
523.0	Cr–O bonding
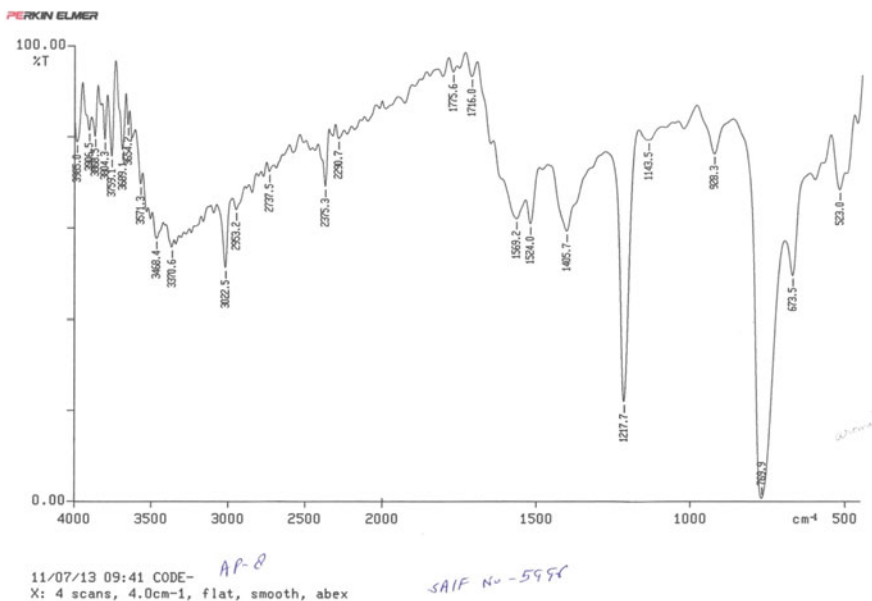
Fig. 1 IR spectra of sample AP-8

7 Discussion

The peak at 3370.6 cm^{-1} shows the O–H stretching and at 3022.5 cm^{-1} shows the aromatic C–H stretch. IR peaks at 1524 and 1405.7 cm^{-1} are due to the presence of COO– groups. The peak at 2375 cm^{-1} is HOH rocking due to the coordinated water. The peak at 769.9 cm^{-1} is very intense absorption peak, and it shows o-disubstituted aromatic compound. The absorption peak at 523.0 cm^{-1} region denotes Cr–O bonding (Fig. 1).

v. **Thermal Analysis of the sample AP-8 (Formula weight—406)**

8 Discussion

On heating AP-8, it loses 90 units of molecular mass. This is probably due to loss of five molecules of water. On further heating at high temperature, there is a loss of 270 units giving CrO as a constant mass residue. The steps involved in the process are all endothermic in character. The elemental analysis, IR analysis along with the sequence of the thermal decomposition shown above support the possible proposed formula as shown below:

$$COO^-$$

$$COO^-$$

. $5H_2O.Cr_2O_3$
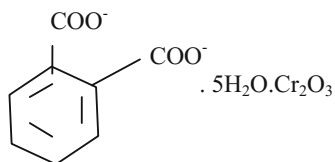
9 Experimental Results and Discussion of Sample AP-9

i. Color of the sample AP-9: brown
ii. Composition of the sample:

Element	%
C	25.64
H	3.42
O	43.12
Cr	27.82

iii. Empirical formula of the sample AP-9: $C_8H_{12}O_{10}Cr_2$
iv. IR peaks in the sample and group assignment

Wave no. (cm^{-1})	Group assignment
3380.5	O–H stretch
3020.8	Aromatic C–H stretch
1574.7	C=O stretching, asymmetric in COO–
1411.9	C=O stretching, symmetric in COO–
1219.2	C–O stretch strong
1032.3	HOH rocking due to coordinated water.
771.3	o-disubstituted benzene
488.4	Cr–O bonding
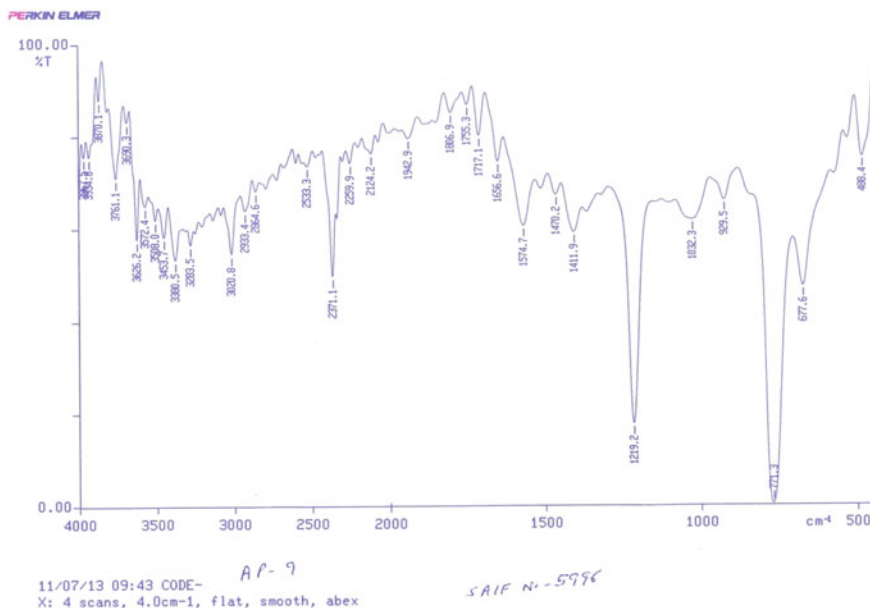
Fig. 2 IR spectra of AP-9

10 Discussion

The peak at 3380.5 cm^{-1} is due to O–H stretch and 3020.8 cm^{-1} shows the aromatic C-H stretch, respectively. IR peaks at 1574.7 and 1411.9 cm^{-1} show the presence of COO– group. The peak at 1219.2 is a C–O stretch, respectively. The peak at 1032.3 cm^{-1} is HOH rocking due to coordinated water. The peak at 771.3 cm^{-1} is o-disubstituted benzene. The peak at 488.4 cm^{-1} region denotes Cr–O bonding (Fig. 2).

v. **Thermal Analysis of the sample AP-9 (Formula weight: 372)**

11 Discussion

On heating AP-9, it loses 36 units of molecular mass. This is probably due to loss of two water molecules. On further heating, there is a great loss and the thermogravimetric curve indicates that whole of the compound is volatile. On the basis of elemental analysis, IR analysis, along with the thermal decomposition sequence, AP-9 may have possible structure as:

$$. \, 4H_2O \, . \, Cr_2O_2$$
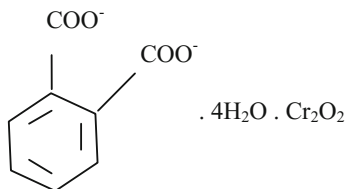
12   Experimental Results and Discussion

  i.   Color of the sample AP-10: brown
 ii.   Composition of the sample:

Element	%
C	29.39
H	3.56
O	35.2
Cr	31.85

iii.   Empirical formula of the sample AP-10: $C_8H_{12}O_{10}Cr$
iv.   IR peaks in the sample and group assignment:

Wave no. (cm^{-1})	Group assignment
3315.2	O–H stretch
3022.6	Aromatic C–H stretch
1584.8	C=O stretching, asymmetric in COO–
1424.0	C=O stretching, symmetric in COO–
1217.4	C–O stretch (strong)
1018.6	HOH rocking due to coordinated water
770.0	O-disubstituted benzene
460.7	Cr–O bonding

13   Discussion

The peak at 3315.2 cm^{-1} shows the O–H stretch and at 3022.6 cm^{-1} shows the aromatic C–H stretching, respectively.IR peaks at 1584.8 and 1424.0 cm^{-1} show the presence of COO– group. The peak at 1217.4 cm^{-1} is a strong peak and is due
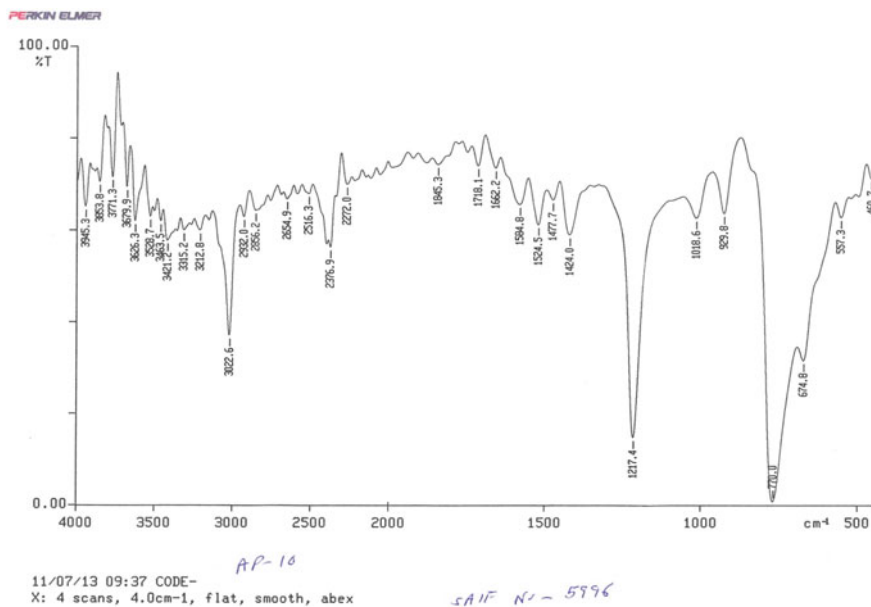
Fig. 3   IR spectra of AP-10

to C–O stretching, respectively. The peak at 1018.6 cm^{-1} is HOH rocking due to coordinated water. And the peak at 770.0 cm^{-1} is very intense absorption peak, and it shows o-disubstituted compound. The absorption peak at 460.7 cm^{-1} region denotes Cr–O bonding, respectively (Fig. 3).
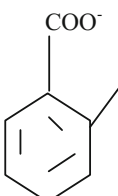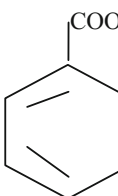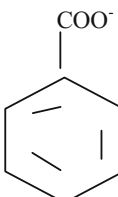
v.   **Thermal Analysis of the sample AP-10 (Formula weight: 320)**:

14   Discussion

On heating AP-10, it loses 54 units of molecular mass. This is probably due to loss of three molecules of water. On further heating, i.e., at high temperature, 244 units are lost giving ½ CrO$_3$ as a constant mass residue. The steps involved in the process are all endothermic in character. On the basis of elemental analysis, IR analysis data, along with thermal decomposition sequence, AP-10 may have the possible structure as shown below :

$. 4H_2O.CrO_2$
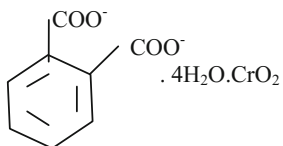
15 Findings Are Given Below

Sample sub:CrO_3	Composition of the product	Structural formulae
AP-8 0.5:1.5	$C_8H_{14}O_{12}Cr_2$	$. \ 5 H_2O . Cr_2O_3$
AP-9 1:1.5	$C_8H_{12}O_{10}Cr_2$	$. 4 H_2O. Cr_2O_2$
AP-10 1:1	$C_8H_{12}O_{10}Cr$	$. 4H_2O . CrO_2$

16 Results of Thermodynamic Analysis

Sample/Empirical formula mass	% left	No. of grams per formula left	Weight loss	Difference in weight loss	Formula left after the loss of fragments
AP-8	78	316	90	–	5 H_2O lost
406	33.5	136	180	90	2 CrO left
AP-9	90.2	336	36	–	2 H_2O lost
372	–	Nil	240	204	–
AP-10	83.1	266	54	–	3 H_2O lost
320	23.7	76	190	136	½ Cr_2O_3 left

17 Conclusion

The degree of oxidation, however, varies with variation of the relative amount of the substrate and the reagent. The results have been supported by thermal analysis. The oxidation state of Cr in the complexes appears to be influenced by the molar
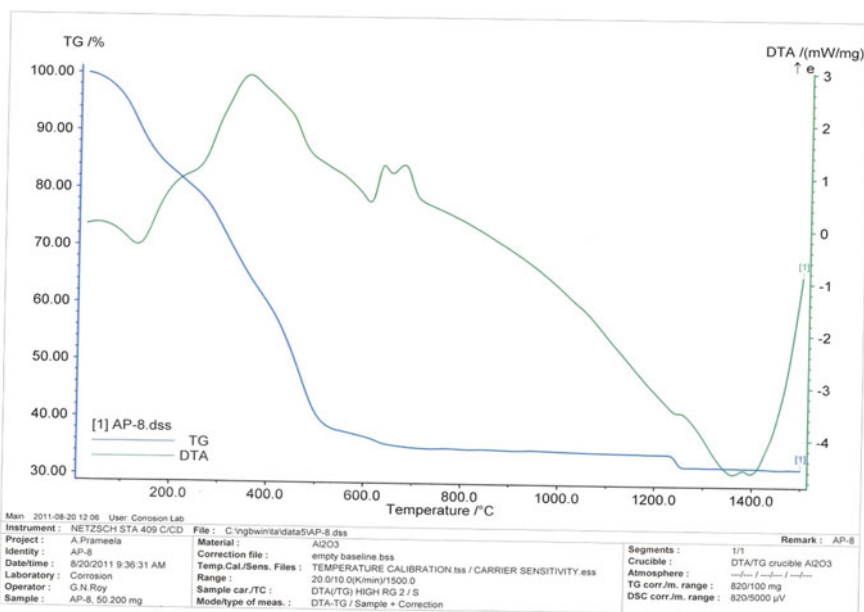
Fig. 4 TG/DTA curves of sample AP-8
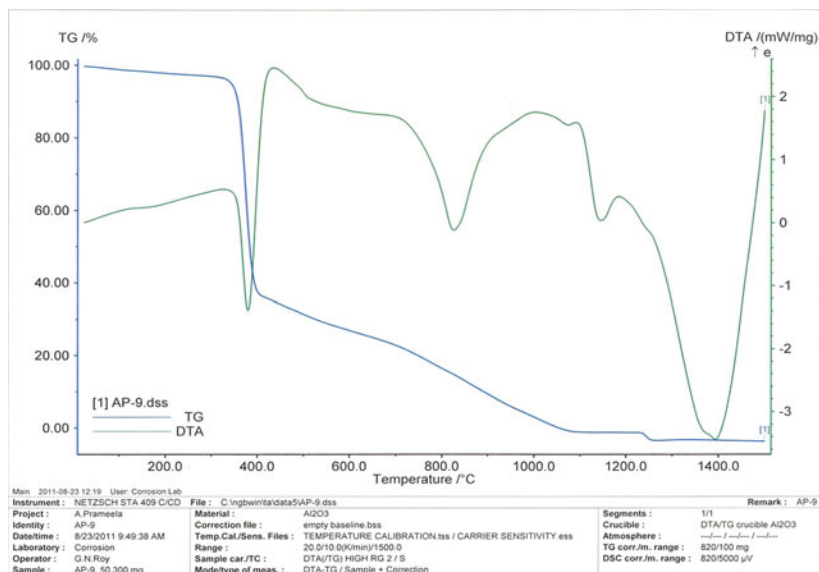
Fig. 5 TG/DTA curves of sample AP-9
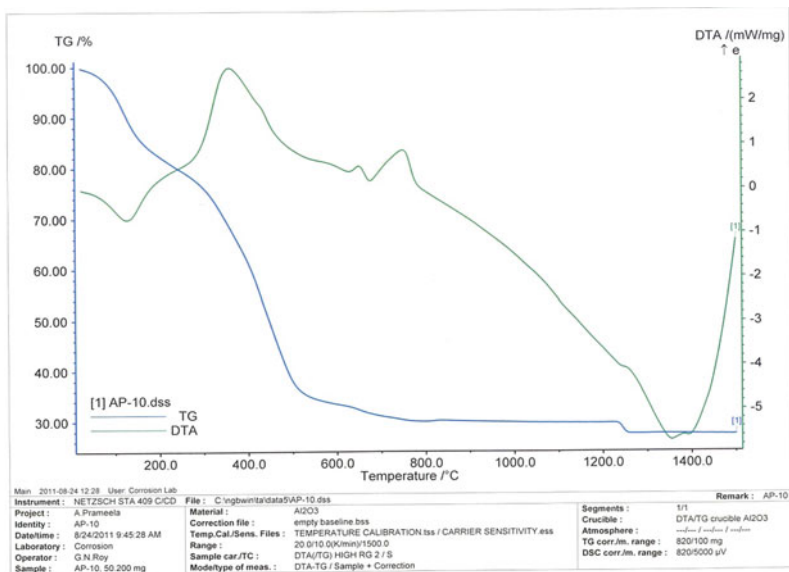
Fig. 6 TG/DTA curves of sample AP-10

substate and oxidant ratio. In general, excess of oxidant appears to give complexes in which chromium has a higher oxidation state. The complexes of chromium with phthalic acid and their degradation products are stable to heating but volatile since finally only chromium oxide complex is left out (Figs. 4, 5 and 6).

References

1. J. Fugita, K. Nakamoto and M. Kobyashy, J. AM. Chem. Soc. 98. 3963, (1956)
2. A. K. Laha & A. B. Kulkarni, J. Sc. Ind. Res. 506 (1985)
3. G. Mishra, M. Alam, Renuka Thakur & N. Mishra, J. Inst. Chem. (Ind.) 63, 166 (1991)
4. G. Mishra, M. Alam, N. Dwivedi & N. N. Mishra, J. Inst. Chem. (Ind.) 63, 169 (1991)
5. R. K. Dubey, U. K. Dubey, C. M. Mishra "Synthesis and physiochemical characterization of some Schiff base complexes of Cr (III) complexes". Indian J. Chem. 45A: 1638–1642 (2006)
6. J. Environ Sci Health A Tox Hazard Subst Environ Eng 2006, 41[18], 1685–97.

Experimental Investigation and Optimization of Welding Parameters on TIG Welding of Stainless Steel AISI 304 Plates

Sanjay Kumar, Pravin K. Singh, D. Patel and S. B. Prasad

1 Introduction

For the optimization of the process parameters, Taguchi is a very useful method. In this method, a special process evolution is used to obtain best and optimum process parameters with less number of experiments. Taguchi's technique provides a simple, proficient and organized approach to optimize the design for good quality, performance and cost. Generally, in engineering applications, if the number of input parameters and the level is high, then the large number of experiments has to be conducted. So, to overcome this difficulty, Taguchi's analysis used an orthogonal array (OA) having less number of experiments and provides proper connection between process parameters and responses [1]. OA can study the effect of entire process parameters on the response values with a small number of experiments and find out the best set of the experiments to get targeted response value. In Taguchi's method, S/N (signal-to-noise) ratio methodology is used for the result verification. There are three characterizations of S/N ratio: nominal-the-better, lower-the-better and larger-the-better [1–3].

Further, the present investigation shows the 3D plot by response surface methodology (RSM). These plots are very important for the visual display of the optimal process parameters with respect to the response surface. The procedural steps for RSM are as follows:

  I. Design of experiment according to the requirement of the responses.

 II. Developing the mathematical model of response surface with the best fitting.

S. Kumar · D. Patel · S. B. Prasad
Department of Manufacturing Engineering, National Institute of Technology, Jamshedpur, India

P. K. Singh (✉)
Department of Mechanical Engineering, AMITY University, Ranchi, India
e-mail: pravinsingh.phd@gmail.com

Table 1 Composition of AISI 304

Element	Influenced weight
C	0.08 max
Mn	2.00 max
Ph	0.045 max
S	0.030 max
Silicon	0.75 max
Cr	18.00–20.00
Ni	8.00–12.00
N	0.10 max
Fe	67–71

Table 2 Mechanical characteristics of AISI 304

Properties	**Metric**
Tensile strength	515 Mpa min
Yield strength	205 Mpa min
Hardness Brinell	201 max
Density	8/00 g/cc

III. Presenting the interaction effects of process parameters by using the three-dimensional plots.

IV. Presenting the effect of optimized process parameters on the responses and presenting the predicted value of response based on the optimized process parameters.

In the present experimentation, the gas tungsten arc welding (GTAW) is used. This process is commonly used for welding hard-to-weld metals such as stainless steel, magnesium, aluminium and titanium [8]. A thin sheet of AISI 304 stainless steel has been used as a base metal having dimensions of length 200 mm, width 50 mm and thickness 3 mm ($200 \times 50 \times 3$ mm). The chemical and mechanical properties of the base metal used in the present investigation are mentioned in Tables 1 and 2. The filler metal for the investigation was E-308L.

In the present investigation, an OA of 27 sets is designed according to which specimen was welded using gas tungsten arc welding (GTAW) process. Minitab 17 software is used for design of experiment. In the present experiment, signal-to-noise ratio has been used to examine the effect of each factor on a particular response. The signal shows the effect of each factor on the response, whereas noise is the measure of the influence on the deviation from the average responses [1–3]. The S/N ratio is based on the previous knowledge and expertise, so it must be carefully chosen. In the current study, responses are associated with the strength of the weld joint, which should be high as possible so the larger-the-better criteria have been chosen. The strength of the weld joint which is generally expected to be high is examined by Eq. 1 [4–6].

Table 3 Input parameters and its levels

Variables	Unit	Levels		
		1	2	3
Current (I)	A	60	70	80
Voltage (V)	V	30	40	50
Root gap (R)	mm	0.5	1.0	1.5
Gas flow rate (G)	L/min	16	18	20

$$\frac{S}{N} = -10 \log_{10}\left(\frac{1}{n}\sum_{i=0}^{n} 1/y_i^2\right) \tag{1}$$

where

n number of experiments
y_i response value
i number of design experiments.

Further, analysis of variance (ANOVA) technique has been used to study the influence of each parameter to the response value [7–9]. The significance level of alpha (α) of 0.05 (95% confidence level) is taken for the ANOVA. After ANOVA observation, RSM is used for a proper combination of statistical and mathematical techniques to analyse, model and optimize the processes [3, 10–13].

2 Materials and Methods

Gas tungsten arc welding (GTAW) operation has been used for butt joint of stainless steel AISI 304 plates of size $200 \times 50 \times 3$ mm. A set of 27 experiments has been designed by Taguchi method. The levels of process parameters are present in Table 3. The design of experiment of the L_{27} orthogonal array (OA) is presented in Table 4. The first column represents current, second is voltage, third represents root gap, and fourth reports final input parameter which is gas flow rate. The response value hardness and bend strength are depicted in column 5 and 6, respectively. To study the effect of each input parameter ANOVA was applied. To generate the regression equation between input parameters and outcomes, the response surface methodology was applied at the basis of full quadratic 6

$$Y = \beta_0 + \sum_{i=1}^{k} \beta_i X_i + \sum_{i=1}^{k} \beta_{ii} X_i^2 + \sum_{i} \cdot \sum_{j} \beta_{ij} X_i X_j \tag{2}$$

where Y is the estimated response (here, hardness and bend strength), β_0 is the constant, and β_i, β_{ii} and β_{ij} represents the coefficients of linear (here, I, V, R and

Table 4 L_{27} orthogonal array experimental data

Sample number	Current (I)	Voltage (V)	Root gap (R)	Gas flow rate (G)	Hardness (H) BHN	Bending (B) strength
	(A)	(V)	(mm)	(L/min)	BHN	(N/mm^2)
1	60	30	0.5	16	110.13	101.66
2	60	30	0.5	18	113.31	111.66
3	60	30	0.5	20	106.95	109.66
4	60	40	1	16	100.70	36.66
5	60	40	1	18	100.70	40.00
6	60	40	1	20	103.14	39.33
7	60	50	1.5	16	121.21	76.66
8	60	50	1.5	18	119.70	71.33
9	60	50	1.5	20	121.41	72.66
10	70	30	1.5	16	92.67	103.33
11	70	30	1.5	18	89.76	102.66
12	70	30	1.5	20	96.78	106.33
13	70	40	0.5	16	138.31	66.66
14	70	40	0.5	18	135.70	63.33
15	70	40	0.5	20	136.32	69.66
16	70	50	1	16	116.95	68.33
17	70	50	1	18	118.31	67.66
18	70	50	1	20	113.70	70.33
19	80	30	1	16	93.70	96.33
20	80	30	1	18	97.53	99.33
21	80	30	1	20	98.17	91.66
22	80	40	1.5	16	114.35	46.66
23	80	40	1.5	18	110.41	41.33
24	80	40	1.5	20	113.31	47.66
25	80	50	0.5	16	148.14	65.33
26	80	50	0.5	18	139.36	61.66
27	80	50	0.5	18	145.47	63.33

G), quadratic (here, I^2, V^2, R^2 and G^2) and cross-product (here, $I*V$, $V*R$, $R*G$ and $G*I$) terms, respectively. X reveals the coded variables that correspond to the studied cutting parameters [3].

Hardness testing was done using a Brinell hardness machine with a 1000-kg force load applied. The hardness is measured at the different locations of weld zone. The way the machine measures the hardness is through a microscope. The digital output displays the distance between the two points and takes that to measure the hardness of the material. Figure 1a shows the Brinell hardness machine, and Fig. 1b shows the bend testing machine. Figure 2 shows the indentation marks after hardness test, and Fig. 3 shows specimen after bend test material. The specimen is bending slowly
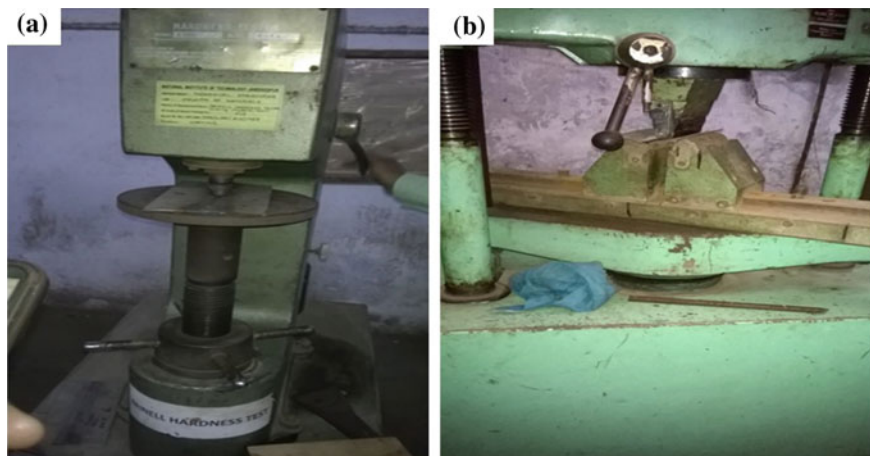
Fig. 1 **a** Brinell hardness machine and **b** bend testing machine with welded specimen
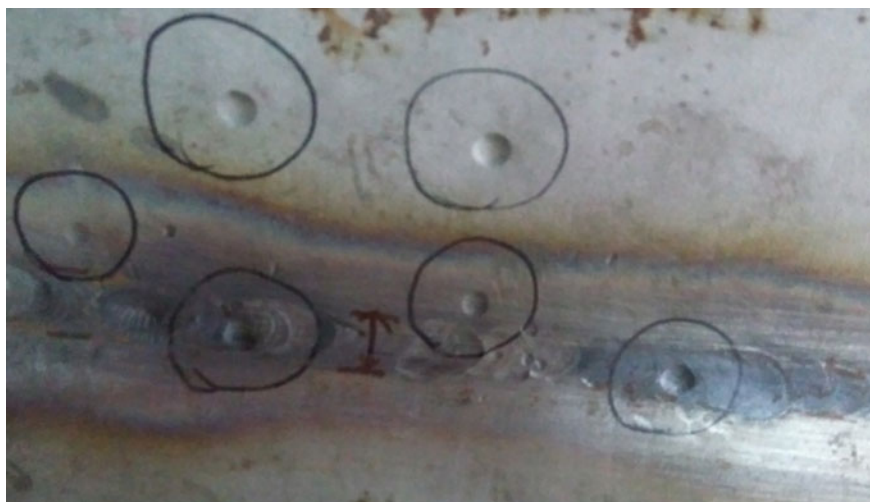
Fig. 2 Specimen showing indentation marks after hardness test

and steadily from the centre around a certain radius. The specimen is acceptable if there are no visible cracks on the outside surface. The bending test was carried out up to 180°, and the test result showed that in all the welded samples no cracks were observed visually in the bent area. Hence, the bend test result is satisfactory.

Fig. 3 AISI 304 stainless steel after bend test material

Table 5 S/N ratio (hardness value)

Level	Current	Voltage	Root gap	Gas flow rate
1	40.72	39.96	42.14	41.12
2	41.36	41.30	40.38	41.07
3	41.08	41.92	40.68	40.87
Delta	0.64	1.95	1.77	0.25
Rank	3	1	2	4

3 Result and Discussion

3.1 Analysis of Micro-hardness

The micro-hardness testing was conducted on the various weld specimens, totally three sets of observation were taken, and an average of the data is recorded. Figure 4 and Table 5 show that the most influencing factor for the hardness property is welding voltage at higher level (50 V) of voltage. The second affecting factor is root gap at its first level, i.e. 0.5 mm, third affecting factor is welding current at its second level (70 A), and finally the last affecting factor is gas flow rate at its first level (16 L/min). To validate the above result, analysis of variance (ANOVA) was applied which is presented in Table 6.

The result shows that the prepared model is significant since the R^2 value is nearer to 1.
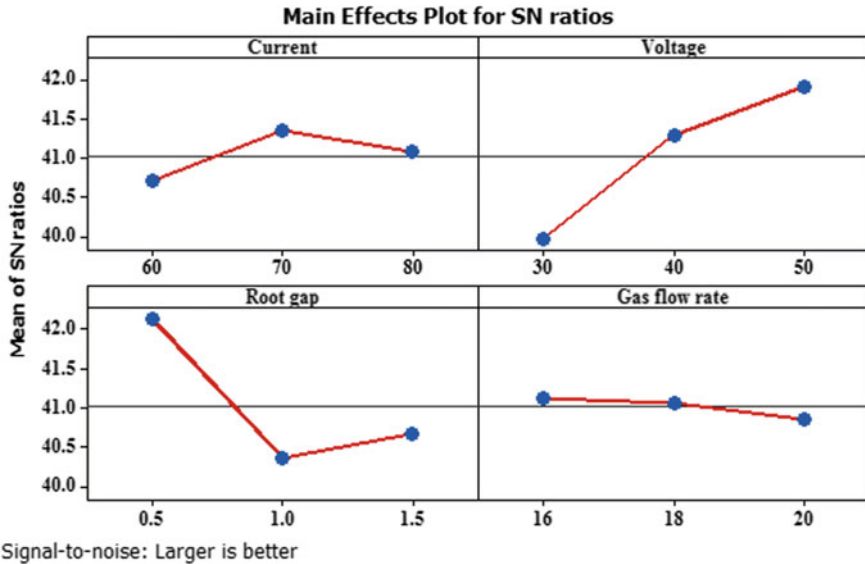
Fig. 4 S/N plot for hardness property

3.2 Analysis of Bend Strength

The bending test was carried out on different welded specimens. The S/N plot graph is presented in Fig. 5, and the response is presented in Table 7. In this investigation, the most affecting factor was again voltage at its first level which indicates that when the voltage increases its strength reduces which is theoretically proved. As voltage is directly proportional to the arc gap when arc gap increases, the voltage increases and in same way arc density reduces. The high voltage causes the welding defect known as lack of penetration and tends to reduce the welding strength. No cracks were found on the outer surface of the welded specimen which were welded under the low-voltage condition. The analysis of variance for the bending strength is presented in Table 8. The values of R^2 are mentioned in Table 8, $R^2 = 99.09$ and R^2 (adj) $= 98.04$. The closeness of the R values indicates the goodness of designed model at states that designed model is valid for the further investigation.

3.3 Regression Analysis by RSM

The regression analysis was done by applying the quadratic model relationship for hardness and bend strength with 95% of confidence level (Eq. 5). As the hardness (H) and bend strength (B) are the function of welding current (I), voltage (V), root gap (R) and gas flow rate (G), so it can be mathematically expressed as:

Table 6 Analysis of variance hardness

Source	DOF	Adj SS	MS	F-value	P-value
Linear	4	2851.57	712.89	106.91	0.00
I	1	102.15	102.154	15.32	0.002
V	1	42.94	42.936	6.44	0.026
R	1	37.95	37.948	5.69	0.034
G	1	0.44	0.440	0.07	0.802
Square	4	1316.81	329.204	49.37	0.0000
I*I	1	60.64	60.643	9.09	0.011
V*V	1	104.02	104.023	15.60	0.002
R*R	1	66.65	66.648	10.00	0.008
G*G	1	0.40	0.400	0.06	0.811
Interaction	6	178.57	29.761	4.46	0.013
I*V	1	29.49	29.491	4.42	0.057
I*R	1	64.99	64.995	9.75	0.009
I*G	1	2.07	2.068	0.31	0.588
V*R	1	53.65	53.650	8.05	0.015
V*G	1	26.62	26.623	3.99	0.69
R*G	1	26.60	26.600	3.99	0.69
Residual Error	12	80.02	6.668		
Lack of fit	11	61.35	5.577		
Pure error	1	18.67	18.666	0.30	0.905
Total	26				

$R^2 = 97.13$; $R^2(\text{adj}) = 96.27$
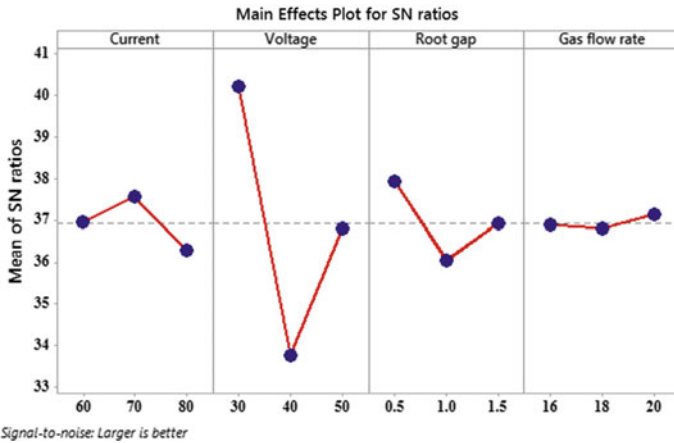
Fig. 5 Main effects plot for S/N ratios for strength property

Table 7 S/N ratio (bending strength)

Level	Current	Voltage	Root gap	Gas flow rate
1	36.94	40.20	37.94	36.88
2	37.55	33.76	36.04	36.79
3	36.29	36.81	36.92	37.13
Delta	1.25	6.44	1.90	0.34
Rank	3	1	2	4

Table 8 ANOVA results for bending strength

Source	DOF	Adj SS	Adj MS	F-value	P-value
Linear	4	3755.3	938.82	85.66	0.000
I	1	52.5	52.55	4.79	0.049
V	1	744.8	744.84	67.96	0.000
R	1	13.8	13.84	1.26	0.283
G	1	2.9	2.92	0.27	0.615
Square	4	5389.0	1347.25	122.93	0.000
I*I	1	303.4	303.43	27.69	0.000
V*V	1	577.1	577.15	52.66	0.000
R*R	1	8.1	8.07	0.74	0.408
G*G	1	3.5	3.46	0.32	0.584
Interaction	6	405.8	67.63	6.17	0.004
I*V	1	38.8	38.67	3.53	0.085
I*R	1	76.3	76.35	6.97	0.022
I*G	1	10.5	10.48	0.96	0.347
V*R	1	93.7	93.72	8.55	0.013
V*G	1	4.7	4.68	0.43	0.526
R*G	1	5.1	5.06	0.46	0.510
Residual error	12	131.5	10.96		
Lack of fit	11	130.1	11.83	8.48	0.262
Pure error	1	1.4	1.39		
Total	26	14,518.3			

$R^2 = 99.09$; $R^2(\text{adj}) = 98.04$

$$H = f(I, V, R, G) \tag{3}$$
$$B = f(I, V, R, G) \tag{4}$$

The quadratic regression equation that represents the response surface 'H' and 'B' is:

$$\begin{aligned} H = &-391 + 12.97I + 1.14V - 36.6R + 0.9G - 0.0891I * I \\ &- 0.1156V * V + 37.0R * R + 0.069G * G + 0.1023I * V \\ &- 3.039I * R - 0.0230I * G + 3.25V * R - 0.0942V * G + 1.883R * G \end{aligned} \tag{5}$$

(a)

Surface Plot of Hardness vs Gas flow rate, Current

(b)

Surface Plot of Hardness vs Gas flow rate, Voltage

(c)

Surface Plot of Hardness vs Root gap, Current

Surface Plot of Hardness vs Voltage, Current

(d)

Surface Plot of Hardness vs Root gap, Voltage

(e)

Surface Plot of Hardness vs Gas flow rate, Root gap

(f)
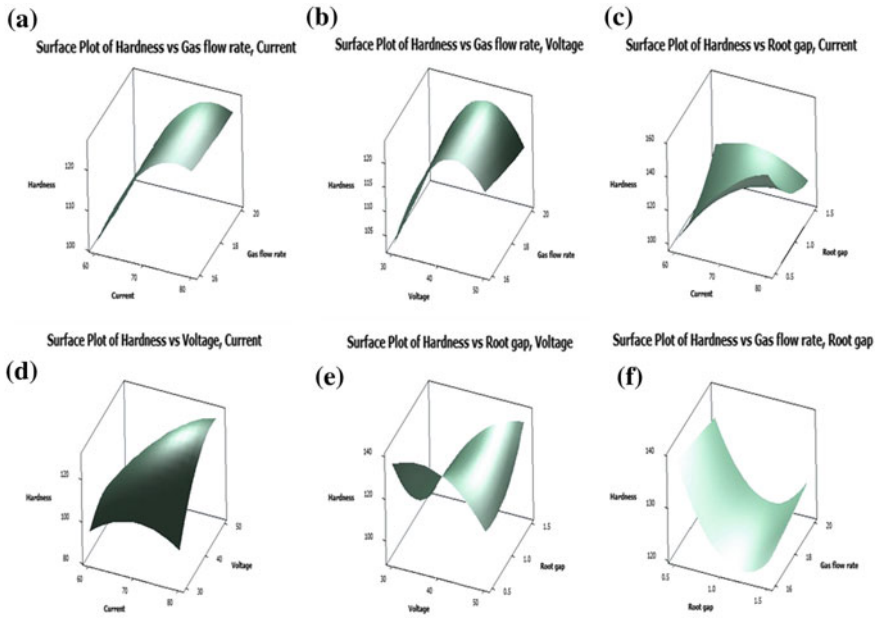
Fig. 6 3D plot for hardness value

$$B = -202 + 28.25I - 36.10V + 54.6R - 1.0G - 0.1993I * I$$
$$+ 0.2724V * V + 12.9R * R + 0.203G * G + 0.1172I * V$$
$$- 3.29I * R - 0.0518I * G + 4.29V * R - 0.0395V * G - 0.82R * G \qquad (6)$$

Equations 4 and 6 show the regression equation for hardness (H) and bend strength (B). Figures 6 and 7 show the interaction plot of process parameters and their effects on the response. These 3D plots explain the performance of response values at various conditions of input parameters.

4 Conclusion

The present investigation developed an empirical connection between process parameters and the response values at 95% of confidence level. The main effect of plot shows that for the response value (both hardness and bending strength) the voltage parameter is a most effective parameter. The highest hardness has been obtained at 70 A (second level of current), 50 V (third level of voltage), 0.5 mm (first level of root gap) and 16 L/min (first level of gas flow rate), whereas the highest bend strength was found at second level of current, first level of voltage, first level of root gap and third level of gas flow rate. ANOVA result shows that voltage is the most affecting factor for changing in mechanical properties of welded joints.
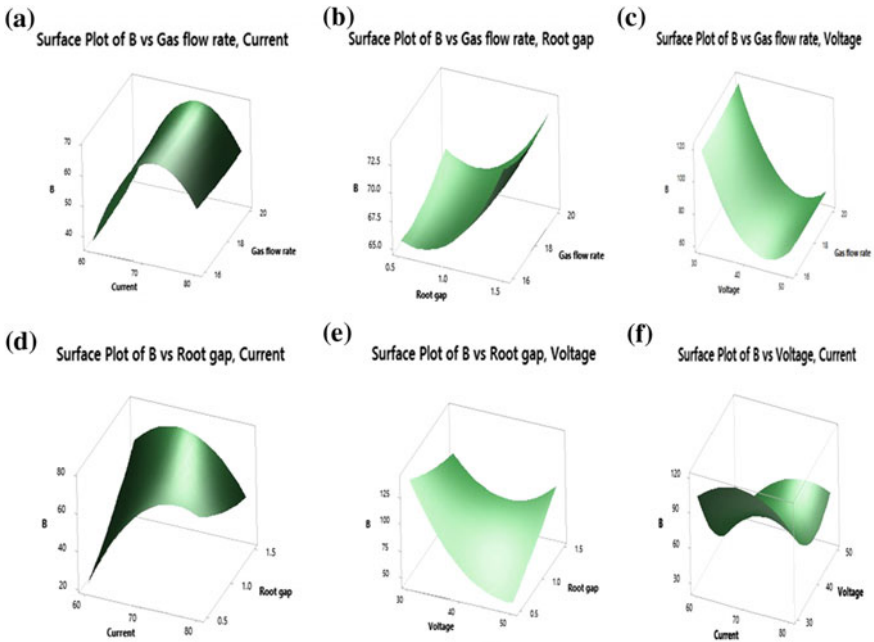
Fig. 7 3D plot for bending strength

A regression relation was developed with the help of RSM, and 3D plot was designed. 3D graph is showing the interactive effect of process parameters on the response values.

References

1. S. D. Kumar, P. R. Vundavilli, S. Mantry et al., " A Taguchi optimization of cooling slope process parameters for production of semi-solid A 356 alloy and A356- 5TiB$_2$ in- situ composite feedstock", Procedia Materials Science, **5**, 2014, pp. 232–241.
2. S D Kumar, P R Vundavilli, A Mandal., "Optimization of process parameters during machining of Thixoformed A 356- 5TiB2 in- situ composite using design of experiments", International conference on RACE 2015, Chennai.
3. Sudhansu Ranjan Das, Debabrata Dhupal and Amaresh Kumar, "Study of surface roughness and flank wear in hard turning of AISI 4140 steel with coated ceramics inserts", Journal of mechanical sciences and technology, **29**, (10) 2015, pp. 4329–4340.
4. R. Kumar and M. Balasubramanian, "Application of response surface methodology to optimize process parameters in friction welding of Ti-6Al-4 V and SS304L rods", Transaction of nonferrous metals society of China, **25**, 2015, pp. 3625–3633.
5. N. Kiaee and M. Aghaie- Khafri, "Optimization of gas tungsten arc welding process by surface methodology", Materials & design, **54**, 2014, pp. 25–31.

6. Pravin Kumar Singh, D. Patel, S. B. Prasad, "Optimization of process parameters during vibratory welding technique using Taguchi's analysis", Perspectives in Sciences, **8**, 2016, pp. 399–402.
7. P.J.Rose, "Taguchi techniques for quality engineering", Second edition, McGraw Hill., New York 1996.
8. P. Bharatha,V.G. Sridharb, M. Senthil kumarb, " Optimization of 316 Stainless Steel Weld Joint Characteristics using Taguchi Technique" Published by Elsevier Ltd. Procedia Engineering., **97**, 2014, pp. 881–891.
9. Arivarasu.M, Devendranath Ramkumar K, Arivazhagan. N, " Comparative Studies of High and Low Frequency Pulsing On the Aspect Ratio of Weld Bead in Gas Tungsten Arc Welded AISI 304L Plates" Published by Elsevier Ltd. Procedia Engineering., **97**, 2014, pp. 871–880.
10. K. M Eazhil S.Mahendran S.Ganesh Kumar "Optimization of Tungsten Inert Gas Welding on 6063 Aluminium Alloy on Taguchi Method" **I**, 2014, IJRSI, pp. 2321–2705.
11. Navid Moslemi, Norizah Redzuan, Norhayati Ahmad, Tang Nan Hor "Effect of Current on Characteristic for 316 Stainless Steel Welded Joint Including Microstructure and Mechanical Propertie. Published by Elsevier B.V. Procedia CIRP **26**, 2015, pp. 560–564.
12. Ajit Khatter, Pawan Kumar, Manish Kumar " Optimization of Process Parameter in TIG Welding Using Taguchi of Stainless Steel-304" IJRMET., **4**, 2014.
13. Prashant S Lugade1, Manish J Deshmukh " Optimization of Process Parameters of Activated Tungsten Inert Gas (A-TIG) Welding for Stainless Steel 304L using Taguchi Method" International Journal of Engineering Research and General Science., **3**, 2015, pp. 2091–2730.

Microbiological and Physiochemical Characteristics of Some Common Fungal Flora Isolated from Various Petroleum-Contaminated Pump Stations of Hazaribag District, Jharkhand, India

Kumar Anand, Priti Kumari, Nikita Kumari and Pritam Bala Sinha

1 Introduction

Variability of living organisms from all sources including terrestrial, marine and sweet water ecosystems is known as Biodiversity. It is well known that it includes the diversity which occurs within the species of ecosystem. Microbial diversity is the number or relative abundance of microbial species in a local area or region. In fact, immense work has already been done on biodiversity by eminent persons all over the world. Not only bacterial [7] but also fungal diversity has been undertaken for various research aspects in the recent years [15]. The microbes were the only form of life on earth for about 2 billion years, and it is also estimated that 50% of the living protoplasm on this planet is of micro-organism and microbes are among the richest range of molecular and chemical diversity in nature. No doubt they are a very important component of all ecosystems. A large population of microbes still remains unidentified, and their taxonomic characterization and identification have yet to be done. The diversity of microbes presently living on earth is known to be high and is thought to be enormous, but the true extent of microbial diversity is still unknown [13]. Microbes are very much important for the living system in many aspects. Without microbes, all form of life would definitely be impossible on earth. Microbial ecology is also a different aspect, where not only identification, but also their interaction with different species of microbes is studied. The microbial world includes an extraordinary diversity in their both taxonomy and ecological functions. The existence of such an immense variety of organisms, combined with the fact that micro-organisms, is too small to see without magnification, makes the

K. Anand · P. Kumari · N. Kumari
University Department of Biotechnology, Vinoba Bhave University,
Hazaribag 825301, Jharkhand, India

P. B. Sinha (✉)
Amity Institute of Biotechnology, Amity University Jharkhand, Ranchi 834002, India
e-mail: dr.pritambalasinha@gmail.com

task of measuring microbial diversity challenging and even daunting. It is to be emphasized that microbial diversity not only involves the isolation, characterization and identification of microbes, but also to study their activity in diverse environments. Till date, quite a few numbers of microbes have been identified. Most of them still remain untapped under the earth surface and are yet to be exploited. The number of different species in an environment shows the evolution of new species which generates the biological diversity [39].

In 1992, The United Nations Conference on Environment and Development held in Rio de Janeiro prepared an Agenda 21 which stressed about the importance of biodiversity in the functionality of ecosystems. The document promoted scientific and international cooperation for a better understanding of the importance of bio-diversity and its functions. As far as the Indian subcontinent is considered, it has a huge geographic area, varied topography and climate with juxtaposition of several biogeographic regions boasts for one of the richest in the biological diversity in the world. India is recognized as one of the 12 mega diversity regions of the world. Nearly 72% of India's bio-wealth is constituted by insects (~40%), fungi (~18%) and angiosperms (~13%). Thus, India's contribution to the global diversity is about 8%. Various and unique types of diverse microenvironments such as different soil orders, boiling waters, springs, deep sea vents, salt pans, acid mine drainage and cold environments are present in India that provide a home to diverse populations of micro-organisms.

Study on the field of microbial biodiversity has grown significantly since 1991 and has resulted in a large body of scientific literature, and also we have witnessed the development of techniques for characterizing diversity in particular at the molec-ular level for both culturable and non-culturable micro-organisms. Various literature available in the field of microbial diversity do not seem proportional to our under-standing of the significance of biodiversity for ecological processes in the microbial world or of the ways in which we can manipulate or manage this diversity. Overall, the past 25 years of research in microbial biodiversity has contributed greatly to the development of methods for characterizing the multiple facets of the richness of microbial world [4]. Our microbial planet largely remains unexplored.

The term petroleum has been used as a synonym to crude oil. It is a dark sticky liquid, a complex mixture of varying molecular weight. Crude oil contains more than 30 parent polymeric hydrocarbons, and it also contains many polyaromatic hydro-carbon compounds such as paraffins, naphtenes, aromatics as well as organic sulphur compounds, organic nitrogen compounds and oxygen-containing hydrocarbons [18, 2]. Microbial breakdown of hydrocarbon pollutants is generally a very slow process [16] with optimum degradation [1] can occur only if the right environment condi-tions such as pH, temperature, nutrients and relevant microbial consortia are present [11, 12, 35]. The pollution of petroleum hydrocarbons causes a major change in the physical and chemical properties of soil [37]. It is an environment concern because contaminated soil may be inappropriate for agricultural, industrial or recreational use and potential sources of groundwater contamination [36, 14].

Soil contamination with hydrocarbons causes extensive damage by accumula-tion of pollutants in animals and plant tissue which may cause mutation or even

Petriplate 1   Petriplate 2

Petriplate 3   Petriplate 4

Petriplate 5   Petriplate 6
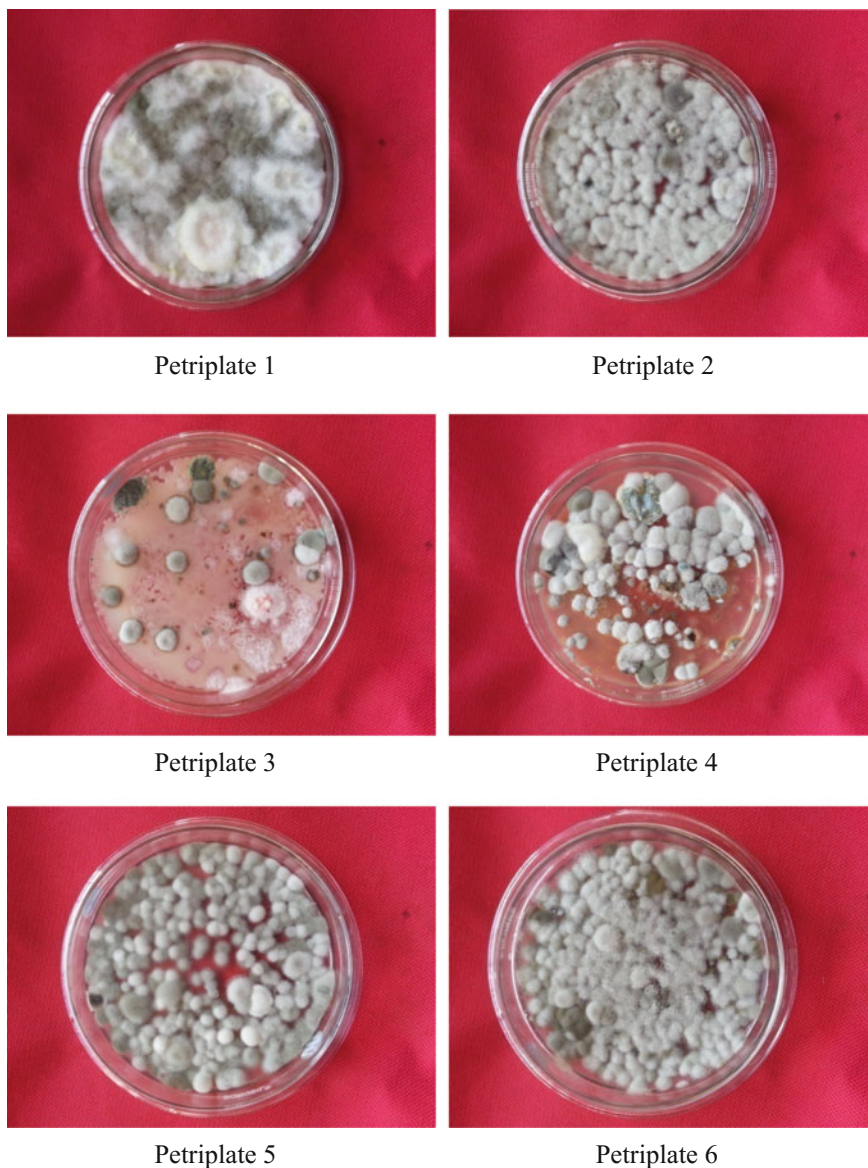
Fig. 1 Photographs of fungal colonies observed on potato dextrose agar media on different dilutions

death. Spillage and extensive exploration of petroleum products results in pollution in the environment. Initiatives can rather be taken for bioremediation of the oil-contaminated sites by fungal biodegradation. Fungi are the large group of eukaryotic organisms that include micro-organisms such as yeast, mould as well as mushrooms.

Strain 1   Strain 2

Strain 3   Strain4
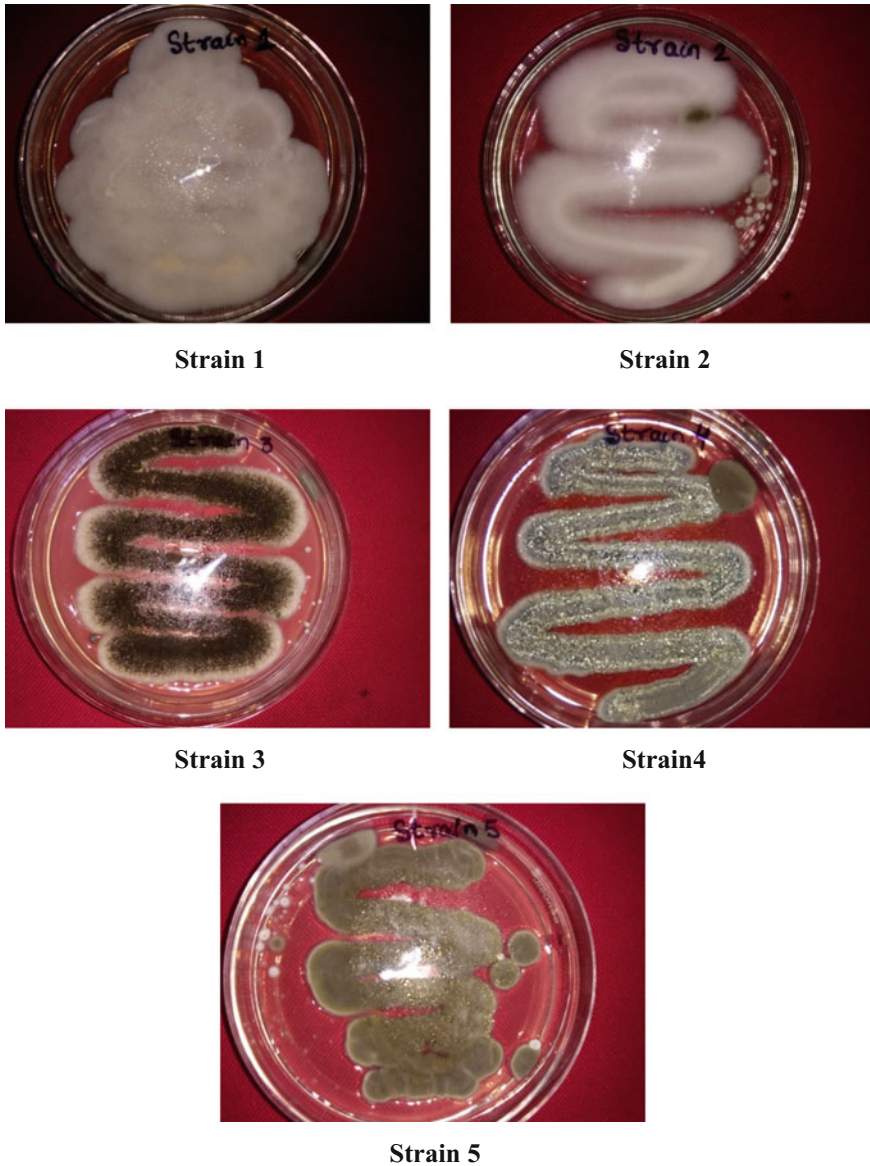
Strain 5

Fig. 2 Photographs of different strains of fungi grown on potato dextrose agar media

Fungi and bacteria have been used in the past for biodegradation [20]. Fungi are known to biodegrade the hydrocarbons. These are notably aerobic and can able to grow easily under stressed conditions such as low pH and poor nutrient status where

bacterial growth might be limited. In laboratory, they are easy to store, transport, can be genetically engineered and produced in large quantities [23].

The present research was conducted with the aim to isolate different strains of fungi from the sampling sites of Hazaribag district using dilution plate method and from which some selected strains are examined for the morphological and physicochemical characteristics and also some are assessed for their cellulase, amylase and phosphatase activity. Moreover, some fungal floras are identified from various sampling sites of Meru petrol pump, old bus stand petrol pump, Konar petrol pump. Further, comparative studies are done of this work with previous works.

2   Materials and Methods

Collection of soil samples: Soil samples were freshly collected in sterilized polythene bags and brought to the Microbiology & Immunology Laboratory of Department of Biotechnology, Vinoba Bhave University (VBU), Hazaribag, Jharkhand. The moisture content of the sample was dried in a hot air incubator at 60 °C to measure constant weight. The pH and temperature were determined using digital pH meter and thermometer, respectively. The soil fungal population was measured using serial dilution technique, by culturing them on Potato Dextrose Agar media and was characterized by using morphological, microscopic observation, physicochemical tests and a few biochemical tests carried out in the Microbiology & Immunology Laboratory of VBU. Following sampling areas were undertaken for investigation.

Sampling sites	Name of sampling site
Sampling Site 1.[SS1]	Meru petrol pump,
Sampling Site 2.[SS2]	Old bus stand petrol pump
Sampling Site 3.[SS3]	Konar petrol pump

Reagents and Chemicals: All media components and chemicals for this study were of analytical grade and purchased from Hi-Media laboratory Pvt. L td, Mumbai and Sd Fine.

pH of Soil Sample: Soil samples were dried at 60 °C for 72 h, powdered in mortar and pestle, filtered through sieve, and then this soil was further used for fungi isolation.

3   Isolation of Micro-organisms

Experiments were conducted to observe the micro-organisms (fungi) by culturing them with serial dilution method on Potato Dextrose Agar media (PDA).

4   Composition of Media

(1)Potato Dextrose Agar media:
    Potato (peeled)—200.0 gm
    Dextrose—20.0 gm
    Agar—15.0 gm
    Distilled water—1 L
    pH—5.6
    In this technique, serial dilution of different soil samples was prepared separately using 0.87% NaCl. Then 0.1 ml from the dilution factors of each 10^{-3} and 10^{-4} test tube was transferred into sterile petriplates, containing prepared PDA media. The diluted samples were used to inoculate the prepared media using pour plate method. Finally, the media containing petriplates were spread with the help of spreader. Plates were kept in incubator at 28 °C for 4–5 days. Growth of different fungi was observed in the petriplates after 4–7 days.

    Purification of isolated fungi: Different colonies from the medium were picked up and purified by looking at their morphology. Some of the common fungi observed on soil contaminated from the above-mentioned sampling sites and grown on PDA medium are as follows:

    The fungal isolates were identified on the basis of macromorphological and micromorphological characteristics. Following **morphological characteristics** like colony growth, colony colour, pigmentation production, presence or absence of aerial mycelium, shape, size, sclerotic, colony, surface texture were recorded. When grown on a variety of media, micro-organisms exhibit differences in the macroscopic experience of their growth. These differences called as "*cultural characteristics*" are used as the basis for separating micro-organisms into taxonomic groups.

    All fungal isolates were obtained in pure culture using standard plating technique by **Gilman** [22]. The technique of **James and Natalie** was adopted for identification of unknown fungi using cotton blue in lactophenol stain. The identification was done by placing a drop of the stain on clean slide with the help of a mounting needle, where a small portion of the mycelium from the fungal cultures was removed and placed in a drop of lactophenol. The mycelium was spread very well on the slide with the help of a needle. A cover slip was gently applied with little pressure to eliminate air bubbles. Slide was then mounted and observed with various objective lenses in the inverted microscope (Olympus). The species to be investigated were identified. Fungal growth was observed on various petriplates with different dilutions, mainly between 10^{-2} and 10^{-4}.

5   Results and Discussion

It is well known that petroleum is one of the most important natural resources and the major fossil fuel of our industrial society and petrochemical industry. It is also

for most life forms; episodic and chronic pollution of the environment by oil causes major ecological perturbations and constitutes a critical impediment to its sustainable use by mankind. Petroleum-based products are the major source of energy for several industry and day to day life. Leaks and accidental spills occur regularly during exploration, refining, transport and storage of petroleum products. Three soil samples were collected and fungi were isolated from petroleum-hydrocarbon-contaminated site by using serial dilution technique, and various fungi were observed and tentatively identified. In their studies, they isolated *Penicillium* and *Aspergillus* sp. from hydrocarbon-contaminated soil and identified as hydrocarbon degrading fungi along with *Trichodema, Fusarium, Rhizopus* sp. Although initiative was done to identify the common fungi, not much work was done so far on the hydrocarbon degrading potential of these fungi. The similar results of our study were observed by Obire and his group [32] in their studies on "Impact of various concentrations of crude oil on fungal populations of soil". They isolated fourteen fungal genera from soil. These include *Alternaria*, *Aspergillus*, *Candida*, *Cephalosporium*, *Cladosporium*, *Fusarium*, *Geotrichum* and some others. Most commonly observed species isolated and identified were: *Aspergillus flavus, Aspergillus niger, Aspergillus terreus, Penicillium* sp. and various other species of genus *Aspergillus* and *Penicillium*. Out of all these isolated fungi, *A. niger* showed highest and fastest growth pattern at temperature 28 °C and pH 5.6. Studies on the isolation of filamentous fungi in the environment containing oil or its subproducts found a very similar diversity of genera to that found in our study, such as: *Aspergillus* and *Penicillium* [16, 30, 31, 28, 38, 40]. Recently, it has been recorded that the genera of fungi such as *Penicillium*, *Aspergillus, Fusarium*, *Rhizopus* and *Mucor* are associated with petroleum-hydrocarbon-contaminated soil [24, 8, 26, 27, 29]. They isolated *Penicillium* and *Aspergillus* sp and also some hydrocarbon degrading fungi such as *Trichodema, Fusarium, Rhizopus* sp were identified in their study [3]. More or less similar results of our study were seen to be obtained [19].

The probable no. of colonies observed on the plates was:

Dilution used	SS1	SS2	SS3
10^{-2}	04	04	03
10^{-3}	03	04	02
10^{-4}	04	03	03
10^{-5}	03	02	03
10^{-6}	03	03	02

Among 40 different isolates, about 5 selected test isolates were finally selected for study. These were designated as Strain 1, Strain 2, Strain 3, Strain 4 and Strain 5. These strains were then characterized at morphological, physicochemical as well as initially at biochemical level [6]. The names of common fungi isolated from various sampling sites are as follows: *Alternaria species, Aspergillus clava-*

tus, Aspergillus terreus, Aspergillus niger, Aspergilllus oryzae, Aspergillus flavus, Aspergillus janus, Aspergillus fumigates, Aspergillus ustus, Aspergillus versicolor, Cladosporium species, Curvularia species, Fusarium spp, Fusarium oxysporum, Fusarium solani, Mucor hiemalis, Mucor racemosus, Penicillium spp., Penicillium chrysogenum, Pythium spp, Rhizopus spp, Rhizopus stolinifer, Trichoderma virdie and Verticillium spp. finally characterized for further study.

Following are their details.

Morphological characterization:

Isolate	Strain 1	Strain 2	Strain 3	Strain 4	Strain 5
Growth on PDA/ Czapek Dox Agar Media	+++	+++	+++	+++	+++
Sporulation	Yes	Yes	Yes	Yes	Yes
Pigmentation	No	No	No	Yes	No
Colour of colony observed	White	White	Black	Silvery green	Dark green

Physicochemical characterization:

(A). Growth of test isolates at different pH

pH	Strain 1	Strain 2	Strain 3	Strain 4	Strain 5
4.2	+	+	+	+	+
6.2	+	+	+	+	+
8.2	+	+	+	+	+
10.2	+	+	+	+	+

(B). Growth of test isolates at different temperatures

Temperature	Strain 1	Strain 2	Strain 3	Strain 4	Strain 5
20 °C	+	+	+	+	+
24 °C	+	+	+	+	+
28 °C	++	++	++	++	++
32 °C	++	++	++	++	++
36 °C	–	–	–	–	–

(C).Growth of test isolates at different NaCl concentration

NaCl conc. (%)	Strain 1	Strain 2	Strain 3	Strain 4	**Strain 5**
0.87	+	+	+	+	+
2	+	+	+	+	+
5	+	+	+	+	+
7	+	+	+	+	+
10	–	–	–	–	–

The selected strains will soon be sent to concerned laboratory for identification and authentication

6   Conclusion

The present study revealed that petroleum-contaminated sites often have a vast array of microbial flora which is capable of utilizing diesel as a carbon and energy source [17, 33]. The ubiquitous/cosmopolitan distribution of fungi with their ready isolation from oil-contaminated environments indicates that they play an important role in the degradation of oil spilled in the environment [9, 10, 5, 25, 32, 34]. Hence, an initiative was taken with the objective, to isolate, characterize and tentatively identity some of the indigenous fungal flora of oil-contaminated soils [24] and to get them catalogued with a suitable MTCC accession number.

Conflict of Interest   There was no conflict of interest in the present study.

References

1. AI-Dossari., (2008) Isolation and identification of some fungi from sediments of Southern marshes of Iraq and their ability in biodegradation of crude oil *in vitro*. Ph.D thesis, Basrah University,Iraq.
2. Al-Ghamdi Ay. (2011). Investigating the ability of five fungal species to utilize gasoline as sole carbon source. *Egyptian Acad. Journal of Biology Science.* Vol 03, No 01, pp 7-12.
3. Al-Jawhari, I.F.H; (2014); "Ability of some soil fungi in biodegradation of petroleum hydrocarbon". *J. Appl.Environ.Microbiol.,* Vol 02, pp 46–52.
4. Ahern D.G. & Mayers S.P. (1976). Fungal degradation of oil in the marine environment. In: Gareth Jones EB (ed). Recenet advances in aquatic mycology. J. Elek, London,pp 125–134.

5. AI-Nasrawi, H; (2012). Biodegradation of crude oil by fungi isolated from Gulf of Mexico. *Journal of Bioremediation and Biodegradation.* Vol 03, No. 04, pp 1–6.

6. Anand K. & Choudhary S.B. (2010). Biochemical characterization of microbes isolated from some selected wetlands of North Bihar. *International Journal of Biological Sciences and Engineering* Vol. 01(02), pp 96–103.

7. Anand K. & Pandey Gaurav Kumar (2014). Estimation of microbial diversity in some selected wetlands: A case study of North Bihar. *International Journal* of Advanced Life Sciences, Vol 07 (02), pp. 217–222.

8. April T.M., Foght J.M. & Currah R.S. (2000). Hydrocarbon degrading filamentous fungi isolated from flare pit soils in Northern and Western Canada. *Canadian Journal of Microbiology.* Vol 46 (1): 38–49.

9. Atagana H.I., Haynes R.J., Wallis F.M; (2006). Fungal bioremediation of creosote contaminated soil: A laboratory scale bioremediation study using indigenous soil fungi, Vol 172, pp 201–219.

10. Atlas R.M. & Bartha R; (1972). Microbial degradation of oil pollutant workshop. La.State Union PubI, No.LSUSG-73-01.pp 283-289.

11. Atlas R.M. & Camiglia C.E. (1995). Bioremediation of petroleum pollutants. *Bioscience,* Vol 45, pp 332–338.

12. Atlas R.M; (1981). Microbial degradation of petroleum hydrocarbons: an environmental perspective, *Microbiology Review.* Vol 45, No. 01, pp 108–109.

13. Baker J.M. (1970). Studies on salt marsh communities. The effects of a single oil spillage. *In: Colwell EB (eds).* The ecological effects of oil pollution on littoral communities. Institute of Petroleum, London, pp 16–43.

14. Bona Ventra C & Johnson F.M.; (1997). "Healthy environments for healthy people: Bioremediation today and tomorrow". Environmental health perspectives, Vol 105, pp 5–20.

15. Bundy J.G., Panton G.I. & Campbell C.D.; (2002). "Microbial communities in different soil types do not converge after diesel contamination". *Journal of Applied Microbiology,* Vol.92. pp 276–288.

16. Cerniglia C.E. (1997). Fungal metabolisms of polycyclic aromatic hydrocarbons : Past present and future applications in bioremediation. *Journal of Ind. Microbiol Biiotechnology, V*ol 19,pp 324–333.

17. Chaudhry S., Luhach J., Sharma V & Sharma C. (2012). Assessment of diesel degrading potential of fungal isolates from sludge contaminated soil of petroleum refinery, Haryana.*Res. of Microbiol.* D.O.I.: https://doi.org/10.3923/jim.

18. Davies J.S. & Westlake D.W.; (1979). Crude oil utilization by fungi. *Journal of Canadian, Microbiology,*Vol 25,No. 02, pp 146–156.

19. Desia A., Jitendra J., Desai D. & Hanson K.G; (1993). "A rapid and simple screening techniques for potential crude oil degrading microorganisms". *Biotechnol.Tech,* Vol.07, No. 10, pp 745–748.

20. Farid W.A.; (2012). Bioremediation of oil contaminated by axenic and mixed cultures of bacteria and fungi. *Journal of AL-Taqani.*Vol 25,No.02, pp 1–16.

21. George- Okafor U., Tasie F.,Muotone-Okafor F.; (2009). "Hydrocarbon degrading potentials of indigenous fungal isolates from petroleum contaminated soils". *J.Physical and Natural Science.* Vol 3, pp 1–6.

22. Gilman J.C. (1998). A manual of Soil fungi. Daya Publishing House,New Delhi. Pp 14–24.

23. Gopinathan R., Prakash M., & Bhartirajan R; (2012). "An experimental study for crude oil biodegradation in contaminated soil". *International Journal of Current Microbiology & Applied Sciences (IJCMAS)*, Vol. 01, pp. 12–16.

24. Hart S. (1996). *In situ* Bioremediation: Defining the limits. *Environmental Science Technology.* Vol 30, No. 09, pp 398A-401A.

25. Hashem A.R.; (2007). Bioremediation of contaminated soils in the Arabic gulf region. Journal of a Review of Kuwait Science. Vol 19, pp 81–91.

26. Klich M.A.; (2002). Identification of common *Aspergillus* species. CBS, Utrech, Netherlands,116.

27. Klich M.A. & Pitt J.I., (1988). A laboratory guide to common *Aspergillus* species and their teleomorphs. CSIRO, North Ryde, Australia, 116.

28. Mance a- Lopez, M.E., Rodriguez M.T., Espariza-carcia., Rios- Leal F., Chauez-Gommez B., Rodriguez- Vazques R & Barrera-Cortes., J; (2007). "Fungi and bacteria isolated from two highly polluted soils for hydrocarbon degradation". *Journal of Acta Chimica Slovenica,* Vol. 54, pp 201–209.

29. Margesin R., Labbe D., Schinner F., Greer C.W. & White L. (2003). Characterization of hydrocarbon degrading microbial population in contaminated and pristine alpine soil. *Journal of Applied Environmental Microbiology.* Vol 69, No.08, pp 3085–3092.

30. Mittal A.R & Singh P; (2009). Studies on biodegradation of crude oil by *Aspergillus niger. The South Pacific Journal of Natural Science.* Vol 27, No., 01. pp 27–60.

31. Mohsenzadeh F., Rad C.A. & Akbari M; (2012). "Evolution of oil removal efficiency and enzymatic activity in some fungal strain for bioremediation of petroleum polluted soil". *Iranian J. Environ Health Sci.Eng.* Vol 09, No. 01, pp 26.

32. Obire D. & Anyanwu E.C; (2009). "Impact of various concentrations of crude oil on fungal population of soil". *Int.J. Environ.Sci.Technol.* Vol6, pp 211–218.

33. Oboh B.O., Moilori Akinyemi J.D. & Adebusoye S.A. (2006). Hydrocarbon degrading potentials of bacteria isolated from a Nigerian Bitumen (Tarsand) deposit. *Nature and Science.*Vol 04, Issue 03, pp 51–57.

34. Okerentugba P.O. & Ezeroye O.U. (2003). Petroleum degrading potentials of single and mixed microbial cultures isolated from rivers and refinery effluent in Nigeria. *African Journal of Biotechnology.* Vol 02, Issue 09, pp 288–292.

35. Oudot J., Duprot J., Halouri S & Roquebert M.F; (1993). "Biodegradation potential of hydrocarbon assimilating tropical fungi". Soil Biology & Biochemistry, Vol 25, pp 1167–1173.

36. Prince C; (2002). "Biodegradation of petroleum and other hydrocarbons" In: Encyclopedia of Environmental Microbiology (g. Bitton,G;ed.).John wiley.New York.pp 2402–2416.

37. Powell S.M., Bowman J.P., Ferguson S.H. & Snape I; (2010). "The importance of soil characteristics to the structure of alkane-degrading bacterial communities on Sub- Antartic Macquarie Island" .*Soil Biol.Biochem*., Vol.42. pp 2012–2021.

38. Santo E.O., Rosa C.F.C., Passos C.T., Sanzo A.V.L., Burket J.F.M., Kalil S.J. & Burket C.A.V. (2008). Pre screening of filamentous fungi isolated from a contaminated soil in Southern Brazil for bioaugmentation purposes. *African Journal of Biotechnology.* Vol 02, No.09,pp 1314–1317.

39. Watanabe T; (2002). "Pictorial atlas of soil and fungi: morphology and key to species".2nd edition, India, CRC Press.

40. Wemedo S.A., Obire O. & Dogubo D.A. (2002). Mycoflora of a kerosene polluted soil in Nigeria. *Journal of Appl.Sci. Environ. Management.* Vol 06, pp 14–77.

Isolation, Identification and Characterization of Fungi from Vinoba Bhave University Campus, Hazaribag District

Kumar Anand, Thirupathi Karuppanapandian and Pritam Bala Sinha

1 Introduction

Biological diversity or biodiversity is generally defined as the study of variability among living organisms on earth. It may also be defined as the variety of life on earth. The term is made by joining words biology, the study of life and diversity, meaning difference and variety. Biodiversity is the sum total of all biotic variation from the level of genes to ecosystem; the diversity in ecosystems, habitats and the prevailing environmental conditions are reflected upon the plant life [1]. For ecologists, biodiversity means the diversity of everlasting interactions among species. It applies not only to species, but also to their immediate environment (biotope) and the eco-regions the organisms live in. In each ecosystem, living organisms are part of a whole, and they interact with one another and with the air, water and soil that surround them [2–4].

Literally, we say that a narrow definition of biodiversity is to focus on genetic diversity and a broader definition is to focus not just on species but on habitat and ecosystem diversity.

Microbial diversity can be defined as the range of different kinds of unicellular organisms, bacteria, archaea, protists and fungi. Micro-organisms are the essential part of biodiversity and play an important role in the structure and functioning of the ecosystems on the earth and also for human welfare. Despite their utility and

K. Anand
University Department of Biotechnology, Vinoba Bhave University, Hazaribag 825301, Jharkhand, India

T. Karuppanapandian
Department of Experimental Biology, Faculty of Science, Masaryk University, Brno 62500, Czech Republic

P. B. Sinha (✉)
Amity Institute of Biotechnology, Amity University Jharkhand, Ranchi 834002, Jharkhand, India
e-mail: sinhapritib@googlemail.com

importance, these minute micro-organisms are rapidly depleting from the biosphere due to the stress of natural and man-made causes. The diversity of microbes presently living on earth is known to be high and is thought to be enormous, but the true extent of microbial diversity is largely unknown. Micro-organisms are much more diverse than any other form of life that we ever imagined, among which not even 10% has ever been tapped. We also lack proper planning to identify and store these organisms. There are several groups working on microbial biodiversity and microbial prospecting all over the country which are isolated from each other. But there are no systematic efforts to take up major projects in these aspects. It is disappointing to see that there is no concerned effort to do proper taxonomy and bacterial classification in India. Microbial diversity constitutes an essential part of the biological diversity on earth. Micro-organisms possess a large size of diversity in terms of number and genetic make-up. The various forms of micro-organisms are bacteria, algae, fungi, protozoa and viruses which are found everywhere in the planet, in the soil, in the water, in the air and in the sea. Among the natural habitats, soil system supports the highest number of microbes with a high degree of diversity based on the number of microbes isolated and identified till date. Water bodies also support a good number of micro-organisms in the nature.

Among all micro-organisms, fungus are eukaryotic, spore-bearing, achlorophyllous organisms that generally reproduce sexually and asexually, and are usually filamentous, branched somatic structures, typically surrounded by cell walls containing chitin or cellulose, or both of these substances, together with many other complex-forming molecules [5, 6]. As saprophytes along with bacteria and animals, fungi play an important role in decomposition of complex remains of dead organisms. They are responsible for the release of nutrients back to soil and atmosphere for plants. Either directly or indirectly, fungi are useful as well as harmful to humankind. Fungi not only produce primary and secondary metabolites, but also produce enzymes as well as biomass. It is indeed difficult to decide the proper place of fungi in the living world. Some of the characteristics of fungi resemble plants and some animals. The current concept about fungi is that fungi are certainly not plants and their variety and natural beauty occupy a very important place in the biological world [7–9]. Till date, unlike bacteriologists, mycologists have been able to explore fungi also, but not to a greater extent. Fungi are not only beautiful, but they play a very important role in agriculture, industry, food industry, medicines, textiles, bioremediation, biofertilizers and in various other ways [10]. Overall, they are very important for human welfare. Fungi are not only fascinating, but also an endless source of biological diversity. Overall, we can say that the number of fungi like bacteria and other microbes still remains unexploited.

Fungi, being cosmopolitan, occur commonly on the decomposing organic matter and in diverse habitats such as soil, air, litter, dung, waste, wood [4, 9, 11]. There are about 1.5 million species of fungi known till date in which about 75,000 species have been described so far. Fungi play an important role as decomposers; also, they are symbionts of plants and animals. In some ecosystems, fungi are also found to be parasites of different plants. They occur not only in the soil but also in the rocks, seawater and freshwater and are also sometimes classified as extremophiles, being

present in cold as well as warm habitats, on dry substrates and on concentrated nutrients. A myriad of fungi occurs in the soil in different habitats [10].

Soil bacteria as well as fungi play a very significant role in biogeochemical cycles [5, 6, 12] and are responsible for the cycling of organic compounds. Majority of fungal species which have so far been named and described are likely occurring in soil environment at some stage of their life cycle [8, 9, 13]. The knowledge of fungal diversity is based largely on the observations of fruiting bodies which are present in an environment. So, the present study is undertaken to isolate different strains of fungi from soil and water samples of various sites of Vinoba Bhave University Campus of Hazaribag, to examine the isolates on the basis of their morphological, physico-chemical and biochemical characteristics on the basis of their cellulase, amylase as well as phosphatase activities and to get the selected strains catalogued with a suitable MTCC no. and preserve these strains in culture collection centres for further study.

2 Materials and Methods

2.1 Collection of Soil Samples

For this research, soil and water samples were collected from different sampling sites and also water samples from two small aquatic bodies near Vivekanand Sabhagar were collected. The details of sampling sites are as follows (Table 1).

Soil and water samples were collected in sterilized polythene bags and dropping bottle. The collected samples were brought to the Microbiology Laboratory of University Department of Biotechnology, Vinoba Bhave University, Hazaribag. The moisture content of the sample was measured in a hot air incubator at 105 °C to constant weight. The pH and temperature were determined using digital pH metre and thermometer, respectively.

Table 1 Sampling sites selected for investigation

Sampling sites	Name
Sampling Site 1.[SS1]	Sir J. C. Bose Building
Sampling Site 2.[SS2]	Central Library
Sampling Site 3.[SS3]	Vivekanand Sabhagar
Sampling Site 4.[SS4]	Samrat Ashok Bhawan
Sampling Site 5.[SS5]	Ravindra Nath Tagore Bhawan
Sampling Site 6.[SS6]	C. V. Raman Block
Sampling Site 7.[SS7]	Sports Complex

2.2   Reagents and Chemicals

All media components and chemicals used in the studies were of analytical grade and purchased from Hi-Media Laboratory Pvt. Ltd, Mumbai.

2.3   pH of Soil Sample

Soil samples were dried at 60 °C for 72 h, powdered in mortar and pestle, filtered through a sieve and then further used for fungi isolation.

2.4   Isolation of Micro-organisms

Experiments were conducted to observe the micro-organisms (fungi) by culturing them with serial dilution method on Potato Dextrose Agar media (PDA) media and Czapek-Dox Agar (CZA) media [11].

2.5   Composition of Media

(1) **Potato Dextrose Agar media**:

Potato (peeled)—200.0 g
Dextrose—20.0 g
Agar—15.0 g
Distilled water—1 L
pH—5.6

(2) **Czapek-Dox Agar media**

Sodium nitrate—2.0 g
Dipotassium hydrogen phosphate—1.0 g
Magnesium sulphate—0.5 g
Potassium chloride—0.5 g
Ferrous sulphate—0.01 g
Sucrose—30.0 g

Agar—15.0 g
Distilled water—1 L
pH—7.3

In this technique, serial dilution of different soil samples and water samples was prepared separately using 0.87% NaCl. Then from the dilution 10^{-3} and 10^{-4} 0.1 ml of sample was transferred into sterile petri plates, containing prepared PDA and CZA media. The diluted samples were used to inoculate the prepared media using the pour plate method. Finally, the media containing petri plates were spread with the help of spreader. Plates were kept in an incubator at 28 °C for 4–5 days. Growth of different fungi was observed in the petri plates after 4–7 days.

2.6 Purification of Isolated Fungi

Different colonies from the medium were picked up and purified by looking at their morphology [14, 15].

3 Results

The isolated fungi were identified on the basis of macromorphological and micromorphological characteristics. Following **morphological characteristics** like colony growth, the presence or the absence of aerial mycelium, colony colour, pigment production, shape, size, sclerotic, colony, surface texture were recorded. When grown on a variety of media, micro-organisms exhibit differences in the macroscopic experience of their growth. These differences called as **"*cultural characteristics*"** are used as the basis for separating micro-organisms into taxonomic groups.

All fungal isolates were obtained in pure culture using standard plating techniques. The technique of James and Natalie [16] was adopted for identification of unknown isolated fungi using cotton blue in lactophenol stain. The identification of these fungi was done by placing a drop of the stain on the clean slide with the help of a mounting needle, where a small portion of the mycelium from the fungal cultures was removed and placed in a drop of lactophenol. The mycelium was spread very well on the slide with the help of a needle. A cover slip was gently applied with little pressure to eliminate air bubbles. Slide was then mounted and observed with various objective lenses in the inverted microscope (Olympus). The species under investigation were identified in accordance with Booth [7]. Fungal growth was observed on various petri plates with different dilutions, mainly from 10^{-2} to 10^{-4}. The probable no. of colonies observed on the plates was as mentioned below [15, 17] (Table 2).

Table 2 Number of fungal colonies observed on PDA and Czapek-Dox Agar media at different dilutions

Dilution used	SS1	SS2	SS3	SS4	SS5	SS6	SS7
10^{-2}	03	02	02	02	02	02	01
10^{-3}	02	03	01	02	01	01	00
10^{-4}	03	02	02	02	02	00	01
10^{-5}	02	01	02	02	01	01	02
10^{-6}	02	02	01	02	01	02	01

A number of fungi were observed in different soil samples.

The isolated fungi were in the following order of their dominance (Table 3):

The names of common fungi isolated from various sampling sites are as follows:

Alternaria species
Aspergillus clavatus
Aspergillus flavus
Aspergillus fumigatus
Aspergillus genus
Aspergillus niger
Aspergillus oryzae
Aspergillus terreus
Aspergillus versicolor
Aspergillus ustus
Cladosporium spp.
Curvularia species
Fusarium chlamydosporum
Fusarium oxysporum
Fusarium solani
Fusarium spp.
Mucor racemosus
Mucor hiemalis
Mycelia sterilia (pink)
Mycelia sterilia (white)
Penicillium chrysogenum
Penicillium spp.
Pythium spp.

Table 3 List of some common fungi isolated from different sampling sites

Name of fungus isolated	Sampling sites							Total colonies	Occurrence %
	SS1	SS2	SS3	SS4	SS5	SS6	SS7		
Alternaria species	1	2	–	1	–	–	–	04	6.88
Aspergillus clavatus	1	–	–	1	1	–	–	03	5.16
Aspergillus flavus	–	–	1	–	–	–	–	01	1.72
Aspergillus fumigatus	–	2	–	1	–	–	–	03	5.16
Aspergillus genus	–	2	–	1	–	–	–	03	5.16
Aspergillus niger	–	2	–	–	–	1	–	03	5.16
Aspergillus oryzae	–	–	–	–	–	1	–	01	1.72
Aspergillus terreus	2	–	–	–	–	–	1	03	5.16
Aspergillus versicolor	–	–	–	–	–	–	1	01	1.72
Aspergillus ustus	–	–	2	–	–	–	–	02	3.44
Cladosporium spp.	–	–	2	–	–	–	–	02	3.44
Curvularia species	–	–		2				02	3.44
Fusarium chlamydosporum	–	–	–	2	–	–	1	03	5.16
Fusarium oxysporum	–	1	–	–	–	–	1	02	3.44
Fusarium solani	–	1	–	–	–	–	–	01	1.72
Fusarium spp.	2	–	–	–	–	–	–	02	3.44

(continued)

Table 3 (continued)

Name of fungus isolated	Sampling sites							Total colonies	Occurrence %
	SS1	SS2	SS3	SS4	SS5	SS6	SS7		
Mucor racemosus	2	–	–	–	–	–	–	02	3.44
Mucor hiemalis	–	–	–	–	–	2	–	02	3.44
Mycelia sterilia (pink)	–			1				01	1.72
Mycelia sterilia (white)	–	–	–	1	–	–	–	01	1.72
Penicillium chrysogenum	1	1	–	–	–	–	–	02	3.44
Penicillium spp.	–	–	–	–	–	–	2	02	3.44
Pythium spp.	1	–	–	–	–		2	03	5.16
Rhizopus stolonifer	2	–	–	–	1	–	–	03	5.16
Rhizopus spp.	–	–	–	–	1	–	–	01	1.72
Trichoderma viride	–	1	1	–	–	–	–	02	3.44
Verticillium spp.	–	1	–	2		–	–	03	5.16
	12	13	06	12	03	04	08	58	

Rhizopus stolonifer
Rhizopus spp.
Trichoderma viride
Verticillium spp.

Among 58 different isolates, about 6 selected test isolates were finally characterized for further study [18]. These were designated as Strain 1, Strain 2, Strain 3, Strain 4, Strain 5 and Strain 6. These strains were then characterized at morphological, physico-chemical as well as at biochemical level initially. Following are their details.

4 Discussion

4.1 Morphological Characterization

See Tables 4 and 5.

Table 4 Morphological characterization of test isolates

Isolates	Strain 1	Strain 2	Strain 3	Strain 4	Strain 5	Strain 6
Growth on PDA/Czapek-Dox Agar media	+++	+++	+++	+++	+++	+++
Sporulation	Yes	Yes	Yes	Yes	Yes	Yes
Colour of colony observed	Light green	White	Light brown	Dark green	Light pinkish white	Black

Table 5 Physico-chemical characterization of test isolates

(A). Growth of test isolates at different pH						
pH	Strain 1	Strain 2	Strain 3	Strain 4	Strain 5	Strain 6
4.2	+	+	+	+	+	+
6.2	+	+	+	+	+	+
8.2	+	+	+	+	+	+
10.2	+	+	+	+	+	+

Fig: Growth of test isolates at different pH
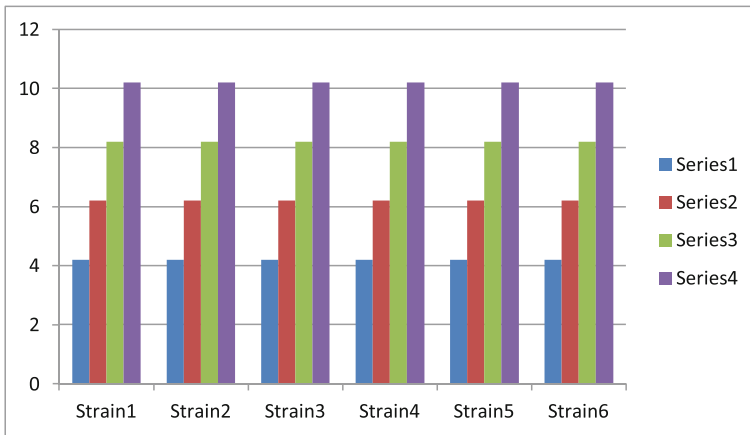
| (B). Growth of test isolates at Different Temperatures						
Temperature	Strain 1	Strain 2	Strain 3	Strain 4	Strain 5	Strain 6
20 °C	+	+	+	+	+	+
24 °C	+	+	+	+	+	+
28 °C	++	++	++	++	++	++
32 °C	++	++	++	++	++	++
36 °C	–	–	–	–	–	–

Table 5   (continued)

Fig: Growth of test isolates at different temperatures (°C)
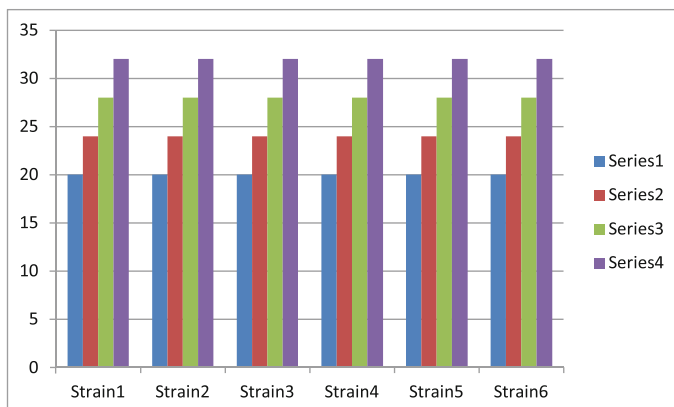
(C). Growth of test isolates at Different NaCl concentrations						
NaCl conc. (%)	Strain 1	Strain 2	Strain 3	Strain 4	Strain 5	Strain 6
0.87	+	+	+	+	+	+
2	+	+	+	+	+	+
5	+	+	+	+	+	+
7	+	+	+	+	+	+
10	-	-	-	-	-	-

Fig: Growth of test isolates at different NaCl concentrations
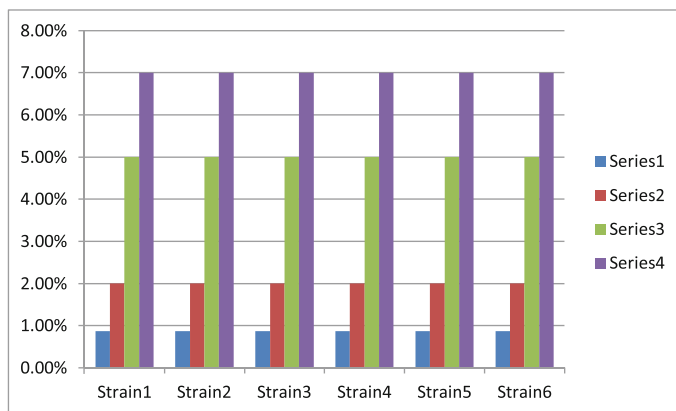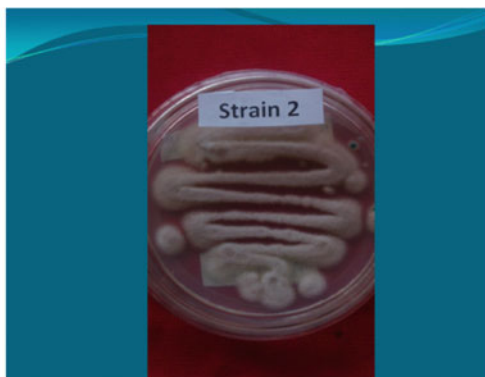
4.2 Biochemical Characterization

An initiative was taken to characterize these test isolates at biochemical level also, so that they can be identified further. Prominent tests among these are amylase, cellulase and phosphatase tests [1, 2]. Some of the test isolates showed positive results for these tests, and some of them showed negative results. Further work will be done in various other aspects (tests) for these test isolates so that they can be identified at species level.

The physico-chemical properties of soil used for isolation of microbes (fungus) were analysed in the present study. Physical analysis of soil samples revealed that a very slight significant variation in soil pH and moisture contents occurred at different sites within the Vinoba Bhave University Campus. The colour of soil samples collected was from brown to slight black with a variation in pH from 4.2 to 10.2. The optimum temperature required for growth of fungus was between 20 and 32 °C. The NaCl concentration required for the growth of the fungus was from 0.87 to 7%. Quite a few no. of fungal isolates also showed amylase, cellulase as well as phosphatase activities. Also, cellulase-producing fungi were more as compared to amylase and phosphatase producers. So, proper biochemical characterization and taxonomic identification must be done for them so they are identified properly and catalogued.

5   Conclusion

In the present study, some natural fungal flora of soil was collected from seven different sites of Vinoba Bhave University Campus of Hazaribag district. A total number of 58 fungal isolates were isolated, characterized and identified at genus level as well as at species level. Some of the common soil fungus which were identified from the above-mentioned sampling sites were *Aspergillus* spp., [16] *Penicillium* spp., *Rhizoctonia* spp., *Fusarium* spp., *Rhizopus* spp., *Mucor* spp., *Cladosporium* spp., *Trichoderma* spp. and others [19]. The present research reports for the first time the existence of these fungi in the Vinoba Bhave University Campus of Hazaribag district of Jharkhand, India. Due to the immense importance of a large number of soil fungi, in agriculture, medicine, industry and also because of their unidentification, there is a need for biologists to get themselves involved in diverse research aspects concerned with fungi. Most of the fungal species were able to grow efficiently. Some pathogenic fungi like *A. fumigatu*s and others might also be present in the soil, so they should be handled properly and their proper taxonomic identification must be done precisely. So far, no reporting has been done by any author for the above-mentioned work for this study area specified. It can also be concluded that not only the soil pH, but also the organic content and other factors affect the fungal population and diversity. *Aspergillus* and *Penicillium* species were found to be dominant. Also

dominant were the *Rhizopus, Fusarium, Mucor* and *Trichoderma* species. Fungal diversity was found to be more in Sampling Sites 1, 2 and 4. Least fungal diversity was found in Sampling Sites 5 and 6 followed by 3 and 8. The fungi identified are as follows:

S. No.	Strain designation	Identified isolates
1	Strain 1	*Aspergillus fumigatus*
2	Strain 2	*Mucor species*
3	Strain 3	*Aspergillus terreus*
4	Strain 4	*Penicillium notatum*
5	Strain 5	*Fusarium oxysporum*
6	Strain 6	*Aspergillus niger*

Conflict of Interest   There was no conflict of interest in the present study.

References

1. Andy Purvis & Andy Hector (2000). Getting the measure of biodiversity, Nature 405, 212–219. https://www.ncbi.nlm.nih.gov/pubmed/10821281
2. Anand Kumar & Pandey Gaurav Kumar (2014). Estimation of microbial diversity in some selected wetlands: a case study of North Bihar. *International Journal of Advanced Life Sciences*: Vol. 7 (02), pp 217–222. http://www.unitedlifejournals.com/ijals/view-pdf.php?id=185
3. Anand Kumar, Kumari Baby & Mallick M.A. (2016). Phosphate Solubilizing Microbes: An effective and alternative approach as biofertilizers. *International Journal of Pharmacy and Pharmaceutical Sciences*. Vol. 8(02), pp 37–40. https://innovareacademics.in/journals/index.php/ijpps/article/view/9747/3811
4. Aghamirian M.R. & Ghiasian S.A. (2012). The prevalence of fungi in soil of Qazvin, Iran, Jundishapur, J. Mircobial:6 (1):76–9. http://en.journals.sid.ir/ViewPaper.aspx?ID=277768
5. Waksman S.A. (1922). A method of counting the number of fungi in soil. *J. Bact.*7: 339–341. https://www.ncbi.nlm.nih.gov/pmc/articles/PMC378974/
6. Waksman S.A. (1922). A method of counting the number of fungi in soil. *J. Bact.* 7: 339–341. https://www.ncbi.nlm.nih.gov/pmc/articles/PMC378974/pdf/jbacter01062-0041.pdf
7. Booth, C. (1971). The genus fusarium commonwealth mycological institute. *Kew. Surrey*, *237*. https://www.cabdirect.org/cabdirect/abstract/19721603830
8. Cheesbrough M. (2000). District Laboratory Practice in Tropical Countries. Part 2. Cambridge University Press, Cambridge, U.K. ISBN: 9780521676311
9. Christensen M. (1989). A view of fungal ecology. Mycologia, 81:1–19. https://doi.org/10.2307/3759446
10. Finlay R, D. (2007). The fungi in soil. In: van Elsas JD, Jansson JK, Trevors JT (Eds.) Modern Soil Microbiology, CRC Press, New York, pp: 107–146. Online Library

11. Grifffin D.M. (1972). Ecology of Soil Fungi. Chapman & Hall, London pp 193. Online Library
12. Klich M.A. (2002). Biogeography of *Aspergillus* species in soil and litter. *Mycologia*. 94 (1):21–27. https://www.ncbi.nlm.nih.gov/pubmed/21156474
13. Alexender M. (1977). Introduction to Soil Microbiology. 2nd Edition. John Wiley & Sons, New York, pp 423–437. Online Library
14. Harold J.B. (2002). Microbiological applications. Laboratory Manuals in General Microbiology, 8th Edition, McGraw-Hill Higher Education. Online Library
15. Dubey R.C. & Maheshwari, D. K. (2007). A manual of practical microbiology. S. Chand and Company limited, Ramnagar New Delhi 1–397.
16. James C.C. & Natalie S. (2001). *Microbiology –A Laboratory Manual*. (Ed). pp 211–223.
17. Warcup J.H. (1951). On the origin of colonies of fungi developing on soil. Vol. 62:4291.
18. Molin & Molin (1997). Defining Soil Quality for a Sustainable Environment. American Society for Agronomy, SSSA Special Publication No. 35, Madison, WI.
19. Dix N.J. & Webster, J. (1995). Fungal Ecology. Chapman Hall, Ch7. Online Library

Prediction of Controllable Process Variables for Various Workpiece Materials in CNC-WEDM

Sabindra Kachhap and Abhishek Singh

1 Introduction

CNC wire electric discharge machining (WEDM) opportunities are appearing every day. In current years, many, a lot of researches have taken place in the field of WEDM; that is, the wire wear, kerf width, white layer, heat affected zone, dielectric fluid, powder mixed dielectric, workpiece material, wire material, material removal rate, surface finish, surface roughness, and roundness. New machine technology and EDM wires are helping to improve machine performance and, in the right application, cutting speeds, making it possible to produce parts faster than ever before. More accurate control of the wire electrode and various adaptive servo technologies are reducing the number of trim passes required to produce an accurate part. An Ishikawa diagram (cause and effect diagram) has been developed as shown in Fig. 1 for the sake of better understanding of various process parameters and their subfactors which play a significant role in the material removal rate (MRR). With the advancements in the field of materials science and engineering, novel and advanced materials are being developed worldwide. In order to justify their application spectrum, it becomes imperative to characterize their manufacturability, in addition to their usual mechanical, physical, and chemical characterization. The advanced steel materials and their high-quality and effective manufacturing present researchers and engineers with a plethora of challenges. Therefore, the machining of steel with unconventional methods such as wire electric discharge machining becomes inevitable.

Liao et al. [1] developed the mathematical model of process parameters on various responses in WEDM of SKD11 alloy steel. Patel and Maniya [2] conducted experiments on EN31 alloy steel with brass wire having 0.25 mm diameter. Singh and Garg [3] investigated the effect of various process parameters of WEDM like

S. Kachhap (✉) · A. Singh
Department of Mechanical Engineering, National Institute of Technology Patna, Bihar 800005, India
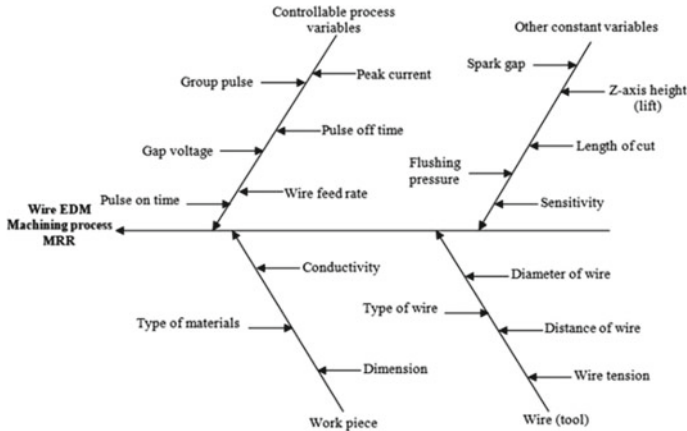e-mail: sabindra08me@nitp.ac.in

Fig. 1 Ishikawa diagram

pulse on time, pulse off time, gap voltage, peak current, wire feed, and wire tension to reveal their impact on MRR of high carbon using brass wire. Singh et al. [4] found that the effect of input parameter on MRR like pulse on time increases the MRR increase and pulse off time and gap voltage decrease MRR increases. Singh and Pradhan [5] optimized the input parameter of WEDM used Taguchi method on AISI D2 steel workpieces with brass wire as an electrode. Tosun et al. [6] investigated the effect and optimization of machining parameters on the Kerf and MRR of AISI 4140 steel (DIN42CrMo4) using brass wire in WEDM process. Tosun [7] carried out the experimental and statistical study of the cutting performance characteristics in WEDM at various input parameters on AISI 4140 steel. Haddad and Tehrani [8] studied the MRR, roughness, and roundness in WEDM of AISI D3 tool steel in terms of machining parameters using response surface method. Datta and Mahapatra [9] carried out modeling and simulation and established a mathematical model to determine MRR of D2 tool steel with used zinc-coated copper wire. Mahapatra and Patnaik [10] observed the optimization and the multiple objectives relationship between control factors and responses in WEDM on D2 tool steel. Huang and Liao [11] analyzed the optimization of machining parameters used statistical method to consider prediction of MRR in WEDM of SKD11 alloy steel. Tarag et al. [12] used the neural network modeling of SUS-304 stainless steel. The objective was to determine the correlation between various parameter and machinability factors. Menzies and Koshy [13] focused on 180-μm-diameter wire used (embedded wire with electrically non-conducting abrasives) and SAE 1018 steel workpiece used to observe the effect on MRR. Mohammadi et al. [14] carried out a statistical analysis to determine MRR in WEDM of 1.7131 cemented steel with brass wire as an electrode.

The most effective machining approach is determined by identifying the different factors affecting the WEDM process and seeking the different ways of obtaining the optimal machining condition and performance. Figure 2 shows a summary of work

Fig. 2 Research studies conducted on WEDM
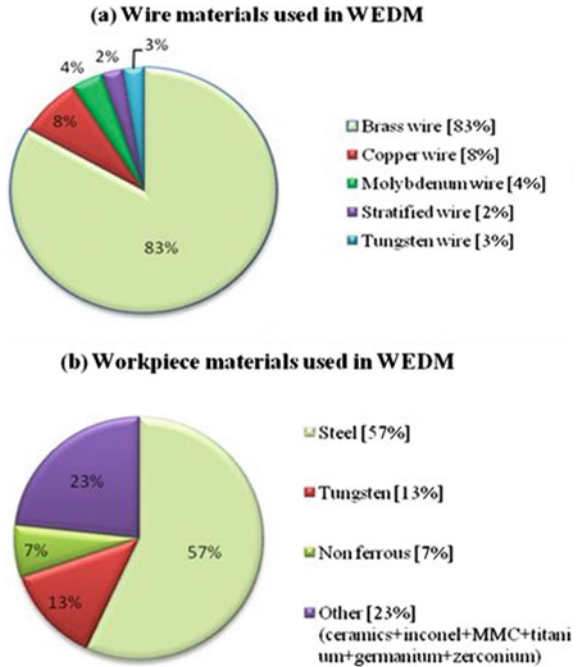
done on wire materials and workpiece materials used in WEDM till date. As evident from figure, most of the work has been reported on brass wire (83%) and common material used for workpiece is steel (57%). Many researches have been investigated on a different level, but few research papers define the achievement on the parametric effect of different wire and use various workpieces materials. In the present work, two wire materials (brass wire and molybdenum wire) and four types of steel alloys (mild steel, hot die steel, high carbon steel, and EN31 steel) as workpiece have been taken to make a comparative study.

2   Experimental Procedure

The computer numerical control Ezeecut Plus CNC WEDM has been used in carrying out the present experimental work. This WEDM allows the operator to choose different input parameters according to the material and the height of the workpiece and wire material; for example, for brass wire, set wire feed speed up to 30–100 m/min. This will help to maintain the wire diameter and prevention of frequent wire breakages) from a manual provided by the WEDM manufacturer. During all the experiments sensitivity (10), wire material and properties (brass wire with 0.25 mm diameter and molybdenum wire with 0.18 mm diameter), z-axis height (100 mm) were
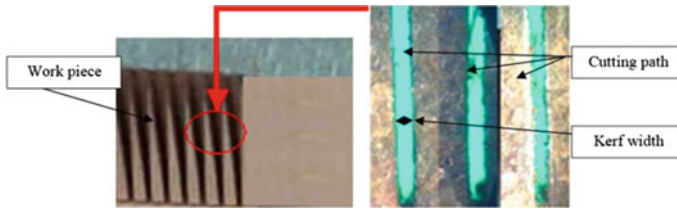
Fig. 3 Cutting path length

kept constant. The spark gap (gap between the wire and workpiece was constantly maintained by a computer controlled positioning system as 0.030 mm) was also kept constant in each experiment. The accuracy was measured using micrometers having a least count of 0.001 mm (1 μm). The quality features analyzed are output parameters such as material removal rate. The 16-mm-thick bars were used in the experiments as various workpiece materials. The cutoff length + spark gap of 11.030 mm and three sampling are used in the measurements.

Each cut consists of a linear path whose total path length is shown in Fig. 3. The operating time and cutting speed were directly measured by the control panel (or 15″ color CRT display unit); kerf width was measured by using the Mitutoyo tool maker's microscope. The cutting speed and Kerf width taken are the mathematical average of three successive measurements in each experimental cut. Therefore, the Kerf width remains constant. The material removal rate (MRR) is calculated according to the following Eq. (1) [15]:

$$\text{MRR} \left(\text{mm}^2/\text{min}\right) = \text{C.S.} \times t \tag{1}$$
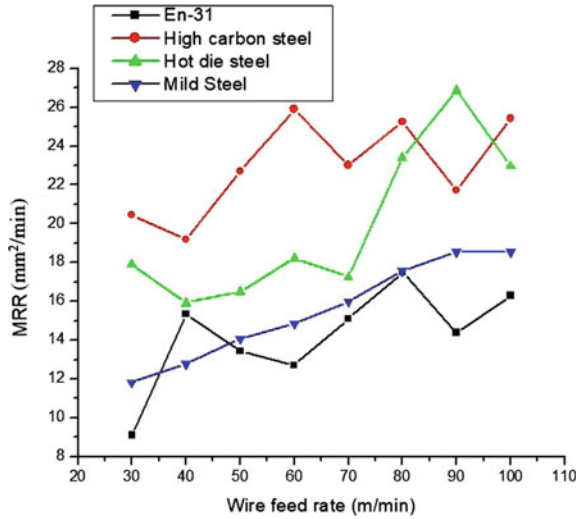
where

C.S. Cutting speed (mm/min);
t Thickness of the workpiece $= 16$ mm.

3 Result and Discussion

The various experiments to find how the output parameter varies with the variation in the input parameters on various workpiece material combinations with brass and molybdenum wire are as follows.

**Fig. 4** Wire feed rate versus MRR plot for brass wire

3.1 Effect of Wire Feed Rate on MRR

The traveling wire feeds from a wire feed drum. The wire moves through the workpiece and is supported under tension between a pair of wire rollers, which are located at the opposite sides of the workpiece. Figure 4 shows the effect of a significant input parameter—wire feed rate (WFR) on the MRR for various workpiece materials with brass and molybdenum wire as the cutting tool. According to process variables, the wire feed rate is gradually increased from 30 to 100 m/min at the interval of 10 m/min with brass wire and molybdenum wire, respectively. This setting controls the speed of wire feed motor. Other controllable process variables such as pulse on time (T_{ON}) = 38 μs, gap voltage (V_g) = 44 V, pulse off time (T_{OFF}) = 9 μs, and peak current (I_c) = 3 A were kept constant during this phase of experiment with respect to brass wire and molybdenum wire. When considering the experiments with brass wire, it was found that WFR has a mixed effect on the material removal rate of the various materials. A gradual increase in MRR has been found in the case of mild steel, whereas in almost all the other materials, a fluctuating nature of the plot is observed as shown in Fig. 4.

The similar procedure has been applied to find out the effects of the WFR on material removal rate (MRR) by considering various workpiece material combinations with molybdenum wire as the cutting tool. In this case, the WFR has mixed effect on the material removal rate. Although regular ups and down have been observed in all the MRR of all the three materials, it has been found that the MRR for mild steel remains nearly constant with variation in the wire feed rate after suffering an initial fluctuation as shown in Fig. 5.

Fig. 5 Wire feed rate versus
MRR plot for molybdenum
wire
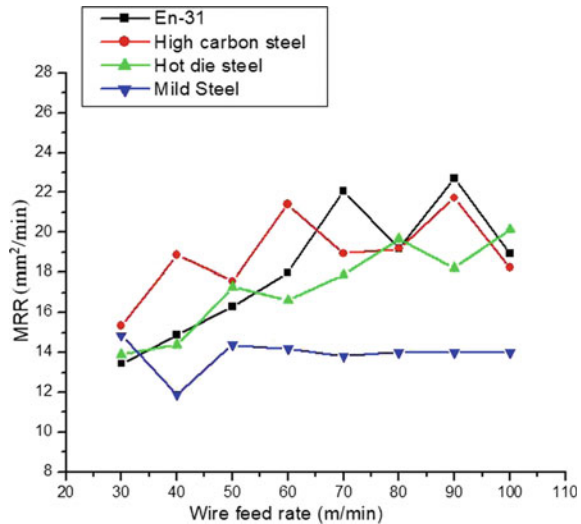
3.2 Effect of Pulse on Time on MRR

The longer the spark is sustained, more is the material removal. The effect of another
input parameter pulse on time on material removal rate was observed. Here, the pulse
on time was subsequently varied from 2 to 98 μs taking intermittent of 12 μs with
brass and molybdenum wire, respectively. Other controllable process variables such
as the wire feed rate (WFR) = 70 m/min, gap voltage (V_g) = 44 V, pulse off time
(T_{OFF}) = 9 μs, and peak current (I_c) = 3 A were kept constant. From the nature of
the plot below, it is easily depicted that the pulse on the time parameter (T_{ON}) has
initially increased with the increase in the material removal rate for all the materials
and after that followed a gradual sinusoidal nature of the plot as the pulse on time is
increased further. It has been noticed that the hot die steel has a prominent frequency
of fluctuation than the other materials as shown in Fig. 6.

According to Fig. 7, for the case of molybdenum wire, the pulse on the time
parameter (T_{ON}) has a direct effect on the material removal rate initially, but, as its
value is gradually increased, fluctuation in the curve is observed in the two workpiece
materials—HCS, HDS. While EN-31 shows a constant MRR with the increase in
T_{ON}, mild steel shows the decrease fluctuating nature ending up with the lowest
MRR as compared to HDS, which has been found to possess the highest MRR for
the maximum value of pulse on time.

Fig. 6 Pulse on time versus
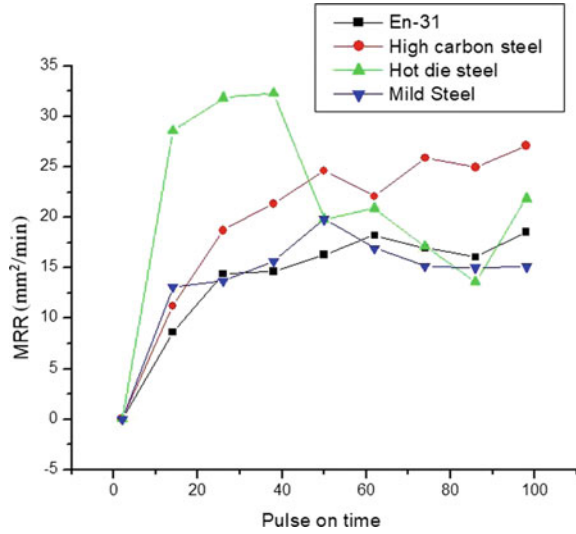MRR plot for brass wire

Fig. 7 Pulse on time versus
MRR plot for molybdenum
wire
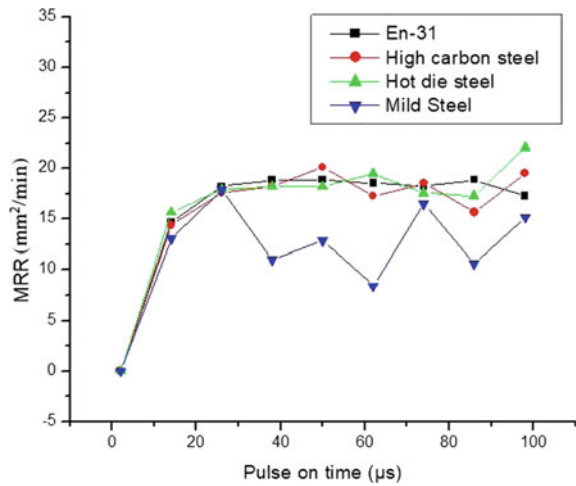
3.3 Effect of Pulse off Time on MRR

The off time also governs the stability of the process. A nonzero pulse off time is a necessary requirement for EDM operation. Pulse off time is altered from 3 to 15 μs keeping a constant interval of 3 μs with brass and molybdenum wire, respectively. Other controllable process variables such as the wire feed rate (WFR) = 70 m/min, pulse on time (T_{ON}) = 38 μs, gap voltage (V_g) = 44 V, and peak current (I_c) = 3 A were kept constant. It could be easily observed from the below Fig. 8 (given below)

Fig. 8 Pulse off time versus
MRR plot for brass wire
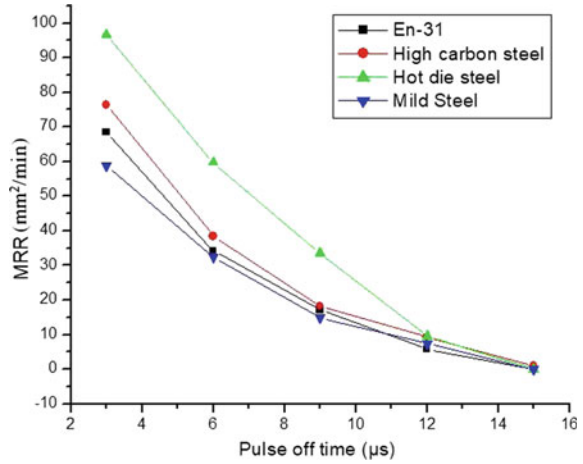
Fig. 9 Pulse off time versus
MRR plot for molybdenum
wire
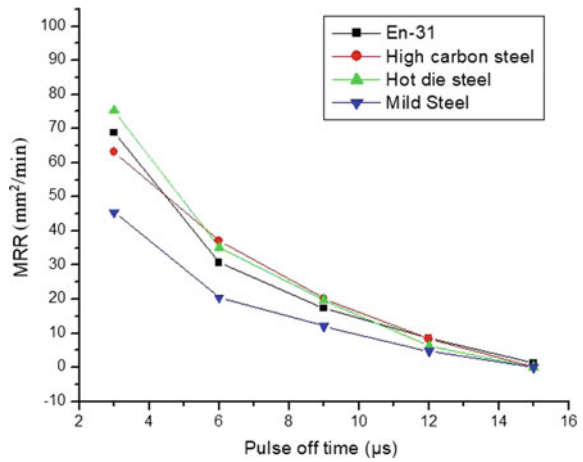
that when the pulse off time (T_{OFF}) is increasing, the material removal rate decreases
from a higher value in the beginning to zero at the final point.

It should be carefully noted that MRR of hot die steel (HDS) has been found to be
highest and mild steel (MS) to be the lowest in the first value of pulse off time. In the
case of molybdenum wire, with the increase in pulse off time (T_{OFF}), the material
removal rate depicts the same trend as in the case of brass wire as shown in Fig. 9.

3.4 Effect of Gap Voltage on MRR

Efficiency gets reduced if gap voltage is increased. Frequent gap short problem
occurs with increase in gap voltage. In normal condition, gap voltage must be kept

Fig. 10 Voltage versus MRR plot for brass wire
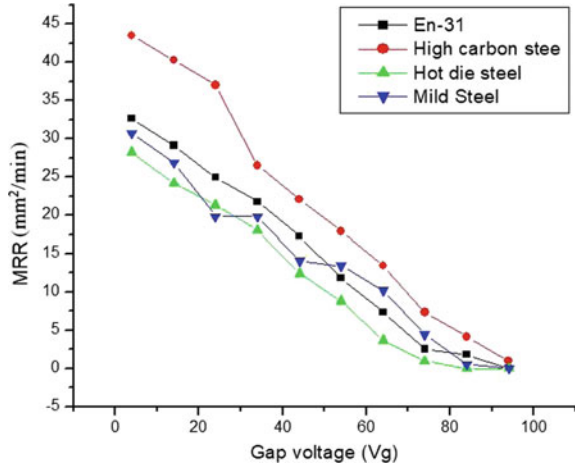
at minimum. A gap voltage detector in a wire cut electric discharge machine is provided, which is capable of eliminating an adverse effect due to a variation in an electric discharge position, thereby detecting a gap voltage between a wire electrode and a workpiece in an accurate manner. Gap voltage has been changed from 4 to 94 V at an interval of 10 V with brass wire and molybdenum wire, respectively. Other controllable process variables such as the wire feed rate (WFR) = 70 m/min, pulse on time (T_{ON}) = 38 μs, pulse off time (T_{OFF}) = 9 μs, and peak current (I_c) = 3 A were kept constant.

From the above pictorial data plot of gap voltage vs material removal rate, it is well understood that with an increase in the gap voltage (GV), the material removal rate has been found to be decreased gradually with the MRR of high carbon steel (HCS) showing the decline from the highest elevation and hot die steel (HDS) from the lowest peak as shown in Fig. 10.

When we used molybdenum wire, then MRR of hot die steel (HDS) and EN-31 has been found to decrease gradually to attain the zero value, but the MRR of two materials—MS and HCS—have been seen to attain the zero value with a little bit of oscillating nature in between, as shown in Fig. 11.

3.5 Effect of Peak Current on MRR

The maximum amount of current which an output is capable of sourcing for brief periods of time is known as peak current. Peak current has been increased gradually from zero to 4 A with an increment of 1 A and the graphs with brass and molybdenum wire, respectively. Other controllable process variables such as the wire feed rate (WFR) = 70 m/min, pulse on time (T_{ON}) = 38 μs, pulse off time (T_{OFF}) = 9 μs, and gap voltage (V_g) = 44 V were kept constant.

It could be easily concluded from Fig. 12 that the peak current possesses a linear relationship with the material removal rate and the most significant effect among the four materials is being shown by high carbon steel (HCS) followed by EN-31, mild steel, and hot die steel, respectively. But in the case of molybdenum wire, with the increase in peak current, the material removal rate has been found to be increased. The MRR in mild steel is seen to be rising slowly as compared to the other three workpiece materials as shown in Fig. 13.

Fig. 13 Plots of peak current versus MRR with molybdenum wire
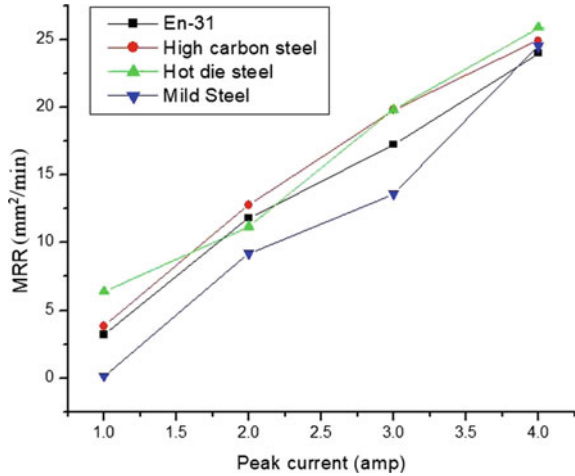
4 Conclusions

Controllable process variables contribute positively with statistically significant effect on the MRR. During this experimental procedure, five controllable process variables were changed (using brass wire and molybdenum wire experimental study on various workpiece materials such as hot die steel, high carbon steel, EN-31, and mild steel). The experimental investigation of controllable factors has been analyzed to maximize MRR. Observations were made whether the material removal rate (MRR) increases/decreases with controllable processes by using brass wire and molybdenum wire on various workpiece material combinations. The experiments were based on one factor experiment strategy. In this methodology, only one input parameter is varied while keeping all others input parameters at constant values. The following conclusions could be drawn from this study within the limits of factors considered in each experimental condition:

- The wire feed rate has a slight positive effect on the material removal rate.
- The pulse on time parameter has a direct effect on the material removal rate, a sharp increase as well as sharp decrease with highest MRR.
- With increase in pulse off time the material removal rate decreases, MRR has been found zero at the highest value of pulse off time.
- The material removal rate has been decreased with an increase in the gap voltage.
- Increasing peak current increases the material removal rate.

References

1. Liao YS, Huang JT, Su HC, A Study on the machining-parameters optimization of WEDM. J. Mater. Process. Technol. 1997; 71: 483–493.
2. Patel JD, Maniya KD, Application of AHP/MOORA method to select Wire cut Electrical Discharge Machining process parameter to cut EN31 alloys steel with brasswire. Materials Today: Proceedings 2015; 2 2496–2503.
3. Singh H and Garg R, Effects of process parameters on material removal rate in WEDM. Journal of achievements in materials and manufacturing engineering. 2009; 2: 70–74.
4. Singh T, Misra JP, Singh B, Experimental Investigation of Influence of Process Parameters on MRR during WEDM of Al6063 alloy. Materials Today: Proceedings 2017; 4: 2242–2247.
5. Singh V, Pradhan SK, Optimization of WEDM parameters using Taguchi technique and Response Surface Methodology in machining of AISI D2 Steel. Procedia Engineering 2014; 97: 1597–1608.
6. Tosun N, Cogun C, Tosun G, A study on kerf and MRR in WEDM based on Taguchi method. Journal of materials processing technology, 2005; 152: 316–322.
7. Tosun N, The Effect of the Cutting Parameters on performance of WEDM" KSME international journal. 2003; 17 (6): 816–824.
8. Haddad MJ and Tehrani AF, Investigation of cylindrical wire electrical discharge turning (CWEDT) of AISI D3 tool steel based on statistical analysis. Journal of materials processing technology. 2008; 198: 77–85.
9. Datta S and Mahapatra SS, Modeling, simulation and parametric optimization of wire EDM process using response surface methodology coupled with grey-Taguchi technique. International journal of engineering, science and technology. 2010; 2 (5): 162–183.
10. Mahapatra SS, Patnaik A, Optimization of WEDM process parameters using Taguchi method. Intentional journal of advanced manufacturing technology. 2007; 34: 911–925.
11. Huang JT, Liao YS, Optimization of machining parameters of Wire-EDM based on Grey relational and statistical analyses. International journal of production research. 2003; 41 (8): 1707–1720.
12. Tarag YS, Ma SC, Chung LK, Determination of optimal cutting parameters in WEDM" International journal of machine tools & manufacture. 1995; 35 (12): 1693–1701.
13. Menzies I and P. Koshy (2008). Assessment of abrasion-assisted material removal in wire EDM. CIRP annals - manufacturing technology. Vol. 57, 195–198.
14. Mohammadi A, Tehrani AF, Emanian E, Karimi D, Statistical analysis of wire electrical discharge turning on material removal rate. Journal of materials processing technology. 2008; 205, 283–289.
15. Ramakrishnan R, Karunamoorthy L, Multi response optimization of wire EDM operations using robust design of experiments. Intentional journal of advanced manufacturing technology. 2006; 29: 105–112.

Synthesis of Graphene by Reduction of Graphene Oxide Using Non-Toxic Chemical Reductant

S. Kumari, A. Panigrahi, S. K. Singh and S. K. Pradhan

1 Introduction

Graphene has generated a huge interest among the scientific community since its discovery in 2004 by Novoselov et al. [1]. Due to its unique, mechanical, chemical, thermal, optical, and electrical properties, it is having a very wide range of applications in electrostatic discharge (ESD), electromagnetic interference shielding (EMI), electronic devices, sensors, energy storages, biomedicals, etc. [2]. Graphene-based ESD and EMI materials find application in cell phone parts and coating to shield frequency for aerospace and electronic devices. Graphene can also be used as reinforcements to form a composite coating with polymer [3] and metal matrix [4]. Single- and few-layer graphene sheets can be successfully prepared by physical techniques such as epitaxial growth [5], mechanical cleavage [1], and chemical vapor deposition [6]. However, it is difficult to yield a scalable quantity of graphene by these physical methods. The most common approach to produce a scalable quantity of graphene is by chemical oxidation of graphite which gives oxidized graphite (graphene oxide in disperse form) and thereafter treating it with reducing agent to yield few-layer graphene or reduced graphene oxide (RGO) [7]. GO is an exfoliated layer of carbon with water molecules and oxygen functional groups. The basal plane of GO mostly consists of epoxy and hydroxyl groups, and the sheet edge of GO consists of carboxy, carbonyl, phenol, and quinine. Due to the distribution of these oxygen-rich functional group which is adsorbed on the surface of GO, it is non-conductive and hydrophilic in nature [8].

S. Kumari (✉) · A. Panigrahi · S. K. Singh · S. K. Pradhan
Advanced Materials Technology Department, CSIR-Institute of Minerals and Materials
Technology, Bhubaneswar 751013, Odisha, India
e-mail: ku_sandhaya@yahoo.com

S. Kumari · A. Panigrahi · S. K. Singh · S. K. Pradhan
Academy of Scientific and Innovative Research (AcSIR), Council of Scientific and Industrial
Research, AnusandhanBhawan, 2 Rafi Marg, New Delhi 110001, India

Most common chemicals used for the desorption of oxygen functional group from the surface of GO to yield RGO are hydrazine, hydrazine hydrate, hydroquinone [9]. However, these chemicals are highly toxic and detrimental to both human and environment. Further, the technique for reduction is also not free from hassle. Hence, there is a need to explore non-toxic reductant and a facile technique for GO reduction.

In this present study, GO is reduced to RGO by single-step in situ process using non-toxic sodium hypophosphite monohydrate as a reducing agent. The aim of this strategy or procedure is to develop hassle-free, very facile, environmentally friendly, energy-saving, and cost-effective process for reduction. This process can also be used to produce a scalable quantity of chemically reduced graphene and find applications in coating industries where the colloidal solution is used for the formation of various functional composites of RGO.

2   Experimental

2.1   Raw Material

Graphite powder (purity $= 99.995\%$, particle size <20 μm) and sodium hypophosphite monohydrate ($NaH_2PO_2 \cdot H_2O$) were procured from Sigma-Aldrich and used as received. Concentrated sulfuric acid (H_2SO_4), potassium permanganate ($KMnO_4$), hydrogen peroxide H_2O_2 (30% w/v), and hydrochloric acid (HCl) were bought from Fisher Scientific.

2.2   Preparation Procedure of GO

Hummer's method with slight modification was followed for the preparation of graphene oxide (GO) [10] using graphite powder, $KMnO_4$, H_2SO_4, and H_2O_2. In brief, 1 g of graphite powder was added to concentrated H_2SO_4 and stirred for 10 mins. Further, this mixture was placed in a bath containing ice, and a required quantity of $KMnO_4$ was added gradually to the mixture and continuously stirred till it becomes pasty brown. After that, de-ionized water was added and again stirred for 10 mins. Sufficient quantity of (30 wt%) H_2O_2 was added drop-wise to the mixture to seize the reaction. The color of the obtained mixture changes to brownish yellow. The mixture was filtered using filter paper and the residue remained on the filter paper was collected and alternately washed with 0.1 M HCl and de-ionized water several times to remove the residual SO_4^{-2} ion, and finally, a pasty brown GO was obtained.

2.3 Chemical Reduction of Graphene Oxide to Graphene

For chemical reduction of GO, 2 mg GO was added to 10 ml of de-ionized water and sonicated. The color of the solution changes to light yellow after sonication. In the well-dispersed GO, 0.25 g of $NaH_2PO_2 \cdot H_2O$ was added and again sonicated. Then, the suspension was heated to 90 °C under magnetic stirring for 4 h. The color of the suspension changes to black indicating the reduction of GO to RGO (or simply, the graphene). The suspension was cooled and filtered, and the black residue was washed in water. The filtrate was dried, and the obtained black RGO was stored in desiccators for further characterization.

2.4 Characterization Techniques

The microstructures of GO and RGO were observed by FESEM using "SUPRA GEMINI 55 (Carl Zeiss, Germany)." Raman spectrometer "Horiba Scientific T64000" was used to obtain the Raman spectra of GO and RGO. Ultraviolet-visible (UV-Vis) spectra of the as-prepared GO and RGO sample were collected on a UV-Vis spectrophotometer (Shimadzu UV-2450). The thermo-gravimetric analyses (TGAs) of samples were carried out on thermal analyzer instrument "NETZSCH, STA 449 F3 Jupiter." The powdered samples of GO and RGO were subjected to TGA in the temperature range of 30–800 °C, heated at the rate of 10 °C/min under an argon atmosphere.

3 Results and Discussion

3.1 GO and RGO

Figure 1 shows the digital image of GO and RGO immediately after dispersion in de-ionized water. GO is observed to be dispersed easily in de-ionized water producing nano-thin sheets of GO, as it contains various oxygen functional groups such as epoxy, hydroxyl, carboxy, carbonyl, phenol and is hydrophilic in nature [11]. GO in dispersion shows yellowish color and does not settle down even after months. On the other hand, RGO in dispersion shows black color which indicates the reduction of GO. RGO lacks functional group containing oxygen. Therefore, RGO is observed to be hydrophobic in nature which settled down after few hours.

Fig. 1 Digital image of **a** GO and **b** RGO dispersed in de-ionized water
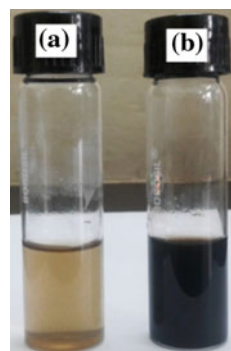
3.2 Morphological and Compositional Analysis of GO and RGO

Figure 2a, b represents the FESEM image of synthesized GO and RGO. The morphology of GO and RGO as observed by FESEM at high magnification shows thin wrinkled sheets. The sheets are efficiently exfoliated indicating the oxidation of GO. The RGO morphology shows more crumpled thin sheets suggesting an increase in disorders. The EDX data reveals the presence of C, O, and Al. Carbon and oxygen are present as GO and RGO are exfoliated layers of carbon with oxygen functional groups in between the layers. Al is present as GO and RGO were examined by FESEM on Al foils. Further, the at. % of oxygen in GO is 23.02. The % C/O (in at.) for GO is 2.69 and for RGO is 8.03 which is three times that of GO. The higher % C/O (in at.) of RGO confirms the removal of oxygen functional group and reduction of GO to RGO.

3.3 Raman Analyses

The reduction of GO to RGO was evaluated by Raman analyses. Figure 3a represents Raman spectrum of GO which displays D-band at 1347.77 cm^{-1} which represents defect or disorder band and sp^3-bonded tetrahedral configuration. The G-band at 1589.14 cm^{-1} is a result of in-plane vibration of sp^2-hybridized C atoms. The normalized intensity ratio of D- and G-bands (I_d/I_g) for GO is calculated to be 0.84. Raman spectrum of RGO shown in Fig. 3b displays D- and G-bands at 1357.12 and 1599.22 cm^{-1}, respectively, with increased ($I_d/I_g = 1.01$) compared to that of GO. The increase in I_d/I_g signifies the reduction of GO to RGO due to the restoration of sp^2 hybridized carbon, decrease in the average size of sp^2 domain of RGO upon reduction [12], and lack of oxygen functional groups in RGO.
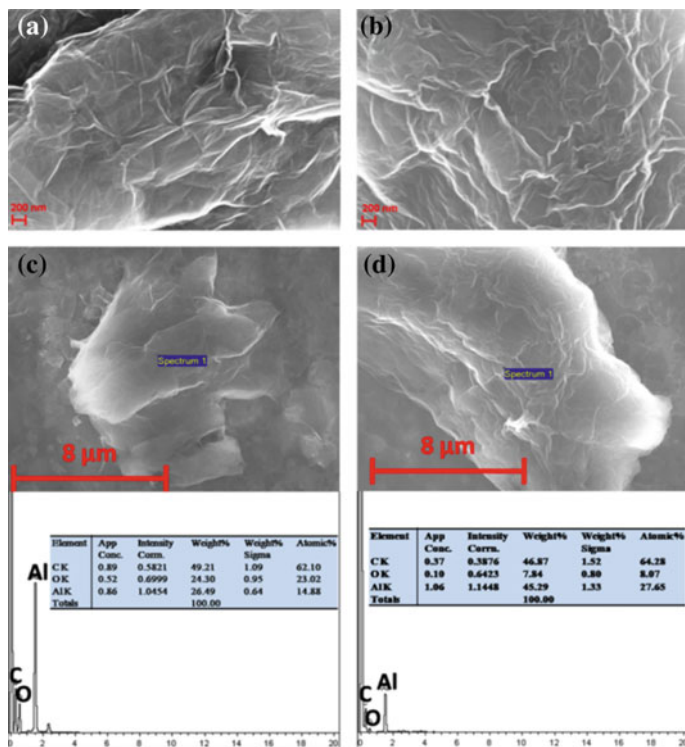
Fig. 2 FESEM image of **a** GO and **b** RGO at higher magnification, respectively, **c** and **d** EDX analysis of GO and RGO respectively

3.4 UV-Visible Spectroscopy

UV-visible spectroscopy data was collected to monitor the oxidation of GO and its reduction to RGO and is presented in Fig. 4. The UV-visible spectroscopy plot of GO shows absorption peak at ~228 nm. This adsorption peak is ascribed to π-π^* electronic transition of the graphitic C=C functional group and another peak at 300 nm attributed to the n-π transition of C=O functional groups. After reduction by $NaH_2PO_2 \cdot H_2O$, the graphitic C=C bond peak in RGO shifted to ~236 nm. The shift is observed due to lack of oxygen functional groups [13] which results in restoration of sp^2-hybridized carbon and revival of conjugated C=C bonds. Also, the absence of shoulder peak confirms the efficient reduction of GO to RGO. Similar results have been reported by Sahu et al. [14].

Fig. 3 Raman spectra of **a** GO and **b** RGO

Fig. 4 UV-visible spectra obtained for **a** GO and **b** RGO

3.5   Thermo-Gravimetric Analysis

TGA curve of GO and RGO under argon atmosphere are shown in Fig. 5. It is noticed that GO is less stable toward the increase of temperature and shows weight loss in three steps. In the first step, i.e., from 30 to 190 °C, the weight loss 27.2% is observed due to the elimination of H_2O molecul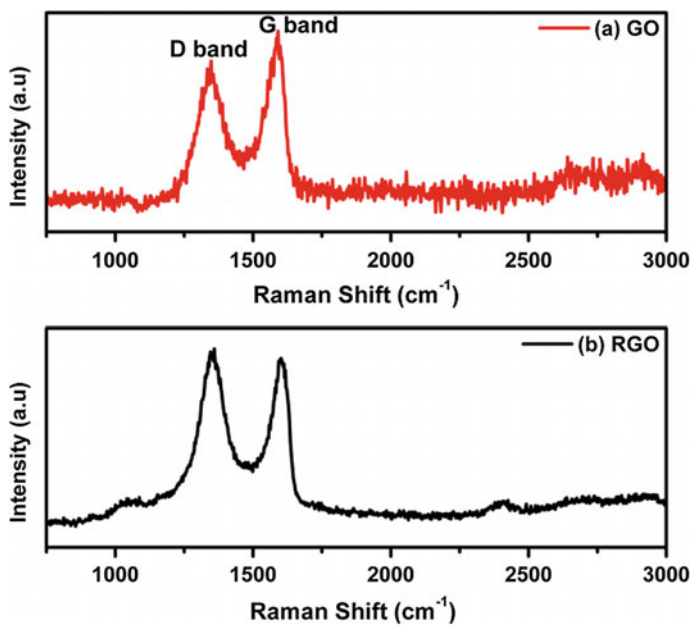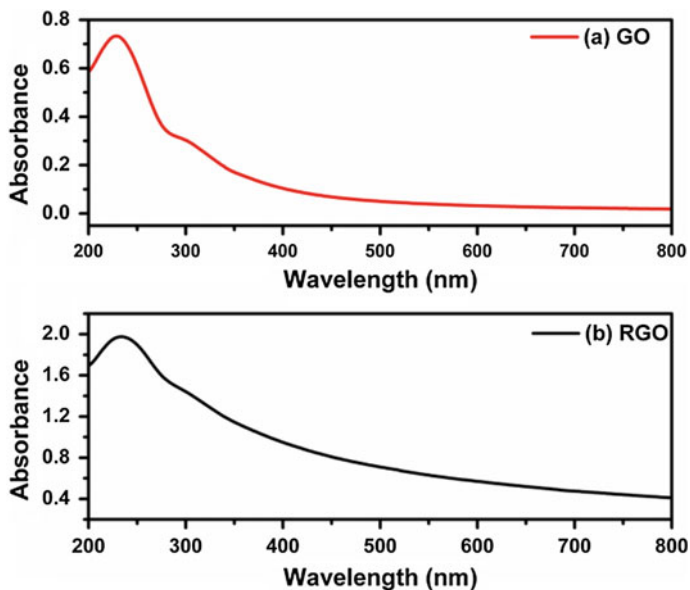es adsorbed in the interlayer of GO. In the second step, there is a maximum weight loss of 61.4% at the temperature of 190 °C. The pyrolysis of oxygen-containing functional groups present in GO is the reason behind this maximum weight loss. The minimum loss in weight is observed in the third step, i.e., in the temperature range of 190–800 °C. In the case of RGO, an increased thermal stability is observed as due to the desorption of thermal liable oxygen functional groups. The weight loss up to 190 °C is similar to GO attributed to the release of an adsorbed water molecule. The weight loss is significantly less in the entire range of temperature from 190 to 800 °C.

4   Conclusion

In summary, we report a facile method for the reduction of GO to RGO by a single-step in situ process using non-toxic reductant $NaH_2PO_2 \cdot H_2O$. The method described here is hassle-free, environmentally friendly, and cost-effective. The morphology of GO and RGO shows thin wrinkled sheets. The EDX analysis of RGO shows increased C/O (in at. %) of 8.03 produced at a temperature less than 90 °C. The absence of shoulder peak in RGO during UV-visible spectroscopy confirms the efficient reduction of GO to RGO. RGO also shows significantly better thermal stability than GO over the entire range of temperature from 30 to 800 °C.

Fig. 5   TGA curves obtained for **a** GO and **b** RGO
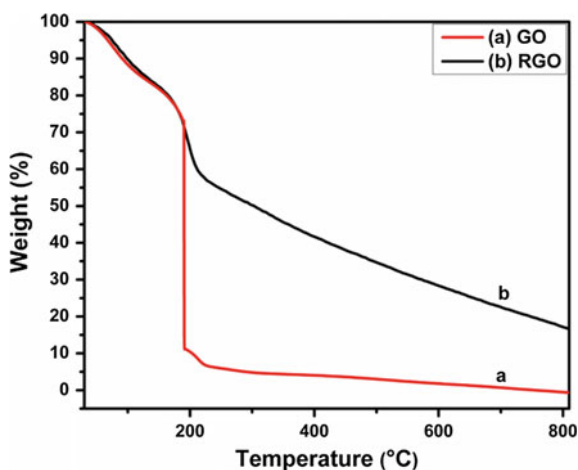
References

1. Novoselov KS, Geim AK, Morozov SV, Jiang D, Electric Field Effect in Atomically Thin Carbon Films, Science 306 (2004) 666–669.
2. Das TK, Prusty S, Graphene-Based Polymer Composites and Their Applications, Polym. Technol. Eng. 52 (2013) 319–331.
3. Kumari S, Panigrahi A, Singh SK, Pradhan SK, Enhanced corrosion resistance and mechanical properties of nanostructured graphene-polymer composite coating on copper by electrophoretic deposition, J. Coatings Technol. Res. (2017). https://doi.org/10.1007/s11998-017-0001-z.
4. Jiang K, Li J, Liu J, Electrochemical codeposition of graphene platelets and nickel for improved corrosion resistant properties, RSC Adv. 4 (2014) 36245–36252.
5. Berger C, Song Z, Li T, Li X, OgbazghiAY, Feng R, Dai Z, Marchenkov AN, Conrad EH, First PN, Heer WA De, Ultrathin Epitaxial Graphite: 2D Electron Gas Properties and a Route toward Graphene-based Nanoelectronics, J. Phys. Chem. B. 108 (2004) 19912–19916.
6. Zhang YI, Zhang L, Zhou C, Review of Chemical Vapor Deposition of Graphene and Related Applications, Am. Chem. Soc. 46 (2013) 2329–2339.
7. Silva KKH De, Huang H, Joshi RK, Yoshimura M, Chemical reduction of graphene oxide using green reductants, Carbon N. Y. 119 (2017) 190–199.
8. Tong Y, Bohm S, Song M, Graphenebased materials and their composites as coatings, Austin J. Nanomedicine Nanotechnol. 1 (2013) 1–16.
9. Hou D, Liu Q, Cheng H, Zhang H, Wang S, Green reduction of graphene oxide via Lycium barbarum extract, J. Solid State Chem. 246 (2017) 351–356.
10. Shahriary L, Athawale A, Graphene Oxide Synthesized by using Modified Hummers Approach, Int. J. Renew. Energy Environ. Eng. 2 (2014) 58–63.
11. Chowdhury DR, Singh C, Paul A, Role of graphite precursor and sodium nitrate in graphite oxide synthesis, RSC Adv. 4 (2014) 15138–15145.
12. Pei S, Cheng HM, The reduction of graphene oxide, Carbon 50 (2012) 3210–3228.
13. Wang J, Caliskan E, Lidija Š, Green reduction of graphene oxide using alanine, Mater. Sci. Eng. C. 72 (2017) 1–6.
14. Sahu S.C. Samantara AK, Juluri RR, SahuRK, JenaBK, Graphene-induced Pd nanodendrites : A high performance hybrid nanoelectrocatalyst, Nano Res. 6 (2013) 635–643.

Modeling and Optimization of Surface Roughness in Hard Turning of AISI 4340 Steel with Coated Ceramic Tool

J. Jena, A. Panda, A. K. Behera, P. C. Jena, Sudhansu Ranjan Das and D. Dhupal

1 Introduction

Hardened steels are more suitable for aerospace as well as automobile industry, and highly precise machine tool manufacturing industries, by virtue of their excellent properties and are strengthened by the addition of chromium. On the contrary of their high fatigue strength, wear and corrosion resistance, better strength-to-temperature ratio make them difficult to machine [1, 2]. Maintaining the high quality and dimensional accuracy of the hardened steel components at the same time, keeping the cost of manufacturing low is a very challenging task. Dry hard turning is widely used in machining of hardened steel because of its low cost, high machining efficiency, and green environmental protection. The cutting mechanism of dry hard turning is different from that of traditional turning because of multi-field coupling effect in machining process. Moreover, modeling along with optimization of several machining parameters for surface roughness is quite crucial so as to get their efficient implementation in hard turning. Numerous researchers were exercised methods concerning experimental, analytical, and statistical approaches for mathematical modeling in order to predict the surface roughness momentarily and for response optimization in order to control the different process parameters (cutting parameters [3–7]; cutting tool materials [8–10]; tool geometry [11–14]; workpiece hardness [15–18]; and environmental conditions [19–22]) in hard turning with different work materials (AISI D2, D3, D6, 1015, 1045, 4140, 4340, 52100, H11, H13). Until now, no systematic study has been made in the absence of cutting force and tool wear during hard turning. Hence, this extensive investigation on modeling and optimization will definitely

J. Jena · A. K. Behera
Department of Mechanical Engineering, SOA University, Bhubaneswar 751030, Odisha, India

A. Panda · P. C. Jena · S. R. Das (✉) · D. Dhupal
Department of Production Engineering, Veer Surendra Sai University of Technology, Burla 768018, Odisha, India
e-mail: das.sudhansu83@gmail.com

create an avenue, beneficial for machining industries' point of view to achieve their goals. Thus, this work focuses on development of mathematical model and response optimization (here, surface roughness) in FDHT of AISI grade 4340 steel cut by coated ceramic tool using statistical approaches such as response surface methodology followed by desirability function analysis.

2 Experimental Procedure

To accomplish the objective of the proposed research work, depth of cut, axial feed, and cutting speed are taken as major process variables with an attempt to analyze surface roughness as the only technological response parameter. The identified cutting parameters with their associated levels are shown in Table 1. Employing the above-mentioned controllable parameters (three) with four different levels, a well-sequential design layout was established based on Taguchi design of experiment (DOE_s) L_{16} orthogonal array in order to perform the dry longitudinal turning operation.

The work material used for experiment is AISI 4340 grade HSLA (high-strength low-alloy) steel in the form of cylindrical bar having machining diameter of 35 mm as well as length of 150 mm. SPECTRO metal analyzer is being used for the confirmation of the workpiece material (AISI 4340 steel) through chemical and elemental composition test, which is illustrated in Table 2. The hardness of specimen has been increased to 49 HRC using heat treatment process followed by oil quenching. A heavy-duty high-precision CNC lathe (make, Bhavya Machine Tools; model, CJK6132) is used for finish turning operation, having 4 kW motor spindle power in which speed varies from 50 to 3000 rpm. For experimentation, commercially available PVD coated ceramic insert, designated as ISO grade CNGA120408 AB2010

Table 1 Parameters and levels

Parameters	Levels			
	1	2	3	4
Axial feed, f (mm/rev)	0.06	0.10	0.14	0.18
Cutting speed, v (m/min)	110	160	210	260
Depth of cut, d (mm)	0.2	0.3	0.4	0.5

Table 2 Chemical composition of HSLA steel

Elements	Cr	C	Mn	Si	Ni	P	Mo	S	Fe
Weight (%)	1.12	0.397	0.78	0.39	1.54	0.053	0.174	0.032	Balance
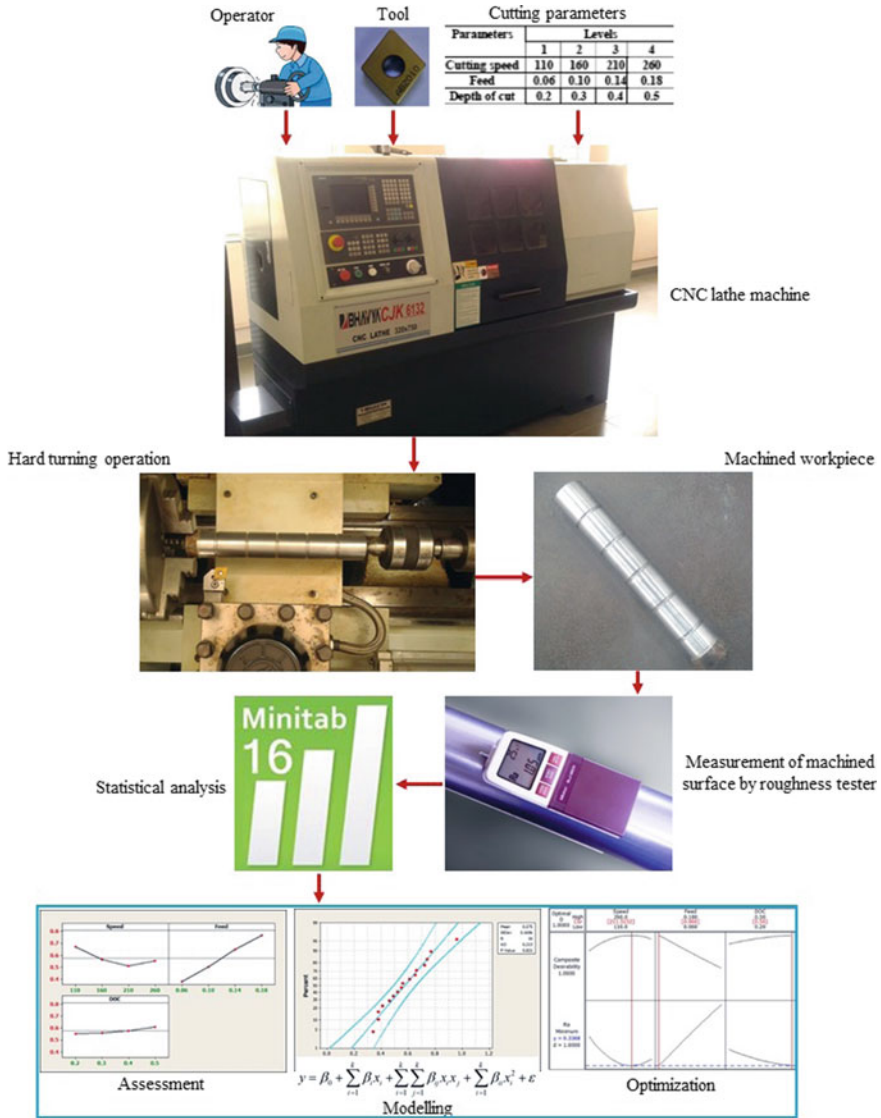
Fig. 1 Layout of methodology proposed

(TaeguTec make), has been used to assess the surface finish of hardened AISI D2 steel under dry cutting surrounding. The coated ceramic insert was rigidly held on a ISO designated toolholder of PCLNL2020K12. Mitotoyo (Surftest SJ201) roughness tester has been employed to quantify the average work surface roughness. The measurement for work surface roughness has been carried out on three different portions of the turned surface of test specimen, and its arithmetic mean has been taken

Table 3 Experimental results

Test no.	Coded values			Actual settings			Surface roughness R_a (μm)
	v	f	d	v	f	d	
1	1	1	1	110	0.06	0.2	0.41
2	1	2	2	110	0.10	0.3	0.55
3	1	3	3	110	0.14	0.4	0.77
4	1	4	4	110	0.18	0.5	0.96
5	2	1	2	160	0.06	0.3	0.38
6	2	2	1	160	0.10	0.2	0.52
7	2	3	4	160	0.14	0.5	0.61
8	2	4	3	160	0.18	0.4	0.74
9	3	1	3	210	0.06	0.4	0.34
10	3	2	4	210	0.10	0.5	0.49
11	3	3	1	210	0.14	0.2	0.56
12	3	4	2	210	0.18	0.3	0.65
13	4	1	4	260	0.06	0.5	0.38
14	4	2	3	260	0.10	0.4	0.46
15	4	3	2	260	0.14	0.3	0.66
16	4	4	1	260	0.18	0.2	0.72

as surface roughness value for the test sample. The schematic view of experimental work and methodology proposed in the current study is illustrated in Fig. 1 along with the experimental results are shown in Table 3.

3   Results and Discussion

3.1   *Statistical Analysis on Surface Roughness*

Experimental results by Taguchi OA are analyzed by employing analysis of variance which involves statistical treatment to access the significance as well as determine the percentage of contribution of each process variable (v, f, d) against a stated level of confidence on R_a. Corresponding to ANOVA results of surface roughness shown in Table 4, the sources axial feed (f) and cutting speed (v) represent the two most significant as well as influential cutting parameters on surface roughness as their P value approaches to zero (i.e., under 0.05) and larger F value (i.e., more than tabulated F value of 4.76) with the contributions 80.28 and 13.25%, respectively, at 95% of confidence level. Moreover, depth of cut does not present a significant as well as major impact on R_a, as its contribution is very low (1.82%). Concerning, error

Table 4 ANOVA for surface roughness

Source	DF	SS	MS	F_{cal}	F_{tab}	P	Cont.
v	3	0.057150	0.019050	5.70	4.76	0.034	13.25
f	3	0.346350	0.115450	34.55	4.76	0.000	80.28
d	3	0.007850	0.002617	0.78	4.76	0.545	1.82
Error	6	0.020050	0.003342				4.65
Total	15	0.431400					100

$S = 0.0578072$
$R^2 = 95.35\%$
$R^2(\text{adj}) = 88.38\%$

contribution accounts for 4.65% of the total variability, which confirms that neither neglected nor avoided any high measurement errors and any major parameter.

Experimental results are further used for 3D surface plot (Fig. 2) to reveal the influence of cutting parameters on surface finish (R_a). Corresponding to Fig. 2a, the increasing effect of feed rate increases surface roughness. Sahoo and Sahoo [23], and Hessainia et al. [24] reported that, at higher feed, the friction predominates between workpiece material and cutting tool because of higher cross-sectional area in deformation zone together with increase in cutting force due to rise in chip load, and therefore, surface roughness increases, generating helicoid furrows due to the resultant nose-shape helicoid tool-workpiece movement. From the surface plot (Fig. 2c), it is observed that raising the cutting speed tends to improve the surface finish, but the effect is minimal at higher speed (110–210 m/min). This trend is expected because of the reduction in machining time, disappearance of unstable BUE formation as well as reduction in cutting force on account of decrease in tool–chip contact length, which in turn stabilizes the machining system, thereby improving surface finish, as described by Suresh et al. [25] and Aziz et al. [26]. Nevertheless, improvement in surface finish was limited to 210 m/min and subsequent rise in cutting speed results increased surface roughness which is probably expected by the feasibility of material side flow [27]. The typical trend curve of roughness versus depth of cut in Fig. 2b shows less considerable effect on surface roughness, and the difference in roughness values is marginal. However, as DOC increases, large volume of material in deforming leads to serious plastic deformation; as a result, the machined components show high roughness due to more contact length between the workpiece and tool. However, it is recommended to use lower values of DOC to avoid the tendency to chatter and subsequently improves surface finish.

3.2 Empirical Modeling for Surface Roughness

The results of response characteristic, i.e., surface roughness (R_a) which were obtained in accordance of L_{16} OA were analyzed in Minitab 16 through response sur-
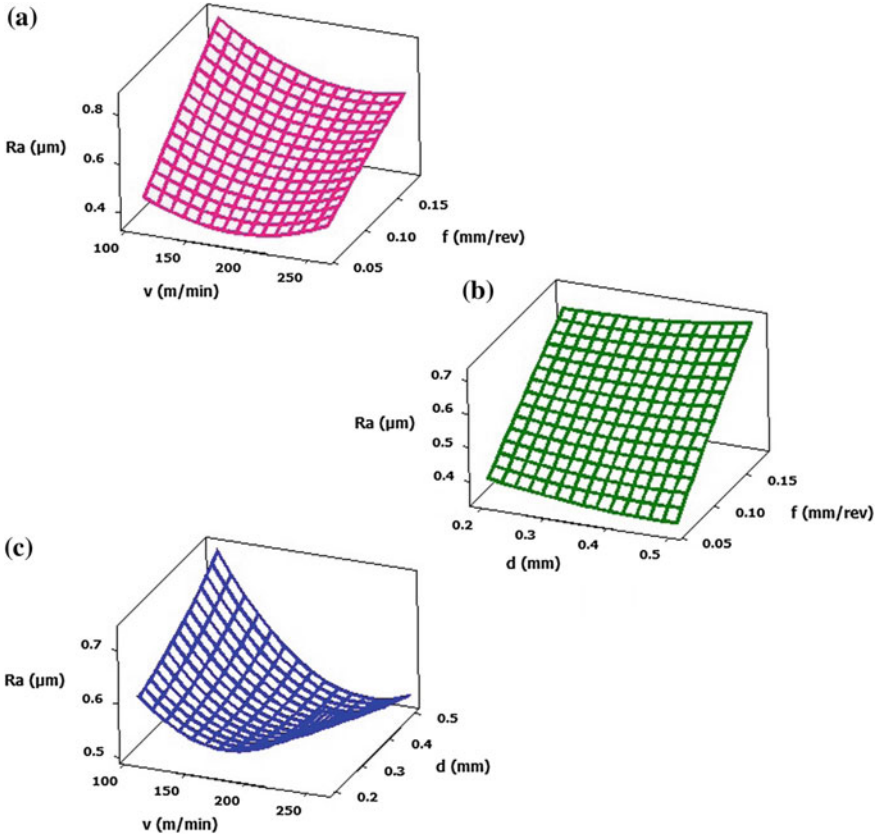
Fig. 2 Surface plots of surface roughness, R_a

face methodology (RSM), developed the mathematical model to find out the best-fit of correlation between the surface finish of the hard-turned component with the input parameters such as depth of cut (d), cutting speed (v), and axial feed (f). Regression equation in the second order (i.e., quadratic model) for the response R_a is presented by:

$$R_a = 0.41829 - 0.00319v + 4.175f + 0.26773d + 0.00002v^2$$
$$- 1.5625f^2 + 0.625d^2 - 0.01068v * f - 0.00541v * d + 2.44318f * d$$
$$R^2 = 97.8\%, \ R^2(adj) = 94.5\% \tag{1}$$

To avoid the misleading conclusion, the performance of proposed RSM model for surface roughness is checked by statistical parameter like coefficient of determination (R^2). The suggested quadratic model explains the R^2 value of 0.97 which is very close to unity (1) ensuring the excellent fit for the model with better predictive

Fig. 3   Normal probability plot for R_a

ability. Finally, normal probability plot combined with Anderson–Darling test for R_a is illustrated in Fig. 3 and confirms the residuals are d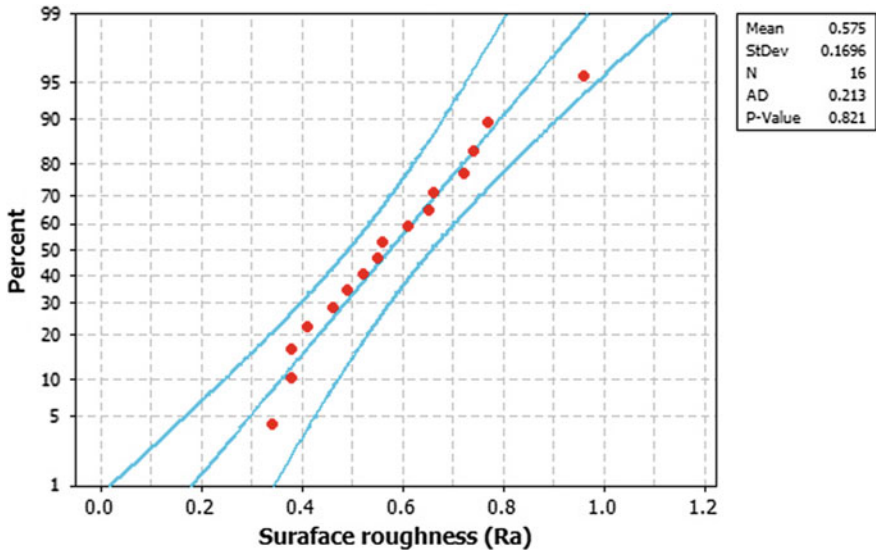istributed nearly close to a straight line, revealing that the errors are dispersed normally and specifying that the terms corresponding to the model are significant. Moreover, its P value (0.821) complimented by Anderson–Darling test is over significance level value (0.05), which confirms the adequacy of model due to favorable reception of null hypothesis.

3.3   Optimization of Surface Roughness Using RSM

In this study, with the goal to minimize the surface roughness, desirability function analysis of RSM is utilized for response optimization which is basically employed to determine the best parametric arrangement for single- and multi-objective optimizations. This optimization unit looks for a combination of parameter levels that concurrently fulfill the necessities placed on each and every one of the responses, and parameter trying to set up the suitable model. Performance of the optimization procedure adopted is given by composite desirability index through gradient algorithm. It is the weighted geometric average of individual desirability indices for different output responses in the range 0–1. If the value of desirability lies nearer to zero, the response would be absolutely rejected. On the other hand, if its value approaches unity, the response would be acknowledged. Optimum cutting speed, axial feed, and DOC during hard turning of AISI4340 steel obtained using RSM technique are
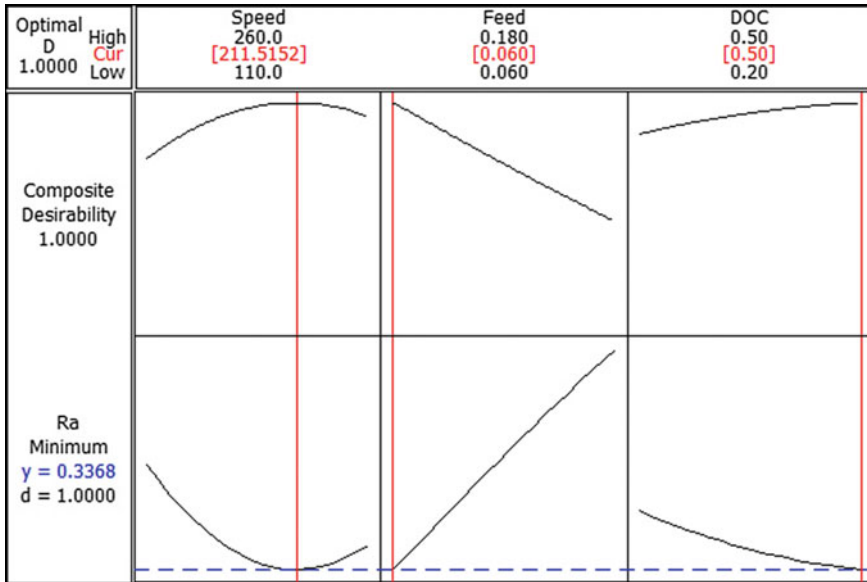
Fig. 4 Optimization plot for R_a

211.51 m/min, 0.06 mm/rev, and 0.5 mm, respectively, for corresponding minimum surface roughness (R_a) 0.3368 μm. Same has illustrated in Fig. 4.

4 Conclusions

Based on experimental findings in FDHT of HSLA steel with coated ceramic tool, the following conclusions are drawn:

- Machined surface quality of HSLA steel with coated ceramic insert produced roughness within 1.6 micron and can be comparable with cylindrical grinding. Surface roughness was principally affected by axial feed which is in well agreement with the ANOVA results.
- Optimization employing RSM technique shows the optimal setting of machining variables in HT operation of AISI 4340 steel by PVD-TiN at DOC of 0.5 mm, axial feed of 0.06 mm/rev, and cutting speed of 211.52 m/min with estimated minimal surface roughness of 0.3368 micron.
- Empirical models proposed for the technological response characteristic (surface roughness) have R-square value close to one, which ensured the greater statistical significance with brilliance of fit for the model. Normal probability plot ensures that the residuals distributed closely near to a straight line showing the normality dispersion of errors as well as implying the sources associated with the model are

significant. Anderson–Darling test for model shows adequacy, as P value is over 0.05 at 95% confidence level.

References

1. Das SR, Kumar A, Dhupal D. Experimental investigation on cutting force and surface roughness in machining of hardened AISI 52100 steel using cBN tool. International Journal of Machining and Machinability of Materials, 2016; 18:501–521.

2. Das SR, Dhupal D, Kumar A. Experimental investigation into machinability of hardened AISI 4140 steel using TiN coated ceramic tool. Measurement 2015; 62: 108–126.

3. Agrawal A, Goel S, Rashid W Bin, Price M. Prediction of surface roughness during hard turning of AISI 4340 steel (69 HRC). Applied Soft Computing Journal 2015; 30: 279–286.

4. Panda, A., Sahoo, A.K., Rout, A.K., (2016). Investigations on surface quality characteristics with multi-response parametric optimization and correlations. Alexandria Engineering Journal, 55, 1625–1633.

5. Xio Z, Lio X, Long Z, Li M. Effect of cutting parameters on surface roughness using orthogonal array in hard turning of AISI 1045 steel with YT5 tool. International Journal of Advanced Manufacturing Technology 2017; 93:273–282.

6. Das SR, Panda A, Dhupal D. Experimental investigation of surface roughness, flank wear, chip morphology and cost estimation during machining of hardened AISI 4340 steel with coated carbide insert. Mechanics of Advanced Materials and Modern Processes 2017; 3:1–14.

7. Das SR, Panda A, Dhupal D. Analysis of surface roughness in hard turning with coated ceramic inserts: Cutting parameters effects, prediction model, cutting conditions optimization and cost analysis. Ciência e Técnica Vitivinícola: Science and Technology Journal 2017; 32:127–154.

8. Kacal A, Yildirim F. Application of grey relational analysis in high-speed machining of hardened AISI D6 steel. Journal of Mechanical Engineering Science 2012; 227:1566–1576.

9. Gunay M, Yucel E. Application of Taguchi method for determining optimum surface roughness in turning of high-alloy white cast iron. Measurement 2013; 46:913–919.

10. Aouici H, Fnides B, Elbah M, Benlahmidi S, Bensouilah H, Yallese MA. Surface roughness evaluation of various cutting materials in hard turning of AISI H11. International Journal of Industrial Engineering Computations 2016; 7:339–352.

11. Meddour I, Yallese MA, Khattabi R, Elbah M, Boulanour L. Investigating and modeling of cutting forces and surface roughness when hard turning of AISI 52100 steel with mixed ceramic tool: cutting conditions optimization. International Journal of Advanced Manufacturing Technology 2014; 77:1387–1399.

12. Zerti O, Yallese MA, Khettabi R, Chaoui K, Mabrouki T. Design optimization for minimum technological parameters when dry turning of AISI D3 steel using Taguchi method. International Journal of Advanced Manufacturing Technology 2016; 89:1915–1934.

13. Khellaf A, Aouici H, Smaiah S, Boutabba S, Yallese MA, Elbah M. Comparative assessment of two ceramic cutting tools on surface roughness in hard turning of AISI H11 steel : including 2D and 3D surface topography. International Journal of Advanced Manufacturing Technology 2016; 89:333–354.

14. Panda A, Das SR, Dhupal D. Surface Roughness Analysis for Economical Feasibility Study of Coated Ceramic Tool in Hard Turning Operation. Process Integration and Optimization for Sustainability 2017; 1:1–13.

15. Kumar P and Chauhan SR. Machinability Study on Finish Turning of AISI H13 Hot Working Die Tool Steel With Cubic Boron Nitride (CBN) Cutting Tool Inserts Using Response Surface Methodology (RSM). Arabian Journal for Science and Engineering 2015; 40:1471–1485.

16. Tang L, Gao C, Huang J, Shen H, Lin X. Experimental investigation of surface integrity in finish dry hard turning of hardened tool steel at different hardness levels. International Journal of Advanced Manufacturing Technology 2015; 77:1655–1669.

17. Kumar S, Singh D, Kalsi NS. Surface quality evaluation of AISI 4340 steel having varying hardness during machining with TiN-coated CBN inserts. Journal of Engineering Tribology. https://doi.org/10.1177/1350650116684243.

18. Mia M, Dhar NR. Optimization of surface roughness and cutting temperature in high-pressure coolant-assisted hard turning using Taguchi method. International Journal of Advanced Manufacturing Technology 2017; 88:739–753.

19. Naigade DM, Patil DK, Sadaiah M. Some investigations in hard turning of AISI 4340 alloy steel in different cutting environments by CBN insert. International Journal of Machining and Machinability of Materials 2013; 14:165–193.

20. Sahu SK, Mishra PC, Orra K, Sahoo AK. Performance assessment in hard turning of AISI 1015 steel under spray impingement cooling and dry environment. Journal of Engineering Manufacture 2014; 229:251–265.

21. Chinchanikar S, Salve AV, Netake P, More A, Kendre S, Kumar R. Comparative Evaluations of Surface Roughness During Hard Turning under Dry and with Water-based and Vegetable Oil-based Cutting Fluids. Procedia Materials Science 2014; 5:1966–1975.

22. Nouioua M, Yallese MA, Khettabi R, Belhadi S, Bouhalais ML, Girardin F. Investigation of the performance of the MQL, dry, and wet turning by response surface methodology (RSM) and artificial neural network (ANN). International Journal of Advanced Manufacturing Technology https://doi.org/10.1007/s00170-017-0589-2.

23. Sahoo AK, Sahoo B. Performance studies of multilayer hard surface coatings (TiN/TiCN/A$_{l2}$O$_3$/TiN) of indexable carbide inserts in hard machining: Part-I (An experimental approach). Measurement 2013; 46:2854–2867.

24. Hessainia, Z, Belbah A, Yallese, MA, Mabrouki T, Rigal JF. On the prediction of surface roughness in the hard turning based on cutting parameters and tool vibrations Measurement 2013; 46:1671–1681.

25. Suresh R, Basavarajappa S, Samuel GL. Some studies on hard turning of AISI 4340 steel using multilayer coated carbide tool. Measurement (2012); 45:1872–1884.

26. Azizi MW, Belhadi S, Yallese MA, Mabrouki T, Rigal JF. Surface roughness and cutting forces modeling for optimization of machining condition in finish hard turning of AISI 52100 steel. Journal of Mechanical Science and Technology 2012; 26:4105–4114.

27. Das SR, Dhupal D, Kumar A. Study of surface roughness and flank wear in hard turning of AISI 4140 steel with coated ceramic inserts. Journal of Mechanical Science and Technology 2015; 29:4329–4340.

Local Strain Analysis
in a Uni-Directional Fiber-Reinforced
Composite: DIC Versus FEA

A. Sharma and S. Daggumati

1 Introduction

In the conventional design of process of composite structures, such as wind turbine blades and aerospace structures, moduli of the glass and carbon fibers were well utilized. However, if the structural design is constrained either by fatigue or impact loads, fiber–matrix interface play a vital role. In general, mechanical properties of fiber-reinforced composites depend on the constituent materials such as fiber, matrix, fiber distribution and orientation, void content. Besides the aforementioned properties, at microscale, the nature of the fiber–matrix interfacial bonds and the mechanisms of load transfer at the interface play an important role [1]. At laminate level, the load transfer mechanism between adjacent plies will contribute to the multi-axial stress–strain state that is present at the fiber–matrix interface. With the advancement of full-field strain measuring techniques, in order to understand the load transfer mechanism at the fiber–matrix interface level, microscopic images combined with the DIC technique was applied to the composites materials [2–4, 8].

Canal et al. [2] conducted the full-field strain measurements inside a scanning electron microscope (SEM) using submicron alumina particles as a speckle pattern on a E-glass-epoxy composite. The aforementioned research work concludes that at higher magnifications (2000×, 6000×) DIC is able to accurately capture the displacement fields. However, quantitative strain values were not accurately obtained. Mehdikhani et al. [3] conducted the experimental strain analysis at microscale with glass-epoxy composite as well as alumina fiber-epoxy composite laminate with aligned carbon nanotubes grown on fibers [4]. In the above-mentioned work, authors used submicron alumina powder as speckles on the surface of the composites specimen. In all the above-referred studies, authors aimed at understanding the strain state at the fiber—matrix interface level. Moreover, region of interest for strain analysis is restricted

A. Sharma (✉) · S. Daggumati
Department of Mechanical Engineering, IIT Indore, Indore, Madhya Pradesh, India
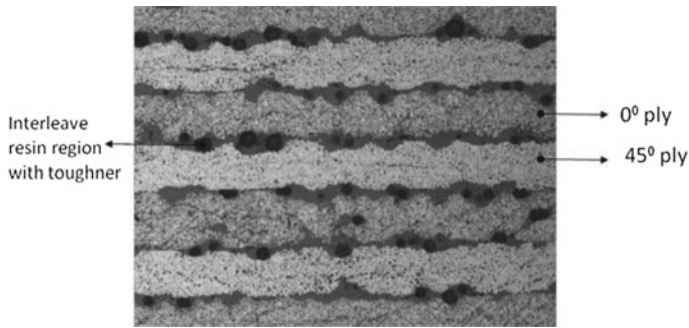e-mail: phd1701103003@iiti.ac.in

Fig. 1 Composite microstructure at $100\times$ magnification

to few fibers. The above studies lead to the following conclusion: (a) for a chosen composite microstructure, speckle patterns as well as DIC parameters need to be optimized to achieve the accurate strain values; (b) micro DIC is able to capture the fiber–matrix surface debondings with very good accuracy. Contrast to the usage of high magnification ($2000\times$) and submicron alumina particle as a speckle pattern, in the current study, authors used low magnification factor ($100\times$) to capture the images of the composite microstructure during the loading process.

This is due to the fact that, in the current study, authors aimed to under the load transfer mechanism within a ply as well as between different plies. Hence, region of interest for the strain analysis is more than one ply. As shown in Fig. 1, at $100\times$ microscopic resolution the constituent material of the composite (fiber, matrix and toughener particles between the plies) are clearly visible and distinguished. The central idea of this work is using the composite microstructure (Fig. 1) as a speckle pattern for the strain calculations, thus eliminating the gross averaging of the local strains associated with the external paint speckles.

2   Mechanical Testing Procedure and Material Used

For the mechanical testing purpose, considered UD composite laminate has IM7 carbon fiber as reinforcement and epoxy as a matrix. Individual carbon fiber, epoxy resin, and the uni-directional composite elastic properties are listed in Table 1. Composite laminate is manufactured using pre-preg plies with an autoclave curing process. Composite samples used for the testing purpose has a cubic shape with the dimensions of $12.5 \times 12.5 \times 12.5$ mm^3.

The composite specimen is polished in such a way that, under the microscope lens at low magnification factor, individual fibers within the ply as well as resin pools between the plies are clearly visible and distinguished. Moreover, at these magnification factors, fibers within the plies and tougheners between the plies act as speckle pattern for image correlation [2]. For microscopic lens, a magnification factor

Table 1 IM7 Carbon fiber and epoxy resin material elastic properties

Material	E_l (GPa)	E_t (GPa)	G_{lt} (GPa)	G_{tt} (GPa)	v_{lt}
IM7 Carbon Fiber [5]	276	56	28	16.7	0.25
Epoxy [5]	4.1	–	1.6	–	0.37
Toughener (rubber) [6]	0.004	–	–	–	0.45
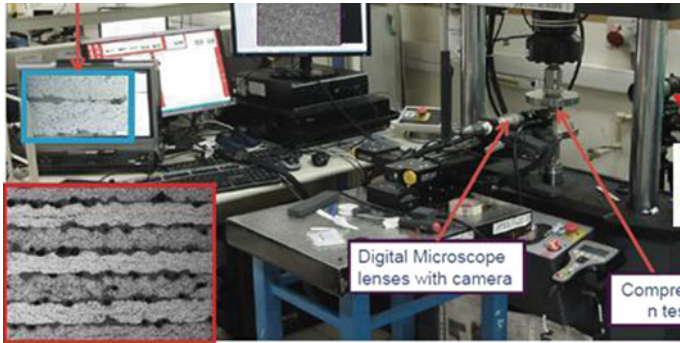
Fig. 2 Test setup for experimental strain evaluation

of 100× was chosen as a compromise between the composite surface areas available for strain correlation to the clarity of the captured images during the deformation process (Fig. 2).

3 Results and Discussion

3.1 Experimental Surface Strain Measurement in the Laminate Thickness Direction

In order to capture the local strain variation during the compression test, an approximate window size of 1.3 × 1.3 mm² was used for the strain correlation. For the full-field strain measurement during the load process, the CCD camera was set to capture 2 images per second over the above-mentioned area. The parameters used for experimental strain computation are listed in Table 2. Using the correlation between initial image before any load application and the consequent images captured during the load process till 0.5% of the global strain, local strain analysis is accomplished on the surface of the laminate as explained in [7]. The average strain in the composite is calculated over the entire window of 1.3 × 1.3 mm². As shown in Fig. 3, for the

Table 2 Details of the strain mapping equipment used and test procedure

Software	VIC 2D
Camera	12-bit grayscale 1392 × 1490 pix
Lens magnification	100×
Correlation subset size (pixels)	75
Correlation step size (pixels)	15
Test speed (μm)	100

Fig. 3 Normal compressive strain variation across the laminate in the thickness direction
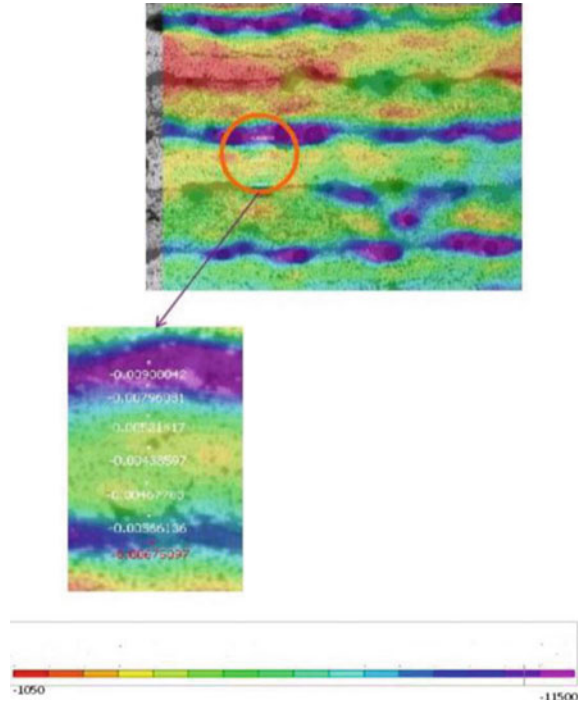
applied average compression strain of 0.5%, the maximum local compressive strain of 0.9% is observed in the toughener (rubber particle) at the interleave resin region.

As we move into the middle of the ply, local compressive strains vary between 0.45 and 0.5%, which is almost equal to the applied far-field compressive strain. Moreover, the local strain profiles for similar material obtained from the similar test methodology [8] indicate that the strain variation across the laminate thickness is in accordance with the elastic module variation of the respective materials. From the DIC strain profile (Fig. 3), it is observed that the local strain gradients are highly influenced by the size of rubber particles and the interleave resin layer thickness.

3.2 Unit Cell FEA

In order to capture the local strain within the ply and at the interleave resin region, microscale unit cell is modeled with two plies under plane stress assumptions. Figure 4a shows the unit cell model that consists of two plies (0° and 45°) along with a interleave resin region consisting of toughener (rubber) particle. For constructing the unit cell FEA, geometrical properties such as fiber diameter, ply thickness, rubber particle diameter as well as interleave resin layer thickness are listed in Table 3. As it can be observed in Fig. 1, there is a variation in rubber particles diameter (12–32 μm) at different locations of the laminate, and hence, there is a variation in the thickness of the interleave resin layers. The above-mentioned variations in the constituent material geometric properties lead to variation in the local strain values (Fig. 3).

In general, for the FE analysis of the unit cell models, often periodic boundary conditions were applied under the assumption that the material has a deterministic and ordered distribution of fibers. However, local stress–strain analysis in a carbon fiber composite leads to the following conclusions: (a) periodic boundary conditions
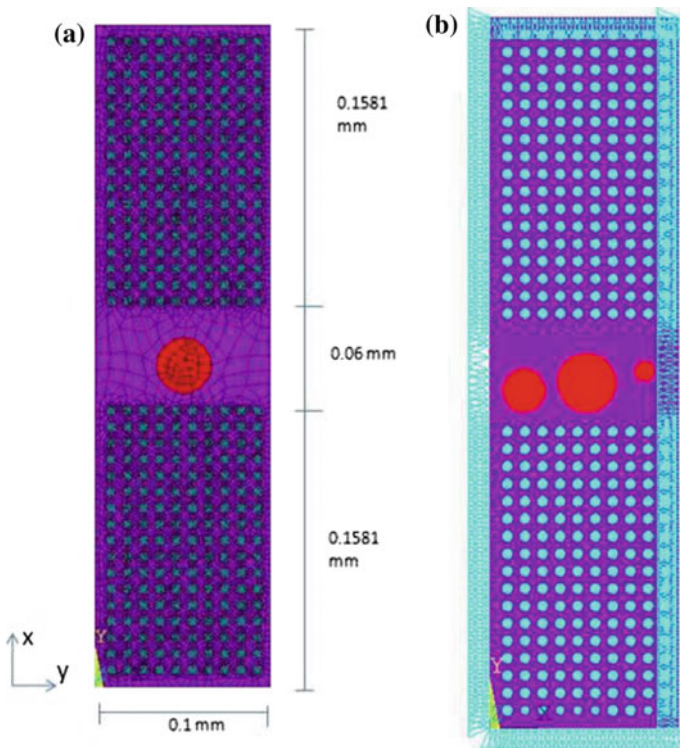

Fig. 4 Unit cell micro-mechanical FE models

Table 3 Geometrical data of the unit cell and its constituents

Unit cell width (mm)	0.1
Unit cell thickness (mm)	0.37
Fiber diameter (μm)	5.2
Rubber particle diameter (μm)	12–32
Interleave resin layer thickness (μm)	60

are well suited for the prediction of the effective elastic constants of the composite when the required accuracy is not so high; (b) in order to predict the local phenomena such as strain variation as well matrix cracking, random unit cell models must be considered [9, 10]. Based on the observation of microscopic images of the composite laminate, in order to capture the local strain gradients influenced by randomness in the unit cell geometry, two different unit cell models were constructed (Fig. 4). Figure 4a, shows the unit cell model consisting of a interleave resin layers with only one rubber particle. Figure 4b shows the unit cell FE model with three rubber particles in the interleave resin region. Once the unit cell FE models were created, for the computational purpose following boundary conditions were imposed on the unit cell: (a) bottom of the unit cell nodes are constrained in *y*-direction and on the top of the unit cell nodes a compressive strain of 0.5% is applied in *y*-direction; (b) in *x*-direction, unit cell nodes are constrained with symmetric boundary conditions (Fig. 4b).

Under the applied flatwise global compressive strain of 0.5%, experimental local normal compressive strain in interleave resin layer is approximately around 0.9% (Fig. 3) around the rubber particles. From the unit cell FE simulations with various interleave patterns; it was observed that the normal compressive strain around the rubber particle is around 1.8% (Fig. 5a, b). In the vicinity of the ply, outer fibrils closer to the interleave resin region experimental normal compressive strain in the laminate thickness direction is approximately around 0.8%. From FE analysis, local compressive strain varies between 0.7 and 0.8% at the ply outer fibrils closer to the resin (marked regions in Fig. 5).

From the experimental DIC results, within the ply the observed local strain values are similar to the applied far-field compressive strain. As shown in Fig. 6, from FE analysis of the unit cell it was observed that the local compressive strain within the fiber is almost negligible. Moreover, between the fibers in the laminate thickness (*y*) direction, local compressive strain in the resin is approximately 1.0%. In the unit cell width direction (*x*-dir), between the fibers, local compressive strain of approximately 0.5% is observed. The obtained strain difference between different constituent materials of the ply is not observed in DIC. This is due to the fact that DIC averages the strain within the ply.
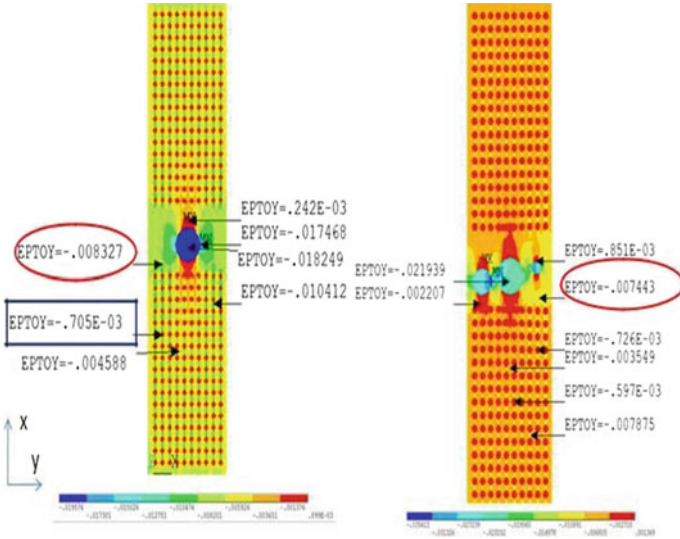
Fig. 5 Normal compressive strain in *y*-direction (laminate thickness direction)

Fig. 6 Local strain variation within the ply
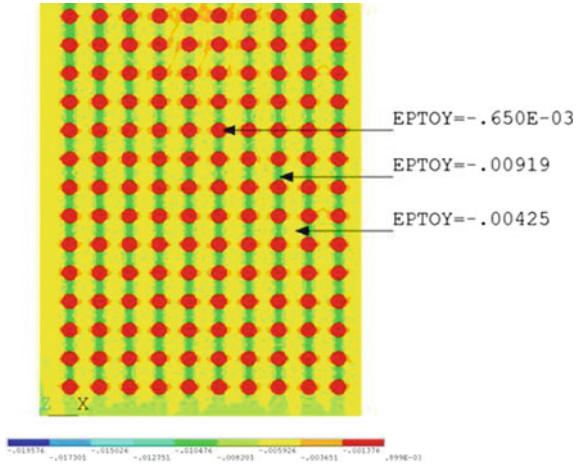
4 Conclusion

In order to experimentally evaluate the local strain profiles in a carbon fiber-reinforced composites under flatwise compression load, DIC technique was used. Contrast to the regular paint speckle pattern, composite microstructure is used for correlating the strains. Following the experimental study, numerical FE analysis is conducted using different unit cells with varying interleave resin layer geometries. Experimental and numerical local strain analyses lead to the following conclusions:

(1) Employed novel experimental methodology using composite microstructure as a speckle pattern to correlate the local strains was able to accurately capture the strain variation between the interleave resin region and the ply outer boundary.

(2) Qualitatively, both FEA and experimental local strain profiles show that the maximum normal compressive strain in the load direction occurs at the rubber particles. However, quantitatively, large difference was observed between the experimental (1.0%) and FE strain (1.7%) values.

(3) The above observed strain difference between DIC and FEA at rubber particle can be attributed to the chosen elastic properties for computations. In FEA, rubber particle elastic module was chosen as 4 MPa. While in reality, due to impregnation with epoxy, effective elastic modules of rubber particle can be higher than 4 MPa.

(4) Within the ply, probed DIC local strain values are similar to the applied far-field global strain. However, FE local strains in the ply indicate three distinct strain patterns. The observed strain difference between FEA and experiment can be attributed to the lack of appropriate speckle pattern between the fibers to correlate the local strains in DIC. This leads to the averaging of the strains within the ply.

References

1. Cs. Varga, N. Miskolczi, L. Bartha and G. Lipóczi, Improving the mechanical properties of glass-fiber-reinforced polyester composites by modification of fiber surface, *Materials & Design*, 31(2010) 185–193.

2. L.P. Canal, C. González, J.M. Molina-Aldareguía, J. Segurado and J. LLorca, Application of digital image correlation at the microscale in fiber-reinforced composites, *Composites Part A: Applied Science and Manufacturing,* 43(2012) 1630–1638.

3. M. Mehdikhani, M. A. Aravand, B. Sabuncuoglu, M. G. Callens, S. V. Lomov and L. Gorbatikh, Full-field strain measurements at the micro-scale in fiber-reinforced composites using digital image correlation, *Composite Structures,* 140(2016) 192–201.

4. M. Mehdikhani, A. Matveeva, M. Ali Aravand, B. L. Wardle, S. V. Lomov and L. Gorbatikh, Strain mapping at the micro-scale in hierarchical polymer composites with aligned carbon nanotube grafted fibers, *Composites Science and Technology,* 137(2016) 24–34.

5. S. J. Hooper, Composite materials testing and design, *ASTM 1998*, 13(1998), ISBN-13: 978-0803124783.

6. D. Koblar, J. Škofic and M. Boltežar, Evaluation of the Young's modulus of Rubber-Like Materials Bonded to Rigid Surfaces with Respect to Poisson's Ratio, *Strojniški vestnik - Journal of Mechanical Engineering,* 60(2014) 506–511.

7. S. Daggumati, E. Voet, W. Van Paepegem, J. Degrieck, J. Xu, S.V. Lomov and I. Verpoest, Local strain in a 5-harness satin weave composite under static tension: Part I – Experimental analysis, *In Composites Science and Technology,* 71(2011) 1171–1179.

8. S. Daggumati, K. Sriram, S. Subramanian and J. Dustin, Multiscale strain measurement using digital image correlation, *Comptest-2015. IMDEA Materials,* Spain, March 2015.

9. A. Arteiro, G. Catalanotti, A. R. Melro, P. Linde and P. P. Camanho, Micro-mechanical analysis of the in situ effect in polymer composite laminates, *Composite Structures,* 116(2014) 827–840.
10. S. Daggumati, W. V. Paepegem, J. Degrieck, J. Xu, S.V. Lomov and I. Verpoest, Local damage in a 5-harness satin weave composite under static tension: Part II – Meso-FE modelling, *Composites Science and Technology,* 70(2010)1934–1941.

Atomic Force Microscopic Characterization of Wire Electrical Discharge Machined Samples

**Hulas Raj Tonday, Pravin Kumar Singh
and Anand Mukut Tigga**

Nomenclature

EDM	Electrical discharge machining
S_a	Surface roughness
ANOVA	Analysis of variance
SS	Sums of squares
MS	Mean of square
F	Fisher's ratio
DF	Degree of freedom
AFM	Atomic force microscope

1 Introduction

Wire EDM is a rival replacement of outmoded machining methods to cut Ni-based, Ti-based superalloys, hardened alloys, WC, and MMCs. In wire EDM, the hot plasma melts tiny pieces from the workpart by applying electro-thermal energy, and then, debris is flushed out by the deionized water [1, 2]. Spedding and Wang [3] evaluated the cutting speed, surface waviness, and surface roughness in wire electrical discharge machining of AISI 420 material. Altug et al. [4] have performed the optimization of parameters of wire electrical discharge machining of Ti6Al4V with the objective of minimizing the kerf width. Various types of heat treatments have been performed

H. R. Tonday (✉) · A. M. Tigga
Department of Manufacturing Engineering, NIT Jamshedpur, NIT Campus, Adityapur 831014, Jharkhand, India
e-mail: hulasnifft.13@gmail.com

P. K. Singh
Department of Mechanical Engineering, AMITY University, Ranchi, India

on workpiece to obtain good microstructure and mechanical properties before wire electrical discharge machining. Hoang and Yang [5] proposed a dry microwire EDM technique in which liquid dielectric is substituted by high-pressure air injection. They have used this method in machining the Ti6Al4V alloy. Aggarwal et al. [6] focused on modeling of input factors of wire EDM process during cutting of Inconel 718 for augmentation of cutting rate and decreasing S_a. They opted spark voltage, on time, off time, wire feed, pulse current, and wire tension as input factors and developed analytical models through multi-response optimization technique. Many of the authors have not studied surface topography and surface morphology of machined samples and effects of machining variables on surface topography. In the current work, the influence of machining factors on surface topography and roughness has been analyzed by using AFM.

2 Materials and Methods

The superalloy Ti6Al4V is exploited as a specimen material as it contains essential characteristics, viz. improved ductility, yield strength, fracture toughness, excellent biocompatibility, wear resistance, and corrosion resistance. This alloy has broad uses in automotive, marine appliances, vessels, medical implants, and airframes. Therefore, the analysis of surface characteristics of Ti6Al4V is significant in recent years [3, 5].

In the present work, Fanuc ROBOCUT CNC wire EDM machine is utilized for cutting the samples of desired shape and size. The brass wire of 0.25 mm diameter is used as an electrode wire, and deionized water is used as a dielectric liquid during cutting operation. The four cutting parameters, namely T_{on}, T_{off}, WT, and VM, have been chosen for statistical analysis, and others have the default values of the machine tool. An atomic force microscope, make of NT-MDT, SOLVER PRO, SPM, Russia, has been employed for surface characterization of Ti6Al4V samples [7, 8].

3 Results and Discussions

In this experimental study, the selected input variables of wire EDM process are T_{on}, T_{off}, WT, and VM, and the output variable is S_a for machining of Ti6Al4V. The input parameters and concerned levels have been shown in Table 1 to set up the design of experiments. Taguchi method has been utilized for creating an L_{16} orthogonal arrays design of input parameters as shown in Table 2, and sixteen numbers of cutting operations have been conducted. After cutting operation, response parameter S_a has been recorded for each sample as illustrated in Table 2. During Taguchi analysis and ANOVA examination of S_a data, smaller is better criterion has been used as the goal is to minimize the S_a values of machined specimens. Table 3 presents the aftereffect of ANOVA test for S/N ratios of S_a values and denotes that VM is the crucial input

Table 1 Cutting parameters of wire EDM process and corresponding levels

Number	Input parameters	Unit	Level 1	Level 2
1	T_{on}	μs	7	11
2	T_{off}	μs	5	8
3	WT	Gram-force	1310	1340
4	VM	V	6	10

Table 2 Design of experiments using Taguchi's L_{16} orthogonal arrays and experimental results

Run	T_{on}	T_{off}	WT	VM	S_a
1	7	5	1310	6	3.22
2	7	5	1310	10	3.84
3	7	5	1340	6	2.94
4	7	5	1340	10	2.46
5	7	8	1310	6	2.59
6	7	8	1310	10	3.98
7	7	8	1340	6	2.89
8	7	8	1340	10	2.87
9	11	5	1310	6	2.61
10	11	5	1310	10	3.08
11	11	5	1340	6	2.69
12	11	5	1340	10	3.58
13	11	8	1310	6	4.06
14	11	8	1310	10	4.21
15	11	8	1340	6	2.55
16	11	8	1340	10	4.37

Table 3 ANOVA results for means of surface roughness

Source	DF	SS	MS	F	P
Ton	1	2.034	2.034	0.92	0.359
Toff	1	3.45	3.45	1.55	0.239
WT	1	4.723	4.723	2.13	0.173
VM	1	9.871	9.871	4.44	0.004
Residual error	11	24.445	2.222		
Total	15	44.524			

parameter because it consists of the highest F-value. The main effects plot of S_a, shown in Fig. 1, demonstrates that mean of *S/N* ratios of S_a increases with the rise of VM as it is the most significant cutting variable.

An atomic force microscope has been utilized to characterize the surface topography and surface morphology of machined samples in nanoscales [9]. In this research, sample-4 and sample-16 are considered for topography examination as these samples
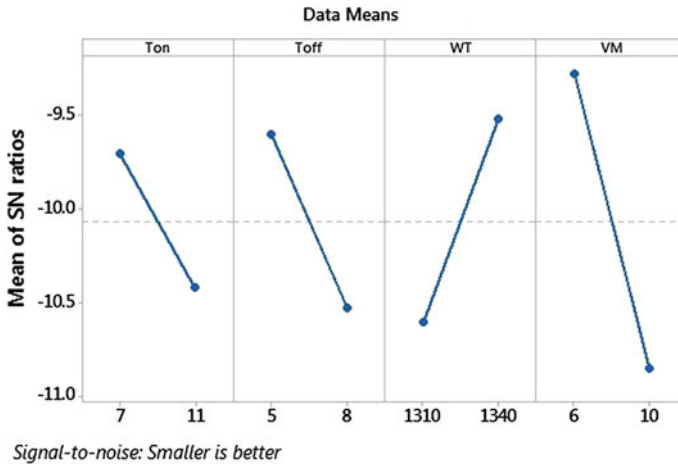
Fig. 1 Main effects plot for S/N ratios of surface roughness

exhibit minimum S_a (2.46 μm) and maximum S_a (4.37 μm), respectively. Figure 2a, b shows the 2-D and 3-D topography image of sample-4 obtained by AFM technique. In these figures, surface height features, ridges, and mounds on sample surface have been clearly illustrated [8, 9]. The cross-sectional profile along the horizontal line on image has been shown in Fig. 3 after analysis by NOVA software. For sample-4, the values of surface parameters such as maximum height, ten point height, average roughness, skewness, second moment, and kurtosis have been acquired as shown in Table 4. Figure 4a, b demonstrates the 2-D and 3-D topography image of the surface of the sample-16. Again, the cross-sectional profile along the horizontal line on image has been shown in Fig. 5. In Table 5, values of surface parameters of sample-16 have been presented in nanoscale. When the results of AFM analysis for sample-4 and sample-16 are compared, it has been detected that both Figs. 3 and 5 possesses different surface features, picks, and valleys at different positions, which indicates that the samples prepared by feeding different cutting parameter set exhibit diverse surface characteristics [7, 8]. It has been also found, after comparing the values of Tables 4 and 5, that the sample-4 comprises lower values of surface parameters rather than sample-16, which is desirable as per the research objective. The AFM results also imply that the cutting factors of wire EDM significantly influences the surface characteristics of machined samples.

4 Conclusion

As per the empirical study of Ti6Al4V specimens produced by wire EDM process and surface analysis by AFM, the following conclusions have been drawn:
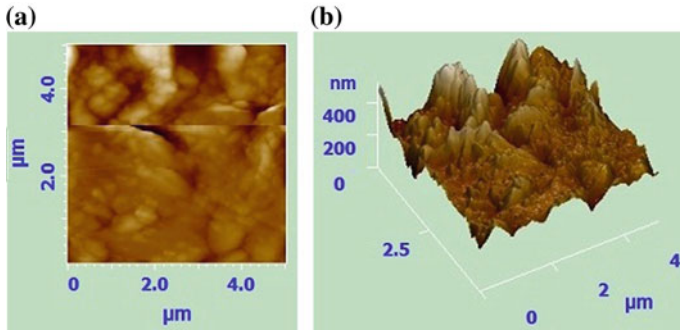
Fig. 2 AFM images of surface topography of sample-4 **a** flatten corrected 2-D image, **b** 3-D image

Fig. 3 Cross-sectional profiles of AFM image of sample-4 **a** horizontal line and **b** related cross-sectional profile graph

Table 4 Surface parameters and related results obtained by AFM analysis of sample-4

Number	Surface parameter	AFM results
1	Maximum height	370.015 nm
2	Minimum height	0.0 nm
3	Peak-to-peak distance	370.015 nm
4	Ten point height	189.008 nm
5	Average roughness	193.748 nm
6	Root-mean-square	27.434 nm
7	Surface skewness	−0.164
8	Kurtosis	1.288

1. It has been found that the experiment number-4 exhibits the minimum surface roughness ($S_a = 2.46\ \mu m$).
2. It has been revealed from ANOVA table that machining voltage (VM) has the greatest impact on S_a.
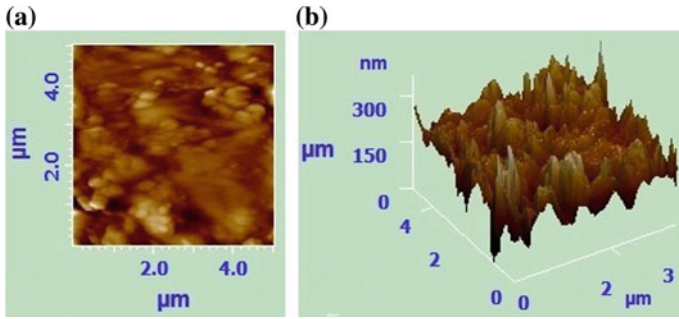
Fig. 4 AFM images of surface topography of sample-16 **a** flatten corrected 2-D image, **b** 3-D image
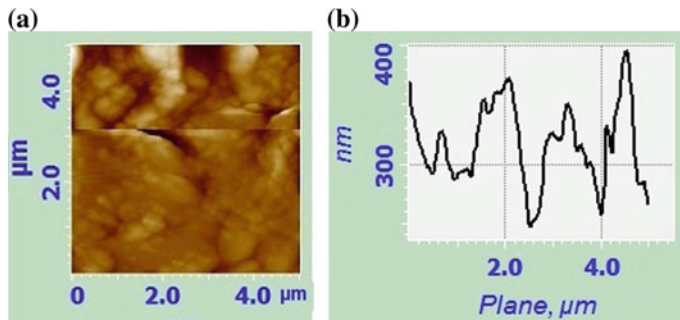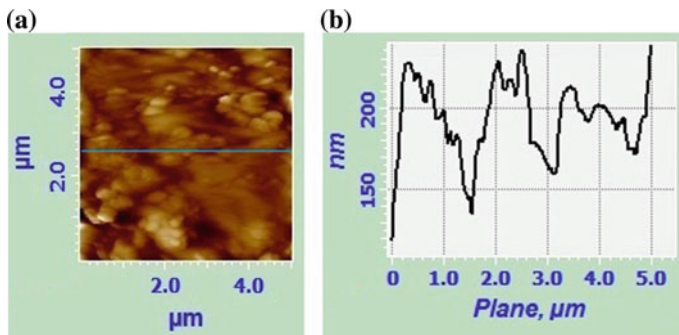

Fig. 5 Cross-section profiles of AFM image of sample-16 **a** horizontal line and **b** related cross-sectional profile graph

Table 5 Surface parameters and related results obtained by AFM analysis of sample-16

Number	Surface parameter	AFM results
1	Maximum height	551.066 nm
2	Minimum height	0.0 nm
3	Peak-to-peak distance	551.066 nm
4	Ten point height	280.35 nm
5	Average roughness	45.42 nm
6	Root-mean-square	60.536 nm
7	Surface skewness	−0.386
8	Kurtosis	4.562

3. This study describes that the surface integrity varies with the changes in machining parameters.
4. The values of surface parameters are in the considerable range of standard values.

5. The capability of wire EDM process in terms of generating considerable surface topography in nanoscales has been evidenced by AFM images.

References

1. S. Sarkar, S. Mitra, B. Bhattacharyya, Parametric analysis and optimization of wire electrical discharge machining of γ-titanium aluminide alloy, J. Mater. Process. Technol. 159 (2005) 286–294. https://doi.org/10.1016/j.jmatprotec.2004.10.009.
2. S. Shakeri, A. Ghassemi, M. Hassani, Investigation of material removal rate and surface roughness in wire electrical discharge machining process for cementation alloy steel using artificial neural network, Int. J. Adv. Manuf. Technol. 82 (2016) 549–557. https://doi.org/10.1007/s00170-015-7349-y.
3. T. A. Spedding, Z. Q. Wang, Parametric optimization and surface characterization of wire electrical discharge machining process, *Precis. Eng.* 20 (1997) 5–15.
4. M. Altug, M. Erdem, C. Ozay, Experimental investigation of kerf of Ti6Al4V exposed to different heat treatment processes in WEDM and optimization of parameters using genetic algorithm, Int. J. Adv. Manuf. Technol. 78 (2015) 1573–1583. https://doi.org/10.1007/s00170-014-6702-x.
5. K.T. Hoang, S.H. Yang, Kerf analysis and control in dry micro-wire electrical discharge machining, Int. J. Adv. Manuf. Technol. 78 (2015) 1803–1812.
6. V. Aggarwal, S.S. Khangura, R.K. Garg, Parametric modeling and optimization for wire electrical discharge machining of Inconel 718 using response surface methodology, Int. J. Adv. Manuf. Technol. 79 (2015) 31–47. https://doi.org/10.1007/s00170-015-6797-8.
7. C.R.A. Valois, L.P. Silva, R.B. Azevedo, Multiple Autoclave Cycles Affect the Surface of Rotary Nickel-Titanium Files : An Atomic Force Microscopy Study, J. Endodontics 34 (2008) 859–862. https://doi.org/10.1016/j.joen.2008.02.028.
8. S. Gebhard, F. Pyczak, M. Göken, Microstructural and micromechanical characterisation of TiAl alloys using atomic force microscopy and nanoindentation, Mater. Sci. Eng. 523 (2009) 235–241. https://doi.org/10.1016/j.msea.2009.05.068.
9. S. Sevim, S. Tolunay, H. Torun, Micromachined sample stages to reduce thermal drift in atomic force microscopy, Microsyst. Technol. 21 (2015) 1559–1566. https://doi.org/10.1007/s00542-014-2251-3.

Friction Stir Welding of Steels—A Localized Thermo-mechanical Processing Technique for Producing Ultrafine-Grained Structures

Md Anwar Ali Anshari and Murshid Imam

1 Introduction

Motivated by increasing demand of ultrafine-grained (UFG) steels in structural applications, various thermo-mechanical processing methods like high-pressure torsion, equal channel angular pressing (ECAP), and accumulative roll bonding have been considered to be promising routes as reported by Tsuji and Maki [1] and Imam et al. [2]. In addition to the various thermo-mechanical processing methods, the recent application of friction stir welding (FSW) in producing ultrafine-grained steels has drawn significant attention. This interest mainly involves the potential applications of UFG structures in the transport and aerospace industries in the fabrication of structural parts, as reported by Fang et al. [3]. Moreover, Nandan et al. [4] and Imam et al. [5] showed that in FSW, the heat generation from toolpiece/workpiece interaction causes the formation of refined and equiaxed grain structures because of the inherently involved severe plastic deformation as well as transients and gradients of strain, strain rate, and temperature. The formation of fine grains is sensitive to the process parameters such as peak temperature, cooling, and strain rates. It has been reported that as a result of post-stirring annealing effect, the grain size increases up to 2–3 μm during weld cooling cycle [6]. Recently, Fujii et al. [7] and Imam et al. [2] suggested that an external forced cooling during FSW is beneficial to avoid the abnormal growth of refined microstructure. Therefore, the main goal of present work is to develop the fundamental understanding of the effect of external cooling on the plastic flow and the resulting microstructural features. It is also believed that this work will provide the framework for industries looking for the development of nano-grained or at least sub-micrometer-grained structures by using current practice of controlling the post-stirring annealing effect during the weld cooling cycle.

M. A. A. Anshari · M. Imam (✉)
Mechanical Engineering Department, Indian Institute of Technology Patna, Bihta 801103, India
e-mail: murshid@iitp.ac.in

2   Experimental Work

In the present work, iron of 99.9 wt% purity and medium carbon S45C steel (0.45 wt% carbon) each of 2 mm thickness were used as work materials. External forced cooling was done with the stream of liquid CO_2 along the weld centerline during welding. For the microstructural analysis of the FSW joints, scanning electron microscopy (SEM) and the electron backscatter diffraction (EBSD) techniques were used. EBSD measurement was done by using the field emission-type scanning electron microscope (FE-SEM, model: JSM-7001FA) operated at 25 kV. Electro-polishing with the electrolyte, a solution of 20 ml $HClO_4$ and 180 ml CH_3COOH, at 10 °C was done to polish the sample. The polished weld cross section was then used to measure the microhardness using a Vickers's microhardness tester at a load of 200 gf with 10 s of dwell time.

3   Results and Discussion

Due to the solid-state nature of welding, FSW process produces higher quality welds with high strength, low-distortion, reduced cost, lower environmental impact, and avoiding solidification problems. These inherent qualities of FSW process prove to be potentially attractive to many industries. It has a potential to become an alternative to fusion welding for steels in many critical industrial applications. However, the key issues in the adoption of the FSW for steels are the selection of tool materials and the occurrence of phase transformation which make the process more complex when compared with the FSW of aluminum alloys. In order to achieve the real potential of FSW for producing the ultrafine ferrite grained steels, it is necessary that the peak temperatures in the stir zone should be less than the phase transformation temperatures. Therefore, the choice of the selection of process parameters plays a vital role in producing UFG steels during FSW process. In the present case, the welds were obtained below A_1 phase transformation temperature as shown in Fig. 1a. For the case of commercially pure iron, the phase change is expected to occur above 912 °C, and for the case of medium carbon S45C steel, it is expected to occur above A_1 phase transformation temperature. To this end, FSW is proposed to use with controlled input parameters along with external cooling to achieve the ultrafine-grained structure as shown by schematic diagram in Fig. 1b. Note that ultrafine-grained steels structures are highly required for high strength and ductility combination applications. Therefore, the present approach is believed to be an effective and beneficial method for the iron and steel industries. Figure 2a, b shows the SEM image and orientation color map of S45C steel and pure iron, respectively, before processing. Figure 2a clearly shows the presence of ferrite and pearlite structures which is typical for plain carbon steel, while in the case of pure iron, the presence of ferrite grains is obvious as shown in Fig. 2b. The orientation color map of EBSD with stereographic triangle shown in Fig. 3 is indicating the crystallographic orientation of the
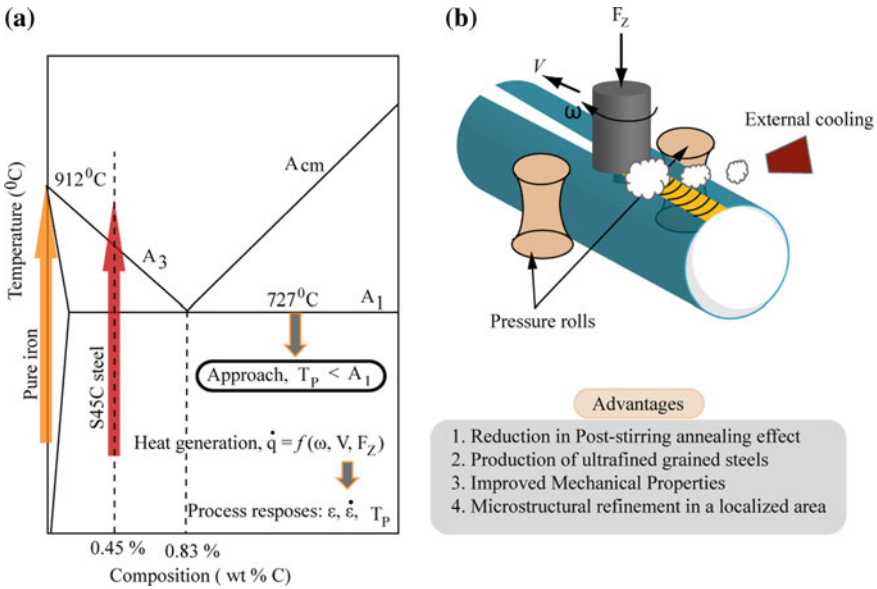
Fig. 1 Schematics showing **a** iron–carbon diagram and **b** friction stir welding process with external cooling approach. Note that ω, V, and F_z are speed of rotation, speed of welding, and axial loading, while ε, $\dot{\varepsilon}$, and T_p are strain, strain rate, and peak temperature (commonly known as process responses), respectively

ferrite grains parallel to the sample normal direction. In case of pure iron, it is worth noting that each basic building block is an individual atom of iron (Fe) which is called a body-centered cubic (bcc) structure at room temperature. On heating pure iron up to 912 °C, spontaneous changes occur in the crystal structure in the form of transformation of bcc to face-centered cubic (fcc) structure, commonly known as austenite. On the other hand, the presence of distributed cementite lamina in ferrite proves to be one of the critical factors affecting the tensile properties of the medium carbon S45C steel as it is closely related to the measure of carbon in steel. Also, in the case of S45C steel, the formation of austenite starts above 723 °C, i.e., A_1 phase transformation temperature. Therefore, the selection of process parameters is done in such a way that the peak temperatures during welding in the case of pure iron should not exceed 912 °C and in the case of medium carbon S45C steel should not exceed above A_1 transformation temperature. Chemical composition of material and processes parameters used in the present work for both the cases are shown in Tables 1 and 2.

The orientation color map of EBSD and SEM image obtained at the center are shown in Fig. 3a, b, respectively. In both the cases, the whole stir zone shows the formation of ultrafine ferrite grained steels, which ensure the peak temperatures in the stir zone below 912 °C and A_1 transformation temperatures. The average grain size of ferrite is observed to be less than 1.5 μm in the case of S45C medium
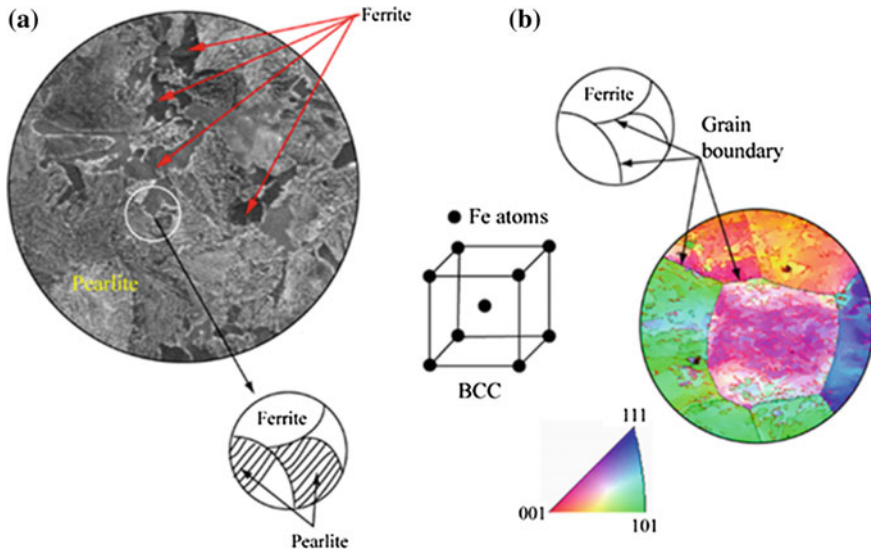
Fig. 2 Base material microstructures **a** S45C steel and **b** pure iron

Table 1 Composition of work materials

Type of material	Elements (wt%)						References
	S	P	Si	C	Mn	Fe	
S45C steel	0.004	0.008	0.220	0.450	0.820	Bal	[2]
Pure iron	–	–	–	–	–	99.9	[8]

Table 2 Welding process parameters

Material type	Welding condition	Sheet thickness (mm)	Speed of rotation (rpm)	Speed of welding (mm/min)	Axial loading (KN)	Weld quality	References
Pure iron	Liquid CO_2 rapid cooling	2	200	100	18	No defect	[8]
545C	Liquid CO_2 rapid cooling	2	100	100	35	No defect	[2]

carbon steel. It is important to note that smaller the particle size of cementite due to rapid cooling restrains the migration of grain boundaries due to Zener pinning effect as reported by Song et al. [9]. This effect further stabilizes ultrafine grains during post-stir annealing. Therefore, the achieving homogeneous distribution of fine cementite particles is another important advantage of external cooling which
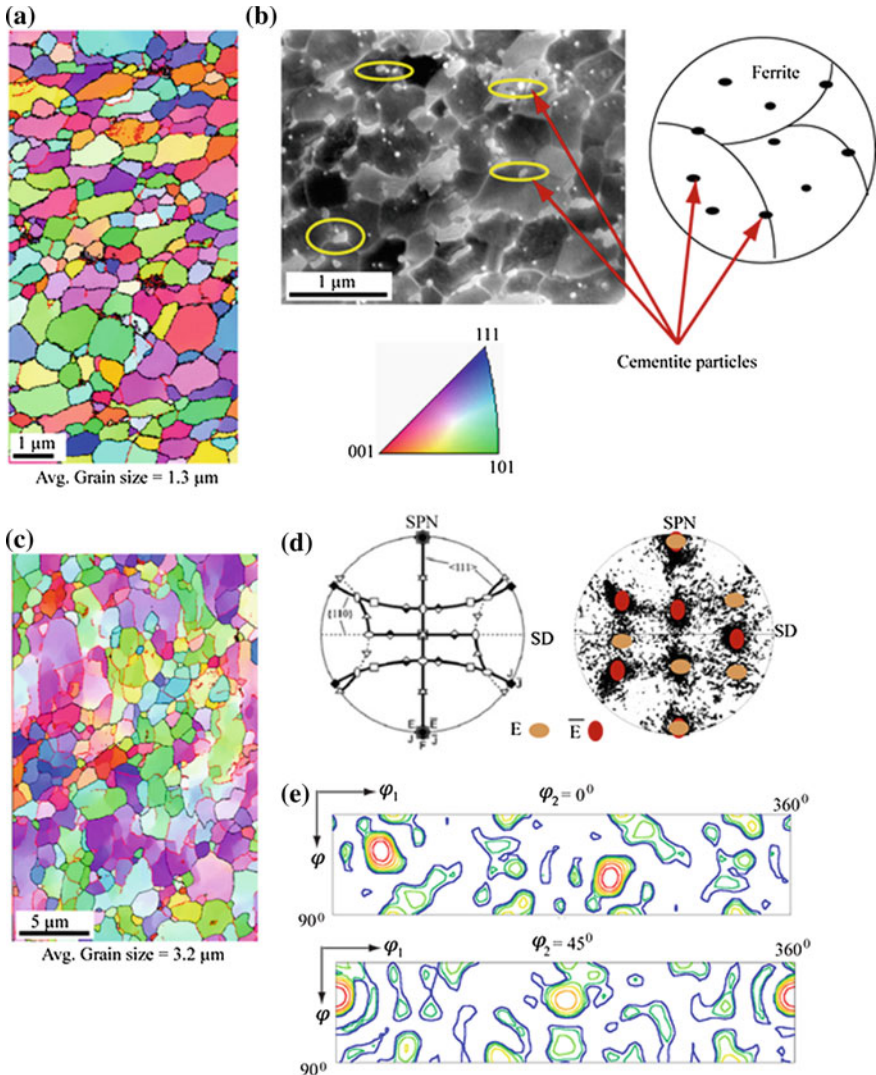
Fig. 3 **a**, **b** EBSD orientation color map and SEM microstructure showing grain structure evolution and distribution of cementite particles in the case of S45C steel, **c–e** EBSD orientation color map, (110) pole figure representing the ideal orientations as well as fiber textures associated with simple shear deformation of bcc structure and $\phi_2 = 0°$ and 45° ODF sections [2, 8], respectively

is the key factor to enhance ductility of the FSW joints. On the other hand, EBSD orientation color map and crystallographic textures represented by (110) discrete pole figure and $\phi_2 = 0°$ and 45° sections of the orientation distribution function (ODF) which is plotted in Euler space using Bunge notations are shown in Fig. 3c–e. The presence of fine grains can be clearly seen from the orientation color map of EBSD in

Fig. 4 Vickers's
microhardness profiles
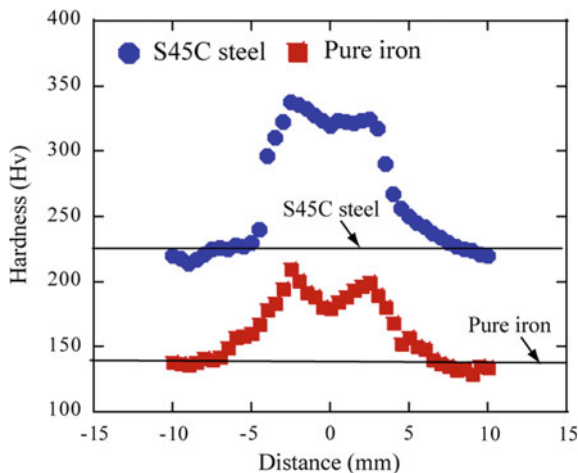obtained at the weld center in
the case of S45C steel and
pure iron

Fig. 3c. Crystallographic texture component formed with ten characteristic poles are
matching with the projections of $E(110)[1\bar{1}\bar{1}]$ and $\bar{E}(\bar{1}10)[\bar{1}11]$ ideal simple shear
texture components reasonably well, in accordance with the adopted convention as
shown in Fig. 3d, e.

A comparison of Vickers's microhardness plots at midsection of welds obtained
in both the cases is shown in Fig. 4. The average stir zone hardness in the case of
S45C steel is about 118 Hv higher than base metal, while in the case of pure iron,
the average hardness is about 40 Hv higher than the base metal. Such an increment
in average hardness has direct connection with the formation of the ultrafine grain
size in both the cases. However, it is important to note that in the case of S45C steel,
the higher hardness in the SZ can also be attributed to the dispersion strengthening
of the fine cementite particles along with ultrafine grained. The finely dispersed
particles of cementite have potential to maintain an improved work hardening rate
even when they contain an ultrafine ferritic grain structure as in the current case. A
model suggested by Ashby allows the estimation of the extra work hardening, $\Delta\sigma$,
caused by dislocations accumulation at particles [9, 10],

$$\Delta\sigma = M^{3/2}DG\left(\frac{bf\varepsilon_t}{2r}\right)^{1/2} \qquad (1)$$

where $M, G, b, f, r, \varepsilon_t$, and D refer to Taylor factor, shear modulus of iron, magnitude
of the Burgers vector, volume fraction of particles, average radius of particle, true
strain, and a constant obtained from the slope of the linear portion of the stress incre-
ment versus $\varepsilon_t^{1/2}$ [9], respectively. Note that the magnitude of D decreases with the
increase of thermally activated plastic relaxation and/or diffusion-controlled disloca-
tion rearrangement and annihilation as the recovery process proceeds simultaneously
during welding. At higher temperatures and lower strain rates, it is most likely that
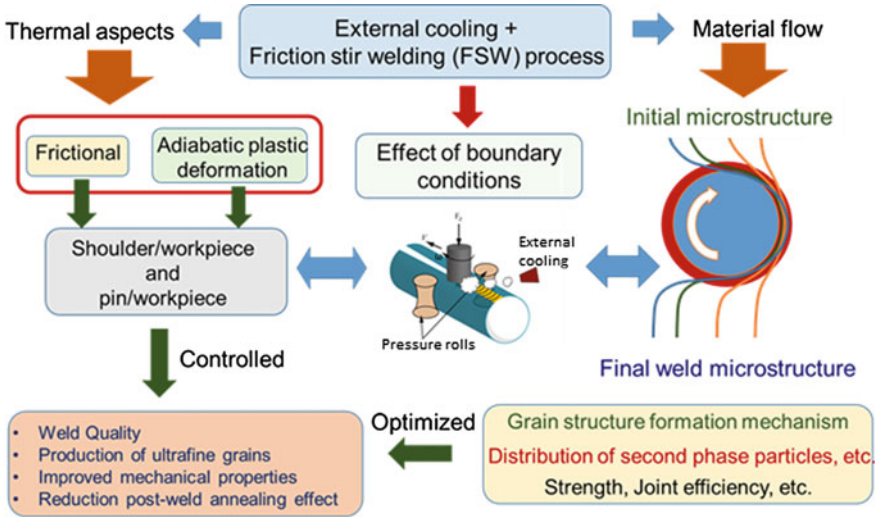
Fig. 5 Schematic illustration of the fundamental understanding of the scientific approach for the use of external cooling and its effect on the FSW welds

particle hardening increases the yield stress but comparatively has little effect on work hardening [11].

4   Conclusions

Ultrafine ferrite grains are obtained for pure iron and medium carbon S45C steel by using the approach of external cooling during FSW process. The underlying physics of the scientific approach for producing ultrafine-grained microstructures using external cooling during FSW process is summarized in Fig. 5. The homogeneously distributed fine cementite particles in the case of S45C steel play a vital role in stabilizing the refined microstructures. Also, the presence of fine cementite is fruitful in the improvement of work hardening rate which can be explained in terms of the geometrically necessary dislocations accumulation around these cementite particles. As a result, improved tensile strength–ductility combination at room temperature of the ultrafine-grained steels even with different sizes of ferrite grains is expected.

Therefore, the approach presented in this work can be particularly attractive to develop ultrafine-grained steels together with the ferrite matrix containing a high volume fraction of fine particles.

References

1. Tsuji N, Maki T. Enhanced structural refinement by combining phase transformation and plastic deformation in steels. Scripta Materialia 2009; 60 (12): 1044–1049.
2. Imam M, Ueji R, Fujii H. Effect of online rapid cooling on microstructure and mechanical properties of friction stir welded medium carbon steel. Journal of Materials Processing Technology 2016; 230: 62–71.
3. Fang F, Hu X, Zhang B, Xie Z, Jiang J. Deformation of dual-structure medium carbon steel in cold drawing. Material Science and Engineering A 2013; 583:78–83.
4. Nandan, R., Debroy, T., Bhadeshia, H.K.D.H., 2008. Recent advances in friction-stir welding – process, weldment structure and properties. Progress in Material Science 53 (6), 980–1023.
5. Imam M, Racherla V, Biswas K, Fujii H, Chintapenta V, Sun YF, Morisada Y. Microstructure-property relation and evolution in friction stir welding of naturally aged 6063 aluminium alloy. The International Journal of Advanced Manufacturing Technology 2017; 91(5–8):1753–1769.
6. Khodabakhshi F, Gerlich AP, Simchi A, Kokabi AH. Cryogenic friction-stir processing of ultrafine-grained Al–Mg–TiO_2 nanocomposites. Materials Science & Engineering A 2015; 620: 471–482.
7. Fujii F, Chung YD, Sun YF. Friction stir welding of AISI 1080 steel using liquid CO_2 for enhanced toughness and ductility. Science and Technology of Welding and Joining 2013; 18 (6), 500–506.
8. Imam M, Sun Y, Fujii H. Interface controlled plastic flow using accelerated cooling in friction stir welding of pure iron. National meetings of JWS June 30 2017, Tokyo.
9. Song R, Ponge D, Raabe D, Improvement of the work hardening rate of ultrafine grained steels through second phase particles. ScriptaMaterialia 2005; 52(11): 1075–1080.
10. Song R, Ponge D, Raabe D, Speer JG, Matlock DK. Overview of processing, microstructure and mechanical properties of ultrafine grained bcc steels. Material Science and Engineering A 2006, 441:1–17.
11. Kosco JB,Koss DA. Work hardening of mechanically alloyed Fe-Y203 alloys. Materials Science and Engineering A 1993;169:1–7.

A Review on Flexibility and Reconfigurability in Manufacturing System

Durga Prasad and S. C. Jayswal

1 Introduction

In present time, the manufacturing environment has become highly uncertain, and it is continuously changing. It has shorter life cycles of products and technologies, shorter delivery time, increased level of customization at the price of the standard product, increased product variety, quality as well as demand variability, and intense global competition. Academicians, as well as practitioners, agree that uncertainty will continue to grow in the twenty-first century [1–3]. Due to the advancement of technologies, complexity is generated and it generates the uncertainty [4]. To deal with uncertainty, flexibility is required. It has become one of the most necessary and useful tools in unpredictable markets [1].

A lot of flexibility in the system increases the complexity and cost. Therefore, the concept of reconfigurability with customized flexibility has emerged. The systems which have reconfigurability are known as reconfigurable manufacturing systems (RMSs). Reconfigurable manufacturing systems have capacity and functions required for a part family; then, these are reconfigured for another part family when a need arises. Reconfigurability is the ability of a manufacturing system which is used to adjust functions and capacity of the system or machine at low cost and time. A reconfigurable manufacturing system has flexibility, but it is customized [5–8].

Since these two terms, flexibility and reconfigurability, are important properties of a manufacturing system, therefore there is a need to discuss and differentiate these. The intention of this article is to provide a clear understanding of flexibility and reconfigurability so that it should become clear that what is the need and what is the

D. Prasad (✉) · S. C. Jayswal
Mechanical Engineering Department, Madan Mohan Malaviya University of Technology, Gorakhpur 273010, Uttar Pradesh, India
e-mail: dp.mmmut@gmail.com; durgaprasad_rsme@mmmut.ac.in

S. C. Jayswal
e-mail: scjme@mmmut.ac.in

difference between the both. Further, this paper discusses the concepts of FMS and RMS and compares both.

2 Literature Review

A lot of authors have worked on flexibility. Some of the researchers are Vokurka and O'Leary-Kelly [9], Buzacott and Mandelbaum [10], Bernardes and Hanna [11], Jain et al. [1], Pérez et al. [12], Alexopoulos et al. [13], Chou et al. [14], Chang [15], Fernandes et al. [16], Urtasun et al. [3], etc.

Vokurka and O'Leary-Kelly [9] reviewed the empirical research done for flexibility in manufacturing system. Alexopoulos et al. [13] discussed a method to estimate the flexibility. The concept was based on dynamic behavior analogy between manufacturing system and mechanical system. Buzacott and Mandelbaum [10] defined three aspects of the flexibility: prior flexibility, state flexibility, and action flexibility.

Bernardes and Hanna [11] reviewed flexibility, responsiveness, and agility. Chou et al. [14] discussed the effects of range and response dimension in process flexible structure. Chang [15] discussed the degree of environmental uncertainty and flexibility improvement in uncertainty. Fernandes et al. [16] proposed a model to support firms making important investment decisions associated with the acquisition of new equipment aimed at allowing firms to increase their manufacturing flexibility to produce both standard and customized products.

Jain et al. [1] reviewed manufacturing flexibility and various issues especially need, concept, measurement, dimensions, etc. Barad [17] described two modeling perspectives of flexibility: bottom-up perspective and top-down perspective. Urtasun et al. [3] discussed the relation between human resource management practices and manufacturing flexibility. Pérez et al. [12] reviewed manufacturing flexibility.

Many researchers have worked on reconfigurable manufacturing system. The concept of RMS has been proposed by Koren and Ulsoy [8]. A survey report on FMS has been presented by Hytler and Ulsoy during 1997 in Engineering Research Center (ERC) for RMS. The details of the survey have been given in [18]. The report describes that many industries are not adapting FMS because it is too expensive and complex. Elmaraghy [19] compared FMS and RMS. This paper also described the opinions of the experts on FMS and RMS. Lee [20] has given some relocation rules for machines. Galan et al. [21] presented a methodology for the selection of part family. Prasad and Jayswal [5, 22] considered reconfigurability in the manufacturing industry. Puik et al. [23] proposed a method to compare alternatives to implement reconfigurations considering resources and lead time.

Gu et al. [24] defined throughput settling time, production loss, and total underproduction time. System resilience was measured, and measured values were used for designing of RMS. The designing factors used were system configuration, buffer capacity, and level of redundancy. Effect of the factors on system resilience was investigated. Dahane and Benyoucef [25] proposed a mathematical model for machine selection problem for machine reliability constraints. Goyal et al. [26] proposed

methods to measure operational capability and reconfigurability of the reconfigurable machine tool (RMT). The developed performance index along with cost was considered for machine assignment. The problem was solved by using NSGA-II and TOPSIS. Hasan et al. [27] used the concept of bowl phenomenon for RMS planning.

In the literature related to flexibility, all the authors have described the need for flexibility and literature related to reconfiguration, and researchers have described the need for reconfigurability. Therefore, from all the literature, it becomes clear that there is a need of both flexibility and reconfigurability in the manufacturing system. Flexibility is required to deal with uncertainty, and lot of flexibility increases the cost and complexity of the system.

3 Flexibility

Flexibility is a wide concept, and its meaning changes in different contexts. Early definitions of flexibility in manufacturing system were based on the adaptability of the system to uncertainties [28, 29]. Many definitions have been given about flexibility. Mascarenhas [30] defined it as "the ability of a manufacturing system to cope with changing circumstances or instability caused by the environment" [30, 31]. Cox [32] defines it as "the quickness and ease with which plants can respond to changes in market conditions." Nagarur [33] defines it as "the ability of the system to quickly adjust to any change in relevant factors like product, process, loads and machine failure." However, a more comprehensive definition might be "the ability to change or react with little penalty in time, effort, cost or performance" [34].

More flexibility in a manufacturing system means that it has more ability to change itself with customer's need and respond to the competitive pressure. Since flexibility is the ability to change, therefore, thinking what can be changed in the system gives the understanding about flexibility. It should be noted that all the resources contribute to flexibility and it costs money. Various types of flexibility can be measured in the manufacturing system, but all of them cannot have the same priority. In a manufacturing system, flexibility is considered at different levels such as production resource, task of production function, performance of the production function, competitive performance of the company [28].

3.1 Types of Flexibility

On the basis of the literature review, at least ten types of flexibilities can be identified [19, 35, 36]. These are:

1. *Machine Flexibility*: It is related to ease of making the changes in the machines that are required for the production of given set of products. It is related to number of operations performed without changing the machine setup.

2. *Material Handling Flexibility*: It is related to the number of paths available for a product due to material handling devices.
3. *Operation Flexibility*: It is related to the number of various process plans which can be used for the manufacturing of the product.
4. *Process Flexibility*: It is related to a group of part types that can be manufactured without major setup changes.
5. *Product Flexibility*: It is related to ease of making a new product into products setup.
6. *Routing Flexibility*: There are two major definitions of routing flexibility. First, it is ratio of number of all routes of all part types to number of part types [19]. Another definition is that it is the ratio of number of operations assigned to a machine to the operations that can be assigned to alternative machines [37].
7. *Volume Flexibility*: It is related to changes in the production volume.
8. *Expansion Flexibility*: It is ease of changing the capacity and capability of the system.
9. *Control Program Flexibility*: It is related to control software, algorithms, and intelligent machines.
10. *Production Flexibility*: It is related to the number of all products that can be manufactured without any setup change.

4   Reconfigurability

Various researchers have viewed reconfigurability in various ways. NSF Engineering Research Center for RMS has defined it as "the ability to adjust the production capacity and functionality of a manufacturing system to new circumstances by rearranging or changing the system's components" [38].

Lee [20] defines it as "the ability of a manufacturing system to be reconfigured at a low cost and in a short period of time." According to Setchi and Lagos [39], "the essence of reconfigurability is to enable manufacturing responsiveness to a change in market conditions - that is, the ability of the production system to respond to disturbances that may be caused by social or technological changes." Wiendahl et al. [40] define it as "it is the operative ability of a manufacturing or assembly system to switch with minimal effort and delay to a particular family of workpieces or sub-assemblies through the addition or removal of functional elements." According to Galan et al. [21] "reconfigurability does not necessarily arise solely from the market or customers but can also emanate from within the company for the sake of relevance." Basically, it is adjustment of the setup of the system at low cost to adjust fluctuation in demand and variety when required.

Table 1 shows the difference between flexibility and reconfigurability. Both flexibility and reconfigurability cost money. Therefore, it becomes a research area that what should be flexibility and reconfigurability of a manufacturing system.

Table 1 Comparison of flexibility and reconfigurability

S. No.	Flexibility	Reconfigurability
1	Flexibility is used in any manufacturing system whether it is dedicated, flexible, or reconfigurable manufacturing system	Reconfigurability is used in reconfigurable manufacturing system; i.e., if there is reconfigurability, it is reconfigurable manufacturing system
2	In flexibility, system changeover takes no time or a little time	In reconfigurability, system changeover takes some time
3	Flexibility deals with uncertainty and risk in almost all the possible ways	Reconfigurability deals with expansion or contraction of capacity or functions. According to Elmaraghy [19], the present definition of reconfigurability seems to be similar to expansion flexibility
4	While considering variety, high flexibility means that any variety of products can be produced	High reconfigurability means that a limited variety of products can be produced and then it is reconfigured for the other variety of products
5	Flexibility is considered for a part family (group of products). Part family consists of a large variety of products	Reconfigurability is considered between two-part families. Part family consists of customized variety

4.1 Measurement of Machine Flexibility and Machine Reconfigurability

Machine flexibility is defined as the ratio of the number of operations that can be performed in the machine without setup change to total operations that can be performed in the machine.

Machine flexibility of pth machine in qth configuration, MF_{pq} can be calculated as

$$\mathrm{MF}_{pq} = \frac{N_{pq}}{N_p} \tag{1}$$

where N_{pq} is the number of operations that can be processed on pth machine in qth configuration; N_p is the total number of operations on pth machine for all the configurations.

Machine reconfigurability is quick adaptability of the reconfigurable manufacturing system in response to the dynamic environment. A reconfigurable machine can be changed in many configurations by adding, removing, or adjusting its auxiliary modules. For ease of reconfiguration, reconfiguration effort (RE) should be minimum. It can be calculated as [7]

$$\text{RE} = \alpha \frac{\text{No. of modules added}}{\text{Total modules}} + \beta \frac{\text{No. of modules removed}}{\text{Total modules}}$$
$$+ \gamma \frac{\text{No. of modules readjusted}}{\text{Total modules}} \tag{2}$$

where α, β, γ are weights assigned for modules addition, removal, and adjustment, respectively. Generally,

$$\alpha > \beta > \gamma \quad \text{and} \quad \alpha + \beta + \gamma = 1.$$

Total reconfiguration effort of machine configuration pth machine in qth configuration, $\text{TRE}_{p,q}$,

$$\text{TRE}_{p,q} = \sum_{j=1, j \neq q}^{j_p} \text{RE}_j \tag{3}$$

where j_p is number of configurations of pth machine.

Machine reconfigurability $\text{MR}_{p,q}$ can be calculated as

$$\text{MR}_{p,q} = \frac{[j_p - 1]^z}{n_p^q \times \text{TRE}_{p,q}} \tag{4}$$

where n^q is number of machines needed to satisfy the required demand rate; z is the power index.

For example, consider company ABC has M_1, M_2, M_3, M_4, and M_5. M_2 is modular machine, and machine M_2 has three configurations M_2^1, M_2^2, and M_2^3. A number of operations that can be processed on machine configuration M_2^3 are 6. A total number of operations on machine M_2 for all the configurations are 12. If configuration of machine M_2 is changed from M_2^3 to M_2^1, number of modules added $= 4$, number of modules removed $= 3$, and number of modules adjusted $= 1$. If configuration of machine M_2 is changed from M_2^3 to M_2^2, number of modules added $= 1$, number of modules removed $= 3$, and number of modules adjusted $= 1$. Required number of machine configuration M_2^3 for the operation $= 3$, $\alpha = 0.5$, $\beta = 0.4$, $\gamma = 0.1$, $z = 2$. Then, flexibility and reconfigurability of the machine configuration M_2^3 can be calculated as follows.

Number of operations that can be processed on machine 2 configuration 3, $N_{2,3} = 6$; total number of operations on machine 2 for all the configurations, $N_2 = 12$; machine flexibility of configuration M_2^3 for operation 2,

$$\text{MF}_{2,3} = 6/12 = 0.5$$

Machine M_2 has three configurations, M_2^1, M_2^2, and M_2^3, i.e., $j_p = 3$.
Reconfiguration effort from changing configuration M_2^3 to M_2^1,

$$\text{RE}_1 = 0.5 \times 4/8 + 0.4 \times 3/8 + 0.1 \times 1/8 = 0.4125.$$

Similarly, reconfiguration effort from changing configuration from M_2^3 to M_2^2, $\text{RE}_2 = 0.36$.

Machine reconfigurability of $\text{MF}_{2,3}$,

$$\text{MR}_{2,3} = \frac{[3-1]^2}{3 \times (0.4125 + 0.36)} = 1.73.$$

4.2 Measurement of System Flexibility and System Reconfigurability

Measurement of system flexibility and system reconfigurability becomes slightly complicated. For flexibility, there are ten flexibilities in the manufacturing system. Each one is measured separately, and combined effect of this flexibility can be calculated by Multi-Attribute Utility Theory (MAUT). According to it, total evaluation is calculated as [41]

$$y(x) = \sum_{i=1}^{n} w_i u(x_i) \tag{5}$$

where $y(x)$ is the total evaluation, w is the weight assigned to each parameter, and $u(x)$ is the value of each parameter.

If MF = machine flexibility, MHF = material handling flexibility, OF = operation flexibility, PF = process flexibility, PDF = product flexibility, RF = routing flexibility, VF = volume flexibility, EF = expansion flexibility, CPF = control program flexibility, PDTF = production flexibility

then system flexibility (SF) can be measured as

$$\begin{aligned} \text{SF} = &\, w_1 \text{MF} + w_2 \text{MHF} + w_3 \text{OF} + w_4 \text{PF} + w_5 \text{PDF} + w_6 \text{RF} \\ &+ w_7 \text{VF} + w_8 \text{EF} + w_9 \text{CPF} + w_{10} \text{PDTF} \end{aligned} \tag{6}$$

Weights are assigned as per requirement, and all the flexibilities are needed to normalize.

For reconfigurability, key characteristics of RMS are considered. These are modularity, convertibility, scalability, diagnosability, customization, and integrability [42]. In brief, these can be defined as

1. *Modularity*: It is related to small identity module which can be added/removed in the system.
2. *Convertibility*: It is ease to convert the system from one setup to other. It includes convertibility of configuration, machine, and material handling system. Convertibility of system (CV) is measured as [43]

$$CV = \theta_1 C_c + \theta_2 C_m + \theta_3 C_h \tag{7}$$

where C_c, C_m, C_h are the configuration convertibility, machine convertibility, and material handling convertibility. θ_1, θ_2, θ_3 are the weights assigned.

$$C_c = \frac{RX}{I} \tag{8}$$

Where R is no of routing connections, X is minimum number of replicated machines at a stage, and I is minimum increment of conversion.

3. *Scalability*: It is related to minimal capacity increment which is needed to add in the system to adjust its capacity. It is defined as [44];

$$\text{scalability} = 100 - \text{smallest incremental capacity in percentage} \tag{9}$$

4. *Diagnosability*: It is related to error detection ability.
5. *Customization*: System is designed for a part family. Therefore, it is related to part family formation and customized flexibility.
6. *Integrability*: It is related to ease to which any module can be added to the system.

If MD = modularity, CV = convertibility, SC = scalability, DT = diagnosability, CS = customization, IN = integrability, then reconfigurability of system (RS) can be calculated by using MAUT as

$$RS = w_1' MD + w_2' CV + w_3' SC + w_4' DT + w_5' CS + w_6' IN \tag{10}$$

Weights are assigned as per requirement, and parameters are needed to normalize.

The author did research work for consideration of reconfigurability in an industry. Reconfiguration effort of the system was considered by removing or adding the modules of the machine shown in Table 2. Details of the measurement are given in [5].

5 Flexible Manufacturing System

A flexible manufacturing system, as its name means, has a very high flexibility. As defined by Groover [45] is "A flexible manufacturing system (FMS) is a highly automated GT machine cell, consisting of a group of processing stations (usually computer numerical control [CNC] machine tools), interconnected by an automated material handling and storage system, and controlled by an integrated computer system." According to Brown et al. [35], "A flexible Manufacturing System is an integrated, computer controlled complex of automated material handling devices and numerically controlled (NC) machine tools that can simultaneously process medium-sized volumes of a variety of part types." According to Tetzlaff [46], "A flexible manufacturing system can be defined as a computer controlled production

Table 2 Machines with machine configurations

Machines	Machine configurations	Auxiliary modules	A	B	C	D
M_2	M_2^1	GIM 1	✓			
	M_2^2	GIM 2		✓		
	M_2^3	GIM 3				✓
	M_2^4	GIM 4			✓	
M_{11}	M_{11}^1	CT 1	✓	✓	✓	
	M_{11}^2	CT 2				✓
M_{12}	M_{12}^1	MM 1	✓		✓	
	M_{12}^2	MM 2		✓		
	M_{12}^3	MM 3				✓
M_{20}	M_{20}^1	ITM 1	✓	✓		
	M_{20}^2	ITM 2			✓	
	M_{20}^3	ITM 3				✓

system capable of processing a variety of part types." According to Mehrabi et al. [18] "Flexible manufacturing system is a programmable machining center configuration which incorporates software to handle changes in work order, production schedules, part programs, and tooling for several part families."

From above definitions, some points are clear; FMS has a high level of automation. There is computerized control of machines, loading, unloading, transfer, etc. It can produce a variety of parts. Generally, it has CNC machines. Some systems which use flexible transfer line have been said as flexible manufacturing system [35]. But nowadays FMS cannot be imagined without CNC machines. Brown et al. [35] have classified types of flexible manufacturing system as: flexible machining cell, flexible machining system, flexible transfer lines, flexible transfer multi-line.

When the concept of FMS was introduced, it attracted the attention of many researchers. Many industries have started to use FMS. But a survey on FMS was conducted, and its conclusion was [18]; two-third of the responded said that FMS is not living up to its full potential, over half reported that they purchased FMS of excess capacity and features; the problems identified with FMS were training, reliability, maintenance, software, cost, and reconfigurability.

Generalization of the feature of FMS increased its cost and very high-level automation stared problem in maintenance. Because of these limitations, a new type of manufacturing system has been introduced named as reconfigurable manufacturing system. However, a flexible manufacturing system is used in many industries in India and worldwide. Even many academic institutions have a flexible manufacturing system for research purpose.

Table 3 Comparisons of system features of dedicated system, RMS, and FMS

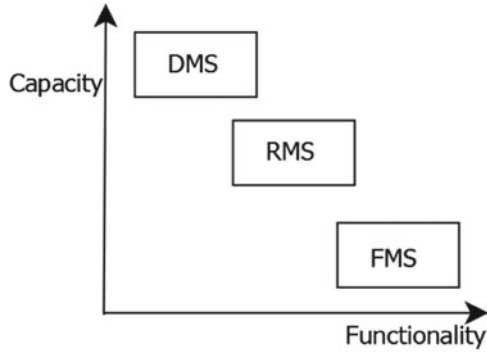|	Dedicated	RMS	FMS
System structure	Fixed	Adjustable	Adjustable
Machine structure	Fixed	Adjustable	Fixed
System focus	Part	Part family	Machine
Scalability	No	Yes	Yes
Flexibility	No	Customized	General
Simultaneously operating tool	Yes	Yes	No
Productivity	High	High	Low
Lifetime cost	Low for a single part, when fully utilized	Medium for production at medium- to high-volume new parts and variable demand during system lifetime	Reasonable for simultaneous production of many parts (at low volume); otherwise high

6 Reconfigurable Manufacturing System

Reconfigurable manufacturing system is a new type of manufacturing system which can change its capacity and functionality very easily and quickly whenever required. Reconfigurable manufacturing system (RMS) has capacity and functionality exactly what is required. RMS is adjustable to the fluctuating demands, and it can be easily upgraded with new process technology [5–8]. RMS has six key characteristics which are modularity, integrability, scalability, convertibility, customization, and diagnosability. These have been described in the previous section. The key characteristics, customization, scalability, and convertibility, are essential RMS characteristics, while the other three (modularity, integrability, and diagnosability) reduce the system configuration time and its ramp-up time [5, 47, 48]. RMS combines features of dedicated and flexible systems.

Reconfigurable manufacturing system has been evolved from dedicated manufacturing system. With the concept of using the modular machine, the concept of reconfiguration arises. But it is not limited to modular machines. Some researchers have given the concept of reconfiguration by material handling systems [49], reconfiguration by relocation [20], reconfiguration process plan [50], etc.

Koren and Shpitalni [51] have given the concept of practical reconfigurable manufacturing system using cell gantry and spine gantry. It is like a special type of layout of flexible manufacturing system. Later, reconfigurable machines were added [42]. Reconfigurability has been reviewed in mining industry [52], mold and die making industry [53], Arvin Meritor industry [54], powertrain industry [42], Continental Automotive [5, 22], etc.

Fig. 1 Comparisons of
DMS, FMS, and RMS [8]

(a) Functionality and capacity of DMS, FMSand RMS
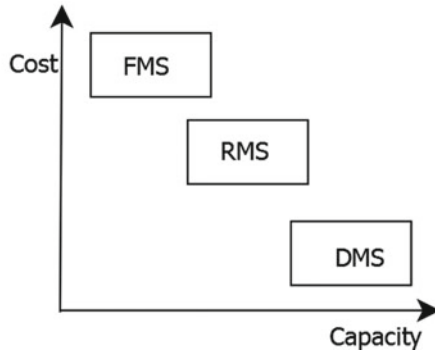
(b) Capacity and system cost of DMS, FMS and RMS

Table 3 compares the features of DML, FMS, and RMS. Figure 1a, b shows the difference between dedicated system, FMS, and RMS. The functions of FMS are very high, but it also increases the cost. The capacity of FMS is lowest, and the reason for it is that in FMS there are CNC machines which use the single-point cutting tool.

Some points can be given based on the comparison: FMS has generalized flexibility, while RMS has limited flexibility. FMS has evolved by combining CNC machines with transfer lines, while RMS evolved by introducing modular machine in dedicated transfer lines. CNC machines in FMS are single-point cutting tool which reduces the production capacity. In RMS, multi-point cutting tool machines can be used. In FMS, very high level of automation is required, while in RMS, it is required as per need. Mostly FMS has been used in machining, while the concept of RMS has been used in machining, mining, mold and die making, etc.

7 Conclusions

Manufacturing flexibility and reconfigurability are widely recognized as the critical components to achieving a competitive advantage in the marketplace. These are the most sought-after properties for manufacturing enterprises. This paper synthesizes the vast literature review on manufacturing flexibility and reconfigurability. This paper discusses the measurement of flexibility and reconfigurability, Sects. 4.1, 4.2, and compares the both, Table 1. This paper also discusses the concept of flexible manufacturing system and reconfigurable manufacturing system and differentiates between them, Sects. 5 and 6. It has been found that both flexibility and reconfigurability have importance, Sects. 3 and 4. But rather than having a lot of flexibility it is better to have some flexibility and some reconfigurability. Both flexibility and reconfigurability cost money, Fig. 1. Therefore, it becomes a research area that what should be flexibility and reconfigurability in a manufacturing system.

References

1. Jain A, Jain P, Chan FT, Singh S (2013) A review on manufacturing flexibility. International Journal of Production Research 51(19):5946–5970
2. D'Souza DE, Williams FP (2000) Toward a taxonomy of manufacturing flexibility dimensions. Journal of operations management 18(5):577–593
3. Urtasun-Alonso A, Larraza-Kintana M, García-Olaverri C, Huerta-Arribas E (2014) Manufacturing flexibility and advanced human resource management practices. Production Planning & Control 25(4):303– 317
4. Shi D, Daniels RL (2003) A survey of manufacturing flexibility: Implications for e-business flexibility. IBM Systems Journal 42(3):414–427
5. Prasad D, Jayswal SC (2017) Reconfigurability consideration and scheduling of products in a manufacturing industry. International Journal of Production Research https://doi.org/10.1080/00207543.2017.1334979
6. Prasad D, Jayswal SC (2017) Scheduling of products for reconfiguration effort in reconfigurable manufacturing system. In: Singh SK (ed) 7th International Conference of Materials Processing and Charac- terization (ICMPC 2017), GRIET Hyderabad, India
7. Goyal KK, Jain PK, Jain M (2013) A novel methodology to measure the responsiveness of RMTs in reconfigurable manufacturing system. Journal of Manufacturing Systems 32(4):724–730
8. Koren Y, Ulsoy A (1997) Reconfigurable manufacturing systems, engineering research center for reconfigurable machining systems (ERC/RMS) report# 1, the university of michigan. Ann Arbor
9. Vokurka RJ, O'Leary-Kelly SW (2000) A review of empirical research on manufacturing flexibility. Journal of operations management 18(4):485–501
10. Buzacott JA, Mandelbaum M (2008) Flexibility in manufacturing and services: achievements, insights and challenges. Flexible Services and Manufacturing Journal 20(1–2):13
11. Bernardes ES, Hanna MD (2009) A theoretical review of flexibility, agility and responsiveness in the operations management literature: Toward a conceptual definition of customer responsiveness. International Journal of Operations & Production Management 29(1):30–53
12. Pérez M, Serrano Bedia AM, López Fernández MC (2016) A review of manufacturing flexibility: systematising the concept. International Journal of Production Research 54(10):3133–3148

13. Alexopoulos K, Papakostas N, Mourtzis D, Gogos P, Chryssolouris G (2007) Quantifying the flexibility of a manufacturing system by applying the transfer function. International Journal of Computer Integrated Manufacturing 20(6):538–547
14. Chou MC, Chua GA, Teo CP (2010) On range and response: Dimensions of process flexibility. European Journal of Operational Research 207(2):711–724
15. Chang AY (2012) Prioritising the types of manufacturing flexibility in an uncertain environment. International Journal of Production Research 50(8):2133–2149
16. Fernandes R, Gouveia JB, Pinho C (2012) Product mix strategy and manufacturing flexibility. Journal of Manufacturing Systems 31(3):301–311
17. Barad M (2013) Flexibility development—a personal retrospective. International Journal of Production Research 51(23–24):6803–6816
18. Mehrabi MG, Ulsoy AG, Koren Y, Heytler P (2002) Trends and perspectives in flexible and reconfigurable manufacturing systems. Journal of Intelligent manufacturing 13(2):135–146
19. ElMaraghy HA (2005) Flexible and reconfigurable manufacturing systems paradigms. International jour- nal of flexible manufacturing systems 17(4):261–276
20. Lee GH (1997) Reconfigurability consideration design of components and manufacturing systems. The International Journal of Advanced Manufacturing Technology 13(5):376–386
21. Galan R, Racero J, Eguia I, Canca D (2007) A methodology for facilitating reconfiguration in manufacturing: the move towards reconfigurable manufacturing systems. The International Journal of Advanced Manufacturing Technology 33(3–4):345–353
22. Prasad D, Jayswal SC (2017) Case study of a reconfigurable manufacturing industry. In: Chauhan AK (ed) International Conference on Innovations and Developments in Mechanical Engineering (IDME17), KNIT Sultanpur, India, pp 32–36
23. Puik E, Telgen D, van Moergestel L, Ceglarek D (2017) Assessment of reconfiguration schemes for recon- figurable manufacturing systems based on resources and lead time. Robotics and Computer-Integrated Manufacturing 43:30 – 38, DOI https://doi.org/10.1016/j.rcim.2015.12.011, special Issue: Extended Papers Selected from {FAIM} 2014
24. Gu X, Jin X, Ni J, Koren Y (2015) Manufacturing system design for resilience. Procedia CIRP 36:135–140
25. Dahane M, Benyoucef L (2016) An Adapted NSGA-II Algorithm for a Reconfigurable Manufacturing System (RMS) Design Under Machines Reliability Constraints, Springer International Publishing, Cham, pp 109–130. https://doi.org/10.1007/978-3-319-23350-5
26. Goyal KK, Jain P, Jain M (2012) Optimal configuration selection for reconfigurable manufacturing system using nsga ii and topsis. International Journal of Production Research 50(15):4175–4191
27. Hasan F, Jain P, Kumar D (2016) Scalability of reconfigurable manufacturing systems based on bowl phenomenon: an implication of modular machines. International Journal of Industrial and Systems Engineering 22(1):73–95
28. Slack N (1987) The flexibility of manufacturing systems. International Journal of Operations & Production Management 7(4):35–45
29. Mandelbaum M, Brill P (1989) Examples of measurement of flexibility and adaptivity in manufacturing systems. Journal of the Operational Research Society pp 603–609
30. Mascarenhas MB (1981) Planning for flexibility. Long Range Planning 14(5):78–82
31. Gupta YP, Goyal S (1989) Flexibility of manufacturing systems: concepts and measurements. European journal of operational research 43(2):119–135
32. Cox Jr T (1989) Toward the measurement of manufacturing flexibility. Production and Inventory Management Journal 30(1):68
33. Nagarur N (1992) Some performance measures of flexible manufacturing systems. International Journal of Production Research 30(4):799–809
34. Upton DM (1994) The management of manufacturing flexibility. California management review 36(2):72–89
35. Browne J, Dubois D, Rathmill K, Sethi SP, Stecke KE, et al (1984) Classification of flexible manufacturing systems. The FMS magazine 2(2):114–117

36. Sethi AK, Sethi SP (1990) Flexibility in manufacturing: A survey. International Journal of Flexible Manufacturing Systems 2(4):289–328
37. Tsubone H, Horikawa M (1999) A comparison between machine flexibility and routing flexibility. International Journal of Flexible Manufacturing Systems 11(1):83–101
38. Harrison R, Colombo A, West A, Lee S (2006) Reconfigurable modular automation systems for automotive power-train manufacture. International Journal of Flexible Manufacturing Systems 18(3):175–190
39. Setchi RM, Lagos N (2004) Reconfigurability and reconfigurable manufacturing systems: state-of-the-art review. In: Industrial Informatics, 2004. INDIN'04. 2004 2nd IEEE International Conference on, IEEE, pp 529–535
40. Wiendahl HP, ElMaraghy HA, Nyhuis P, Z¨ah MF, Wiendahl HH, Duffie N, Brieke M (2007) Changeable manufacturing-classification, design and operation. CIRP Annals-Manufacturing Technology 56(2):783–809
41. Huber GP (1974) Multi-attribute utility models: A review of field and field-like studies. Management Science 20(10):1393–1402
42. Koren Y (2013) The rapid responsiveness of rms. International Journal of Production Research 51(23– 24):6817–6827
43. Maler-Speredelozzi V, Koren Y, Hu S (2003) Convertibility measures for manufacturing systems. CIRP Annals - Manufacturing Technology 52(1):367 – 370
44. Wang W, Koren Y (2012) Scalability planning for reconfigurable manufacturing systems. Journal of Manufacturing Systems 31(2):83–91
45. Groover MP (2007) Fundamentals of modern manufacturing: materials processes, and systems. John Wiley & Sons
46. Tetzlaff UAW (1990) Flexible manufacturing systems, Physica-Verlag HD, Heidelberg, pp 5–11. https://doi.org/10.1007/978-3-642-50317-7
47. Koren Y (2006) General rms characteristics. comparison with dedicated and flexible systems. In: Dashchenko AI (ed) Reconfigurable Manufacturing Systems and Transformable Factories, Springer Berlin Heidelberg, Berlin, Heidelberg, pp 27–45, https://doi.org/10.1007/3-540-29397-3
48. Prasad D, Jayswal SC (2017) Design of reconfigurable manufacturing system. In: National conference on Futuristics in Mechanical Engineering (FME-2016), Madan Mohan Malaviya University of Technology, Gorakhpur, India
49. Oke A, Abou-El-Hossein K, Theron NJ (2011) The design and development of a reconfigurable manufacturing system. South African Journal of Industrial Engineering 22(2):121–132
50. Youssef AM, ElMaraghy HA (2006) Assessment of manufacturing systems reconfiguration smoothness. The International Journal of Advanced Manufacturing Technology 30(1–2):174–193
51. Koren Y, Shpitalni M (2010) Design of reconfigurable manufacturing systems. Journal of manufacturing systems 29(4):130–141
52. Makinde O, Mpofu K, Popoola A (2014) Review of the status of reconfigurable manufacturing systems (rms) application in south africa mining machinery industries. Procedia CIRP 17:136–141
53. Oke A, Abou-El-Hossein KA, Theron NJ (2011) Reconfigurability approach in manufacture of moulds and dies. In: Advanced Materials Research, Trans Tech Publ, vol 264, pp 1708–1713
54. Abdi MR, Labib AW (2003) A design strategy for reconfigurable manufacturing systems (RMSs) using analytical hierarchical process (ahp): a case study. International Journal of production research 41(10):2273–2299

Effect of Mg Concentration on the Structural, Morphological and Optical Properties of Ternary ZnMgO Nanocrystalline Thin Films

Shashikant Rajpal and S. R. Kumar

1 Introduction

In recent decades, the semiconductor and display applications were predominantly focused by electronic industry, You et al. [1]. Among II–VI semiconducting materials ZnO is a wide band-gap (3.37 eV) semiconductor having hexagonal wurtzite structure. The luminescence efficiency of ZnO enhances due to its higher exciton binding energy (~60 meV). It has direct band-gap energy, which makes its transparent in the ultraviolet and visible region and most of the activity in the ultraviolet/blue region, Norris et al. [2], Choi et al. [3], Sun et al. [4]. For strong spontaneous and piezoelectric polarization, the doping scheme using varying composition can be applied to any semiconductor crystal such as ZnO-based material, Choi et al. [5]. By alloying different elements like Cd and Mg, the optical properties of ZnO can be modified, Janotti et al. [6], Kang et al. [7]. A number of techniques have been employed in the synthesis of high-quality ZnMgO thin film such as magnetron sputtering, Gowrishankar et al. [8], chemical vapour deposition, Rivera et al. [9], molecular beam epitaxy, Hua et al. [10], spray pyrolysis, Zhang et al. [11], Pulsed laser deposition, Maemoto et al. [12], hydrothermal method, Heo et al. [13], sol-gel method, Xu et al. [14]. To obtain oxide materials with specific chemical and physical properties, electrodeposition is widely used among above-mentioned methods. Using an electrodeposition technique for oxide film formation has several advantages over other deposition techniques. By the electrodeposition technique, one can deposit thin films with a specific composition and good adhesion between thin films and substrate, Karuppuchamy et al. [15]. In the present study, we synthesized ZnMgO films by electrodeposition technique with varying concentration of Mg and investigated the influence of Mg on the structural, morphological and optical properties of ZnO film. Different approaches have been

S. Rajpal (✉) · S. R. Kumar
Department of Applied Sciences and Humanities, National Institute of Foundry and Forge Technology, Ranchi 834003, Jharkhand, India
e-mail: sraj1162@gmail.com

adopted to tune the band gap of ZnO by alloying with different elements like Cu, Mg and Cd. To achieve the purpose, mainly physical techniques like magnetron sputtering, metal organic chemical vapour deposition, spray pyrolysis are used. However, few reports are there in chemical technique like electrodeposition, but in electrodeposition process the reported work is on three-electrode geometry. Little work has been performed by two-electrode geometry in electrodeposition for the development of ZnMgO thin films. Thus, it is of interest to explore the possibility of using a different salt bath for ZnMgO electrodeposition. Using the electrodeposition technique, we report the solid-state and optical properties of ZnMgO thin films. The results will be useful for applications in photovoltaic solar cells and optoelectronic devices.

2 Experimental Details

2.1 Materials

All the chemicals used for the deposition of ZnMgO thin film were of analytical grade and used reagents without any further purification. It includes AR grade sodium citrate, $Na_3C_6H_5O_7 \times 2H_2O$ (Merck), AR grade magnesium chloride, $MgCl_2 \times 6H_2O$ (Merck), AR grade 30% hydrogen peroxide, H_2O_2 (Merck). During the preparation of electrolyte AR grade ammonia solution, NH_3 (Merck) was used as a complexing agent. Substrate used as electrode was AR grade zinc plate (ALFA AESAR).

2.2 Sample Preparation and Experimental Setup

The ZnMgO thin films were deposited by electrodeposition technique. The zinc sheets used as substrate of about 1 mm thickness with a surface dimension of 1.5×1.0 cm^2 were first polished by 600 grit carborundum paper, washed with soap solution and distilled water. 40 ml of distilled water was taken in a beaker and 0.1 M $Na_3C_6H_5O_7 \times 2H_2O$, xM ($x = 0.00263$, 0.00525 and 0.01313 M) $MgCl_2 \times 6H_2O$ and 30% H_2O_2 were added. By using ammonia solution, pH of the electrolyte was maintained between 9.5 and 10. The electrolyte was stirred moderately and maintained at room temperature. Both the zinc plates were put in the electrolyte in parallel configuration with an inter-electrode separation of 1 cm. The deposition was carried out cathodically at -4 V at room temperature. The duration of the deposition was 20 min. The Zn cathode with the deposited products was washed with distilled water for several times, dried at room temperature and examined in terms of their structural, compositional and optical properties.

2.3 Characterization of Samples

The compound formation was studied using X-ray diffractometer fitted with curved position-sensitive detector (X'pert pro Panalytical BV PW3040160). Compositional and structural data for thin films were obtained using energy dispersive spectroscopy attached with scanning electron microscope (Jeol JSM 6480LV) and atomic force microscopy (Nano-surf EZ2). Optical measurements of ZnO thin films were carried out using UV–Vis spectroscopy (Lambda-25 Perkin) spectro-fluorophotometer (Shimadzu RF5301PC).

3 Results and Discussion

The as-deposited ZnMgO thin films were developed by electrodeposition technique with potential -4 V. Electrodeposition technique has divers advantage among physical techniques which are low capital cost, low-temperature growth, ability of bandgap engineering and the ability to control the film thickness by varying the deposition time and potential. In this process, synthesis is taking place due to cathodic deposition process. The zinc substrate is oxidized due to the presence of oxygen and formation of ZnO film. The Mg ions get reduced at cathode, and the formation of ZnMgO film takes place. The deposited ZnMgO films with varying concentration of Mg ($x = 0.00263$, 0.00525 and 0.01313 M) were deposited on zinc substrate. Let us assume sample A, sample B and sample C for as-deposited ZnMgO films with Mg concentrations 0.00263, 0.00525 and 0.01313 M, respectively. The films are physically stable and show good adhesion. The X-ray diffraction spectra of samples A, B and C are shown in Fig. 1. The XRD pattern indicates that all the ZnMgO films with varying concentration of Mg exhibits peaks attributed to (101) plane with reflection at $2\theta \simeq 36°$ corresponds to wurtzite structure and its intensity increases with the increase of Mg composition in the films. All the varying Mg content ZnMgO films have the same characteristics and show the same preferential orientation. XRD spectra' data gives the information that the concentration changes. The film exhibits good crystallinity and all the peaks are indexed for a hexagonal ZnO lattice. Reflections (100), (101) and (102) planes are also observed due to zinc substrate at 39.03°, 43.26° and 54.36°. The average crystalline size (D) of varying Mg content ZnMgO films were calculated using the Scherrer formula, given in Eq (1).

$$D = 0.9\lambda/\beta \cos\theta \tag{1}$$

where β is the full width at half maxima (FWHM), λ is the wavelength of the X-ray (1.542Å), and θ is the angle of diffraction, Cullity et al. [16]. The average crystalline size for sample A, B and C is observed to be 45, 47 and 44 nm, respectively. It is observed that the crystalline size value (D) increases with small increase in the

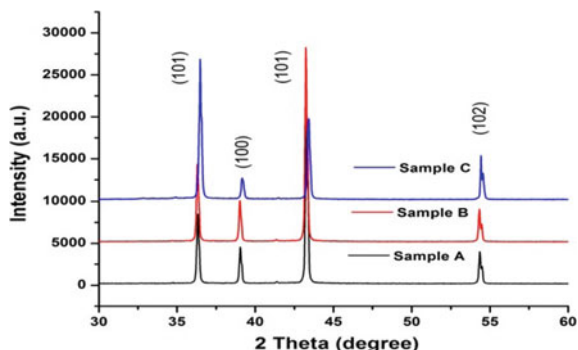**Fig. 1** XRD spectra of as-deposited ZnMgO thin film with varying concentration of Mg

Table 1 Elements, concentration (M), FWHM (XRD), crystalline size (nm) and hkl plane of ZnMgO thin films

Element	Concentration (M)	FWHM (°/Radian)	Crystalline size (nm)	Plane (hkl)
ZnMgO	0.00263	0.1831	45	(101)
ZnMgO	0.00525	0.1778	47	(101)
ZnMgO	0.01313	0.1887	44	(101)

concentration of Mg and decreases with further higher concentration of Mg in the films which are shown in Table 1.

The surface morphology using SEM of as-deposited ZnMgO films with varying concentration is shown in Fig. 2a–c. The magnification was fixed 5000× in all the concentrations. The surface morphology of ZnMgO is found to be very similar as that of ZnO. The incorporation of Mg plays a vital role in influencing the surface morphology of the film. In Mg-doped sample, the grains are of bigger size and spherical. The micrograph reveals compact surface with grains interconnected to each other. The grains of the film surface were less densed when doped Mg concentration was 0.00263 M, whereas after doping with Mg concentration 0.00525 and 0.01313 M, grains are heavily densed. The grains are unevenly distributed over the surface. This may be probably due to the formation of colloidal particle in the solution. Ionic radius of magnesium is smaller than that of zinc, so Mg can easily penetrate into ZnO to form heavily densed surface. The ZnMgO film surface is smooth, equal sized uniform spherical shaped grains. The larger crystallite sizes are achieved by high molar concentration of magnesium. The increased crystallite size after the Mg introduction is in agreement with XRD results, which shows in Fig. 1.

The composition from varying concentration of ZnMgO thin films by EDS is shown in Fig. 3a–c. Different concentrations of ZnMgO thin films were deposited on the zinc substrate. The peaks of Zn, Mg and O are observed in the films as it is evident from EDS spectra. Table 2 shows the atomic percentage and weight percentage of ZnMgO films with varying concentration.
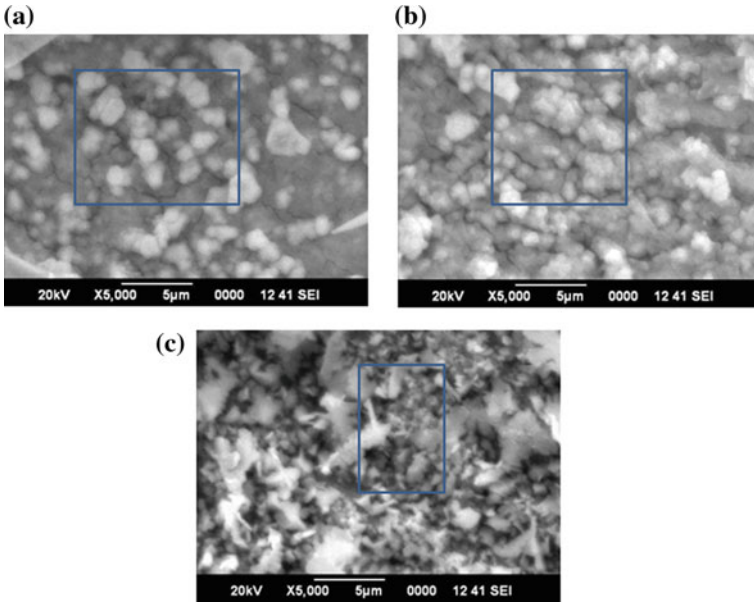
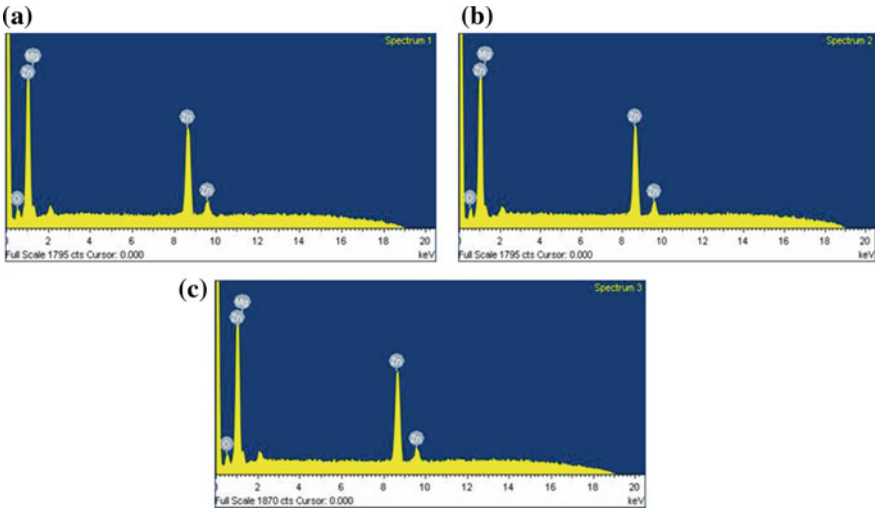**Fig. 2 a–c** SEM images of as-deposited ZnMgO thin film (sample A, B and C) with varying concentration of Mg

Fig. 3 a–c EDS spectra of as-deposited ZnMgO thin film (sample A, B and C) with varying concentration of Mg

Table 2 Atomic percentage of ZnMgO thin film with varying Mg concentration

Element	Atomic% (0.00263 M)	Atomic% (0.00525 M)	Atomic% (0.01313 M)
Zn	68.50	68.34	65.31
Mg	11.03	12.09	12.73
O	20.57	19.57	21.95

Fig. 4 Photon energy versus $(\alpha h\nu)^2$ plot for as-deposited ZnMgO thin film (sample A, B and C) with varying concentration of Mg
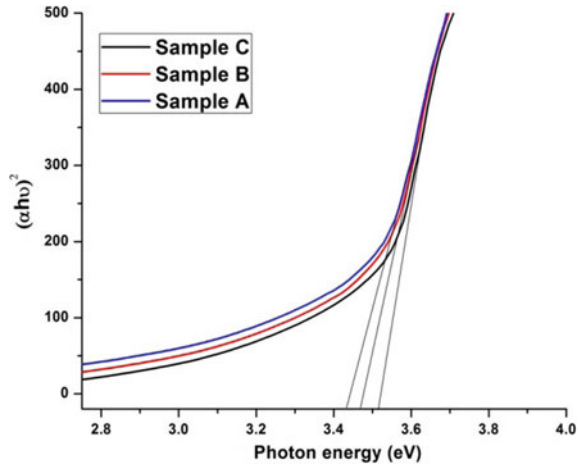
The energy band gap of the semiconducting ZnMgO films was determined from the absorbance data by plotting $(\alpha h\nu)^2$ versus $(h\nu)$, where the interception of linear portion on the energy axis gives the energy band gap of the material. The plot of $(\alpha h\nu)^2$ versus energy is shown in Fig. 4. The optical absorbance spectra have been studies from the wavelength of 250–700 nm. The absorption spectra confirm that the Mg concentration increases, and absorption edges shift towards the short wavelength. The relationship between absorbance coefficient (α) and photon energy $(h\nu)$ is expressed to calculate the energy band gap of ZnMgO film with varying Mg concentration by the Tauc's relation, Eq. 2, Lin et al. [17].

$$\alpha h\nu = A(h\nu - E_g)^{1/2} \tag{2}$$

The band gap (E_g) obtained for each Mg concentration is different. Due to Mg concentration increases, band gap also increases indicates that the formation of solid solution. Higher-energy band gap developed in the films due to higher Mg concentration indicates the presence of secondary phase in small quantity. The increase of band gap is due to the magnesium ions replaced zinc ions in the ZnO lattice. For sample A, B and C, band gap is observed to be 3.43, 3.46 and 3.52 eV, respectively.

Figure 5 shows the photoluminescence spectra of ZnMgO films with varying concentration of Mg_x ($x = 0.00263$, 0.00525 and 0.01313 M). Photoluminescence is a process in which an electron excited by a monochromatic beam of energy undergoes

Fig. 5 Photoluminescence spectra for as-deposited ZnMgO thin film (sample A, B and C) with varying concentration of Mg
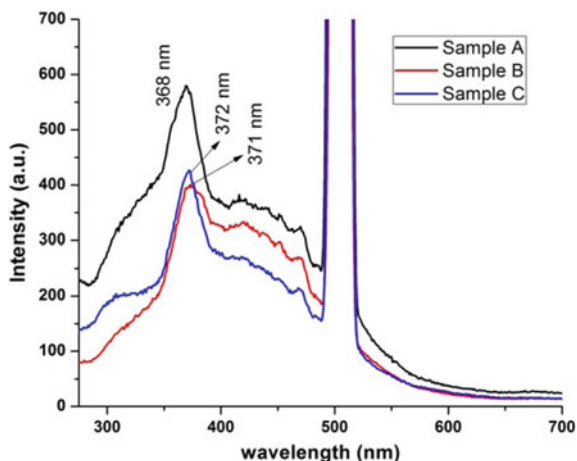
radiative recombination at band-edge luminesces or at red-shifted luminesces within the forbidden energy gap, Sivaraman et al. [18]. Due to excitation at higher energy level, emission peak observed at 368, 371 and 373 nm attributed to sample A, B and C, respectively. Peaks around 470 are observed due to the recombination of exciton or trapped hole pair. The emission peak appears as a blue shift from 373 to 368 nm with increasing the Mg content in the source solution.

4 Conclusions

This paper investigates the possibilities for development of ZnMgO thin film with varying the concentration of Mg. ZnMgO thin film with different Mg concentrations can be synthesized using electrodeposition technique. Attention was paid to analyzing the structural, compositional and optical properties of as-deposited ZnMgO film. On the basis of the results of the present study, the following conclusions can be drawn. The results indicated that the deposited films are crystalline in nature. The crystallite sizes were measured by XRD analysis. The as-deposited films are smooth, uniform, free from pinholes, pits, etc. With increase in Mg concentration, the energy band gap increases. Photoluminescence indicates that peaks of near-band emission appeared as a blue shift with increasing the Mg content. The wider band gap of the deposited films makes them suitable for optoelectronic devices, for instance window layer in solar cells.

References

1. Hsin Chiang You. Indium Doping Concentration Effects in the Fabrication of Zinc-Oxide Thin-Film Transistors. Int. J. Electrochem. Sci. 2013; 8: 9773–9784.
2. Norris BJ., Anderson J, Wager JF, Keszler DA. Spin-coated zinc oxide transparent transistors. J. Phys. D: Appl. Phys. 2003, 36:105.
3. Choi JH, Kar JP, Khang DY, young M. Enhanced performance of ZnO nanocomposite transistor by simple mechanical compression. J., J. Phys. Chem. 2009; 113:5010.
4. Sun B, Sirringhaus H. Solution-Processed Zinc Oxide Field-Effect Transistors Based on Self-Assembly of Colloidal Nanorods. Nanolett 2005; 5: 2408.
5. Choi WS, Yoonb JG. Optical characterization of band gap graded ZnMgO films, Solid State Communications 2012; 152: 345–348.
6. Janotti A, Walle CGVD, Fundamentals of zinc oxide as a semiconductor. Rep. Prog. Phys. 2009; 72: 126501.
7. Kang TD, Hosun L, Won P, Chul YG, J. Korean Phys. Soc 2004; 44:129–132.
8. Gowrishankar S, Balakrishnan L, Gopalakrishnann N. Band gap engineering in $Zn_{(1-x)}Cd_xO$ and $Zn_{(1-x)}Mg_xO$ thin films by RF sputtering. Ceramics International2014; 40: 2135–2142.
9. Rivera A, Mazady A, Anwar M. Co-axial core–shell ZnMgO/ZnO NWs. Solid-State Electronics 2015; 104:126–130.
10. Hua SY, Chou WC, Weng YH. Effects of magnesium contents in ZnMgO ternary alloys grown by molecular beam epitaxy. Journal of Alloys and Compounds 2015; 636: 81–84.
11. Zhang X, Li XM, Chen TL, Bian JM, Zhang CY. Structural and optical properties of $Zn_{1-x}Mg_xO$ thin films deposited by ultra sonic spray pyrolysis. Thin Solid Films 2005; 492: 248–252.
12. Maemoto T, Ichiba N, Ishii H, Sasa S, Inoue M. Structural and optical properties of ZnMgO thin films grown by pulsed laser deposition using ZnO-MgO multiple target. Journal of Physics: Conference Series 2007; 59: 670–673.
13. Heo YH, Varadarjan V, Kaufman M, Kim K, Norton DP, Ren F, Site-specific growth of Zno nanorods using catalysis-driven molecular-beam epitaxy, Appl Phys Lett 2002;81:3046.
14. Xu L, Su J, Chen Y, Zheng G, Pei S, Sun T, Wanga JF, Lai M, Journal of Alloys and Compounds, 2013;548: 7–12.
15. Karuppuchamy S, Ito S. Cathodic electrodeposition of nanoporous ZnO thin films from new electrochemical bath and their photo induced hydrophilic properties, Vacuum 2008;82: 547–550.
16. Cullity BD. Elements of x-ray diffraction. USA: Addison-wesley Reading, 1972.
17. Lin MC, Chen PY, Sun IW. Electrodeposition of Zinc Telluride from a Zinc Chloride-1-Ethyl-3-methylimidazolium Chloride Molten Salt. Journal of The Electrochemical Society 2001; 148 (10):C653–C658.
18. Sivaraman T, Nagarethinam VS, Balu AR. CdS thin films fabricated by a simplified spray technique from different substrate temperatures-Structural, morphological, optical and electrical analysis. Res. J.Mater. Sci. 2014; 2: 6.

Study and Optimization of Erosive Behavior of Carbon Black–Epoxy Polymer Composites Using Taguchi Method

Narasingh Deep and Punyapriya Mishra

1 Introduction

Solid particle erosion (SPE) corresponds to the loss of material that resulted from the continuous striking of erodent particles traveling at a substantial velocity. This causes local damage combined with the progressive loss of original material from a solid surface due to the micromechanical interaction between that surface and solid particle. Wear-resistant material is used in many applications such as aerospace industry, hydraulic machine, pipe carrying abrasive slurry structure which is used in desert environments [1]. Ever since the investigation, the erosive behavior of materials has extended from metals to polymer composites. A wide range of reinforcing techniques using hard ceramics fillers or fiber fillers consisting glass fibers are being used nowadays to enhance the wear-resisting properties of the polymer even up to "three times the order of magnitude" [2]. Such particulate fillers are incorporated into the polymer matrix for a whole range of applications, primarily for cost reduction, stiffness improvement. Fillers like red mud [3], Al_2O_3 [4, 5], silicon carbide [6], fly ash [7], and CNT [8] have been dispersed into the polymeric materials and observed that there is a noticeable reduction in wear rate with the incorporation of hard particulate fillers. Harsh et al. have summarized the experiments of carbon which is one of the wonder materials for having distinctive allotropic forms, with exceptionally varied physical and chemical properties due to the distinct chemical bond and spatial arrangements of carbon atoms [9–12]. Carbon black (CB) is an elemental form of carbon consisting of fine particles having an amorphous molecular structure. It is generally prepared by charring agricultural by-products and organic materials. It can also be produced by combusting of hydrocarbons, coal, and other vegetable oils. Due to excellent electronic, mechanical, tribological, and optical properties, CB is

N. Deep (✉) · P. Mishra
Department of Mechanical Engineering, Veer Surendra Sai University of Technology, Burla 768018, Odisha, India
e-mail: nsdeep121@gmail.com

broadly used as the reinforcing material in both thermoset and thermoplastic polymers. It boosts the UV protection, electronic conductance, opacity when used as reinforcement material in plastics, paints, and elastomers [13, 14]. Wu et al. worked on calorimetry effect of the carbon filler on epoxy. Compared to carbon nanofiber and CB, the heat of curing is greatly influenced by the ozone-treated carbon fiber. The incorporation of carbon filler decreases the heat flowing temperature which facilitates the curing reaction. Due to large surface area, the presence of CB accelerates the curing reaction. Increase in surface area-to-volume ratio of the reinforcement material boosts the curing time of polymeric material; however, it negligibly affects the heat of the curing reaction. Reinforcing epoxy polymer with "ozone-treated" carbon filler in the presence of a linear amine curing agent increases the heat of the curing reaction. Poly-ether-ether-ketone (PEEK) incorporated with unidirectional carbon fiber behaves as a semi-ductile material with erosion rate at 60° [15].

Taguchi methods or robust design methods are statistical methods used for improving engineering productivity. It facilitates flexible designs and concurrent engineering considering all the noise factors associated with it. It consists of system design, parameter design, and tolerance design to achieve a robust process and to identify different parameter settings to get the best level of quality characteristics with minimum variation. To reduce product cost, improve quality and reduce simultaneous development interval, Taguchi statistical method is found to be a powerful tool. Taguchi's approach to the design of experiments has gained wide popularity for its simplicity. It specified three conditions, i.e., larger the better, smaller the better and on-target, minimum variation. The parameters are optimized by considering different conditions. Signal-to-noise ratio in the robust design is used as the quality characteristic of choice.

Many research have been reported on the carbon black pigment [16, 17] and epoxy resin [18] in mechanical, electrical, and thermal areas; however, there is a limited number of works available on tribological behavior. The work on the carbon black-reinforced polymer composite in the field of tribology and the effects of the process variable is scantily available. Carbon black, due to its different particle size, structure, and composition of different functional groups like hydroxyl and carboxyl on the surface, has a large effect on practical properties such as blackness, dispersibility. Because of its cost-effectiveness, easy availability, and other tailored properties, here, an attempt has been made to disperse carbon black into the epoxy resin.

In the present work, polymer composites were prepared by incorporating varying weight percentages of carbon black into epoxy resin. The effects of the carbon black content on the wear resistance were studied. The tribological behavior of the composites was studied with different input parameters. A systematic plan of experiments was conducted on the basis of Taguchi experimental design. The erosion rate of the composite was optimized considering different influential parameter using MINITAB. An attempt was made toward the possible application areas in various impact and erosive environments.

2   Experiment

2.1   Materials Used

The CB is "Vulcan XC72R GP-3820" procured from "Cabot Corp., Billerica, MA." The CB powder has a particle size of 30 nm with 0.2% maximum ash content. It has larger specific surface area and a density of 1.7–1.9 g/cm^3.

The epoxy resins used in the present work is the diglycidyl ether of bisphenol A (DGEBA) a liquid epoxy resin which represents greater than 75% of the resin used in industrial applications. It is available under trade name Araldite$^®$ GY 257 which is the registered trademark for Huntsman Advanced Materials' commercial resins. This epoxy resin was supplied by M/S-Singhania Suppliers, Kolkata. Polyamines and polyamidoamines, etc., are widely used as curing agent for this resin. In the present work, the curing agent/hardener used was A-140. "Aradur$^®$"—140 is the trademark of Huntsman Advanced Materials limited for commercial hardeners.

2.2   Preparation of Composites

Epoxy resin and carbon black were heated separately in a vacuum oven for 1 h at 60 °C [±2 °C]. Mixing of resin with carbon black was carried out by H.S.M (high-intensity mechanical liquid stirrer) at approximately 500 rpm speed and 60 °C [±2 °C] for 1 h. The curing agent was added to the mixture at predetermined parts per hundred ratios. The solution was gently mixed for 15–20 min to prevent any air bubble formation. The colloidal solution free from air bubbles was poured into a preheated brass mold ($165 \times 165 \times 3$ mm^3) at 80 °C [±2 °C] and cured in the vacuum oven at −760 mm of Hg for 1 h. Post-curing was carried out in two phases: First at 120 °C [±2 °C] for 2 h inside vacuum oven and then at room temperature for 48 h. The above procedure will be repeated for different wt% (0–7) of carbon black to get the sheets of composites. Different test specimens were cut from the fabricated composites.

2.3   Test Parameters

The different main input test parameters are described below and listed in Table 1.

2.3.1   Impingement Angle

Impingement angle is the angle between the sample holder and the nozzle from which the erodent impinging. When the sample holder is perpendicular to the nozzle, then the angle is 90°, and when it is parallel to the nozzle, then the angle is 0°.

Table 1 Erosion conditions

Parameters	Particulars
Erodent	Silica sand
Erodent size (μm)	370
Impingement angle ($\alpha°$)	30, 45, 60
Impact velocity (m/s)	109
Erodent feed rate (gm/min)	1.467 ± 0.02
Erodent shape	Angular
Nozzle to sample distance (mm)	10
Hardness of silica particles (HV)	17.894

With an increasing in impingement angle, the wear rate of the material increases. The material type can be predicted based on the impingement angle on which the maximum and minimum erosion take place. For brittle material and ductile material, the maximum erosion take place in-between 80°–90° and 15°–30°, respectively. If maximum erosion takes place within 45°–50°, then the material is semi-ductile in nature.

2.3.2 Impact Velocity

Impact velocity corresponds to the velocity at which the particle strikes the sample. It is the indirect input in the erosion test. Pressure is the main input while determining impact velocity. By varying pressure, compressed air brings about a change in striking velocity. Double-disc methods were used for determining the impact velocity of the erodent.

2.3.3 Nozzle to Sample Distance

It is the distance between the nozzles from which the erosive parties are falling to the job holder stand. The erosion rate decreases with the increase in a stand of distance due to the increase in the time of flight. But when the erodent size is considered, the erosion rate increases with increase in distance.

2.3.4 Test Temperatures

The test temperature is the climatic condition at which the experiment is taken place. Based on the temperature effects, the erosion wear varies also depending upon the material properties and melting point.
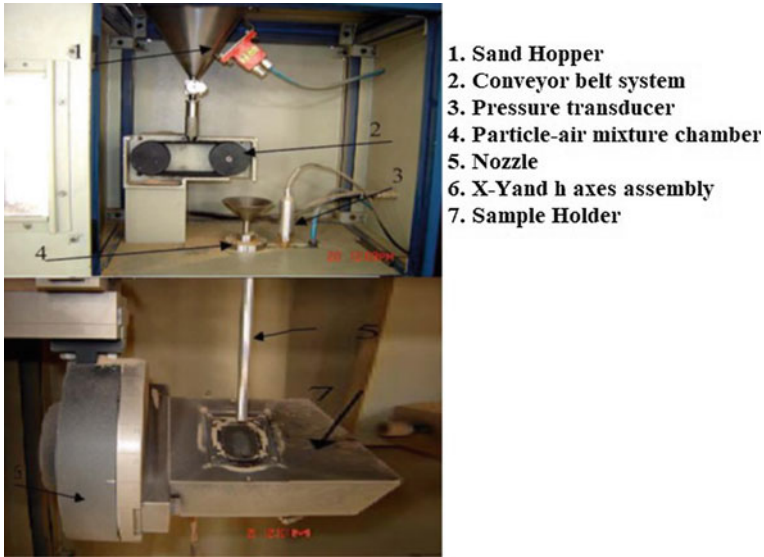
Fig. 1 Solid particle erosion test rig

2.3.5   Erosion Wear Test

The wear test was conducted according with ASTM G76 standard on the SPE test rig. It consists of different parts like compressor, air drier, sample holder as depicted in Fig. 1 [19]. A jet of dry and compressed air along with abrasive sand particle is supplied continuously into the mixing unit by conveyor belt system.

The pressurized sand (erodent) passing out of the nozzle strikes upon the test specimen. The composite material of varying weight percentages (1, 3, 5)is impinged at different impact angles (i.e., at 30°, 45°, and 60°) with a striking velocity of 109 m/s (i.e., 6 bar pressure) with erodent size 370 µm. Standard double-disc method was employed for evaluating the impact velocity. The experiments were conducted at room temperature with a relative humidity of 30%.

2.3.6   Measurement of Erosion Rate

The measure of the erosion wear of the material was done based on the weight loss of the sample. This is determined by the estimating the weight loss of the test specimens at a regular interval during the test duration. Micro-weighing balance with 0.001 mg accuracy was employed for weight measurement of the samples. Weights of each test specimen before and after every experiment were recorded. The wear rate is evaluated as the "weight loss per unit erodent mass (gm/gm)." The input parameters

Table 2 Experimental layout erosion rate, erosion efficiency at different test conditions

Percentage	Angle	Impact velocity (m/s)	Input	Output	Wt. loss (g)	Erosion rate (g/g)	Erosion efficiency
1	30	109	2.676	2.670	0.06	0.672	1.26
	45	109	4.998	4.980	0.018	0.202	0.38
	60	109	4.612	4.600	0.012	0.134	0.25
3	30	109	3.417	3.410	0.007	0.078	0.15
	45	109	5.393	5.380	0.013	0.146	0.27
	60	109	5.412	5.400	0.012	0.134	0.25
5	30	109	3.515	3.510	0.005	0.056	0.11
	45	109	6.445	6.430	0.015	0.168	0.03
	60	109	6.853	6.840	0.013	0.146	0.27

for the wear tests are three angles and three different percentages of filler material which is shown in Table 2.

3 Results and Discussion

The process of erosion is thought to be taken place in both micro- and macro-level of the wearing surface. Changes occurring at the wearing surface are caused by the combining effect of particle impact, microcutting, and target melting. When a jet of projectile impinges upon a target surface, weight loss by the erosion starts from the first impinging particles that would machine the material. The kinetic energy of the high velocity projected abrasive particles transformed into plastic deformation and subsequently into heat within the target. Below a certain depth of the wearing surface, the temperature decreases to a level where plastic deformation caused by the impact gradually reduces the cohesive strength and the target materials are removed from the surface. The erosion rate was calculated using Eq. (1).

$$E_r = \frac{\Delta W}{W_e} \tag{1}$$

where ΔW is "weight loss," and W_e is the "erodent weight." ΔW is estimated by weighing the test specimen before and after each run using a micro-weighing balance. The erosion efficiency (η) is calculated using Eq. (2)

$$\eta = \frac{2E_r H}{\rho V^2} \tag{2}$$

where E_r is the erosion rate, V is the impact velocity, H is the hardness, and ρ is the density of the target material.
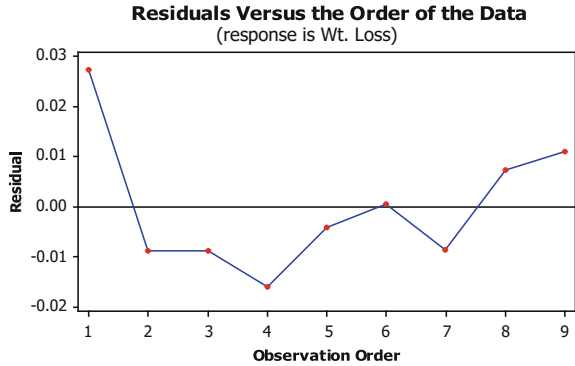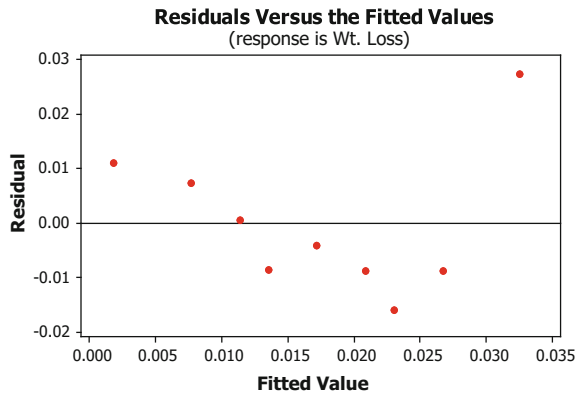
Fig. 2 Residual versus order of the data

Residuals Versus the Order of the Data
(response is Wt. Loss)

Fig. 3 Residual versus fitted values

Residuals Versus the Fitted Values
(response is Wt. Loss)

The regression model is employed for evaluating the residuals of experimental trials. The difference between the actual value and predicted is termed as "residual." These are recorded in increasing fashion. Figure 2 shows the interaction between the residuals and observation data. From this run of positive and negative residuals, it indicates the presence of an ascertained correlation between the actual and predicted results. Moreover, it is clear from the plots that the residuals are found to be almost uniformly distributed on both side of the zero line. Thus, the data are independent. Figure 3 depicts the "residuals versus the fitted values" that shows the maximum variation of −0.5 to 0.5 mm in weight loss between the residuals and the fitted values. The normal probability plot of residuals is shown in Fig. 4 which verifies the normality predictions. As from Fig. 5, it represents the data are scattered roughly along the straight line, so which confirms the main effect. The response mean is different across all level factors.

Fig. 4 Normal probability
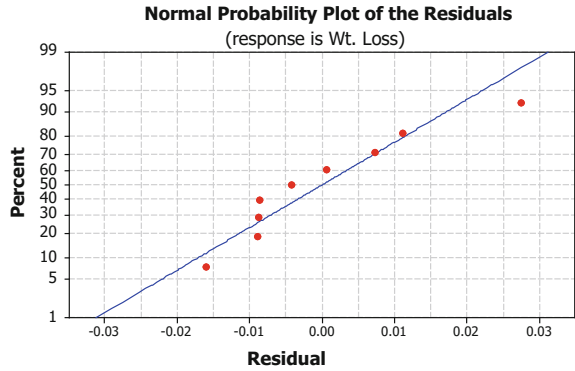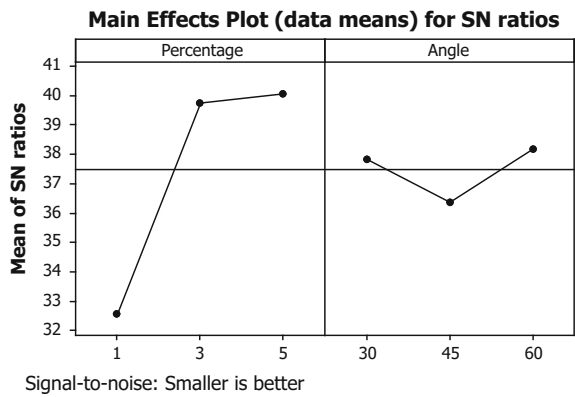plot of the residuals

Fig. 5 Effects of controlling
factors on wear rate

4   Conclusion

The experiments were conducted to study the wear behavior of varying weight per-
centages of CB-epoxy composite with the sand particle as erodent. The fabrications
of different percentages of carbon black–epoxy composite (1, 3, and 5%) were done.
The erosion wear behavior of the fabricated composites has been studied under dif-
ferent parameters like impingement angles and percentages of reinforcements. It is
obtained from the graph that the erosion rate is 0.674 and erosion efficiency is 1.2%
which are maximum at 1wt% of CB and 30° impingement angle. From the above
graph, it has been assumed to behave as a semi-ductile in nature. Hence, this com-
posite material finds its use in pipe, housing, ships, sports equipment, and door and
window panel.

References

1. U.S. Tewari et al., Solid particle erosion of carbon fibre – and glass fibre – epoxy composites, *Compos. Sci. Technol.* 63 (2003) 549–557.
2. W.G. Sawyer et al., A study on the friction and wear behavior of PTFE filled with alumina nanoparticles, *Wear* 254 (5–6) (2003) 573–580.
3. S. Biswas and A. Satapathy, Tribo-performance analysis of red mud filled glass-epoxy composites using Taguchi experimental design, *Mater. Des.* 30 (8) (2009) 2841–2853.
4. S. Biswas and A. Satapathy, A study on tribological behavior of alumina-filled glass-epoxy composites using Taguchi experimental design, *Tribol. Trans.* 53 (4) (2010) 520–532.
5. A. Patnaik et al., Parametric Optimization Erosion Wear of Polyester-GF-Alumina Hybrid Composites using the Taguchi Method, *J. Reinf. Plast. Compos.* 27 (10) (2008) 1039–1058.
6. A. Patnaik et al., Implementation of Taguchi Design for Erosion of Fiber-Reinforced Polyester Composite Systems with SiC Filler, *J. Reinf. Plast. Compos.* 27 (10) (2008) 1093–1111.
7. V.K. Srivastava and A.G. Pawar, Solid particle erosion of glass fibre reinforced flyash filled epoxy resin composites, *Compos. Sci. Technol.* 66 (15) (2006) 3021–3028.
8. P. Mishra and N. Deep, Fabrication, Modeling and Analysis of The Erosive Wear Properties of Multi Walled Carbon Nanotube Reinforced PMMA Composite Using Taguchi Approach, *Int. J. Recent Sci. Res.* 6 (10) (2015) 6802–6806.
9. A. Suresh, a. P. Harsha, and M.K. Ghosh, Solid particle erosion of unidirectional fibre reinforced thermoplastic composites, *Wear* 267 (9–10) (2009) 1516–1524.
10. A.P.S. Chauhan and K. Chawla, Comparative studies on Graphite and Carbon Black powders, and their dispersions, *J. Mol. Liq.* 221 (2016) 292–297.
11. L.A. Kartsova and A.A. Makarov, Properties of Carbon Materials and Their Use in Chromatography, 75 (11) (2002) 1725–1731.
12. O. a. Shenderova and D.M. Gruen, *Ultrananocrystalline Diamond: Synthesis, Properties and Applications*, (2012).
13. W. Zhang, R.S. Blackburn, and A.A. Dehghani-Sanij, Effect of carbon black concentration on electrical conductivity of epoxy resin-carbon black-silica nanocomposites, *J. Mater. Sci.* 42 (18) (2007) 7861–7865.
14. J.W.M. Noordermeer and W.K. Dierkes, Carbon Black Reinforced Elastomers, *in* Encycl. Polym. Nanomater., *Springer Berlin Heidelberg*, Berlin, Heidelberg, (2015): pp. 1–14.
15. A. Rout et al., Erosion wear performance analysis of polyester-GF-granite hybrid composites using the Taguchi method, *Procedia Eng.* 38 (2012) 1863–1882.
16. M. Barekat, R.S. Razavi, and F. Sharifianjazi, Synthesis and the Surface Resistivity of Carbon Black Pigment on Black Silicone Thermal Control Coating, *Synth. React. Inorganic, Met. Nano-Metal Chem.* 45 (4) (2015) 502–506.
17. S.A.E. Kassim et al., Modelling the DC electrical conductivity of polymer/carbon black composites, *J. Electrostat.* 72 (3) (2014) 187–191.
18. R. Sengupta et al., A review on the mechanical and electrical properties of graphite and modified graphite reinforced polymer composites, *Prog. Polym. Sci.* 36 (5) (2011) 638–670.
19. A.P. Harsha and S.K. Jha, Erosive wear studies of epoxy-based composites at normal incidence, *Wear* 265 (7–8) (2008) 1129–1135.

Al MMC Reinforced with Al_2O_3 and CU Prepared by Stir-Casting Method

Rajeev Ranjan and Abhay Ranjan Kumar Singh

1 Introduction

Metal matrix composites (MMCs) Stir casting an economical process for the fabrication of aluminium metal matrix composites. There are many parameters for this process as for like to improve the strength and mechanical properties and fine-tune the microstructure. Aluminium MMCs are widely used in aircraft, automotive industries and aerospace and other fields. Aluminium metal matrix composites materials are the combination of two or more constituents in which one is reinforcements and other is matrix; when we are making three composites, specimen of aluminium and Al_2O_3 and copper are mixed with each other by stir-process method in a crucible at 660 °C temperature. The speed of rotation of stir is 160–210 rpm. The control of speed is very important for successful casting. Rotational speed makes an influence on the structure. But we also mixed magnesium (Mg) to make flowability of molten metal, because it is easy to pour molten metal in the mould and give desirable shapes. And each specimen has the same amount of Al, 500 g. But the percentage of alumina (Al_2O_3) and copper is of different–different percentage in aluminium. And 4 g of Mg is mixed in each specimen for flowability (Table 1).

Stir casting: Stir casting is a liquid phase of composite material fabrication in which ceramic particles (non-metallic particles) are mixed with metal by mechanical stirring

- to achieve uniform distribution of the reinforcement material;
- to achieve flowability (wettability) between two metals (substances);

R. Ranjan (✉)
Department of Mechanical Engineering, Amity University Jharkhand, Ranchi, India
e-mail: raj.apx.mech@gmail.com

A. R. K. Singh
Department of Mechanical Engineering, Poornima University, Jaipur, Rajasthan, India
e-mail: ab.singh444@gmail.com

Table 1 Properties of Al

Properties of Aluminium	Melting point temp. (°C)	Density (g/cm^3)	Density at molten state (g/cm^3)	Molar mass (g/mol)	Boiling temp. (°C)
	660.3	2.7	2.37	101.9	2977

Fig. 1 Stir-casting machine set-up

- to achieve homogenous composites (Fig. 1).

2 Process Parameters

2.1 *Stirring Speed*

Stirring speed is very important for binding between matrix and reinforcement; i.e. it makes flowability (wettability) and homogeneous mixture of both metals. In our project, stirring speed is 160–210 rpm. The blade angle and number blades decide

the flow pattern of the liquid metals. All are required for uniform distribution of reinforcement in liquid metal to achieve a uniform mixture of composites.

2.2 Stirring Temperature

Aluminium melts at 660 °C and copper melts at 1084 °C. But when aluminium melts at 660 °C, copper melts at high temperature. Copper is a reinforcement metal and it is mixed with aluminium metal. So, copper is also preheated and then mixed with aluminium; before mixing, copper and Al$_2$O$_3$ are kept at the same temperature as aluminium, because if mixed in homogeneous temperatures it removes all moisture as well as gases present in the reinforcement. Reinforcement is heated to 660 °C for 35–40 min. Casting process Aluminium metal matrix composites due to very low wettability of Aluminium metal. And the result is non-uniform distribution and poor mechanical properties.

Before moulding, preheating of the mould is good for pouring the metal in mould because it helps in the remove all corrosion and entrapped gases from the slurry go into the mould. Mould is heated at 500 °C for 1 h.

2.3 Addition of Magnesium

Magnesium is two times mixed with aluminium alloy, without mixing Al$_2$O$_3$ and CU and after mixing Al$_2$O$_3$ and copper.

When aluminium is melted in crucible furnace, magnesium is wrapped in Al foil and then mixed with Al liquid in the crucible. After some time, mixed alumina and copper in the crucible is again mixed with Mg after 5 min in aluminium alloy, because it helps to make flowability of material easy when molten metal is poured into the mould.

3 Experimental Works

The simple and most commercially used techniques are stir-casting technique and vortex technique. At first, all apparatus and equipment are cleaned like crucible, aluminium metal pieces and mould. After cleaning the Al, weigh it on weight balance machine. Weigh three times aluminium metal of 500 g and place it in separate space, and then again weigh three times copper powder on weight balance machine with different–different percentage of 500 g aluminium and place it in separate space to easily understand the sample of group. After copper is weighed again, weigh Al$_2$O$_3$ powder three times with different–different percentage of 500 g aluminium and add

4 g magnesium in each specimen to increase the flowability of the reinforcement
alloy.

After weighing, these are made into three sample groups; each group having Al,
Al_2O_3, Cu and Mg. Because it is easy to understand the composition of sample 1,
sample 2, sample 3. When there are make composite of reinforcement in the furnace
so that it is very important preplan work.

For the first sample, the machine starts with placing empty crucible in the furnace.
Put 500 g of aluminium in the crucible. The heating temperature is then gradually
increased up to 660 °C. After one hour, aluminium melts and then required amount
of the reinforcement powder is mixed. Reinforcement is heated for 45 min at tem-
perature 660 °C. When matrix is reached at semisolid condition at 645–650 °C, then
4 g of magnesium is mixed with the reinforcement alloy. Magnesium is wrapped in
foil of aluminium and then mixed with reinforcement alloy. After 3–5 min, the scum
powder is added which forms a scum layer of impurity on liquid surface which is
to be removed. After this, stirring is started and continues up to 5–15 min; stirring
rpm is gradually increased from 0 to 210 rpm. Speed control is very necessary for
making successful composition. Preheated reinforcement is added during 5 min of
stirring by pouring the reinforcement with the help of conical hopper. The flow rate
reinforcement measured is 0.7 g per second. Stir rpm is gradually decreased to zero.
The molten composite is poured in the metallic mould very fast with time taken for
the composite matrix to settle down at the crucible bottom. The flow rate of molten
material is made uniform to avoid the tapping of gas in the specimen (Figs. 2, 3 and
4; Table 2).

Fig. 3 Weight balance
machine

Fig. 4 Melting the base
metal (Al) in the furnace

Table 2 Compositions of samples

Sample No.	Aluminium (g)	Copper (%)	Alumina (%)	Mg (g)
1	500	2	3	4
2	500	3	4	4
3	500	4	5	4

4 Result

We have prepared three different specimens of different compositions to improve the
strength-to-weight ratio of aluminium.

5 Conclusions

Following conclusions are obtained from the present work:

1. Stir-casting process is economical for the manufacturing Al MMCs having low density.
2. Isotropic material can be manufactured successfully.
3. Addition of magnesium is important to increase flowability.
4. Preheating the copper at 660 °C will solidify the copper. So, preheat the copper at 1084 °C and then reinforce it in the aluminium metal matrix.
5. Preheat temperature of reinforce of material and mould.

Author Index